Mixing, velocity and turbulence characteristics of shaken bioreactors

Weheliye Hashi Weheliye

A thesis submitted for the degree of
Doctor of Philosophy
in the
University of London

University College London
Department of Mechanical Engineering
Fluid Mechanics Group

September 2013

In the name of Allah, the Beneficent, the Merciful.

Abstract

The thesis describes an experimental investigation of the flow in a shaken bioreactor of cylindrical geometry with a flat bottom. Several reactor designs can be distinguished that attain mixing in different ways: oscillatory flow mixers (OFM), static mixers, stirred vessels and shaken bioreactors. Shaken bioreactors are often small-scale mixers (microwells) employed in the early stage of bioprocess development (i.e. microbial fermentation, bioconversion and product recovery techniques), before the developed process is implemented in a large-scale industrial stirred tank. However, despite their wide use, little is known about the fluid mechanics of these systems. In the present study Particle Image Velocimetry (PIV) measurements are carried out to determine the variation of the flow dynamics in a cylindrical shaken geometry for different operating conditions such as medium height, shaking frequency, orbital shaking diameter, cylinder inner diameter and fluid viscosity.

In the first part phase-resolved measurements are carried out with PIV to provide a thorough characterisation of the flow and mixing dynamics occurring in a cylindrical shaken bioreactor for a fluid of low viscosity (i.e. water). From this analysis a flow scaling law based on the Froude number, Fr, is identified, which correlates the shape and inclination of the free surface to the occurrence of a flow transition. More specifically it was found that at low Fr the mean flow is

characterised by a toroidal vortex with its axis aligned along the azimuthal direction, while after flow transition the free surface exhibits a phase lag and a vortical structure with a vertical axis that precesses around the cylinder axis is present.

In the second part of the thesis flow characteristics, such as the interfacial area, circulation time, vortex size and location, kinetic energy and viscous dissipation rate of kinetic energy for a fluid of low viscosity are analysed in depth. The free surface interfacial area was directly measured by image analysis to assess oxygen transfer potential and was compared to an analytical solution valid for low Fr. The non-dimensional time and length scales of the vortical structures occurring in the cylindrical bioreactor were determined to provide an insight into the mixing dynamics, while a Reynolds decomposition analysis of the kinetic energy was carried out to assess the onset of a laminar-turbulent flow transition with increasing Fr. Direct measurements of the viscous dissipation rate of the kinetic energy, ϵ, were obtained across the tank to help assess micro-mixing and identify regions in the bioreactor experiencing higher levels of viscous stresses that can potentially affect cell growth.

In the third part of the thesis the flow obtained with Newtonian fluids of higher viscosity is investigated and the flow scaling law determined for water is extended to a broader range of viscosity. A flow transition map based on Fr and Re is identified and four main regions characterised by different mean flow dynamics are shown. The turbulent kinetic energy levels and shear rate magnitudes are assessed for different combinations of Fr and Re.

The results offer valuable new information for the design of mixing processes and crucial data to validate computational fluid dynamics simulations of cylindrical shaken bioreactors.

Acknowledgements

I would like to acknowledge the precious help of my two supervisors, Dr. Andrea Ducci and Professor Michael Yianneskis. I feel great pleasure in expressing my gratitude to my first supervisor Dr. Andrea Ducci for his expert guidance and constant encouragement throughout the period of the project work. I am extremely indebted for his motivation, professional acumen and precious time that he devoted for the successful completion of my project work. I am also indebted to my second supervisor Prof. Michael Yianneskis for his expert guidance, teaching and a personal interest in my success.

I would also wish to thank all the PhD students that I met within the walls of our PhD office for all the conversations, jokes and drinks we shared.

Finally and most importantly, I am indebted to my family for their trust and endless support throughout my studies. Especially my mother for her constant support, encouragement, everlasting care and love throughout my studies. Last but not least, I am very thankful to my wife who is always there to hold and support me during the most painful moments of my life.

My research has been funded by the Engineering and Physical Sciences Research Council (EPSRC), for whose support I am most grateful.

Contents

Nomenclature

CFD	Computational Fluid Dynamics
PIV	Particle Image Velocimetry
3D	Three-Dimensional
2D	Two-Dimensional

$\varDelta\alpha$	Angle between two stagnation points	°
$\varDelta\beta$	Angle delay of the precessional vortex	°
$\varGamma^*$	Space average of the circulation intensity for the phase average flow field	s^{-1}
$\overline{\varGamma}^*$	Space average of the circulation intensity for the ensemble-average flow field	s^{-1}
ϵ	Viscous dissipation rate of kinetic energy	$\mathrm{m}^2/\mathrm{s}^3$
η_k	Smallest dissipative scale	m
θ	Free surface angle	°
μ	Dynamic viscosity	kg/(s m)
ν	Kinematic viscosity	m^2/s

ν_w	Kinematic viscosity of water	m^2/s
ρ	Density of fluid	kg/m^3
ϕ	Phase angle of the table	°
Φ_v	Rate of viscous dissipation of kinetic energy per unit of viscosity	s^{-2}
ω_i	Vorticity components in the ith direction	s^{-1}

a	Gas-liquid interfacial area per unit of volume	m^{-1}
a_o	Constant of proportionality	-
a_{ow}	Constant of proportionality for water	m
d_i	Inner diameter of the cylinder	m
d_o	Orbital diameter	m
d_v	Toroidal vortex diameter for the phase average flow field	m
$\overline{d_v}$	Toroidal vortex diameter for the ensemble-average flow field	m
F_c	Centrifugal force	kg m/s^2
F_g	Gravitational force	kg m/s^2
Fr	Froude number	-
Fr_c	Critical/transitional Froude number	-
g	Gravitational acceleration	m/s^2
h	Fluid height at rest	m
h_f	Fluid height at the left hand side wall	m

$\varDelta h$	Free surface height	m
I_a	Gas-liquid Interfacial area	$\mathrm{m^2}$
k_{ij}	Kinetic energy of the periodic motion estimated from the ith and jth velocity components	$\mathrm{m^2/s^2}$
k_{ij}^*	Space average of the kinetic energy of the periodic motion	$\mathrm{m^2/s^2}$
k'_{ij}	Kinetic energy due to the random velocity fluctuations in the ith and jth directions	$\mathrm{m^2/s^2}$
k'^*_{ij}	Space average of the kinetic energy due to the random velocity fluctuations	$\mathrm{m^2/s^2}$
k_L	Gas-liquid mass transfer coefficient	m/s
k_La	Volumetric gas-liquid mass transfer coefficient	$\mathrm{s^{-1}}$
m	Mass	kg
N	Shaking frequency	$\mathrm{s^{-1}}$
P	Power consumption	$\mathrm{kg\ m^2/s^3}$
P_v	Volumetric power consumption	$\mathrm{kg/(m\ s^3)}$
Re	Reynolds number	-
r_i	Inner radius of the cylinder	m
r_o	Orbital radius	m
r_{wc}	Radial location of the centre of the vortex	m
S_{ij}	Strain rate tensor	$\mathrm{s^{-1}}$
S_{ij}^*	Space average of the strain rate tensor	$\mathrm{s^{-1}}$

t_m	Mixing time	s
$\mathit{\Delta} T$	Time between two consecutive images	s
T^*	Space average of the circulation time for the phase average flow field	s
$\overline{T}^*$	Space average of the circulation time for the ensemble-average flow field	s
u_i	Velocity in the ith direction,	m/s
$\langle u_i \rangle$	Phase average of the velocity component in the ith direction	m/s
u_i'	Random velocity fluctuations in the ith direction	m/s
V_f	Nominal fluid volume	m^3
V_{fm}	Measured fluid volume	m^3

List of Tables

List of Figures

Chapter 1

Introduction

1.1 Background

Mixing operations play a key role in the chemical and biochemical process industries (Butcher and Eagles, 2002). Industrial costs related to mixing operating problems are estimated to be 0.5-3% of total turnover ($2-11 billion/year). Static mixers, stirred and shaken vessels are the main types of the most widely used reactors in chemical and biochemical industries. In static mixers mixing is induced by series of geometric elements fixed within a pipe. In stirred tanks and shaken flasks mixing is achieved by the rotating motion of an impeller and of the tray that is holding the flasks, respectively.

In recent years micro-scale technology has been employed in the early stages of bioprocess development (for example, microbial fermentation, bioconversion and recovery techniques), before the developed process is implemented in a large-scale industrial stirred tank. One such micro-scale approach relies on the use of microwell plates, where complete mixing is achieved by shaking rather than stirring. However, despite the extended use of shaken bioreactors (flasks and microwells), it has been reported that less than 2% of the publications dealing with engineering aspects of bioreactors are dedicated to shaken bioreactors (Büchs, 2001), and their importance for many biochemical processes is often underestimated. To put into perspective a vast amount of publications on bioprocess design is already available in stirred tank reactors (see for example the works of Lavery and Nienow, 1986; Escudie *et al.*, 2004), and accurate scaling between shaken and stirred bioreactors is hindered by the lack of engineering works for shaken devices.

Ensuring effective mixing in such devices is essential, as the presence of spatial gradients in culture parameters (such as dissolved gasses, concentration and shear rate) is often an important - and potentially problematic - consideration in bioreactors (Lara *et al.*, 2006). Such gradients are often strongly affected, if not controlled, by the hydrodynamic phenomena in the bioreactors, but accurate knowledge of and information on the physical parameters affecting the cultures is lacking, while little is known about their characteristic properties, and often the few publications available provide contradictory advice concerning the most appropriate operating conditions to be employed (Büchs, 2001). Only relatively recently methods that facilitate the selection of optimized culture conditions have been described (Klöckner and Büchs, 2012).

Furthermore, larger shaken bioreactors have become available in pilot and industrial scale in the form of single use cylindrical bags on controllable shaken platforms (Zhang *et al.*, 2009, 2010). This offers a novel scale-up platform and eliminates current bottlenecks by improving process reproducibility and robustness upon scale-up. From this perspective a systematic characterization of transport phenomena in the bioreactor under different conditions is timely and necessary to derive scaling laws and parameters.

The motivation of the present study is to address the lack of detailed knowledge of the mixing processes outlined above and to enhance understanding of the phenomena involved in orbitally shaken bioreactors. To this end, it is essential to throw light on the magnitude and distribution of mixing, interfacial area, energy dissipation, shear stress and volumetric power consumption involved, in order to help improve reactor design and operation. For some of the phenomena studied, techniques and methodologies previously employed to improve understanding of and optimize mixing in stirred vessels (Ducci and Yianneskis, 2005; Ducci *et al.*, 2008; Bouremel *et al.*, 2009; Doulgerakis *et al.*, 2011) are harnessed in this work to shed light into the corresponding processes encountered in a shaken reactor.

In the following section the main findings and techniques employed in previous numerical and experimental investigations of the flow characteristics in a shaken bioreactor are reviewed. The survey was used to formulate the objectives of the present investigation, which are listed in Section 1.3. Finally, the chapter closes with an outline of the thesis in Section 1.4.

1.2 Literature review

The current literature review aims at providing a thorough account of the experimental and computational works dealing with shaken bioreactors. The performance of shaken bioreactors, in terms of mixing and mass transfer, is inferior to that obtained with conventional stirred tank fermentors. Mixing in stirred tanks relies on the mechanical agitation of the impeller, usually in conjunction with baffles. This is a much more efficient mechanism of dispersal of fluid elements. Various devices are employed in shaken bioreactors to try to improve the mixing action, including indentations in the walls, and hanging one or more baffles from the lid of the flask. Baffled shaken bioreactors are employed when high or increased levels of oxygenation are required as reported by Peter *et al.* (2006).

The downside of baffled shaken bioreactors consists in the danger of a wetted sterile plug and lower reproducibility of experimental results (McDaniel *et al.*, 1965; Henzler and Schedel, 1991). Only few studies dealing with baffled shaken bioreactors are available in the literature, and there is practically no characterisation of this reactor type from a chemical engineering viewpoint (Peter *et al.*, 2006). Unbaffled shaken bioreactors can be used in many experiments which can be carried out simultaneously with minimal material expense and practically no supervision. Furthermore, many types of shaken bioreactors are available in the market, but the most widely used are microwells, Erlenmeyer flasks, spherical and cylindrical vessels.

The literature review has been organised in five sub-sections with the intent to highlight the main findings on the following engineering aspects, which are the most relevant to the process design of shaken bioreactors:

- Flow dynamics
- Mixing time, M_t
- Power consumption, P
- Interfacial area, I_a
- Oxygen Transfer Rate, OTR, and volumetric mass transfer coefficient, k_La

1.2.1 Flow dynamics

Before proceeding with the discussion it is necessary to make a short digression into the definition of the Froude number, Fr, which is an essential parameter to obtain a characterisation of the flow and to formulate an accurate scaling law of the bioreactor system. The Froude number is the ratio between the characteristic flow velocity and the wave propagation velocity:

$$Fr = \frac{v}{\sqrt{gl}} \tag{1.1}$$

Where v is the characteristic velocity, l is the characteristic length scale and g is the gravitational acceleration. In their work, Tissot *et al.* (2010) used this definition, and estimated their characteristic velocity based on the average of the orbital and cylinder diameters, while the inner cylinder diameter, d_i, was taken as the characteristic length scale (Equation 1.2).

$$Fr = \frac{(d_i + d_o)\pi N}{\sqrt{g d_i}} \tag{1.2}$$

In some studies more emphasis is given to the ratio between inertial and gravitational forces, and the first power of the gravitational acceleration is sought. In these cases the definition of Fr is the squared version of that in Equation 1.1 (Massey, 1990). In the field of shaken bioreactors, the latter definition has been extensively used by Büchs *et al.* (2000a), who distinguished between axial, Fr_a, and radial, Fr_r, Froude numbers based on Equation 1.3, where the characteristic length scale used, d, is either the orbital or flask diameter, respectively.

$$Fr = \frac{2(\pi N)^2 d}{g} \tag{1.3}$$

For consistency with most of the published literature in shaken bioreactors, the Froude number definition of Equation 1.3 with the orbital diameter, d_o, being the characteristic length scale is employed in the rest of the thesis.

The study of Gardner and Tatterson (1992) is one of the first reported in the published literature that investigated the flow and mixing dynamics in a shaken, partially-filled, cylindrical vessel. Dye visualization techniques with different degrees of mixture of water and corn syrup were employed to assess the variation of the homogenization time with increasing Reynolds number, $Re = NT^2/\nu$, where the characteristic length scale, T, is the beaker diameter, while N and ν are the shaking frequency and fluid viscosity, respectively. The authors identified three mixing regimes: i) a laminar regime, for Re=0.8-1000, controlled by a toroidal vortex and characterised by the homogenization time being inversely proportional to Re; ii) a transitional regime, for $Re\sim$1000, characterised by a vertical axial vortex inducing unmixed dye regions at the top and at the bottom of the filling volume; iii) a turbulent regime at higher Re where the flow is dominated by severe splashing and the homogenization time is nearly constant.

Experimental flow visualisations in shaken bioreactors, were also carried out by Büchs *et al.* (2000a) who were the first to identify the so called “out-of-phase” phenomenon. This phenomenon was characterised by an amount of liquid not following the movement of the shaking table, and the authors claimed it was associated with a reduction in the volumetric power consumption, mixing time and the gas/liquid mass transfer. However no explanation was offered for this phenomenon. The operating conditions for the occurrence of the out-of-phase phenomenon were determined by Büchs *et al.* (2000a), by combining experimental visualisations and volumetric power consumption measurements. The out-of-phase phenomenon was characterised in a Erlenmeyer flask, and was shown to depend on a non-dimensional number denoted as the phase number, Ph, which is given in Equation 1.4.

$$Ph = \frac{d_o}{d_i}\left\{1 + 3log_{10}\left[\frac{(2\pi N){d_i}^2}{4\nu} \times \left(1 - \sqrt{1 - \frac{4}{\pi}\left(\frac{{V_f}^{1/3}}{d_o}\right)^2}\right)^2\right]\right\} \tag{1.4}$$

According to Büchs *et al.* (2000a) for $Ph > 1.26$ and $Fr_a > 0.4$ the flow is “in-phase” while “out-of-phase” conditions occur for $Ph < 1.26$ and $Fr_a > 0.4$. In agreement with Equation 1.4 the experiments of Büchs *et al.* (2000a) showed that out-of-phase conditions are more likely to occur for fluids of higher viscosity.

Flow dynamics in shaken bioreactors has been extensively studied using Computational Fluid Dynamics (CFD). Kim and Kizito (2009) carried out numerical simulations and experimental observations of the flow in a cylindrical shaken bioreactor, with internal diameter, d_i=87 mm, moving on a circular orbit with diameter of d_o=40 mm. They compared the ensemble-averaged flow fields (Equation 1.5) obtained for different operating conditions: $\nu=1 \times 10^{-6}-1.6 \times 10^{-5}$ m^{2}s^{-1}, N=60−120 rpm and V_f=119−238 ml.

$$\overline{\mathbf{u}}(r, z) = \frac{\sum \mathbf{u}(r, z, t)}{N_\phi} \tag{1.5}$$

Where N_ϕ is the total number of velocity fields (i.e. across all time steps) irrespective of the angle ϕ. The boundary conditions at the free surface consisted of zero tangential stresses and negligible normal stresses, provided that the free surface is assumed nearly horizontal. The no-slip boundary condition was applied at the solid walls. For an operating condition of V_f=238 ml and $\nu=1\times10^{-6}$ m^{2}s^{-1}, two large counter-rotating vortices denoted as "A" in Figure 1.1 (a) are observed closer to the cylinder axis, while two small vortices, denoted as "B", are found next to the walls of the cylinder when ν is increased (Figures 1.1 b-d). It should be noted that the smaller vortices are rotating in the opposite direction of the "A" pair. From Figures 1.1 (a-d) it is evident that, as the viscosity of the fluid is increased, the "A" vortices start to shrink while vortices "B" increase in size. For the maximum value of viscosity examined, vortices "A" have completely disappeared as illustrated in Figure 1.1 (d). Based on these considerations it is considered evident that Re plays a key role in the flow dynamics of shaken bioreactors.

The numerical simulations of Discacciati *et al.* (2013) and Zhang *et al.* (2009) allowed visualisation of the free surface shape in a cylindrical bioreactor. The cylindrical shaken bioreactor considered in the simulation of Discacciati *et al.* (2013) had an inner diameter, d_i=144 mm, and was filled to a height of 100 mm with an aqueous solution of 98.5% glycerin (μ=1 Pa s). They run simulations for several shaker table speeds, N=85-125 rpm, for an orbital diameter of, d_o=25 mm. Two sets of simulations were carried out to assess the accuracy of the free surface prediction when the no-slip condition was applied at the wall either to the vertical or tangential velocity components.

The free surface wave amplitude measured by Discacciati *et al.* (2013) with the vertical slip condition showed good agreement with their visual observation at low shaking frequencies, N=85-105 rpm. However for higher shaking frequencies, N=110- 125 rpm, the simulation showed larger free surface amplitude waves in comparison to the experimental observation. Furthermore, with the vertical slip boundary condition, the simulated wave amplitude increased by a factor of 3 between 105 rpm and 125 rpm, although the visual observation data showed a two-fold increase.

When the tangential slip boundary condition was imposed on the side walls of the cylinder, the numerical simulation of the free surface wave amplitude showed a good agreement with that of the experimental measurements for both low shaking frequencies, N=85-105 rpm, and high shaking frequencies, N=110-125 rpm. They concluded that the boundary condition selected did not affect significantly the free surface at low shaking speeds, while when the shaking frequency was increased beyond 105 rpm, the choice of the boundary conditions became a critical aspect.

Zhang *et al.* (2009) also examined the free surface shape numerically and experimentally. The cylindrical shaken bioreactors considered by Zhang *et al.* (2009) had an inner diameter of 172 mm and 287 mm and were filled to fluid heights of 110 mm and 190 mm, respectively, with μ=1 mPa s (water-like viscosity). They conducted experiments and simulations for several shaking frequencies, N=60-120 rpm, and for an orbital diameter, d_o=50 mm. Zhang *et al.* (2009) observed that the free surface shape was mainly influenced by two parameters: shaking frequency, N, and the container diameter, d_i. The free surface exhibited a smooth and elliptic shape at low shaking frequencies of N=80 rpm and 60 rpm, for bioreactor sizes of d_i=172 mm and 287 mm, respectively. At higher shaking frequencies, N=120 rpm and 100 rpm, an inclined vortex and a wavy free surface were observed for d_i=172 mm and 287 mm, respectively. These results suggest that improved scaling protocols should predict a lower speed for a larger container in order to achieve analogous flow conditions between shaken bioreactors of different size.

The flow fields in a 250-ml Erlenmeyer flask and in 24-well and 96-well bioreactors were analysed by Zhang *et al.* (2005) and Zhang *et al.* (2008), respectively. Table 1.1 shows the operating conditions investigated in the two studies. Zhang *et al.* (2005) presented the instantaneous velocity vector field and the energy dissipation profile of the air and liquid in a 250-ml Erlenmeyer flask for d_o=40 mm and N=200 rpm. In this study no-slip boundary conditions were applied at the bioreactor walls. The instantaneous flow field showed that on one side of the flask, near the bottom of the bioreactor, the velocity magnitude and direction of the liquid was uniform, while at the opposite side of the flask they found that the gas velocity flow field was more randomly distributed. The energy dissipation contours showed that the majority of the energy was being dissipated in the regions close to the walls of the flask and the maximum energy dissipation level was ϵ=0.01 m^2s^{-3}.

Zhang *et al.* (2008) investigated the instantaneous velocity vector field of the gas and liquid phases and the energy dissipation distribution of 24-well and 96-well bioreactors for d_o=3 mm and N=1000 rpm. For the 24-well bioreactor two vortices were observed below the free surface of the liquid. However the vortices were relatively small ($\approx \frac{1}{3}d_i$) and extended only over the upper half of the filling volume. For these shaking conditions the magnitude of the liquid velocity decreased at the base of the well. For the 96-well bioreactor the velocity vectors indicated a significantly different flow, with the bulk of the liquid phase moving across the reactor diameter. For both the 24-well and 96-well bioreactors the majority of the kinetic energy was dissipated at the walls. A comparison between the energy dissipation rates for the two geometries showed that a larger fraction (approximately 90%) of the total liquid and gas volume is exposed to higher kinetic energy dissipation in the 96-well bioreactor than in the 24-well bioreactor. However for both bioreactors considered in their study the maximum energy dissipation obtained was ϵ=0.1 m^2s^{-3}.

1.2.2 Mixing time, M_t

Mixing of the medium around the cells is necessary for successful cell growth. Mixing provides more uniform distribution of gases, concentrated additives, fixatives and nutrients to cells. Nevertheless, intense mixing can cause damage to the cells in the shaken bioreactor. Mantell and Smith (1983) found that in many circumstances a turbulent flow should not be used to obtain a higher degree of mixing, because plant cells are very susceptible to shear deformation from the surrounding fluid. Suh (2000) reports that there are two aspects affecting the cellular growth, the stirring effect and shear deformation, and it is desirable to enhance the former while keeping the latter to low levels.

Two approaches can be employed to measure mixing time: local and global. Local approaches are based on physical measurements such as pH and conductimetry. These physical measurements provide information on mixing at the location where the probe is situated. Global methods (e.g. colorimetric) are often performed using visual observation (Kaeppel, 1979).

Tissot *et al.* (2010) carried out an extensive study on mixing time in cylindrical shaken bioreactors. In their study mixing time was measured by the Dual Indicator System for Mixing Time (DISMT) which can be used to gain insight into the local and global mixing occurring in the shaken vessel. DISMT is a colorimeteric method using an acid/base reaction in the presence of two pH indicators. With this method, the mixing time is defined as the time needed for the liquid to become completely yellow, corresponding to 95% of the final mixing time (Melton *et al.*, 2002). Tissot *et al.* (2010) carried out DISMT experiments to investigate the effects of the liquid filling volume, V_f, of the orbital diameter, d_o, and of the inner diameter, d_i, on the mixing time.

To study how the filling volume, V_f, affected the mixing time, experiments were carried out on a 30 l cylindrical vessel for filling volumes of V_f=8 l,13 l and 18 l, shaking frequencies of N=80-130 rpm, an inner diameter of d_i=287 mm and an orbital diameter of d_o=50 mm. For all three filling volumes similar free surface shapes were observed for the same shaking frequency, N. Furthermore, for V_f=18 l at N=80-85 rpm, a zone appeared in the liquid close to the bottom of the cylinder in which mixing occurred mainly due to diffusion. Their study showed that the diffusional zone disappeared with increasing N, when the wave formed by the free surface was at least half the liquid height at rest. For all the fluid heights tested they observed a poorly mixed zone in the centre of the bulk liquid, while mixing was more pronounced near the walls.

The second experiment aimed at determining the effect of the orbital diameter on mixing time. Experiments were again carried out on a 30 l cylindrical vessel for a filling volume of V_f=13 l, shaking frequencies of N=90-140 rpm, an inner diameter of d_i=287 mm and orbital diameters, d_o=25 mm and 50 mm. For N <115 rpm, the mixing times at d_o=50 mm were less than those for d_o=25 mm over the range of N tested. However, for N >115 rpm, no difference in the mixing time measured with the two shaking diameters was observed. It should be noted that Tan *et al.* (2011) concluded that the shaking diameter d_o had no significant effect on the mixing time in unbaffled Erlenmeyer flasks, in contrast to the study of Tissot *et al.* (2010) for a cylindrical shaken bioreactor.

The third study carried out by Tissot *et al.* (2010) addressed the effect of the inner diameter of the container on mixing time. Experiments were carried for a filling volume V_f=1 l, shaking frequencies N=100-140 rpm, inner diameters d_i=100, 130 and 160 mm and an orbital diameter d_o=50 mm. The shortest mixing time was observed in the cylinder with the largest d_i, whilst the cylinder with smallest d_i had the longest mixing time over the range of N tested. Further mixing time experiments were carried out by Tissot *et al.* (2010) in a production scale bioreactor of 1500 l nominal volume and comparisons with those obtained in a 30 l bioreactor showed that the main parameters affecting the mixing number, NT_m, were Fr, defined in Equation 1.2, and the orbital to cylinder diameter ratio, d_o/d_i. The mixing time scaling law of Equation 1.6 was formulated to scale between the two bioreactor sizes (e.g. 1500 l and 30 l), provided that d_o/d_i is kept constant for the two configurations.

$$(NT_m)_{1500l} = (NT_m)_{30l}\frac{d_{o_{30l}}}{d_{o_{1500l}}} \tag{1.6}$$

where $d_{o_{30l}}$ and $d_{o_{1500l}}$ are the orbital diameters for bioreactors with nominal volume of 30 l and 1500 l, respectively. The correlation between the mixing time and the free surface shape allowed to identify three different Fr ranges characterised by different dynamics. For low Froude number, Fr <0.7, the free surface was flat and the majority of the mixing occurring in the cylinder was due to diffusion. However near the free surface more rapid mixing was observed due to convection. The overall mixing time in the reactor was measured to be 270 s. At Fr=0.8, the mixing time decreased to 60 s and the diffusional zone started to decrease in size. For higher Froude number, Fr=0.9, they observed turbulence and small vortices at the free surface and the mixing time was reduced further to 30 s. It should be also noted that the shape of the free surface was wavy at Fr=0.9.

Mixing time measurements in a cylindrical shaken bioreactor were obtained by Kato *et al.* (2001) using a conductivity probe (local approach). In their study a pole, referred to as the "current pole", was placed at the centre of the cylinder in order to improve mixing. Several experiments were carried out with operating parameters such as inner cylinder diameter, orbital diameter, shaking frequency and fluid height varying in the ranges of d_i=85-206 mm, d_o=10-40 mm, N=100-200 rpm, and h=85-206 mm, respectively. From their study they demonstrated that the "current pole" improved significantly the vessel mixing dynamics, with a 20-30 % reduction in mixing time depending on the pole diameter employed.

Barret *et al.* (2009) carried out a detailed characterisation of liquid mixing and gas liquid mass transfer in microwell systems and their impact on suspension cell cultures. In their study mixing time was measured by the "iodine clock reaction" which is a global mixing time measurement method. In this case, mixing time is defined by the complete decolorisation of iodine. They carried out mixing time measurements on a 24-standard round well (24-SRW) plate for filling volumes of

V_f=800 μl, 1000 μl and 2000 μl, shaking frequencies of N=120-300 rpm, inner diameter of d_i=16 mm and an orbital diameter of d_o=20 mm. Similar results as those found by Tissot *et al.* (2010) were observed with mixing time decreasing for increasing N for all three liquid volumes examined, with the greatest variation occurring for the smallest V_f considered. Barret *et al.* (2009) showed that at high shaking frequencies, $N \geq$200 rpm, mixing seemed to have a positive effect on the cell growth, which did not occur for N=120-160 rpm at any of the three volumes examined.

1.2.3 Power consumption, P

Power consumption plays an essential role in fermentation of aerobic microbes and it is regarded as one of the most important factors in process scale up. As reported by Peter *et al.* (2006) the power consumption is related to oxygen transfer, carbon dioxide removal, hydrodynamic stress, and mixing time. Three different techniques are normally used to measure the power consumption in shaken bioreactors:

- Temperature measurement
- Torque measurement
- Direct measurement of the viscous dissipation rate of kinetic energy

The temperature method was first implemented by Sumino and Akiyama (1987) and is based on the heat balance of Equation 1.7.

$$\underbrace{mc_p\frac{dT_f}{dt}}_{\text{Thermal Energy}} = \underbrace{-UA(T_f - T_o)}_{\text{Heat Transfer}} + \underbrace{\dot{G}}_{\text{Heat Generation}} \tag{1.7}$$

Where m is the mass of the fluid, c_p the specific heat capacity, T_f the temperature of the fluid, T_o the surrounding temperature, UA the overall volumetric coefficient of heat transfer and $\dot{G}$ the rate of heat generated from the kinetic energy dissipated inside the shaken bioreactor. From the temperature data measured over an interval of time $\frac{dT_f}{dt}$ can be determined numerically by using a forward differentiation scheme. The coefficients UA and $\dot{G}$ can be estimated by finding the line that best fits the measured $\left(T_f - T_o, \frac{dT_f}{dt}\right)$ data points, where $UA/(mc_p$ is proportional to the slope of the line, while $\dot{G}/(mc_p)$ is the point of interception with the ordinate axis.

Kato *et al.* (2004) measured the volumetric power consumption, P_v, using the temperature measurement method described above for a large vessel with 5 l nominal volume, using both an insulated and a non-insulated configuration. Their study showed that similar values of the volumetric power consumption, P_v, were obtained for both the insulated and non-insulated vessels at fixed operating conditions. Kato *et al.* (2004) concluded that for smaller vessels (V_f ≈200 μl), such as Erlenmeyer flasks, which are similar to those reported in Sumino *et al.* (1972), heat insulation is required to obtain an accurate estimate of P_v because the temperature variation within the flask would be too fast for a non-insulated configuration, whilst for larger vessels heat insulation is not necessary. It is worth mentioning that the sensor used to measure the fluid temperature inside the vessel was attached to a pole placed vertically along the vessel axis. Based on a preliminary study of the group, Kato *et al.* (1997), Kato *et al.* (2004) assumed that the pole did not affect the power consumption within the shaken bioreactor.

A different method to determine the power consumption in shaken bioreactors is based on the measurement of the torque delivered by the drive of the shaker table. This method was first implemented by Büchs *et al.* (2000b). Mechanical friction losses and wind resistance of the shaken bioreactor are compensated by measuring the torque delivered by the drive of the shaker table when the shaken bioreactor is full of a solidified agar of the same weight as that of the working liquid. The volumetric power consumption is then estimated from the difference between the measurements of the torque obtained with the working liquid and the solidified agar as defined in Equation 1.8.

$$\frac{P}{V_f} = \frac{(M_1 - M_2)\, 2N\pi}{Z_f V_f} \tag{1.8}$$

Where M_1 is the torque delivered by the drive when the shaken bioreactor is full of working liquid, while M_2 is the one delivered when solidified agar is used and Z_f is the number of shaken bioreactors mounted on the shaker table.

Büchs *et al.* (2000b) conducted experiments on Erlenmeyer flasks with nominal volumes of 100-2000 ml, fluid viscosity of ν=1 × 10^{-6} $\mathrm{m^2 s^{-1}}$, filling volumes of V_f=4-400 ml, shaking frequencies of N=80-380 rpm, orbital diameters of d_o=25 mm and 50 mm and inner diameters of d_i=60-160 mm. As expected, Büchs *et al.* (2000b) found that the volumetric power consumption increased with increasing N. With increasing V_f the volumetric power consumption decreased, because the frictional area between the glass walls and liquid does not increase proportionally to fluid filling volume. However by varying the flask size for two different orbital diameters, d_o, they found that a higher volumetric power consumption is obtained for a larger flask compared to that obtained for a smaller flask for the same filling volume, V_f. As for the variation of orbital diameter, d_o, no significant effects were reported when fluids of low viscosity were considered. Other studies who implemented the torque measurement technique to estimate the volumetric power consumptions for low and high ν in baffled and unbaffled Erlenmeyer flasks include those of Büchs *et al.* (2000a, 2001) and Peter *et al.* (2004, 2006).

Klöckner *et al.* (2012) extended the work of Büchs *et al.* (2000b) to estimate the volumetric power consumption of cylindrical shaken bioreactors. Initially they examined the influence that the orbital diameter, d_o, had on the volumetric power consumption using the torque method. Measurements were carried out for the following configurations: V_f=6 l, d_i=286 mm, N=40-180 rpm, d_o=25-100 mm and ν=1×10^{-6} m^{2}s^{-1}. When d_o was increased a clear increase in the volumetric power consumption was observed. The influence of the fluid volume, V_f, on the volumetric power consumption, P_v, for a cylindrical bioreactor was studied employing the same operating conditions as before except for d_o that was kept fixed at 50 mm and V_f was ranged from 2-10 l. They observed that the volumetric power consumption increased with decreasing V_f.

A more rigorous approach in estimating the volumetric power consumption from a fluid mechanics point of view is reported by Zhang *et al.* (2005) and Zhang *et al.* (2008). In there studies the velocity field is first resolved by means of CFD simulations and the volumetric power consumption is then computed by integrating the local dissipation rate over the fluid volume as reported in Equation 1.9.

$$\frac{P}{V_f} = \frac{\int_v \mu \mathit{\Phi}_V dV_f}{V_f} \tag{1.9}$$

Where μ is the kinematic viscosity, V_f is the filling volume and $\mathit{\Phi}_V$ is the viscous dissipation function (see Equation 1.10), which can be expressed in terms of the strain and shear rates.

$$\begin{gathered}\mathit{\Phi}_V = 2\left[\left(\frac{\partial u}{\partial x}\right)^2 + \left(\frac{\partial v}{\partial y}\right)^2 + \left(\frac{\partial w}{\partial z}\right)^2\right] \ldots.. \\ + \left(\frac{\partial u}{\partial y} + \frac{\partial v}{\partial x}\right)^2 + \left(\frac{\partial v}{\partial z} + \frac{\partial w}{\partial y}\right)^2 + \left(\frac{\partial u}{\partial z} + \frac{\partial w}{\partial x}\right)^2\end{gathered} \tag{1.10}$$

Zhang *et al.* (2005) and Zhang *et al.* (2008) showed that for the operating conditions reported in Table 1.1, the volumetric power consumption (based on the direct measurement of the viscous dissipation rate of kinetic energy) increases with shaking frequency, N, and decreasing filling volume, V_f.

1.2.4 Interfacial area, I_a

The size of the interfacial area is a very important parameter in mixing operations where aeration/oxygenation of the shaken bioreactor is required. CFD analysis by Zhang *et al.* (2005) showed that the specific oxygen exchange area, a ($=I_a/V_f$), is a function of the energy dissipation rate for a 250-ml Erlenmeyer vessel, as reported in Equation 1.11.

$$a \propto \epsilon^{0.25} \tag{1.11}$$

However for the operating conditions shown in Table 1.1 for a 250-ml Erlenmeyer flask the relationship between the specific surface area, a, and the shaking frequency, N, for fixed orbital diameter, d_o, was found to be:

$$a \propto N^{0.6} \tag{1.12}$$

The interfacial area, I_a, for a cylindrical bioreactor was further investigated numerically and experimentally by Zhang *et al.* (2009). Initially they found that the interfacial area was mainly influenced by the inner diameter of the cylinder, d_i, and the shaking frequency, N. They first examined the interfacial area in a cylindrical bioreactor with an inner diameter, d_i=27 mm, orbital diameter, d_o= 50 mm, and shaking frequencies, N=160-240 rpm, and observed that the free surface was smooth and of elliptic shape with I_a=7.6 cm^2 and 9.2 cm^2 for N=200 rpm and 240 rpm, respectively. It should be noted that the interfacial area was estimated by photographic imaging. The second configuration employed in their study to investigate I_a consisted of a cylindrical bioreactor with an inner diameter, d_i=287 mm, orbital diameter, d_o= 50 mm, and shaking frequencies, N=70-80 rpm. In this case the interfacial area was determined from numerical simulations. The I_a obtained for this configuration at N=70 rpm was 671 cm^2, while at a higher shaking frequency, N=80 rpm, the free surface shape exhibited a wavy form with the interfacial area increasing to 743 cm^2. Similarly Zhang *et al.* (2009) observed that the cylinder to orbital diameters ratio affected significantly the free surface shape, with a wavy free surface present at low shaking frequencies when $d_i > d_o$, and at high shaking frequencies when $d_o > d_i$.

1.2.5 Oxygen transfer rate (OTR) and volumetric mass transfer coefficient, k_La

The oxygen transfer rate, OTR, is another parameter that strongly affects cell growth, especially for microbial cultures. In order to estimate the OTR in shaken bioreactor a method was established by Hermann *et al.* (2001) based on sulphite oxidation. This method relies in the pH drop occurring when the sulphite is oxidised to a more acidic sulphate. The decrease in pH is visualised by the color change of a pH-indicator such as the bromothymolblue, and the OTR is then determined by Equation 1.13.

$$OTR = \frac{C_{Na2SO3} \cdot v_{O2}}{t_{ox}} \tag{1.13}$$

Where C_{Na2SO3} is the molar concentration of sodium sulphite, v_{O2} is the stoichiometric coefficient for oxygen and t_{ox} is the reaction time for the complete oxidation. Pena *et al.* (2007) observed that, for a 500-ml Erlenmeyer flask, filling volumes, V_f=25-100 ml, an orbital diameter, d_o=25 mm, and shaking frequency, N=200 rpm, the OTR increased exponentially during the first 4 hr of cultivation, until it achieved a maximum value and maintained this value for a further 6 hr of cultivation. A drop in OTR was only rerecorded between the 10hr and 22 hr of cultivation. Pena *et al.* (2007) also investigated the effect of the filling volume on the OTR. Their study showed that the maximum value of the oxygen transfer rate, OTR$_{max}$, was inversely proportional to the filling volume, V_f. It is worth to point out that for higher filling volumes the OTR maintained a maximum constant value for a period longer than those obtained for lower filling volumes.

Beside the oxygen transfer rate, the volumetric mass transfer coefficient, k_La, is employed to assess the mass transfer taking place at the interfacial area between the liquid and the gas phases. Several methods have been proposed to describe the transfer mechanism of k_La. The oxygen transfer rate, OTR, can be used to estimate the volumetric mass transfer coefficient, k_La, as reported in Equation 1.14.

$$k_La = \frac{OTR}{L_{O2} \cdot p_{gO}} = \frac{C_{Na2SO3} \cdot v_{O2}}{t_{ox} \cdot L_{O2} \cdot p_{gO}} \tag{1.14}$$

Where L_{O2} is the oxygen solubility and p_{gO} is the partial oxygen pressure in the gas phase. Suijdam *et al.* (1978), Henzler and Schedel (1991) and Veljkovic *et al.* (1995) have all carried out measurements of the volumetric mass transfer coefficient, k_La, for a 500-ml Erlenmeyer flask, V_f=100 ml and d_o=25 mm. Their studies have shown that for increasing N the volumetric mass transfer coefficient, k_La, also increased.

The k_La in a cylindrical shaken bioreactors was investigated by Zhang *et al.* (2009). They carried out measurements in a shaken cylinder of diameter, d_i=172 mm, and fluid volume, V_f=1.5-3 l. Initially they determined the values of k_La for different shaking speeds, N, and orbital diameter, d_o. Within the range of shaking speeds tested (70-130 rpm), k_La values were higher for d_o=50 mm than those for d_o=20 mm. A significant increase of k_La was observed when the shaking frequency was raised from 90 to 100 rpm for d_o=50 mm, and from 105 rpm to 120 rpm for d_o=20 mm. They also investigated the effect of varying the shaking frequency and filling volume for a fixed orbital and inner diameter of 50 mm and 172 mm, respectively. For each shaking frequency the k_La value was higher with a filling volume V_f=2.5 l, compared to that for 3.5 l, implying that the the lower the filling volume the greater the k_La.

1.2.6 Main findings

The preceding literature review highlighted the following aspects which are the most relevant for optimisation of mixing in shaken bioreactor.

- **Flow dynamics:** The filling volume, V_f, shaking frequency N, orbital diameter d_o, inner diameter d_i and the fluid viscosity ν have a significant impact on the flow field of shaken bioreactors. Flow visualisations for a cylindrical bioreactor have shown that a laminar region occurs for *Re*=0.8-1000, with a toroidal vortex present below the free surface, whilst for *Re* ≈1000 the flow is dominated by a whirlpool vortex and severe splashing occurs at the free surface for *Re* >1000. Kim and Kizito (2009) have shown that the flow fields drastically change when the fluid viscosity, ν, is varied.

  An out-of-phase condition was observed and a non-dimensional number was formulated by Büchs *et al.* (2000a) denoted as the phase number, Ph. All operating conditions at which $Ph > 1.26$ and $Fr_a > 0.4$ were “in-phase”, while “out-of-phase” conditions occur for $Ph < 1.26$ and $Fr_a > 0.4$. Out-of-phase conditions were found to significantly affect the mixing and oxygen transfer rate to the cell culture. The free surface shape was mainly influenced by two parameters: the shaking frequency, N, and the container diameter, d_i. Finally it was observed from CFD simulations that most of the energy in shaken bioreactors is dissipated near the vessel walls.

- **Mixing time:** Two different approaches have been adopted to measure the mixing time in shaken bioreactors. A global approach based on a colorimetric method and a pH reaction was employed by Tissot *et al.* (2010) who observed two types of mixing regions. For a low shaking frequency, N, a region where mixing was rapid was observed near the walls, while a region where mixing was mainly driven by diffusion occurred near the bottom and at the centre of the cylinder. The latter region decreased in size for increasing shaking frequency, N. Local and global mixing approaches based on conductivity measurements and a decolorisation technique were employed by Kato *et al.* (2001) and Barret *et al.* (2009), respectively, who observed that mixing time decreased for increasing Reynolds number, Re.

- **Power consumption:** Three methodologies, two indirect and one direct, have been mostly used to estimate the power consumption, P, in shaken bioreactors. The first indirect method is based on the heat balance equation where the thermal energy generated within the bioreactor through viscous dissipation of kinetic energy is determined by measurements of the fluid and of the surrounding temperatures. The second indirect method is based on torque measurements where the power consumption is estimated from the difference between the torques required to shake the bioreactor when it is filled with working fluid and hardened agar liquid. The final method is based on direct estimates of the different terms comprising the local energy dissipation rate, and the power consumption is obtained from the integral of ϵ over the fluid volume.

- **Oxygen transfer rate (OTR), volumetric mass transfer coefficient, (k_La) and interfacial area, I_a:** OTR is one of the most important parameter for cell cultures in shaken bioreactors. The sulphite oxidation method developed by Hermann *et al.* (2001) was found to be the most suitable to estimate the OTR in shaken bioreactors. In the literature it is reported that the interfacial area plays a key role to determine the amount of k_La and the OTR into the cell culture. The interfacial area in cylindrical shaken bioreactors is mainly influenced by two main parameters: the inner diameter of the cylinder, d_i, and the shaking frequency, N. From the literature it was found that the free surface shape is affected by the cylinder to orbital diameter ratio, with a wavy free surface being observed at low shaking frequency when $d_i > d_o$, and at high shaking frequency when $d_o > d_i$.

1.3 Aims and objectives

From the literature review it is evident that the flow dynamics occurring in a shaken bioreactor affects either directly or indirectly the main parameters (e.g. mixing, interfacial area, OTR, mass transfer coefficient, power consumption) controlling cell growth. From this point of view the present work aims at providing a thorough characterisation of the flow and mixing dynamics occurring in a shaken bioreactor of cylindrical geometry, with the final scope to identify non-dimensional parameters that can be used to predict the flow conditions (i.e. laminar or turbulent) occurring in the bioreactor, and to formulate a flow scaling law between bioreactors of different size. The objectives of the present study have been formulated from the findings of the preceding literature review and are summarised hereafter.

1. To examine the flow fields in a cylindrical bioreactor at high Re regimes (e.g. low viscosity fluid) for varying ϕ, h, N and fixed d_o and d_i;

2. To study the flow dynamics for varying d_o and d_i and identify the different flow regimes and critical flow conditions that can be associated and explain the documented “in phase” to “out-of phase” flow transition;

3. To formulate a flow scaling law at high Re (e.g. low viscous fluid) based on non-dimensional parameters comprising h, N, d_o and d_i;

4. To investigate the interfacial area, I_a, of the free surface and formulate an equation to estimate I_a for different operating conditions;

5. To determine the non-dimensional time, length scale and location of the vortical structures occurring in the cylindrical shaken bioreactor under different flow regimes;

6. To examine the onset of a laminar to turbulent flow transition in the cylindrical shaken bioreactor by assessing the variation of the kinetic energy content of the flow at different N and Re regimes;

7. To estimate the viscous dissipation rate of kinetic energy, ϵ, in the bioreactor and identify those regions in the bioreactor experiencing higher levels of viscous stresses;

8. To experimentally determine the volumetric power consumption in a cylindrical shaken bioreactor using the integral of the viscous dissipation rate of kinetic energy and validate the methodology with a temperature based measurement technique;

9. To study the flow behaviour at lower Re regimes for varying h, N, d_o and d_i and extend the flow scaling law to high viscous fluids.

1.4 Thesis outline

The remainder of this thesis is subdivided into six chapters. In the following chapter the flow configurations and the experimental set up utilised for the present investigation are described. A brief outline of the principles that govern PIV is then given, together with an analysis of the errors involved in the PIV measurements. In particular, the extent to which the optical distortion due to the free surface can affect the accuracy of PIV measurements is considered, and the problems encountered in the characterisation of the flow in a cylindrical shaken bioreactor by means of phase-resolved measurements are addressed. In Chapter 3, phase-resolved measurements carried out with PIV are presented to provide a thorough characterisation of the flow and mixing dynamics occurring in a cylindrical shaken bioreactor for a fluid of low viscosity (i.e. water). In the first part of Chapter 3 the flow dynamics for varying phase angle, ϕ, fluid height, h, shaking frequency, N, and fixed orbital and inner diameter of 25 mm and 100 mm, respectively, are investigated, while in the latter part of the chapter a thorough characterisation of the flow dynamics occurring in a cylindrical shaken bioreactor are studied when operating conditions such the orbital shaking diameter, d_o, and inner diameter of the cylinder, d_i, are varied. From this analysis a flow scaling law based on the Froude number, Fr, is identified, which correlates the shape and inclination of the free surface to the occurrence of a flow transition. In Chapter 4 the flow characteristics of a low viscosity fluid (i.e. water) are investigated. These flow characteristics include the interfacial area, circulation time, vortex size and location, kinetic energy and dissipation rate of kinetic energy. In Chapter 5 the flow dynamic behaviour for fluids of higher viscosity are examined. A similar experimental procedure to that reported in Chapter 3 is also used in the first part of Chapter 5 to extend the flow scaling law determined for water to fluids of higher viscosity. Based on flow and kinetic energy content analyses a Fr-Re map is built to distinguish between the four main different flow conditions occurring in the bioreactor for varying operating conditions. Finally, conclusions and recommendations for future work are provided in Chapter 6.

Parameters	**250-ml Erlenmeyer flask**	**24-well bioreactor**	**96-well bioreactor**
ν	1×10^{-6} m^{2}s^{-1}	1×10^{-6} m^{2}s^{-1}	1×10^{-6} m^{2}s^{-1}
V_f	25 ml	0.5-4 ml	0.1-0.5 ml
N	50-200 rpm	300-1400 rpm	300-1400 rpm
d_o	20-50 mm	1.8-6 mm	1.8-6 mm
d_i	8.1 mm	17 mm	8 mm

Table 1.1: Operating conditions investigated by (Zhang *et al.*, 2005) in a 250-ml Erlenmeyer vessel and by (Zhang *et al.*, 2008) in 24-well and 96-well microteter plates.

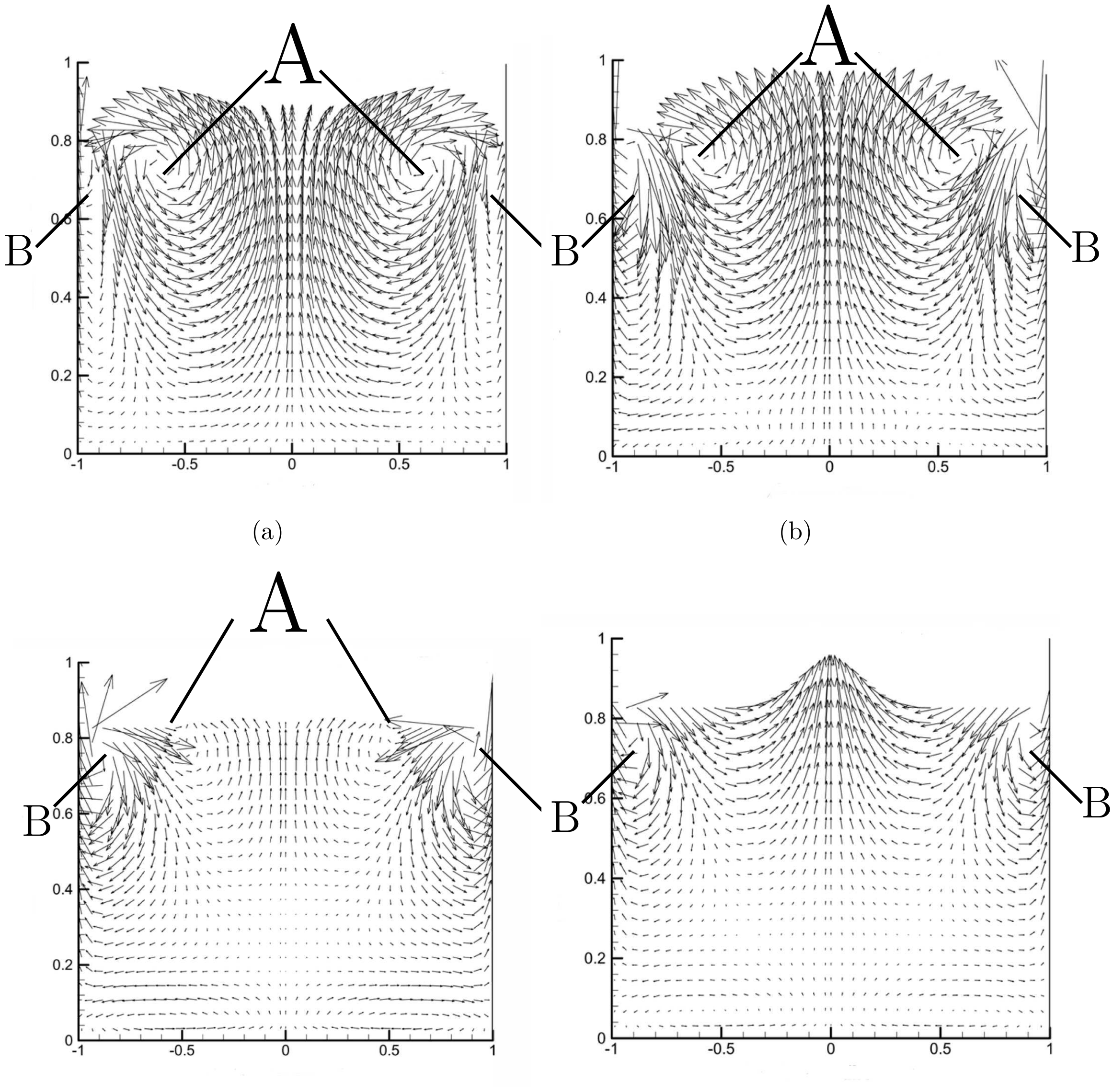

(a)

(b)

(c)

(d)

Figure 1.1: Space-averaged mean velocity field obtained in vertical planes for different viscosities (h/d_i=0.46, r_o/d_i=0.23 , N=60 rpm): (a) ν=1×10^{-6} m^2s^{-1}; (b) ν=3×10^{-6} m^2s^{-1}; (c) ν=1×10^{-5} m^2s^{-1}; (d) ν=1.6×10^{-5} m^2s^{-1} (from Kim and Kizito, 2009).

Chapter 2

Flow configuration, PIV apparatus and technique [†]

2.1 Introduction

This chapter provides a detailed description of the rig and of the PIV system used to investigate the flow in a cylindrical shaken bioreactor. The experimental rig and the working principles of PIV are described in Sections 2.2 and 2.3, respectively. The procedure developed to track the motion and shape of the free surface of the fluid in the shaken bioreactor is reported in Section 2.4, whilst the reproducibility of the flow generated by the shaken bioreactor and associated error sources are assessed in Section 2.5.

2.2 Experimental rig and shaker table

A purpose-built rig was constructed to allow 2D PIV measurements. A schematic diagram of the glass cylinder used in this study is shown in Figure 2.1. The cylin-

---

[†] Most of the results presented in this chapter are included in:

Weheliye, W., Yianneskis, M. and Ducci, A. (2012), “PIV measurements in a shaken cylindrical bioreactor”, *Proc. 16th Int. Symposium on Applications of Laser Techniques to Fluid Mechanics*, Paper 3.5.5.

der is polished borosilicate glass mounted on a rigid base with an open top. The base of the cylinder is transparent so as to provide optical access to the bioreactor from the bottom. The cylinder is placed in a trough with polished Perspex surfaces and filled with water so that refraction effects are minimised and optical distortions at the curved cylinder wall, which might impair the image-based measurement techniques used, are prevented. In this thesis experiments were carried out in cylindrical bioreactors of three different sizes with inner diameters, d_i=70 mm, 100 mm and 130 mm, while the cylinder height and wall thickness were fixed and equal to 250 mm and 5 mm, respectively.

The lab-shaker LS-X manufactured by Kühner AG utilised in this study is shown in Figure 2.2. The LS-X lab shaker is commonly used in the bioprocess industry with bioreactors of different size and geometry. For example its universal tray allows to accommodate Erlenmeyer flasks, test tube and microtiter plates to mention but a few. Several lab-shaker motions were described in the literature but the type investigated in this thesis is the orbital motion. The main characteristic of this motion is that the bioreactor maintains its orientation in space as it proceeds along the circular orbit. For example the point denoted as A in Figure 2.3 is constantly positioned at the same extreme of the cylinder diameter, while the system is shaken with a rotational speed ω about the eccentric axis. In the rest of the thesis the origin of the angular coordinate, ϕ, denoting the position of the tray/cylinder along its clockwise orbit corresponds to the point furthest to the left when the system is viewed from the top, as shown in Figure 2.3. For the present study the orbital diameter is varied in a range, d_o=15-50 mm.

2.3 Particle Image Velocimetry (PIV) and rig set up

2D PIV was used to characterise the flow field in the shaken bioreactor. PIV is a non-intrusive optical technique that provides measurements of the instantaneous velocity vector field in a plane located in the flow region of interest. PIV is a well-established technique and has been employed in a broad range of flows including several related to chemical and biochemical engineering applications. For example PIV has been used to study the flow in stirred vessels, oscillatory flow mixers and Taylor-Couette systems. In the present section, only a brief description of the principles of PIV is provided. In PIV neutrally buoyant tracer particles are employed to follow the flow. The position of the tracer particles is detected by illuminating the plane of measurements by means of a high-powered laser light sheet. Digital images are taken to capture the position of the tracer particles. By capturing two images at successive time instants, it is then possible to estimate the velocity field within the plane of measurement by a correlation analysis. A schematic diagram of the PIV working principle is shown in Figure 2.4.

The 2D PIV system employed in this study to characterise the flow field in the cylindrical bioreactor consisted of a continuous diode laser, a cylindrical lens, a high speed intensified camera and a timing box. It should be noted that the laser, mirror and camera were all rigidly mounted on the tray of the shaker table. The laser employed has an output power of 300 mW with a wavelength of 532 nm and the size of the laser head is 30 × 50 × 120 mm. A cylindrical lens was mounted in front of the laser to create a laser light sheet of approximately 1 mm thickness. Schematic diagrams of the PIV system set up for measurements on vertical and horizontal planes are provided in Figures 2.5 (a) and (b), respectively. Depending on the measurement to be carried out, two different mirrors were used.

A rectangular mirror was used to deflect the horizontal laser plane by 90° and illuminate the vertical plane of measurement that bisects the cylinder into two halves (see Figure 2.5 a). A larger rectangular mirror was used when the camera was positioned underneath the laser and allowed to have optical access from the bottom window of the bioreactor and obtain PIV measurements on horizontal planes (see Figure 2.5 b).

In order to carry out phase-resolved measurements the PIV system was synchronised with a magnetic encoder mounted on the shaker table. The encoder is placed on the shaker table while the magnet is fixed to the drive, so that a signal is triggered when the magnet faces the encoder at the position denoted by ϕ=0° in the sketch of Figure 2.3. The encoder is connected to a timing box and a time delay can be selected through the DANTEC software to trigger the camera at the desired angular positions of the shaker table and to collect the pair of images required to carry out PIV processing. Silver coated hollow spherical particles of 10 μm diameter were used to identify at each phase angle the shape of the free surface, while for the PIV measurements it was preferred to use 20-50 μm rhodamine particles, because they helped minimise reflections at the walls and at the free surface. For the latter case an orange filter with cut-off wavelength of 570 nm was mounted on the 45 mm and 60 mm camera lenses, that were alternatively used to change the measurement resolutions and study the large scale flow structures and the dissipative scales, respectively.

An adaptive correlation analysis of the full image was applied with an initial interrogation window of 256 × 256 pixels and a final window of 32 × 32 pixels. A 50% window overlap was used for a final resolution of 16 x 16 pixels, corresponding to an area of 1.3 × 1.3 mm^2 for a cylinder of diameter, d_i=100 mm when the 45 mm lens was used. Similarly, spatial resolutions of 1.5 × 1.5 mm^2

and 1.7 × 1.7 mm^2 were obtained for cylinders of diameter, d_i=70 mm and 130 mm, respectively. The number of images obtained for each experiments varied in a range of 100-1000, while the image acquisition frame rates were set between 0.02 - 1 kHz. It should be noted that all the experiements carried out in this thesis were conducted at room temperature. In the rest of the thesis a cylindrical coordinate system, r, θ, z is employed with the origin positioned at the cylinder axis on the bioreactor base.

The presence of the free surface posed a complex problem that had to be carefully addressed to ensure that the illumination of the entire area of investigation was uniform and not subject to reflections and shadows created by the free surface oscillations. From this perspective the last part of this section aims at highlighting the major issues encountered when different PIV arrangements were employed and indicating why the two optical setups presented in Figure 2.5 (a) and (b) were selected. In this respect four different arrangements were attempted but only two of them provided a viable solution.

1. Laser plane shone from the side of the cylinder (see Figure 2.6 a)
2. Laser plane shone from the top of the cylinder (see Figure 2.6 b)
3. Laser plane shone from the bottom of the cylinder (see Figure 2.6 c)
4. Laser plane shone from the front of the cylinder (see Figure 2.6 d)

Three out of the four arrangements employed were used to obtain velocity measurements on a vertical plane (Figure 2.6 a-c), while the fourth PIV set-up was used to obtain measurements on a horizontal plane.

The first set-up (Figure 2.6 a) consisted in illuminating the bioreactor from the side with the camera and the laser being placed in front of two adjacent sides of the cylinder/trough system. The degree of illumination achieved with this set up is shown in Figures 2.7 (a) and (b) for two snapshots taken at phase angles ϕ=0° and 180°, respectively. To better comprehend the inclination of the free surface with respect to the laser light sheet a sketch is provided next to each snapshot.

From Figure 2.7 (a) it is evident that when the free surface lowest height is on the side of the laser the flow region of interest is split into two areas with very different illumination. For this phase angle (ϕ=0°) the free surface acts as a mirror reflecting back most of the laser light and a large triangular shadow zone is observed below the free surface. In the shadow zone tracer particles do not scatter any light and PIV measurements cannot be carried out. The illumination of Figure 2.7 (a) corresponds to the worst possible scenario, but it is representative of the lack of illumination encountered to a lesser degree at phase angles, -90° $< \phi <$ 90°, where the free surface is tilted towards the opposite side of the laser. When the shaker table reaches the orbital position at ϕ=180° the free surface lowest height is on the opposite side of the laser and a better illumination is obtained throughout the region of interest (see Figure 2.7 b). This type of illumination occurs for 90° $< \phi <$ 270°. It is worth noting the presence of laser reflection lines below the free surface (see Figure 2.7 b), due to ripples on the free surface, which can result in erroneous velocity vectors after PIV post processing. This, combined with the poor illumination on the left hand side of the field of view, discouraged the use of this set up for the PIV measurements.

The second PIV setup (Figure 2.6 b) is similar to the first one except that the laser is entering the bioreactor from the top of the glass cylinder. The disadvantage of this set-up is due to the fact that the free surface changes continuously its orientation and therefore the laser plane entering the fluid from the top is refracted at different angles and is never aligned with the vertical plane of focus of the camera.

Different types of optical distortion problems were encountered with the configurations finally selected to carry out the PIV measurements (Figure 2.6 c). These are illustrated in Figures 2.8 (a) and (b). For phase angles in the range, ϕ=180°-360°, there is no optical distortion and the image is uniformly illuminated (see right side of Figure 2.8 a). As shown on the left of Figure 2.8 (a), for this range of angles the highest side of the free surface is on the same side of the PIV camera. In this case light travelling along paths A and B in Figure 2.8 (a) crosses the same extent of media (air and water) between the camera and the focal plane.

On the contrary, when phase angles ϕ <180° are considered, the image distortion shown on the right side picture of Figures 2.8 (b) is observed. In this case the part of the image encircled is de-magnified (or minified), while the bottom part is subjected to the same optical path as for phase angles, ϕ >180°. This demagnification effect can be explained by considering the sketch on the left hand side of Figures 2.8 (b), and the different media crossed by the camera light when travelling along paths A or B. It should be noted that for, ϕ <180°, the free surface lower height is on the side of the camera. As a consequence, the light along path A travels inside the cylinder only through air and then enters the water on the plane of focus, whilst the light of path B travels only through water. In between the two reference paths, light will travel through different amounts of air and water depending on the height considered. This results in the image distortion shown on the right of Figure 2.8 (b), where the different proportion of air-water light paths results in the de-magnification lens effect previously described. For this range of angles, ϕ <180°, it was not possible to carry out PIV measurements, as the calibration factor would have changed at different axial coordinates, depending on the free surface shape and inclination. Nevertheless, it is worth pointing out that the periodic nature of the shaken motion is such that the characteristic flow field for ϕ=0°-180° is the same as that for ϕ=180°-360°, but with the flow being in the opposite direction. This, combined with the fact that PIV measurements were simultaneously carried on both sides of the bioreactor axis, confirmed that measurements along one-half of the shaker orbit are sufficient to fully characterise the flow periodic nature.

For the horizontal plane measurements the cylinder was raised to make space for the larger rectangular mirror underneath it, while the camera was positioned below the laser as it is shown in Figure 2.6 (d). A horizontal laser sheet was shone through the front of the cylinder creating a region where the seeding particles can be seen from the mirror under the cylinder. The mirror was inclined at 45° and was placed in front of the camera. The illumination problem discussed for the third PIV set-up does not, of course, occur when measurements are obtained with this set-up, provided that the plane of illumination is kept below the free surface during the entire orbit.

2.4 Free surface tracking algorithm

The shape of the free surface was determined for two reasons: (i) to estimate the interfacial area available for oxygen transfer which is a critical parameter for cell growth; (ii) to assess to what extent masking of the free surface affects the accuracy of the measured flow field after the PIV adaptive correlation routine is applied. An image analysis algorithm comprising of three steps was developed to identify the free surface position at any phase angle. The first step aimed at making the top part of the PIV image, that above the free surface, as uniform as possible, and therefore reflections of the laser light at the cylinder walls were removed. Characteristic reflections are denoted as points 1, 2 and 3, in the raw PIV image of Figure 2.9 (a). In this case every pixel with a light intensity $i > 0.9$

(where an intensity value i=1 indicates white) is converted to an intensity value of 0 (i.e. black).

The second step consisted of determining the coordinates of the points positioned on the free surface by exploiting the differences in illumination texture of points above and below the free surface. A close up of the blue squared region of Figure 2.9 (a) is provided in Figure 2.9 (b) where three points above, on and below the free surface are denoted as A, B, and C, respectively. It is evident that points A and B are located in regions with a more uniform illumination texture, while the presence of seeding particles gives an accentuated inhomogeneity of scattered light below the free surface (point C). To estimate the level of inhomogeneity of the local illumination texture a window of 3x3 pixels was created around each pixel of the image and the local standard deviation, σ, of the light intensity of the nine points within the window was calculated using Equation 2.1.

$$\sigma = \sqrt{\frac{1}{N_w}\sum_{i=1}^{N_w}(i_k - i_m)^2} \tag{2.1}$$

Where N_w is the number of points in the window, i_m is the mean value of the light intensity in the window and i_k is the light intensity of the k^{th} point of the window. It should be noted that the standard deviation was estimated for every pixel of the image. The variation of the standard deviation along the vertical direction, y, at a characteristic radial location x, is shown in Figure 2.9 (c). It should be mentioned that the origin of the image is located in the upper left corner, and therefore increasing y corresponds to points further down the image. From Figure 2.9 (c) it is evident that the value of the standard deviation, σ, is low at small values of y (i.e. for the upper part of the image) where most of the image is dark and the local illumination texture is uniform. As the upper edge of the free surface is approached a sharp increase of σ occurs. This is due to the fact that the 9-point interrogation window is right across the upper edge of the free surface and therefore a significant difference in light intensity occurs between points above and inside the free surface. A further increase in y results in the interrogation widow being completely inside the region of the free surface scattering the largest amount of light, and therefore the standard deviation σ is locally characterised by the sudden decrease denoted as point B in Figure 2.9 (c), which also corresponds to point B in Figure 2.9 (b). A second peak of σ occurs when the interrogation window is across the bottom edge of the free surface at y=430. For y >430 the interrogation window is completely inside the seeded flow region and it varies around a value of 10 which is greater than that occurring above the free surface for y <350, because of the light inhomogeneity due to the presence of the seeding particles. The presence of the two peaks of σ together with the pronounced minimum occurring in between allows identifying the edges and the centre of the free surface, respectively. The same procedure was repeated for each horizontal coordinate x until the entire free surface profile at a given phase angle ϕ was determined. A representation of the free surface profile obtained with the described procedure is illustrated in Figure 2.9 (d). It is evident that the algorithm identifies most of the points on the bottom edge of the free surface with only few erroneous detections in the middle of the flow.

The third step involved a local regression that was applied to smooth the detected profile of the free surface, as well as to identify and discard those outliers whose distance from the free surface was greater than a fixed threshold. A mask was then applied to each raw image and the values of all pixels above the free surface profile were converted into black.

A flow chart of the algorithm used to determine the free surface along with the three main steps previously described is shown in Figure 2.10. The first step addressed the removal of those pixels exhibiting light intensity above 0.9 in the image (i.e. the wall reflection and free surface line). Subsequently the calculation of the standard deviation, σ, for each column is shown along with the estimation of the free surface point, p_s, in step 2. The iterative program repeats the second step until the last column of the image is reached. In step 3 the raw profile of the free surface is smoothed and a mask is applied to the PIV image.

2.5 Measurement errors, uncertainty and flow assessment

In this section an analysis is carried out to identify the different sources of error affecting the PIV measurement. A clear distinction is made between systematic and random (statistical) errors in Sections 2.5.1 and 2.5.3, while Section 2.5.2 focuses on the procedure used to estimate the calibration factor together with the associated error, and provides an assessment of the flow measurements in the shaken bioreactor.

2.5.1 Systematic errors inherent in the PIV measurement

In this part the different systematic errors affecting the PIV measurements are investigated. The errors may be categorised as follows: (1) the error made in aligning the laser with the vertical plane that bisects the cylinder into two halves, ϵ_{SL}; (2) the error made in aligning the encoder to the phase position ϕ, ϵ_{SE}; and (3) the error due to the variation of the fluid viscosity with temperature, ϵ_{SV}.

The error related to the alignment of the vertical laser plane, $\varDelta\phi_{Lmax}$ (Figure 2.11), is considered at first. In an ideal condition the angle $\varDelta\phi_{Lmax}$ should be 0°. The alignment of the vertical laser plane was made by using two reference holes with diameter of 4 mm, which were made in the steel bottom base to the side of the circular window (see sketch of Figure 2.11). It should be noted that the sketch shown in Figure 2.11 is not to scale and its purpose is to demonstrate how the alignment of the laser plane was carried out. The alignment of the laser plane with the two holes was assessed at the beginning and at the end of the experiment. Taking into account the alignment procedure, the maximum error made on the angle $\varDelta\phi_{Lmax}$ corresponds to the extreme condition when the laser plane is tangent to the opposite sides of the two reference circles. This condition is well illustrated in Figure 2.11 by the two lines inclined at an angle of $\pm\varDelta\phi_{Lmax}$. An estimate of the maximum angle can be obtained from Equation 2.2.

$$\varDelta\phi_{Lmax} = \arctan\left(\frac{d_h}{X_h}\right) \tag{2.2}$$

Where d_h and X_h are the diameter and distance of the two holes, respectively. The maximum error $\varDelta\phi_{Lmax}$ was 2.08° for a cylinder of inner diameter d_i=100 mm, corresponding to a maximum percentage error ϵ_{SL}=$\varDelta\phi_{Lmax}/180°$=1.16%. Once the laser was positioned an additional method was used to assess its alignment. This consisted in checking that the seeding particles were in focus over the entire interrogation area. If only part of the image was in focus, the laser and camera alignment procedure was repeated.

A second source of systematic error is due to the alignment of the encoder with the phase angle ϕ=0° corresponding to the position of the tray furthest to the left when see from above. The alignment was made by marking on the shaker table the position further to the left hand side of the shaker tray and placing a ruler underneath the shaker table with the zero corresponding to the marked position. The encoder was then connected to an oscilloscope and the tray was slowly moved around the ϕ=0° position until a signal was triggered on the oscilloscope. The position of the tray was then checked on the ruler and if it was not aligned with the ruler zero edge, the position on the shaker rotor of the magnetic component of the encoder was changed and the alignment procedure described was repeated. The maximum discrepancy between the actual and ideal positions of the tray was in the order of 1 mm, corresponding to systematic errors of ϵ_{SE}=4% and 2% for orbital diameter d_o=25 mm and 50 mm, respectively.

The alignment procedure was refined during the course of the project and a "feedback assessment" of the encoder alignment was obtained from the phase resolved velocity field for the in-phase condition (for low shaker table speed, N). More specifically, it was found that at low speed the flow exhibits two well defined counter rotating vortical cells which are completely separated at ϕ=0°. An example of such a flow is provided in Figure 2.12 for h/d_i=0.3 and N=80 rpm. If the flow at ϕ=0° did not show the expected flow pattern at such low shaking speeds then the encoder alignment was repeated. More details on the flow associated to in-phase conditions are given in Chapter 3. It should be noted that in Figure 2.12 and in some of the plots reported in the remainder of the thesis reference is made to negative radial coordinate, r, which, although not consistent with the cylindrical coordinate system employed, it is used here solely to discriminate between points to the left and right hand sides of the bioreactor axis.

A third source of error that affected the PIV measurements is related to the temperature variation of the fluid viscosity. In the present study different mixture of glycerine and water were utilised to assess the flow variation for different viscosity. Regular temperature measurements were carried out with a high resolution thermometer before and after the experiment for fluid mixture of glycerine (90%) and water (10%) in order to montior the fluid temperature and therefore ν. The temperature of the fluid inside the bioreactor was approximately constant at 20°C before and after the experiment with a maximum error of ±0.1°C for a shaking time of 10 minutes. It should be noted that 10 minutes is the maximum time required to carry out PIV measurements. The fluid viscosity, ν, is 1.77×10^{-4} m^2s^{-1} at a fluid temperature of 20°C for a fluid mixture of glycerin (90%) and water (10%), whilst at fluid temperature of 19.9°C and 20.1°C the fluid viscosity, $\nu\approx1.76\times10^{-4}$ m^2s^{-1} and 1.77×10^{-4} m^2s^{-1}, respectively. Therefore the error made on the fluid viscosity, ϵ_{SV}=0.56%.

The overall experimental uncertainty of the PIV measurement is estimated from Equation 2.3 in agreement with Moffat (1988):

$$\epsilon_u = \sqrt{{\epsilon_{SL}}^2 + {\epsilon_{SE}}^2 + {\epsilon_{SV}}^2} \tag{2.3}$$

Combing the uncertainties given above yields an estimate for the total uncertainty of the measured velocity of 4.2%.

2.5.2 Calibration and flow assessment

Two methods were employed to determine the calibration factor. The first method is based on the utilisation of the inner diameter of the shaken bioreactor. For instance when d_i=100 mm, the number of pixels (i.e. the number of columns) from one end of the cylinder to the other is approximately 1230 pixels, corresponding to a calibration factor based on the inner diameter of the cylinder, CF_{d_i}=0.0813 mm/pixel.

The second method of estimating the calibration factor is based on using a calibration board, which was placed near the furthest left wall of the cylinder. It should be mentioned that the wall curvature and refractive index difference between the cylinder and the working fluid may produce an optical distortion which is accentuated towards the sides of the cylinder. In order to assess the variation of the calibration factor with the curvature of the cylinder, the calibration factor CF_b was calculated between points which are apart by a distance of Δx_i, where the first point is always the closest to the wall. For instance Δx_1 refers to the distance between the first and second adjacent dots, whereas Δx_2 refers to the distance between the first and third dots (see Figure 2.13 a). It can be seen from Figure 2.13 (b) that the calibration factor based on the calibration board, CF_b, tends to be constant throughout the horizontal profile with an average value of 0.08158 mm/pixel. Thus there is good agreement between the average value of CF_b and that obtained from the internal diameter, CF_{d_i}, with a discrepancy of 0.34%. This is well within the range of variation of CF_b ($\pm 0.4\%$) reported in Figure 2.13 (b) for different distances, Δx_i. For the rest of the thesis the calibration factor employed was the one based on the inner diameter of the cylinder.

In order to characterise the flow in the cylindrical shaken bioreactor it is necessary to define the phase resolved velocity, $\langle \mathbf{u}_i \rangle$, and variance, $\langle \mathbf{u}_i'^2 \rangle$, reported in Equations 2.4 and 2.5, respectively.

$$\langle \mathbf{u}_i \rangle = \frac{1}{N_\phi} \sum_{i=1}^{N_\phi} \mathbf{u}_i \tag{2.4}$$

$$\left\langle \mathbf{u}_i'^2 \right\rangle = \frac{1}{N_\phi} \sum_{i=1}^{N_\phi} (\mathbf{u}_i - \langle \mathbf{u}_i \rangle)^2 \tag{2.5}$$

Where $\mathbf{u}_i$ is the instantaneous velocity field and N_ϕ corresponds to the number of measurements taken at a phase angle, ϕ. A measure of the amplitude of the velocity fluctuation can be obtained from the *root mean square* (rms) of the velocity time series shown in Equation 2.6.

$$\mathbf{u}_i{}' = \sqrt{\langle \mathbf{u}_i'^2 \rangle} \tag{2.6}$$

Initially an analysis was carried out to determine to what extent using a mask can affect/improve the accuracy of the velocity field determined by the PIV adaptive correlation algorithm. The analysis was applied to the velocity field shown in Figure 2.14 (a) for d_o/d_i=0.25, h/d_i=0.5, ϕ=0° and N=90 rpm. Figures 2.14 (b) and (c) show a comparison of the axial profiles of the velocity magnitude when the velocity field was obtained with and without masking for the two different radial positions r/d_i=-0.2 and 0.3 reported in Figure 2.14 (a), respectively. It can be noted from both plots that near the centre and bottom of the cylinder no difference is observed between the velocity magnitude profiles obtained from unmasked and masked PIV images. However near the free surface a difference between the velocity magnitudes for masked and unmasked conditions is present. This difference is more evident for a limited number of points, namely 2 and 3 for r/d_i=-0.2 and 0.3, respectively, in close proximity of the free surface. For example the maximum discrepancy obtained for the velocity magnitude profile at a radial position r/d_i=-0.2 is 7%, while at a radial position of r/d_i=0.3 a maximum discrepancy of 5% was observed. Even though the flow measured in the entirety of the bioreactor, which is the main objective of the current study, is not significantly affected by masking of the free surface, for the remainder of this thesis it was preferred to apply a mask to all the PIV images acquired before proceeding with the PIV adaptive correlation algorithm.

In order to assess the consistency of the measurements, a comparison of the velocity profiles obtained from measurements in horizontal and vertical planes is provided in Figure 2.15, where the radial profiles of the phase-resolved radial velocity component, $\langle u_r \rangle$, measured in the vertical and horizontal planes are shown. The data of Figure 2.15 show two pairs of radial profiles obtained for z/d_i=0.08 and z/d_i=0.15. Subscripts h and v indicate data obtained in horizontal and vertical planes of measurement, respectively. The two sets of profiles present above and below the zero ordinate value in Figure 2.15, refer to the left and right hand sides of Figure 2.14 (a), where the local radial velocity component is negative (directed towards the cylinder centre) and positive (directed outwards from the cylinder centre), respectively. Close to the walls, at r/d_i around 0.5, the data show a near-zero radial velocity component as the local flow is mainly dominated by the tangential and axial components, while the maximum magnitude of $\langle u_r \rangle$ is reached near the centre of the cylinder at r/d_i=0.01-0.05. The maximum velocity is greater at the highest elevation considered (z/d_i=0.15) because it is closer to the free surface, which provides the flow driving mechanism. The radial profiles from the vertical and horizontal planes of measurements are in good agreement for both elevations considered, with an average discrepancy between the two of 2.6% and 3.1% for z/d_i=0.08 and 0.15, respectively.

Due to the rotational nature of the flow considered an analysis was made to establish which velocity component is dominant in different region of the cylinder and therefore determine what is the optimal PIV time delay to fully resolve the flow. As shown in Figure 2.16 (a-b), when PIV measurements are carried out at $\phi < 60°$ the greatest velocity is u_θ both at the inner ($r < 0.25$) and outer ($r > 0.25$) regions of the cylinder. However for $\phi > 60°$ (see Figure 2.16 c-d), u_r becomes the dominant velocity at the inner region of the cylinder, whilst u_z becomes the dominant velocity component at the outer region of the cylinder. The sketch reported in Figure 2.17 provides a summary of the regions where different velocity components are dominant.

This analysis is useful to select the optimum time $\mathit{\Delta T}$ between two images that minimise out of plane particle displacement. This problem is relevant for measurement on vertical plane at small angles when u_θ, which is the out-of-plane velocity component, dominates the flow. For this reason $\mathit{\Delta T}_1$=10 ms was selected for -60°<ϕ<60°, while for 60°<ϕ<120° $\mathit{\Delta} T_2$ as large as 50 ms could be selected without having the seeding particles moving out from the plane of measurement. In this study the time interval between the PIV images for vertical plane measurements (large scale flow field) was $\mathit{\Delta} T_1$=10 ms for any given phase angle, whilst a $\mathit{\Delta} T$ as small as 1 ms was selected when a close-up of the velocity field near the wall was obtained to measure the dissipation rate of kinetic energy. For the horizontal plane measurement $\mathit{\Delta} T_2$ ($\leq$50 ms) was employed for any given phase angle.

2.5.3 Statistical errors

The major purpose of the reproducibility test described below was to determine whether the size of the sample of experiments repeated at a given phase angle is large enough to minimise statistical errors. From this point of view the mean velocity magnitude, defined in Equation 2.7, was estimated for an increasing sample size, N_s at different points in the flow.

$$|\langle u_r \rangle + \langle u_z \rangle| = \sqrt{\frac{\sum_{i=1}^{N_s}({u_{r_i}}^2 + {u_{z_i}}^2)}{N_s}} \tag{2.7}$$

with u_{r_i}, and u_{z_i}, being the radial and axial velocity components of the i^{th} experiment. The test was made on the velocity field obtained at ϕ=270° and N=90 rpm. A typical velocity field for this phase is shown in Figure 2.18 where points denoted as A, B, C and D identify the location where the variation of the velocity magnitude was assessed against the sample size N_s. It can be seen that for a sample size $N_s > 50$, the average velocity magnitude of all the points considered tends to converge to a nearly constant value. A conservative choice was made for the rest of the measurements shown in this work and a sample size of N_s=500 was selected to minimise statistical errors.

2.6 Concluding remarks

In this chapter an overview of the flow configuration and of the measurement methodology employed was provided. The rig and the shaker table adopted were briefly described at the beginning, while the principle of Particle Image Velocimetry (PIV) was illustrated. A thorough analysis has been carried out to identify the optimum arrangement of the laser and camera with respect to the bioreactor rig to obtain a satisfactory and uniform illumination of the interrogation region. This analysis showed that the inclination and shape of the free surface can significantly affect the quality of the PIV images acquired, with poor illumination and significant optical distortion being present for a specific range of phase angle, ϕ, of the cylinder along its orbit. More specifically, it was found that for the final arrangement selected measurements could be carried out only for phase angles $180° < \phi < 360°$ when the lens effect induced by the different proportion of media (air-water) crossed by the laser reflected light did not occur. Despite this the periodic flow field could be fully resolved over the entire range of phase angle ϕ=0-360°, because the PIV measurements were simultaneously carried out on both sides of the bioreactor axis. An algorithm for tracking the free surface profile of the flow was also implemented. An error analysis to estimate the overall error made on PIV measurements was carried out and the total percentage error affecting the velocity ϵ_u was found to be approximately 4.2%. An analysis was carried out to assess to what extent masking the PIV images can affect the final velocity field. The discrepancies between the velocity profiles obtained with and without masking were found to be negligible in the largest part of the field of view, with exception of a few points in proximity of the free surface. A comparison of the radial velocity component profiles obtained from measurements in horizontal and vertical planes was also provided and good agreement between the two was found.

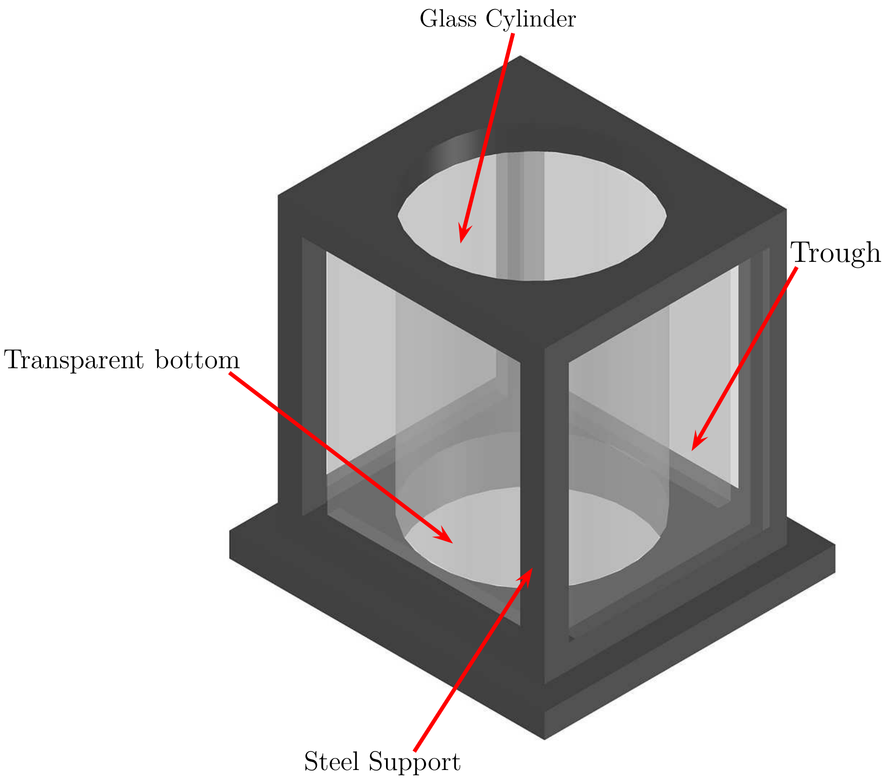

Figure 2.1: Three-dimensional sketch of the cylindrical bioreactor.

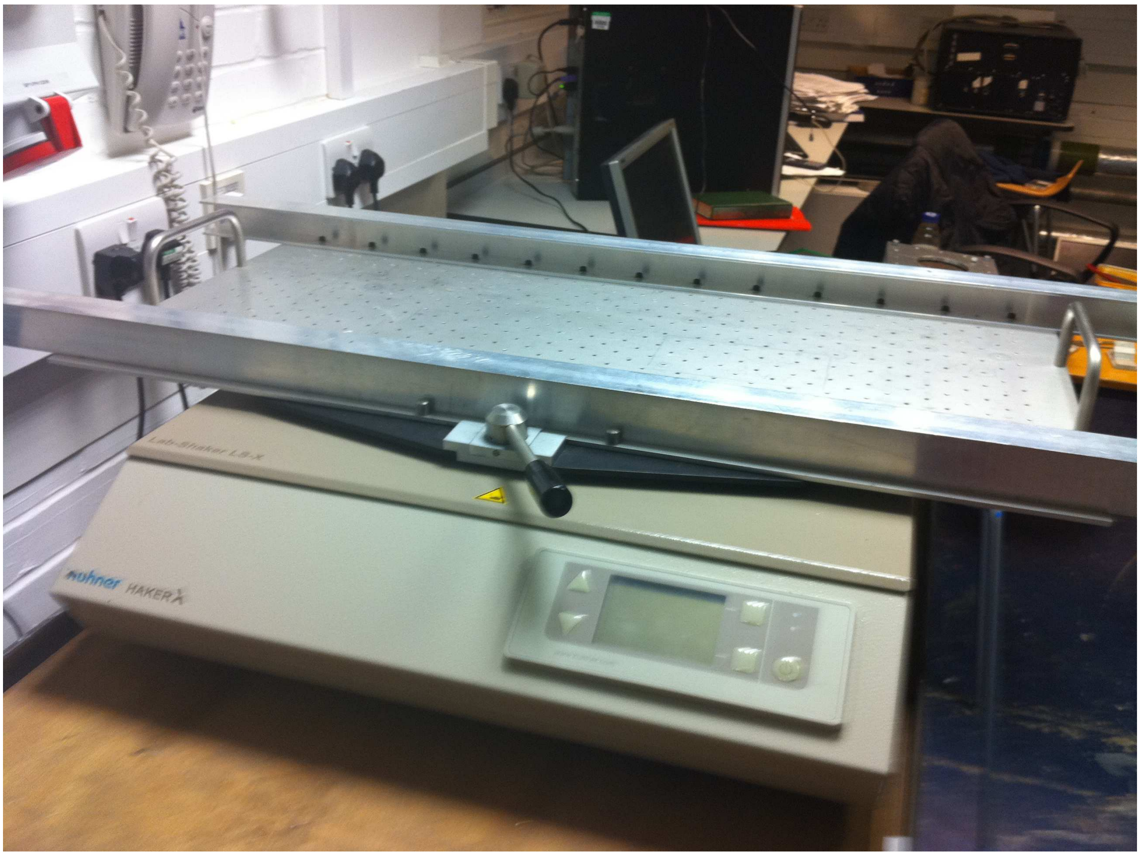

Figure 2.2: Kühner LS-X lab-shaker.

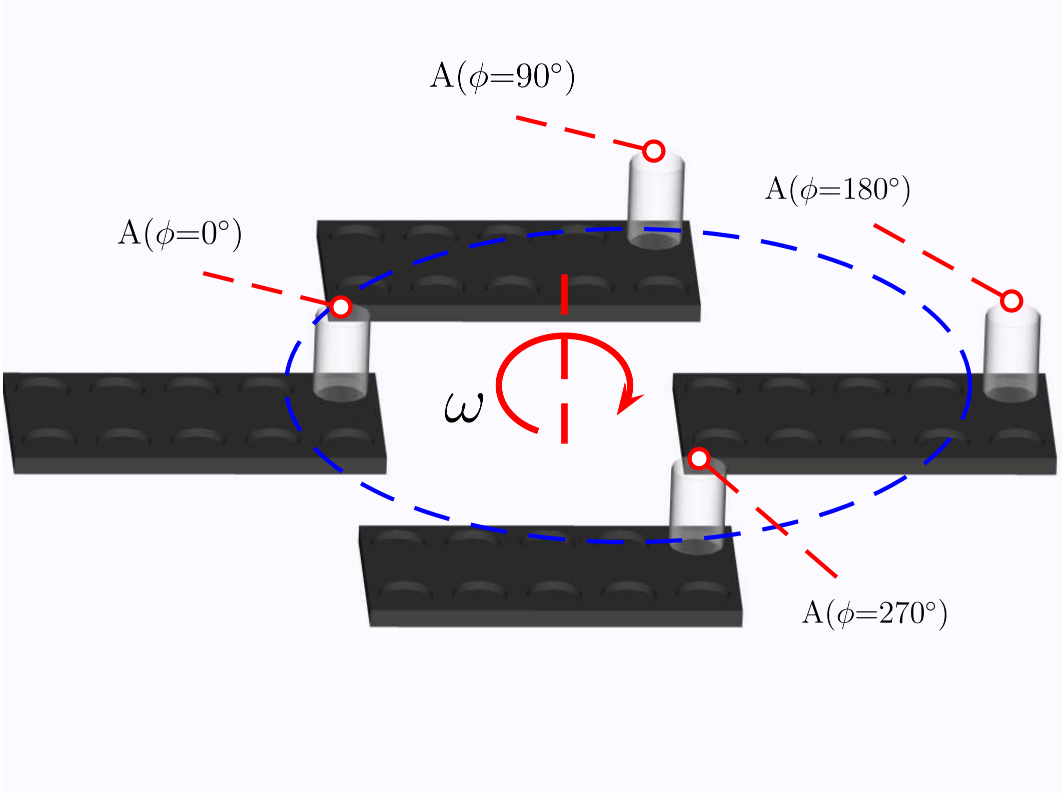

Figure 2.3: Sketch of the positions assumed by the bioreactor and the tray along the circular orbit.

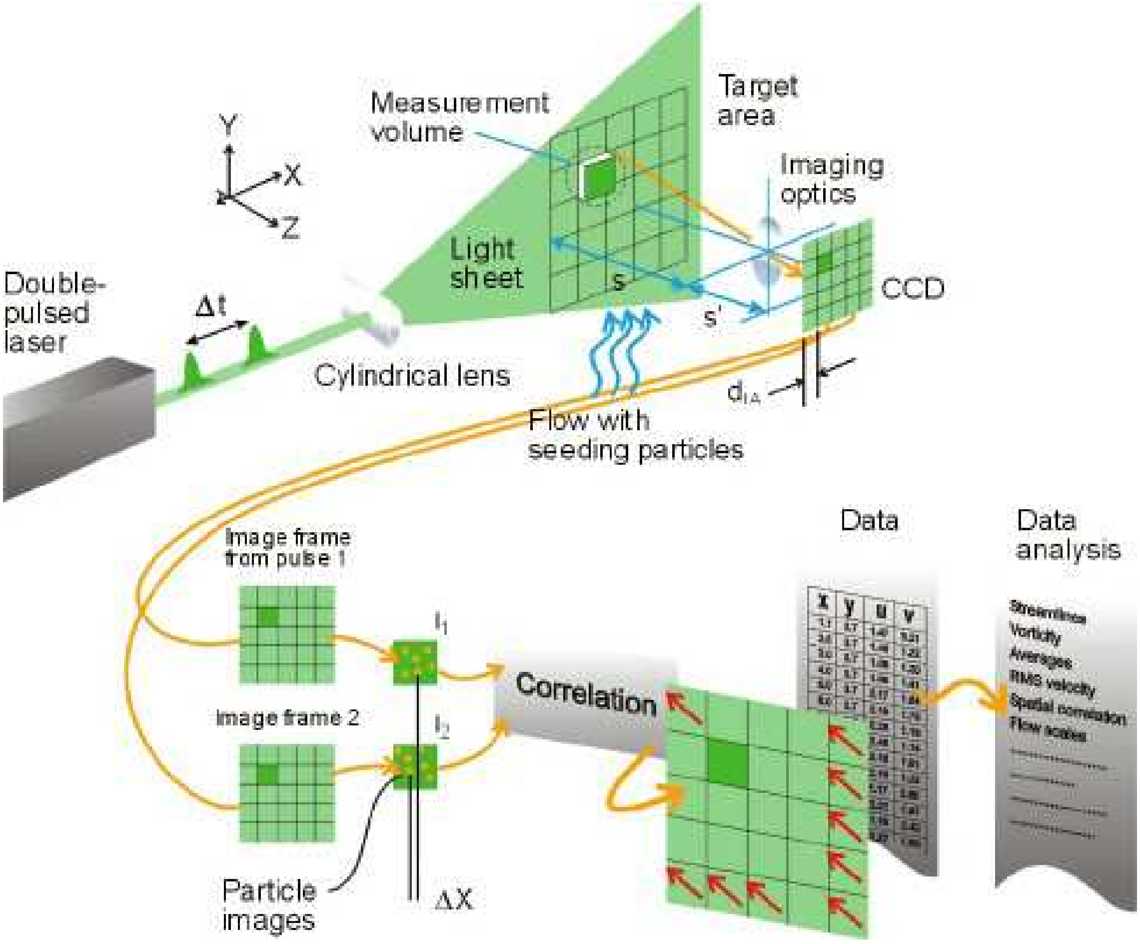

Figure 2.4: Schematic diagram showing PIV working principles (from www.dantecdynamics.com).

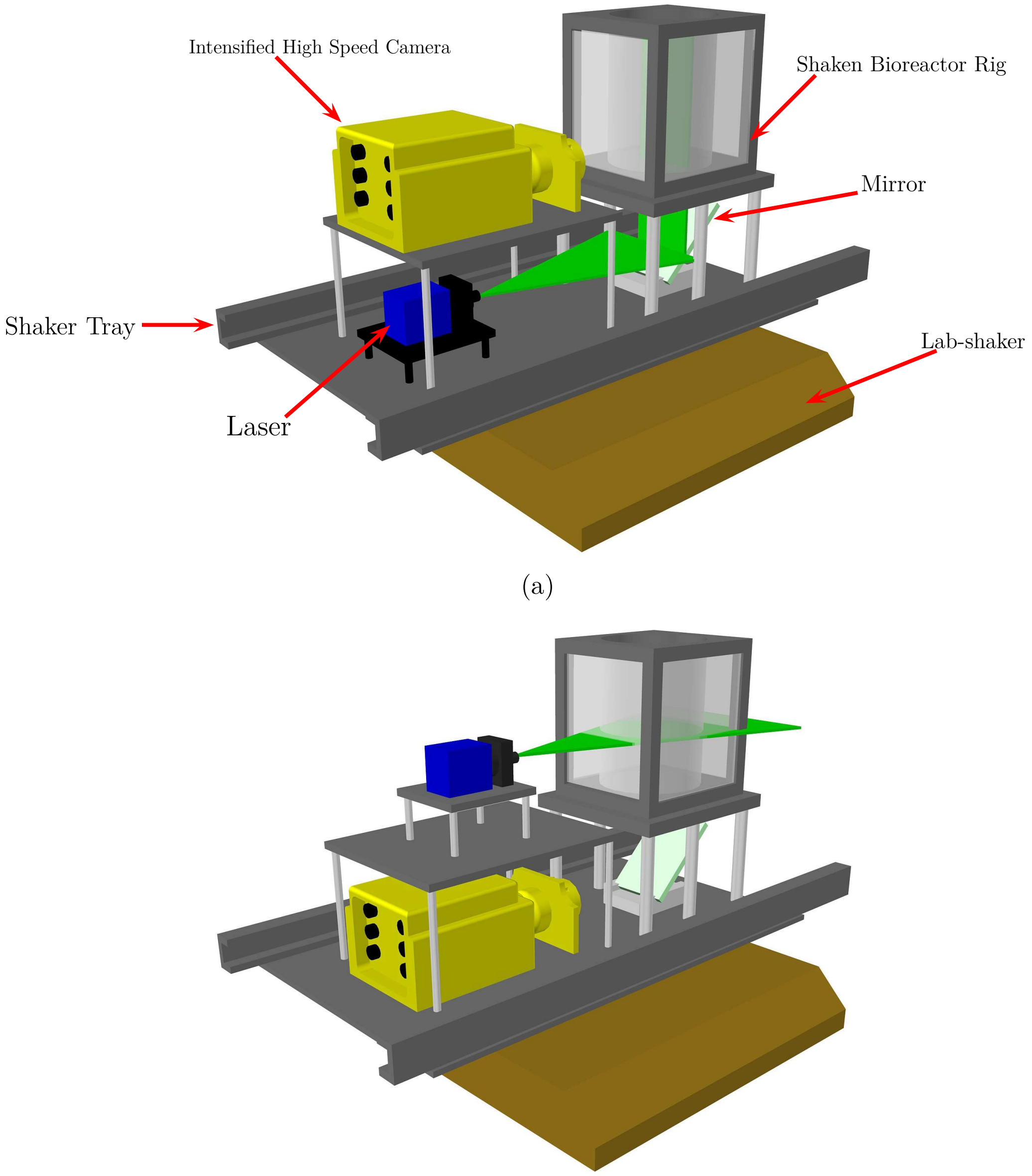

(a)

(b)

Figure 2.5: Sketch of the two PIV system set-ups used to measure the velocity field on a: (a) vertical plane; (b) horizontal plane.

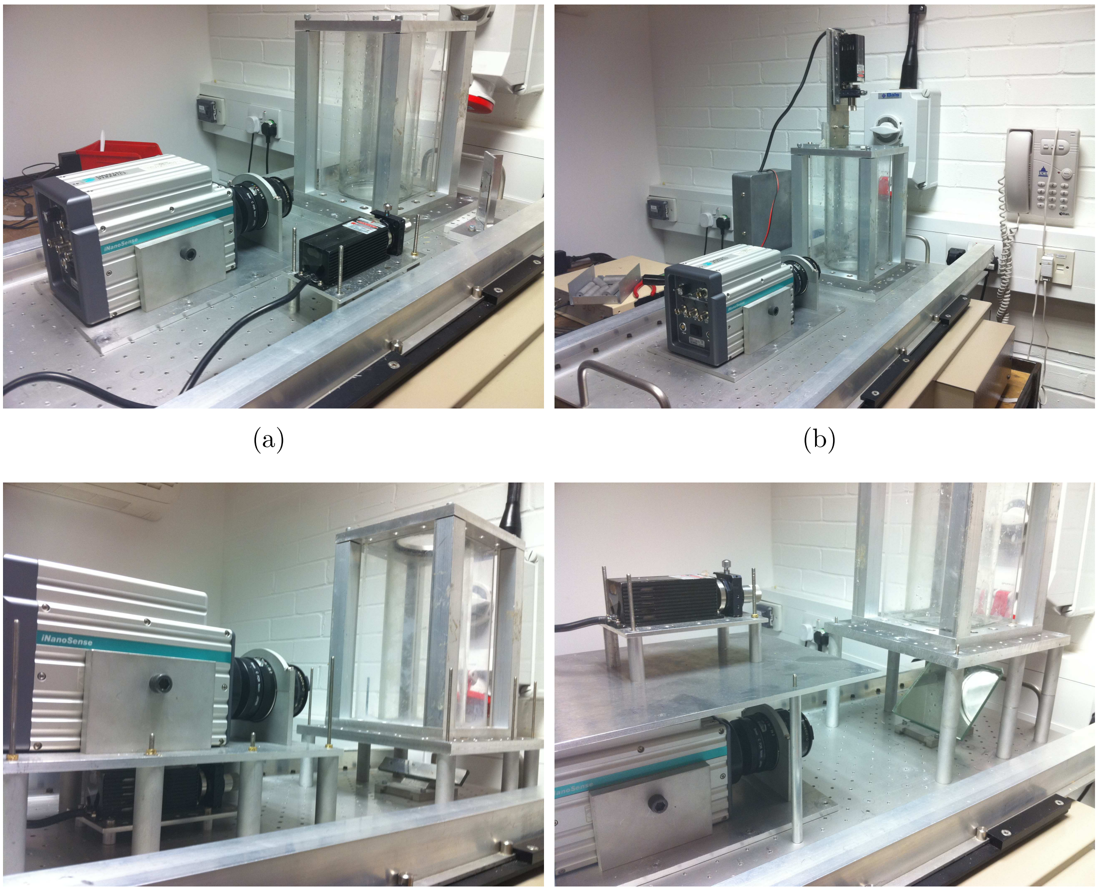

(a) (b) (c) (d)

Figure 2.6: Photographs of the different arrangements tried and used to carry out PIV measurements: (a) PIV set-up 1; (b) PIV set-up 2; (c) PIV set-up 3; (d) PIV set-up 4.

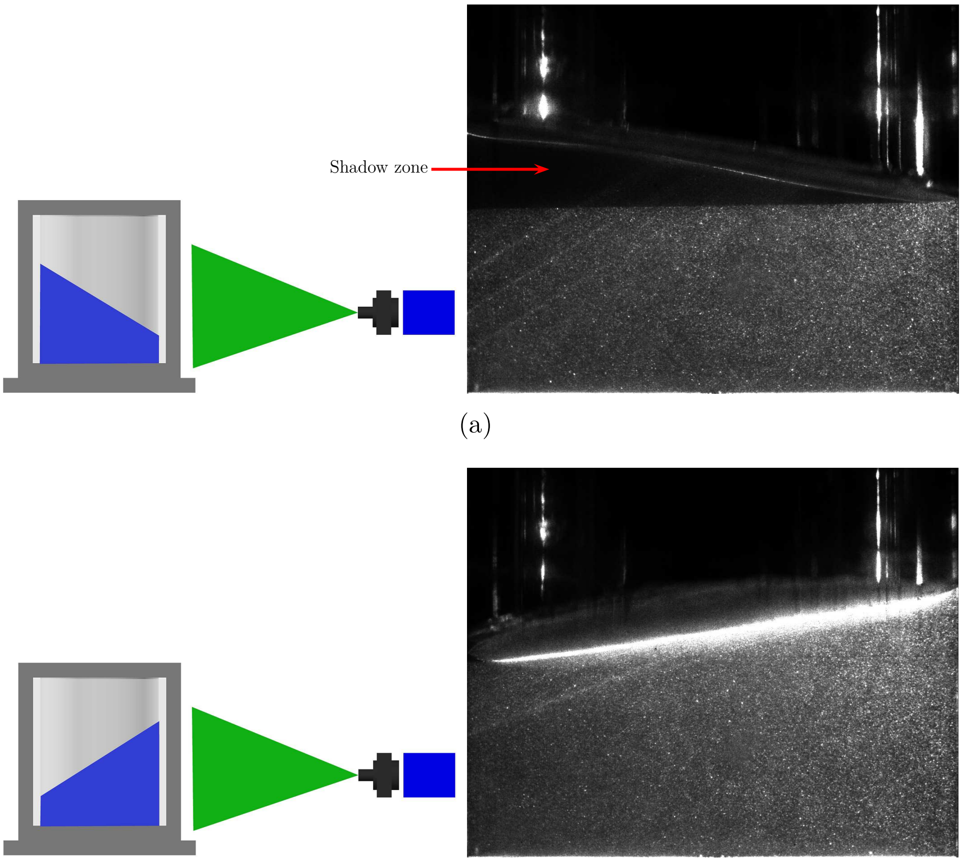

(a)

(b)

Figure 2.7: Variation of the illumination of the investigation area when the laser is entering from one side of the bioreactor for two different phase angles: (a) ϕ=0°; (b) ϕ=180°.

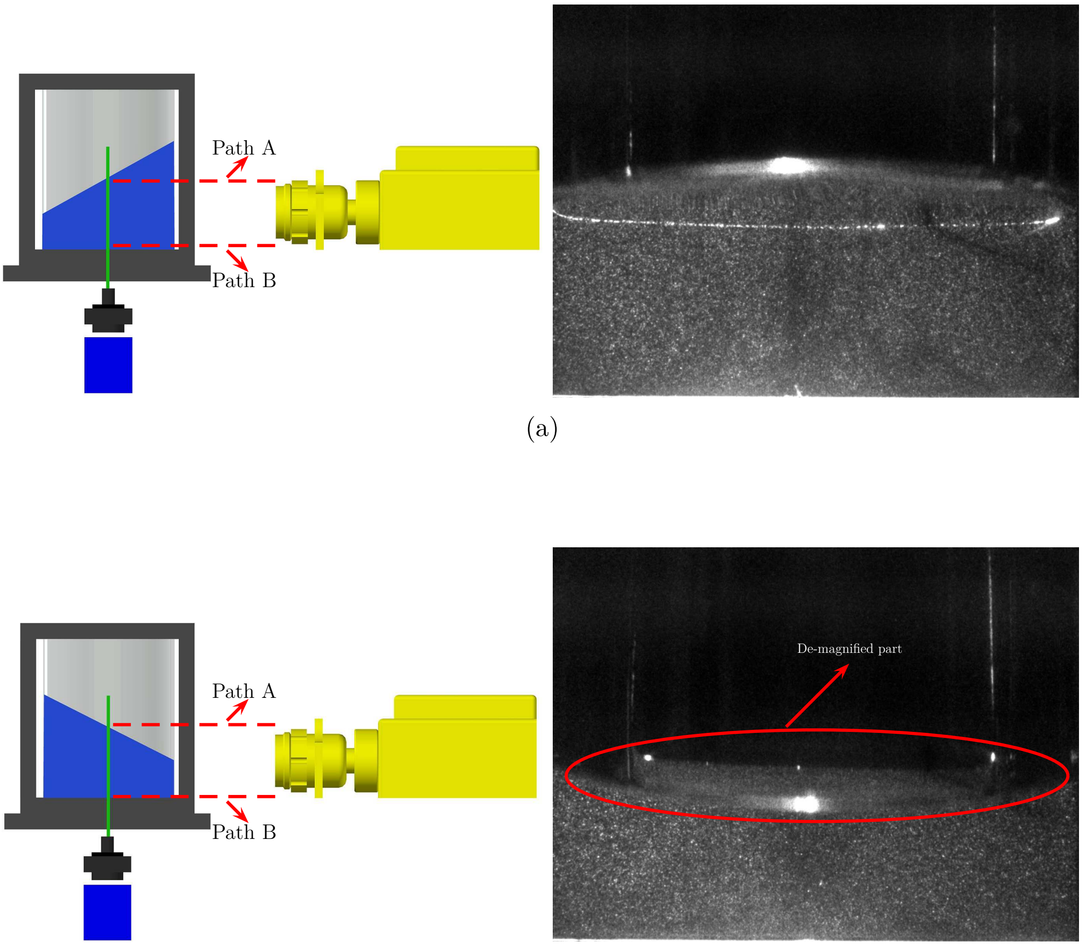

(a)

(b)

Figure 2.8: Degree of optical distortions for different phase angle, ϕ, when the laser is entering from the bottom of the bioreactor: (a) ϕ=270°; (b) ϕ=90°.

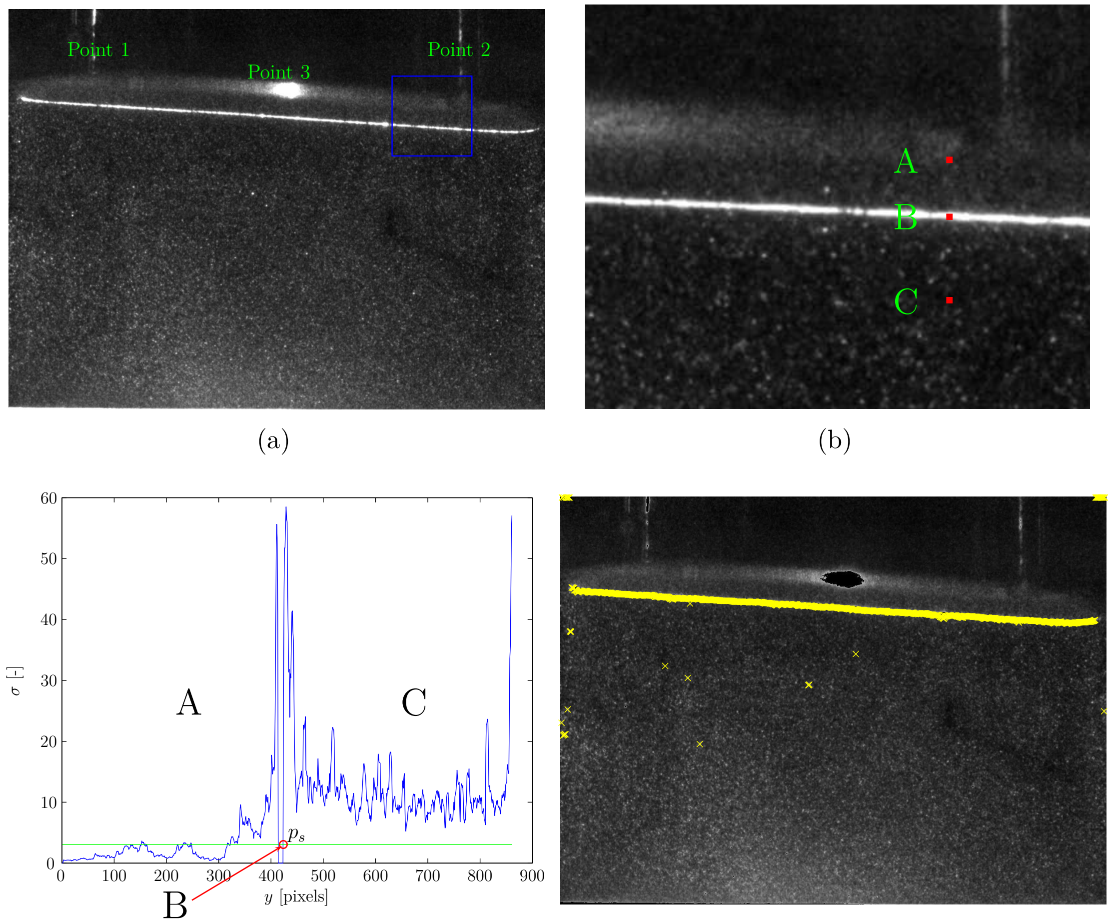

(a) (b)

(c) (d)

Figure 2.9: Description of the steps comprised in the detection algorithm of the free surface: (a) Identification of laser reflections by the bioreactor walls; (b) Close up of the squared blue region to show three different positions of the averaging window used to estimate σ; (c) Variation of σ along the vertical height of the bioreactor; (d) Raw profile of the free surface detected after the standard deviation analysis.

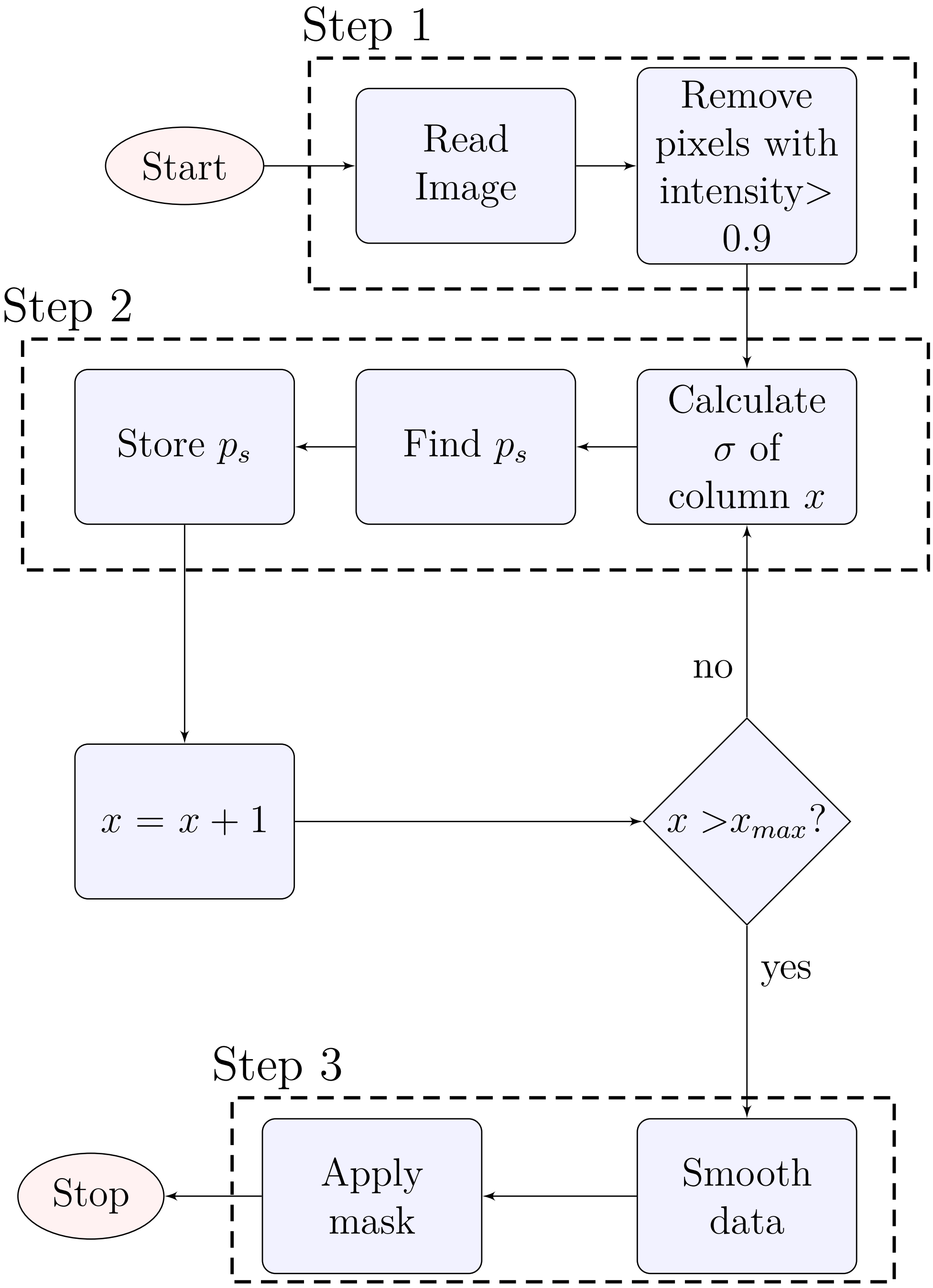

Figure 2.10: Flow diagram for the free surface tracking.

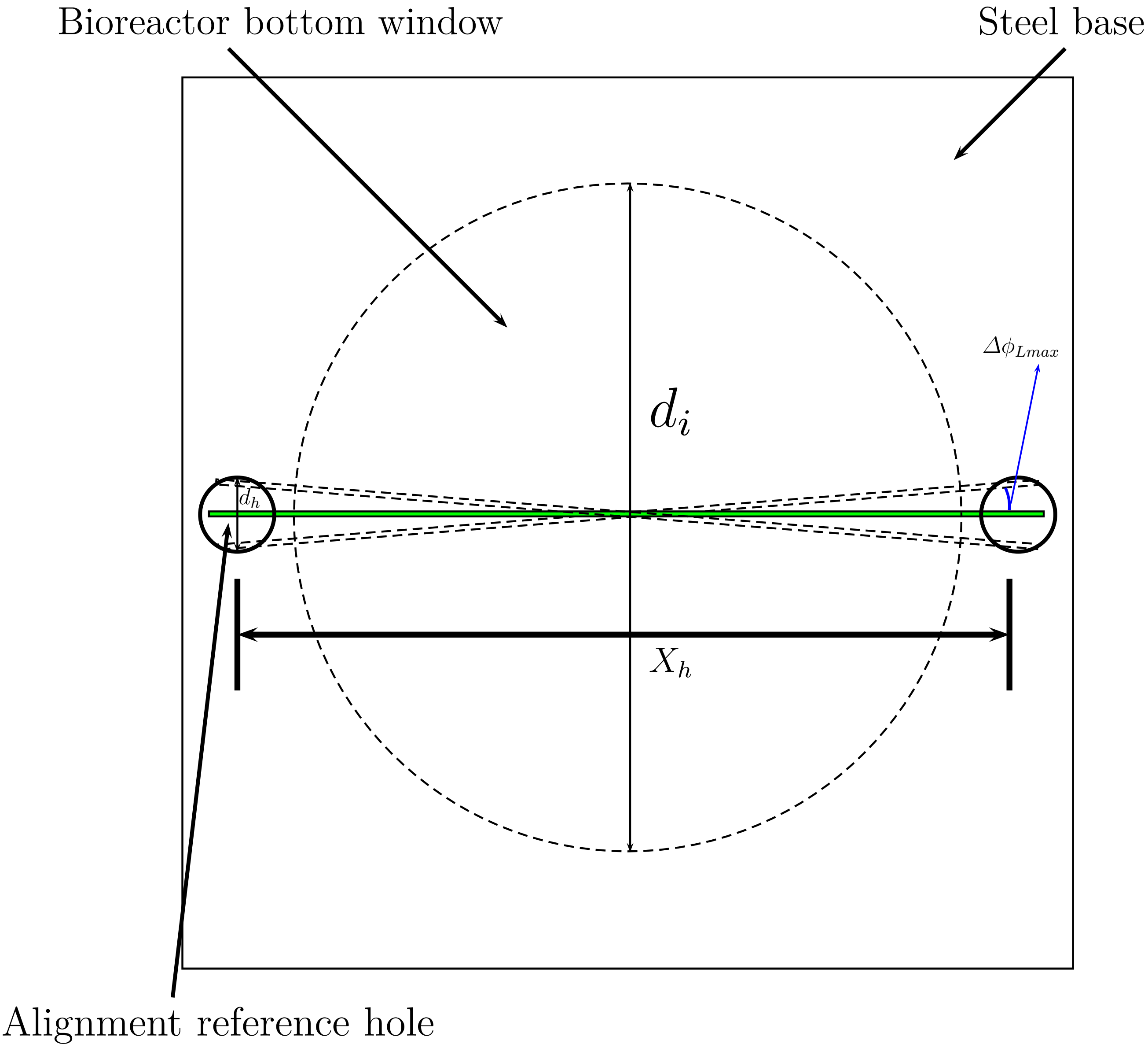

Figure 2.11: Sketch representing the maximum error $\Delta\phi_{Lmax}$ made during the alignment of the vertical laser with the two reference holes positioned at the bottom of the tank (not to scale).

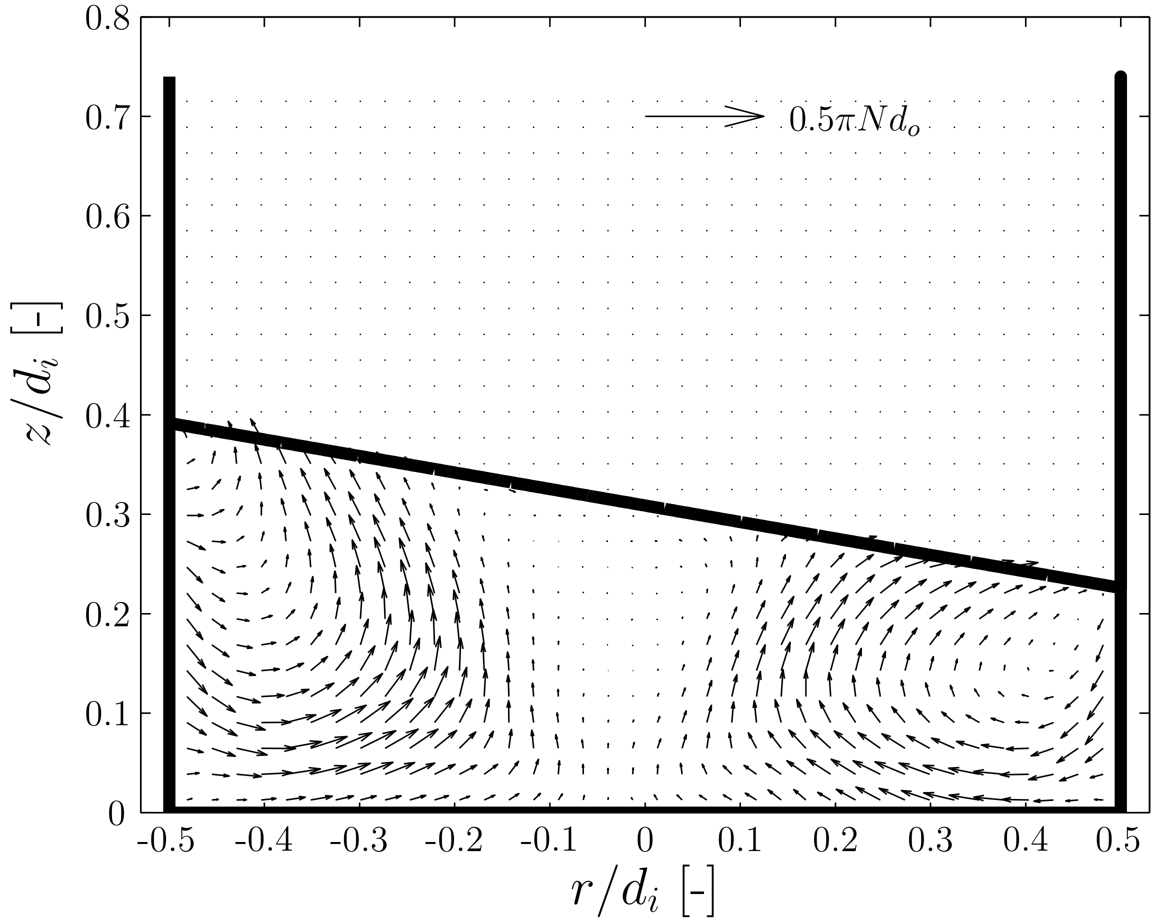

Figure 2.12: Typical velocity vector field for ϕ=0° (h/d_i=0.3 and N=80 rpm).

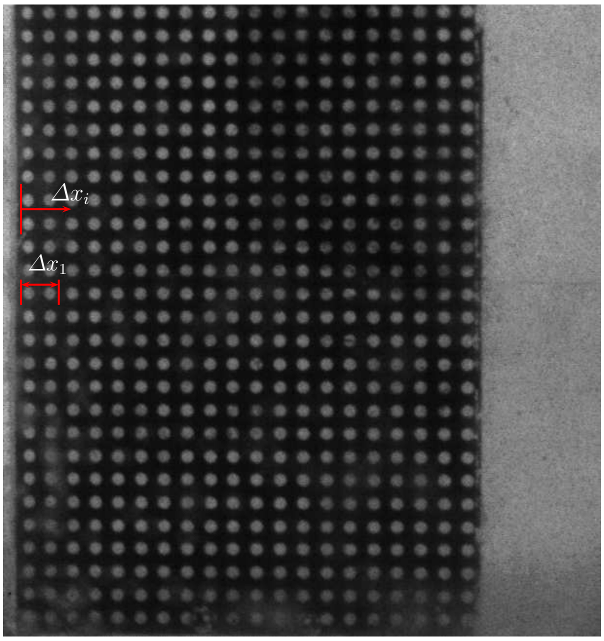

(a)

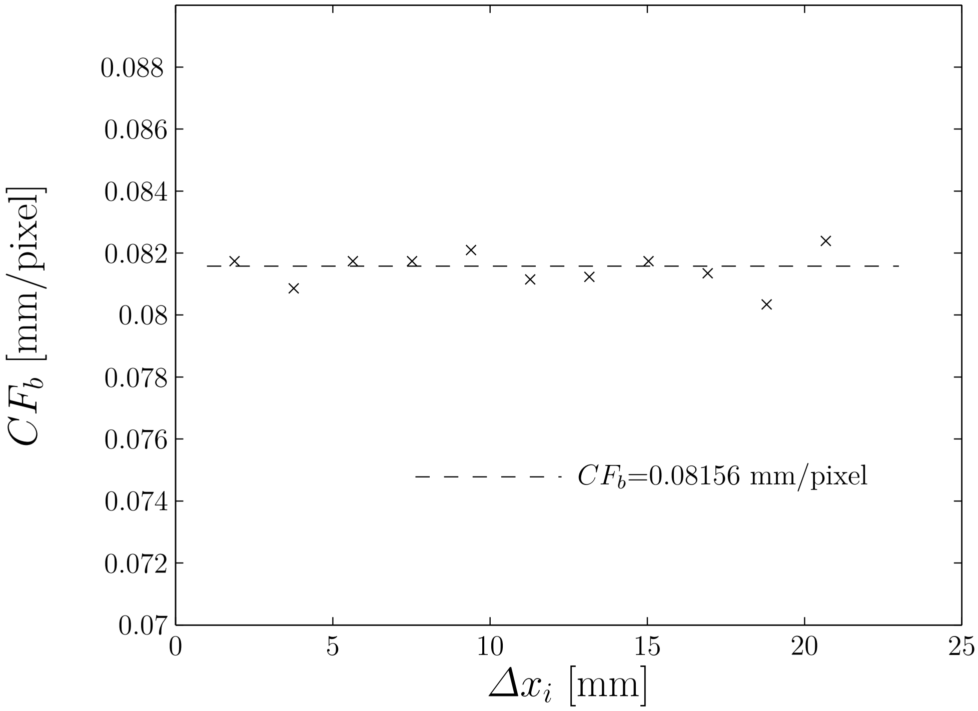

(b)

Figure 2.13: (a) Image of the calibration board with transparent circular dots positioned next to the wall of the cylinder; (b) Variation of the calibration factor, CF_b, with increasing horizontal distance, Δx_i, from the left cylinder wall.

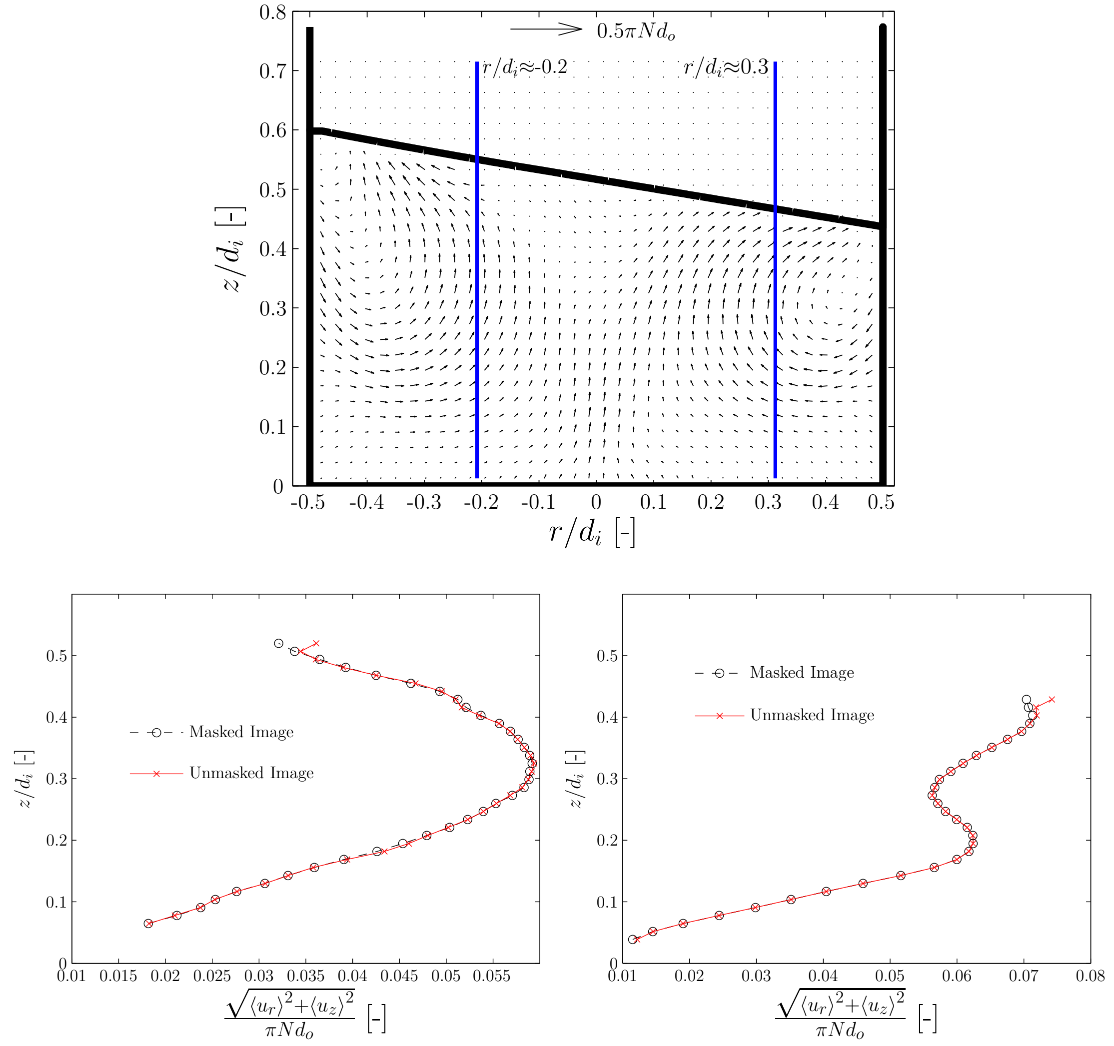

Figure 2.14: (a) Velocity vector field for ϕ=0°, h/d_i=0.5 and N=90 rpm; Comparison of the velocity magnitude profiles obtained for two radial positions with and without masking: (b) r/d_i=-0.25; (c) r/d_i=0.38.

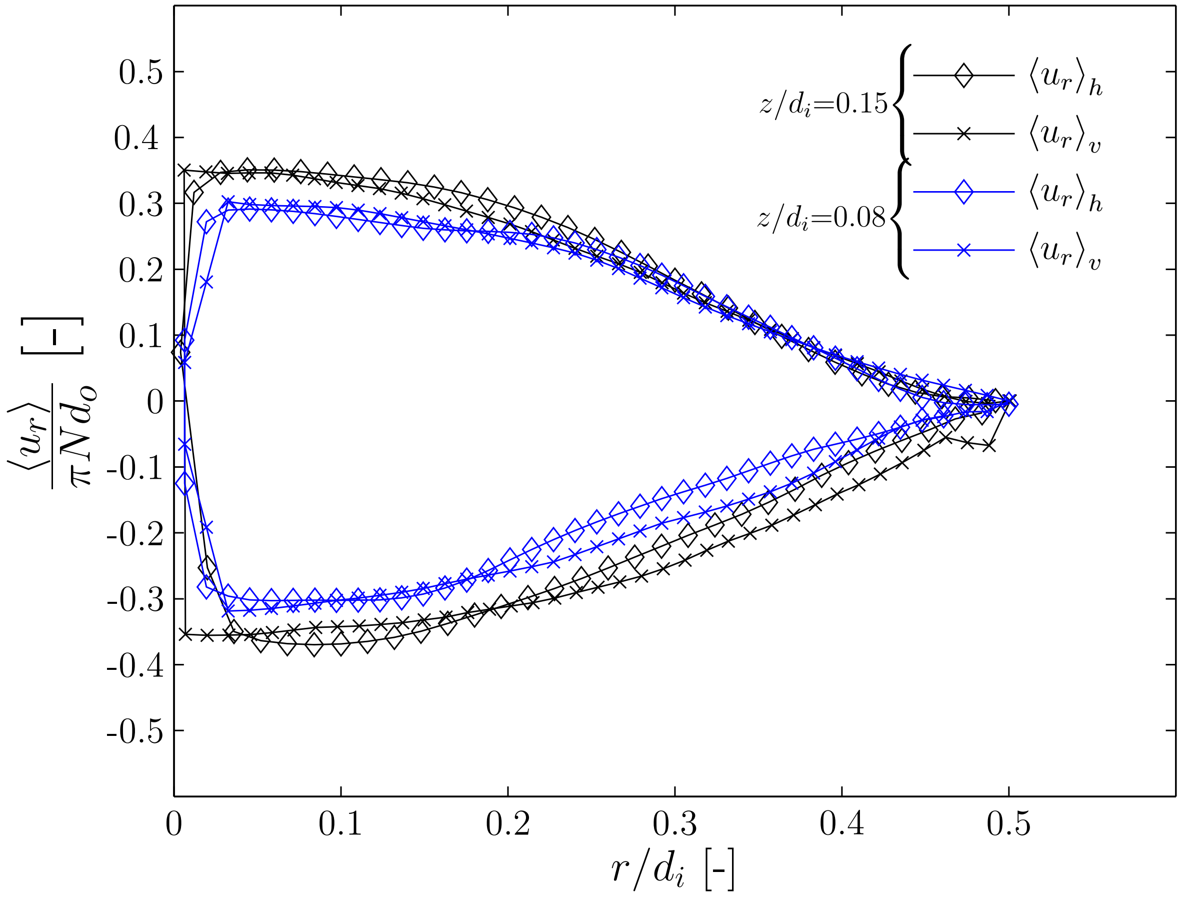

Figure 2.15: Comparison of the radial profiles of the phase-resolved radial velocity component, $\langle u_r \rangle$, obtained from vertical and horizontal plane measurements at z/d_i=0.08 and 0.15 (N=90 rpm, ϕ=270°).

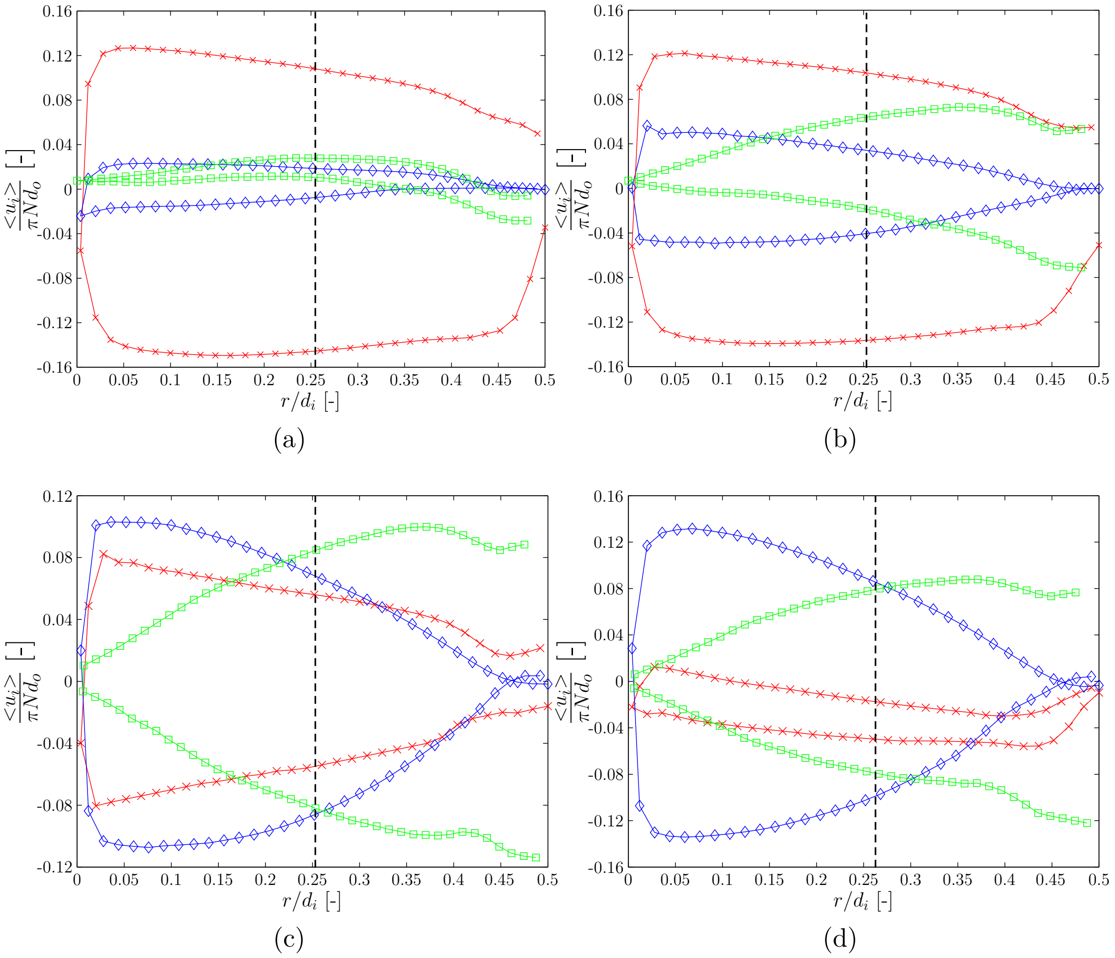

(a) (b)

(c) (d)

Figure 2.16: Velocity profile of $\frac{<u_z>}{\pi N d_o}$(□),$\frac{<u_r>}{\pi N d_o}$(◇) and $\frac{<u_\theta>}{\pi N d_o}$(×) for ($h/d_i$=0.3, N=60 rpm and z/d_i=0.2): (a) ϕ=0°; (b) ϕ=30°; (c) ϕ=60°; (d) ϕ=90°.

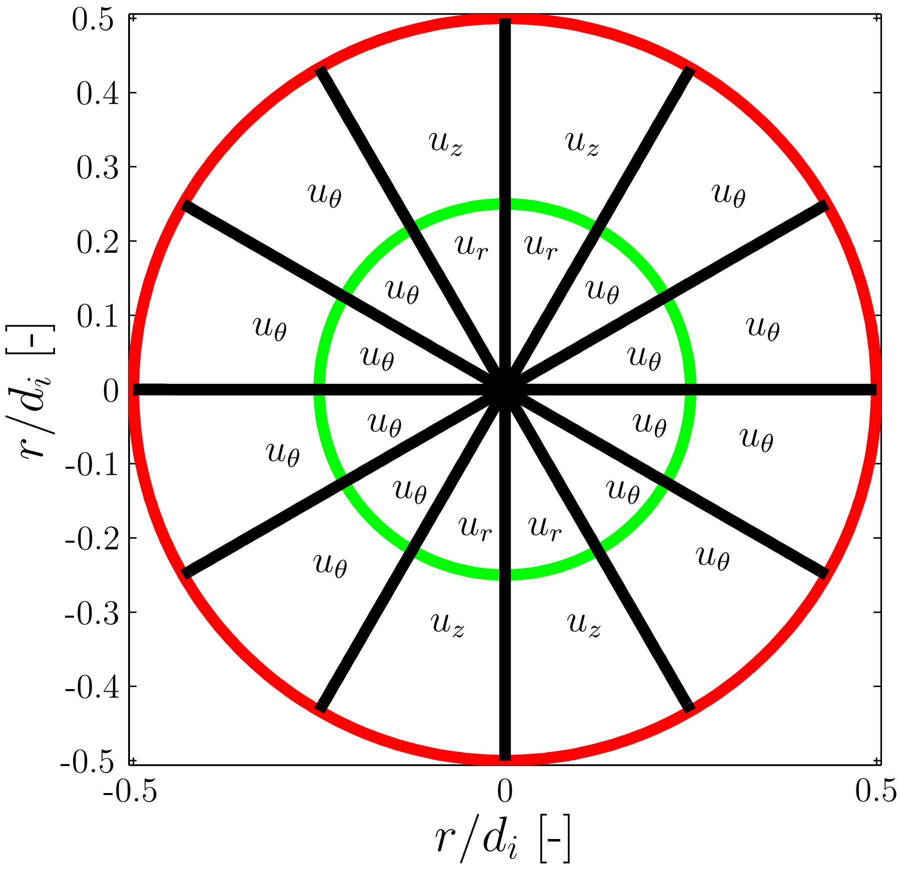

Figure 2.17: Diagram showing which velocity component is dominant at different radial positions, r/d_i, and phase angles, ϕ.

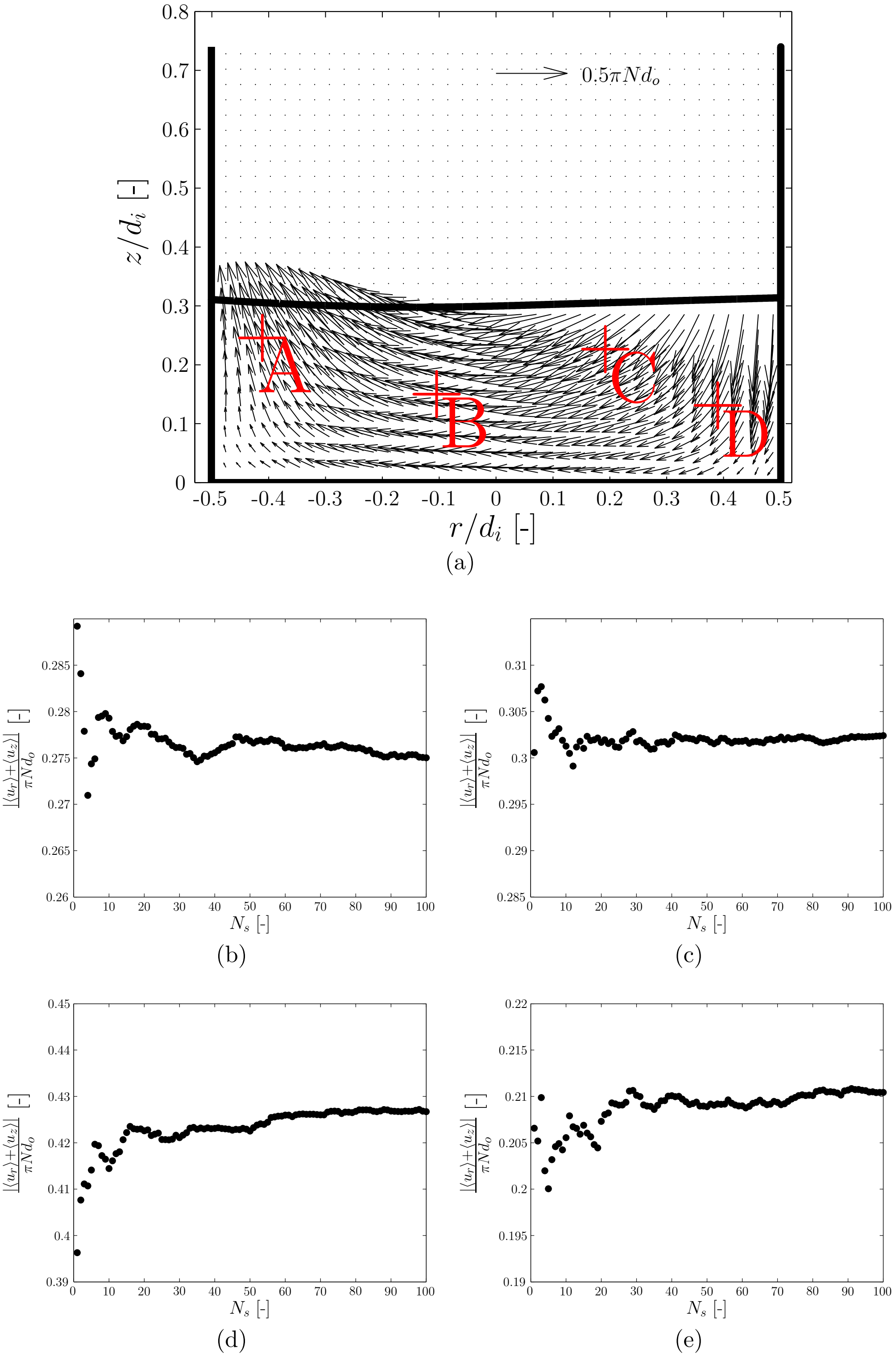

(a)

(b)

(c)

(d)

(e)

Figure 2.18: (a) Velocity vector field for ϕ=270°, h/d_i=0.3, N=90 rpm with visualisation of the points A, B, C and D; Variation of $\frac{|\langle u_r\rangle+\langle u_z\rangle|}{\pi N d_o}$ versus the number of snapshots, N_s at point: (b) A; (c) B; (d) C; (e) D.

Chapter 3

Flow characterisation, transition and scaling law for low viscosity fluids[†]

3.1 Introduction

The results presented in this chapter provide a thorough characterisation of the flow and mixing dynamics in a cylindrical shaken bioreactor, when water is used as the working fluid (ν=1×10^{-6} m^2s^{-1}) and operating conditions such as medium height, h, shaking frequency, N, orbital shaking diameter, d_o, and inner diameter of the cylinder, d_i, are varied. In Section 3.2 a phase-resolved analysis is carried out to determine the flow characteristics for a reference operating configuration with h/d_i=0.3, Fr=0.11 (N= 90 rpm) and d_o/d_i=0.25. In Section 3.3 the variation of the flow field with increasing shaking frequency, N, is presented

---

[†] Most of the results presented in this chapter are included in:

Weheliye, W., Yianneskis, M. and Ducci, A. (2012), "On the flow dynamics and out-of-phase phenomena in orbitally shaken bioreactors", *Proceedings of the 14th European Conference on Mixing*, pp. 509-514; and

Weheliye, W., Yianneskis, M. and Ducci, A. (2013) , "On the fluid dynamics of shaken bioreactors - Flow characterization and transition.", *AIChE J.*, 59, 334-344.

for non-dimensional fluid heights, h/d_i=0.5 and 0.7 at ϕ=0°. The out-of-phase phenomenon that is often discussed in the literature is further investigated and the flow fields associated are presented in Section 3.4. A preliminary flow scaling law based on fixed orbital and inner diameters (d_o=25 mm and d_i=100 mm) is formulated in Section 3.5 to determine the shaking frequency associated to the flow transition between in-phase and out-of-phase conditions. Flow characterisation of in-phase conditions is presented in Section 3.6, where the scaling law previously determined is extended to different combinations of fluid height, h, shaking frequency, N, orbital diameter, d_o, and inner diameter, d_i.

3.2 Characterisation of in-phase flow

Before proceeding with the discussion it is necessary to provide information on the methodology used to estimate the vorticity which is employed later to characterise the large scale flow structures occurring in the cylindrical shaken bioreactor. The PIV data provide a phase averaged velocity field on a two-dimensional grid, and by finite differentiation an estimation of the spatial derivatives of the velocity gradient tensor can be obtained. It is standard methodology to estimate the gradients using a central differentiation scheme and obtain the vorticity in the k^{th} direction, orthogonal to the plane of measurements, from Equation 3.1.

$$\omega_k = \left(\frac{\partial u_i}{\partial x_j} - \frac{\partial u_j}{\partial x_i} \right) \tag{3.1}$$

In the present study, the circulation method is used, which employs the velocity data from the 8 points around the point of interest (Raffel *et al.*, 1998). The estimation of the vorticity at a point (x_i,x_j) is provided by Equation 3.2, which is based on the circulation, $\mathit{\Gamma}_k(x_i, x_j)$, in the k^{th} direction orthogonal to the plane of measurements.

$$\omega_k(x_i, x_j) = \frac{\mathit{\Gamma}_k(x_i, x_j)}{4\mathit{\Delta} x_i \mathit{\Delta} x_j} \tag{3.2}$$

Where x_i and x_j are the coordinates of the point, $\mathit{\Delta} x_i$ and $\mathit{\Delta} x_j$ are the grid spacing and $\mathit{\Gamma}_k(x_i, x_j)$ is the circulation along a path comprising the 8 points around the point (x_i,x_j) (see Equation 3.3).

$$\begin{aligned}\mathit{\Gamma}_k(x_i, x_j) = {} & \tfrac{1}{2}\mathit{\Delta} x_i[u(x_i - \mathit{\Delta} x_i, x_j - \mathit{\Delta} x_j) + 2u(x_i, x_j - \mathit{\Delta} x_j) + u(x_i + \mathit{\Delta} x_i, x_j - \mathit{\Delta} x_j)] \\ & + \tfrac{1}{2}\mathit{\Delta} x_j[v(x_i + \mathit{\Delta} x_i, x_j - \mathit{\Delta} x_j) + 2v(x_i + \mathit{\Delta} x_i, x_j) + v(x_i + \mathit{\Delta} x_i, x_j + \mathit{\Delta} x_j)] \\ & - \tfrac{1}{2}\mathit{\Delta} x_i[u(x_i + \mathit{\Delta} x_i, x_j + \mathit{\Delta} x_j) + 2u(x_i, x_j + \mathit{\Delta} x_j) + u(x_i - \mathit{\Delta} x_i, x_j + \mathit{\Delta} x_j)] \\ & - \tfrac{1}{2}\mathit{\Delta} x_j[v(x_i - \mathit{\Delta} x_i, x_j + \mathit{\Delta} x_j) + 2v(x_i - \mathit{\Delta} x_i, x_j) + v(x_i - \mathit{\Delta} x_i, x_j - \mathit{\Delta} x_j)]\end{aligned} \tag{3.3}$$

The circulation method reported in Equation 3.2 performs better than the central differentiation scheme of Equation 3.1 because more data points enter in the vorticity estimation. This aspect is documented in Raffel *et al.* (1998) who reported that the uncertainty in the vorticity estimate, ϵ_w, from Equation 3.2 is $\epsilon_w \approx 0.61\epsilon_u/\mathit{\Delta} x_i$, while for the central differentiation scheme of Equation 3.1 it is $\epsilon_w \approx \epsilon_u/\mathit{\Delta} x_i$, where ϵ_u is the uncertainty affecting the velocity estimate.

In this section data are first presented for a reference operating configuration with h/d_i=0.3 and N=90 rpm. The 2D phase-resolved velocity fields and the contour plots of the tangential components of the vorticity, ω_θ, are shown in Figures 3.1 (a-d) for four phase angles. The sketches above the plots indicate the angular position of the cylinder (blue circle) along its orbit (dotted circle). In Figure 3.1 (a) two counter-rotating vortices are observed close to the walls of the cylinder. The intensity of the two vortical structures is similar in magnitude with absolute vorticity levels varying in the range $|\omega_\theta/\pi N|$=0-1. Figure 3.1 (a) captures the flow field when the tray reaches its position furthest to the left, ϕ=0°, and the fluid experiences the maximum centrifugal acceleration in the plane of measurement. In this case the free surface assumes its maximum inclination, and the two vortical cells are completely separated with little or no fluid being exchanged between the two.

As the cylinder proceeds along its orbit (Figures 3.1 b and c) the free surface oscillates, and a radial flow develops with the left vortical cell pumping fluid towards the right one. Despite the presence of this strong radial swing motion, the two vortical structures are still identifiable from the vorticity contour plots, even if their maximum absolute intensity has decreased and reached a minimum $|\omega_{\theta max}/\pi N|$=0.4, for ϕ=90° (Figure 3.1 c). With increasing ϕ the left vortical cell keeps pumping fluid into the right one until the free surface reaches its highest position on the right-hand side of the plane of measurement for ϕ=180° as it is shown in Figure 3.1 (d). At this mid-cycle stage a new cycle starts but in this case the radial swing flow is in the opposite direction and the vortical cell on the right-hand side pumps fluid into the left one. A more comprehensive understanding of the flow dynamics induced by the free surface oscillation can be gained from the flow reconstruction included in the video enclosed in the attached CD (filename: Shaken.avi), and from the phase lock mixing time measurement video by Rodriguez *et al.* (2013) (filename: Mixing.avi). If the vorticity contour plots of increasing ϕ are azimuthally stacked after each other a 3D visualisation of the flow can be obtained, denoting the constant presence of an inclined toroidal vortex in the cylinder. The highest/lowest sides of the torus are always aligned with the centrifugal acceleration of the shaker table that changes its direction as ϕ increases.

The ensemble-averaged velocity field and vorticity contour plots are shown in Figure 3.2. These plots were purposely made to compare with the simulations carried out by Kim and Kizito (2009), which is the only work available in the literature that provides a qualitative characterisation of the flow occurring in an orbitally shaken cylinder. The current results agree well with their ensemble-averaged vector fields for a fluid of analogous viscosity (ν=1×10^{-6} m^{2}s^{-1}), with two symmetrical counter-rotating vortices, one on each side of the cylinder. It should be noted that the vorticity range of the ensemble-average vector field is approximately half of the vorticity range associated to the phase resolved flow for ϕ=0°, implying that time-averaged circulation times, controlling macro-mixing, are approximately double those encountered at the phase angle where the fastest mixing occurs.

A further analysis was carried out to asses how the circulation of the toroidal vortex varied with the phase angle, ϕ. The circulation, Γ^*, was estimated from Equation 3.4 where the integral is carried out over the area, A_ω, which corresponds to a vorticity level $\frac{\omega_\theta}{\pi N}$ >0.3. A visualisation of the areas $A_{\omega R}$ and $A_{\omega L}$ for the right and left hand side vortices, respectively, is shown in Figure 3.3 (a) at ϕ=180°.

$$\Gamma^* = \frac{\int_{A_\omega} |\omega_\theta| dA_\omega}{A_\omega} \tag{3.4}$$

The variation of Γ^* for different ϕ is shown in Figure 3.3 (b). It can be noted that the greatest space-averaged circulation, Γ^*, is observed at ϕ=0°, while the lowest Γ^* is observed at ϕ=90°. This behaviour can be explained by considering that at ϕ=0° the two counter-rotating vortices are well defined from the velocity vector field and the vorticity contour plots with $|\omega_{\theta max}/\pi N|$=1, whilst at ϕ=90° the flow field is dominated by the radial swing motion and the vortical structures are less pronounced with maximum vorticity levels, $|\omega_{\theta max}/\pi N|$=0.4. This plot also shows that the circulations of the vortices at the two sides of the bioreactor where the local free surface is at its minimum or maximum height are comparable and independent of the local orientation of the vortex, which shows an oblong shape aligned either in the horizontal or vertical direction depending whether the free surface is locally low or high, respectively (cf. Figure 3.3 a).

3.3 Toroidal vortex growth for in-phase condition

The phase-resolved velocity field and vorticity contour plots for three shaking frequencies, N=70, 90 and 110 rpm, are shown in Figures 3.4 (a-c) for a non-dimensional fluid height, h/d_i=0.5 at a fixed angular position, ϕ=0°. Similarly to the flow dynamics described previously for h/d_i=0.3, two counter-rotating vortices can be distinguished in all the plots. As the shaking frequency, N, is increased (Figures 3.4 a-c), the two counter-rotating vortices start to extend towards the bottom of the cylinder and their intensity increases in magnitude, with the maximum absolute non-dimensional vorticity being more than double ($|\omega_\theta/\pi N| = 0.4 \rightarrow 1$). For a shaking frequency, N=110 rpm, the two counter-rotating vortices extend over the entire fluid height (Figure 3.4 c) and completely control the flow inside the bioreactor.

The results are consistent with the findings of Tissot *et al.* (2010), who measured the mixing time in a cylindrical shaken bioreactor by means of a colourisation technique, and reported that for a low shaking frequency two different zones could be distinguished inside the reactor: a first zone close to the free surface where mixing was enhanced by convection, and a second zone close to the bottom of the cylinder where mixing was dominated by diffusion. Their results corroborate the present findings as the two counter-rotating vortices of Figures 3.4 (a-c) are responsible for the transport processes observed by Tissot *et al.* (2010) in the region below the free surface that they denoted as “convection zone”. Similarly the so-called “diffusion zone” can be correlated to those regions of Figures 3.4 (a) and (b) below the vortical structure where flow activity is less intense. In Figures 3.4 (a-c) the horizontal line provides a visual reference to define the boundary between the convection (Zone A) and the diffusion (Zone B) regions. It should be noted that the line has been drawn by arbitrarily selecting a fixed value of the vorticity ($|\omega_\theta/\pi N| = 0.1$) and drawing a horizontal line which is tangent to the lowest part of the vorticity contour value selected.

Figures 3.5 (a-d) show the phase-resolved flow field obtained for h/d_i=0.7 at $\phi = 0°$ for increasing N. This set of experiments was carried out in order to study the growth of the toroidal vortex for a greater h/d_i and assess whether a limit occurs over this expansion towards the bottom of the tank. The two zones can be clearly seen, similarly to what was observed earlier for h/d_i=0.5 (see Figures 3.4 a-c), where the two counter-rotating vortices are observed near the free surface and the vortices increases in size with increasing N. In this case however for the highest shaking frequency investigated, N=130 rpm, the flow field exhibits a different behavior as the free surface shows a curved profile (Figure 3.5 d) and for this liquid height ratio, h/d_i=0.7, a shaking frequency, N, for which the vortices extend all the way to the bottom of the cylinder was not found. Another interesting point worth mentioning is the fact that at a shaking frequency, N=70 rpm, for a non-dimensional fluid height, h/d_i=0.5 and 0.7, the free surface angle, $\varDelta h/d_i$, and the length of the vortices shown in Figure 3.4 (a) and Figure 3.5 (a) are comparable. This behaviour is also true for N=90 rpm and 110 rpm (cf. Figures 3.4 b-c and Figures 3.5 b-c).

The variation of the circulation, $\overline{\varGamma}^*$, for the three non-dimensional fluid heights considered, h/d_i=0.3, 0.5 and 0.7, with increasing Fr is shown in Figure 3.6 (a). It should be noted that the circulation, $\overline{\varGamma}^*$, was estimated by applying Equation 3.4 to the ensemble-average velocity and vorticity fields. Figure 3.6 (b) provides a visualisation of the area $A_{\omega E}$ ($\frac{\omega_\theta}{\pi N}$ >0.1) used to estimate $\overline{\Gamma}^*$. It is worth noting that the ensemble-average is symmetrical, and therefore the analysis was limited to the right vortical structure of Figure 3.6 (b). As it can be seen from Figure 3.6 (a) higher circulation levels are observed for increasing Fr and decreasing non-dimensional fluid height, h/d_i. For Fr <0.09 similar circulation levels are observed for all the three non-dimensional fluid heights investigated, while for Fr >0.11 the circulation levels for h/d_i=0.3 ($\frac{\overline{\Gamma}^*_{\omega=0.1}}{\pi N}$=0.22) is higher when compared to that of the other two non-dimensional heights, h/d_i ($\frac{\overline{\Gamma}^*_{\omega=0.1}}{\pi N}\approx$0.18). This behaviour can be explained by considering that at $Fr = 0.11$ the vorticity intensity of the two counter-rotating vortices h/d_i=0.3 is greater than that for h/d_i=0.5 and 0.7 (cf. Figure 3.1 a, Figure 3.4 b and Figure 3.5 b).

3.4 Characterisation of the flow for incipient out-of-phase condition

As mentioned in Chapter 1 an "out-of-phase" phenomenon occurs at a high shaking frequency, N, and is characterised by an amount of fluid not being in phase with the movement of the table. It has been observed by Büchs *et al.* (2000a) that the out-of-phase flow is fully established for Ph <1.26, where Ph is estimated from Equation 1.4. Such data concern vessels of somewhat different wall/bottom shapes and have been obtained for Fr >0.4, when most of the fluid is spread over the bioreactor walls. The results presented in this section focus at Fr <0.4, when most of the fluid is in contact with the cylinder base, and therefore comparisons with the data of Büchs *et al.* (2000a) must be made with care. The current measurements indicate that the transition from in-phase to out-of-phase flow takes place gradually and show evidence that the onset of out-of-phase flow is already present for Fr <0.4.

The PIV and free surface tracking measurements show that at lower N for in-phase conditions, the free surface can be approximated by an inclined elliptical disk, whose longer (shorter) axis is the inclined (horizontal) straight line at the intersection between the free surface for ϕ=0° (ϕ=90°) and the vertical laser plane. At higher N the free surface becomes three dimensional and its intersection with the vertical laser plane exhibits a wavy profile. This analysis is in agreement with the free surface snapshots of Zhang *et al.* (2009), which clearly show the transition of the free surface from an elliptical disk to a more complex 3D shape, when the shaking frequency is increased. Under these conditions a significant change in the flow pattern occurs.

This is well illustrated by the vector field and vorticity contour plots of Figures 3.7 (a) and (b), which were obtained for N=110 rpm and 130 rpm, respectively (h/d_i=0.3, ϕ=0°). When comparing the flow fields produced at N=90 rpm (Figure 3.1 a) with that obtained for N=110 rpm (Figure 3.7 a), it is evident that as N is increased the two characteristic vortices tend to be pushed toward the walls, and at even greater N, 130 rpm (Figure 3.7 b), the flow pattern changes with the tangential vorticity direction at the two walls being opposite to that of in-phase condition. It is interesting to point out the similarity between the flow fields observed for h/d_i=0.3 at N=110 rpm (Figure 3.7 a) and for h/d_i=0.5 at N=130 rpm (Figure 3.7 c). In both cases the two vortices are pushed towards the walls of the cylinder and transition from the in-phase to the out-of-phase condition is observed. These results corroborate the findings of Section 3.3, and highlight that for greater h/d_i transition to out-of-phase will occur with similar dynamics but at a greater shaking frequency, N.

The variation in flow pattern is more evident when a comparison is made between the measurements taken on horizontal planes for in-phase and incipient out-of-phase conditions, for ϕ=0°. Figure 3.8 shows the contour plots of the axial vorticity, ω_z, and the velocity vector fields at three different planes. For an operating condition h/d_i=0.3 and N=90 rpm (Fr=0.11, in-phase flow), three different horizontal planes are considered at z/d_i=0.1, 0.15 and 0.2. It should be noted that for these operating the toroidal vortex reaches to the bottom of the tank, and therefore all the elevations considered are within the “convection zone” region. On each plane two stagnation points associated to nearly zero in plane velocity can be identified close to the wall on opposite sides of the bioreactor. A better visualisation of the two stagnation points is given on the planar view of Figure 3.9, where two distinct streams of opposite direction emanating from and merging at the stagnation points denoted as B and A are clearly present.

The variation of the angle $\Delta\alpha$ between the lines joining the stagnation points to the center of the cylinder, and its relation to the diameter of the toroidal vortex, d_v, obtained from the vertical plane measurements is reported in Tables 3.1 and 3.2 for h/d_i=0.3 and h/d_i=0.5, respectively. From Tables 3.1 and 3.2, it is evident that before flow transition Fr <0.11 (0.17) for h/d_i= 0.3 (0.5) occurs, the angle $\Delta\alpha$ increases together with the toroidal vortex diameter d_v for increasing Fr. With the onset of flow transition, both $\Delta\alpha$ and the toroidal vortex diameter decrease as the vortex is pushed towards the cylinder wall.

Figure 3.10 shows the axial vorticity, ω_z, for a non-dimensional fluid height, h/d_i=0.7, and shaking frequency, N=70 rpm (Fr=0.068, in-phase flow), at three different horizontal planes, two of which are in the “diffusion zone” at elevations z/d_i=0.1, and 0.35, and one in the “convection zone” at an elevation z/d_i=0.6. In the diffusion zone (z/d_i=0.1) the flow is locally characterised by an axial vortex centered on the cylinder axis. A close view of the axial vortex characteristic at

z/d_i=0.1 can be seen from Figure 3.11. As higher planes are considered, the local flow exhibit a behaviour similar to that described in Figure 3.8 for h/d_i=0.3 and N=90 rpm, where two stagnation points with nearly zero in-plane velocity, can be distinguished near the wall for z/d_i=0.6.

When the transition to out-of-phase condition is induced at a speed of N=130 rpm (Fr=0.24) for h/d_i=0.3 (Figure 3.12), the two stagnation points disappear and a vortex along a vertical axis is formed on the side of the bioreactor opposite to the highest side of the free surface. The intensity of this vortex with vertical axis is similar at each of the elevations considered. This vortex is also present in the instantaneous free surface visualisation of Zhang *et al.* (2009) for the greatest speed they considered (h/d_i=185 mm, N=100 rpm, d_o=50 mm and d_i=287 mm). It is worth noting that for the incipient out-of-phase condition the maximum intensity of the non-dimensional vorticity in the axial direction ($|\omega_{zmax}/\pi N| \approx 5$), is approximately five times greater than that exhibited for in-phase flow by the tangential vorticity component, ($|\omega_{\theta max}/\pi N| \approx 1$), for the same height h/d_i=0.3 (cf. Figures 3.1 a and 3.13). This implies that non-dimensional circulation times for incipient out-of-phase flow are approximately five times smaller than those for in-phase flow. Taking into account all the differences between the two experiments and systems, this value compares reasonably well with the non-dimensional mixing time, $(NT)_m$, measured by Tissot *et al.* (2010) who found for similar rotational speeds of 90 rpm and 110 rpm dimensionless mixing times of $(NT)_m$≈60 and ≈16 with a ratio of approximately 3.75 between the two.

The extent of the flow transition to out-of-phase can be determined by estimating $\Delta\beta$, the angle defined by the direction of the centrifugal acceleration for the phase condition considered (a horizontal line for ϕ=0°) and the direction of the line joining the bioreactor and vortex centers (Figure 3.13). For the operating conditions of Figure 3.13 the out-of-phase angle was found to be $\Delta\beta \approx 20^o$. Experiments were repeated for the three different phase angles ϕ=0°, 90° and 180° and it was found that $\Delta\beta$ is independent of the phase angle considered (see Figure 3.14). It can be concluded that the vortex with the vertical axis precesses around the cylinder axis as the tray proceeds along its orbit.

The transition to the out-of-phase flow was further investigated by conducting image analysis of the variation of the height, h_f, of the point on the free surface profile at the left wall of the bioreactor (see Figure 3.15) for different phase angles, ϕ. Measurements of h_f were carried for the following operating conditions: h/d_i=0.3, $0° < \phi < 360°$, and N=60 rpm (Fr=0.05), 90 rpm (Fr=0.11), 120 rpm (Fr=0.2) and 130 rpm (Fr=0.24). The variation of h_f/h_{fmax} with ϕ is shown in Figure 3.16, where h_{fmax} is the maximum value of h_f. For Fr=0.05 and 0.11, h_f/h_{fmax} is maximum (h_f/h_{fmax}=1) for ϕ=0°, which means that the free surface is in phase with the orbital movement of the shaken bioreactor. At high shaking frequencies, N=120 rpm (Fr=0.20) and 130 rpm (Fr=0.24), the maximum value of h_f was found at ϕ=15° and 20°, respectively. The latter value is in good agreement with the one found at the same speed from the PIV measurements carried out on horizontal planes. These results corroborate the hypothesis that a transition to out-of-phase flow starts being manifested at low values of Fr, and increases with increasing N until the fluid reaches the fully-established out-of-phase conditions reported by Büchs *et al.* (2000a).

3.5 Flow transition and scaling law for fixed d_o and d_i

The current section aims at deriving a scaling law based on dimensionless parameters that can be used to have more control over the bioprocess by selecting the most appropriate flow conditions for fixed orbital diameter, d_o, and inner diameter, d_i. The free surface motion is the flow driving mechanism of the shaken bioreactor, and its maximum inclination, θ, is related to the non-dimensional wave amplitude, $\mathit{\Delta} h/d_i$, according to the left hand side of Equation 3.5.

$$\tan(\theta) = \frac{\mathit{\Delta} h}{d_i} \propto \frac{a_c}{g} = \frac{2(\pi N)^2 d_o}{g} = Fr \tag{3.5}$$

From fluid mechanics considerations the local inclination of the free surface is also expected to be proportional to the ratio between the centrifugal acceleration, a_c=$(\pi N d_o)^2/(0.5 d_o)$, determined by the orbital motion and gravity, g (see the right hand side of Equation 3.5). A visualisation of the centrifugal and gravitational accelerations and their relationship with the angle θ is presented in Figure 3.17. The variation of the free surface angle, θ, with Fr is provided in Figure 3.18 (a) for fluid of low viscosity (water, ν=1×10^{-6} $\mathrm{m^2s^{-1}}$) and three different non-dimensional fluid heights, h/d_i=0.3, 0.5 and 0.7, at $\phi = 0°$. It can be noted that for all the three non-dimensional fluid heights h/d_i considered approximately the same free surface angle, θ, is obtained for any given Fr.

The variation of $\mathit{\Delta} h/d_i$ against Fr is plotted in Figure 3.18 (b) for different combinations of non-dimensional fluid heights, h/d_i, and non-dimensional orbital to cylinder diameters ratio, d_o/d_i, at ϕ=0°. It should be mentioned that the data of Figure 3.18 (b) were obtained for three cylinders of diameter, d_i=70 mm, 100 mm and 130 mm, and several orbital diameters in the range, d_o=15-50 mm. From Figure 3.18 (b) it is evident that at a given Fr, for selected combinations of N and d_o, the free surface will assume a fixed inclination that is independent of the fluid height, h/d_i. The linear relationship is more consistent at lower Fr when the flow is in-phase and the free surface inclination is constant across the free surface profile, while at a higher Fr, the data are more scattered about the reference line due to the wavy nature of the free surface for transitional out-of-phase conditions. For these conditions the local inclination of the free surface varies along the radial coordinate and therefore the inclination, $\Delta h/d_i$, reported in Figure 3.18 (b) is the average across the radial profile. The constant of proportionality, a_{ow}=1.4, is directly related to the fluid considered (water in this chapter) and its value is greater than unity because it takes into account the extra inertial forces, besides the centrifugal acceleration of the tray, due to the movement of the fluid inside the cylindrical bioreactor.

For an orbital diameter, d_o/d_i=0.25, it was found that the toroidal vortex extends to the bottom of the tank for a non-dimensional critical wave amplitude, $(\Delta h/h)_c \approx 0.5$. This is also evident from the plots of Figures 3.1 (a) and 3.4 (c) for h/d_i=0.3 (Fr=0.11) and 0.5 (Fr=0.17), respectively. In both cases a further increase in Fr would determine the onset of the out-of-phase condition. Based on these considerations Equation 3.5 can be re-arranged as in Equation 3.6, where the non-dimensional fluid height, h/d_i, is directly and inversely proportional to the Froude number, Fr, and the non-dimensional wave amplitude, $\Delta h/h$, respectively.

$$\frac{h}{d_i} = \frac{h}{\Delta h}\left(\frac{2(\pi N)^2 d_o}{g}\right) a_{ow} \tag{3.6}$$

Based on Equation 3.6 a map of h/d_i, Fr combinations is provided in Figure 3.19 to help predict the flow transition. Three inset diagrams reproducing the characteristic flows before, at and after flow transition are present at the left, center and right hand sides of Figure 3.19, respectively. They are associated to three different regions in the figure, that are indicated by the gray shaded area and those on either side of it. It is worth remarking that this map is valid only for d_o/d_i=0.25. Positions on the left hand side of Figure 3.19, at low Fr, are characterised by a toroidal vortex, which is increasing in size as Fr increases (cf. inset diagram on the left hand side). In this case two regions in the (Fr, h/d_i) plane can be identified before flow transition. For h/d_i <0.5 transition occurs when h/d_i=$2a_{ow}Fr$ (($\Delta h/h)_c \approx 0.5$), while for h/d_i >0.5 it occurs at a constant Fr for $a_{ow}Fr$=0.25 (cf. Figure 3.5 c for h/d_i=0.7). In the latter case the toroidal vortex does not reach the bottom of the vessel for any Fr. In Figure 3.19 the gray dashed lines are associated with constant values of $\Delta h/h$, and can be used to determine the extent of the diffusion zone beneath the toroidal vortex. The extent of the diffusion zone decreases as $\Delta h/h$ increases and therefore according to Equation 3.6 the slope of lines of greater $\Delta h/h$ decreases and reaches its minimum inclination of 2 at the onset of flow transition for h/d_i <0.5. The data points in the gray shaded area are those where flow transition occurs and the toroidal vortex either reaches the bottom of the tank (h/d_i <0.5), or grows to its maximum size (h/d_i >0.5). To the right of the gray shaded area, at greater Fr, the flow is characterised by a vortex with vertical axis as shown by the inset flow diagram on the right hand side of Figure 3.19. The data points in Figure 3.19 represent the combinations of h/d_i and Fr that have been tested with both the PIV and the free surface image analysis to validate the proposed methodology to identify flow transition.

3.6 Extended flow transition and scaling law for different d_o and d_i

In Section 3.5 it was observed that the two counter-rotating vortices either extended all the way to the bottom of the cylinder for $(\Delta h/h)_c$=0.5 and $(\Delta h/d_i)$ <0.5, or grew to their maximum size and did not reach the bottom of the vessel at any given Fr for h/d_i >0.5 when d_o and d_i are 25 mm and 100 mm, respectively. The aim of this section is to assess the occurrence of the flow transition and identify its critical wave amplitude, $(\mathit{\Delta} h/h)_c$, for different combinations of d_o and d_i.

The first set of experiments addresses the variation of the critical condition for different d_o when d_i is kept fixed. Figure 3.20 shows the characteristic vector fields and the associated vorticity contour maps of incipient flow transition (toroidal vortex reaching to the bottom of the tank) for three different orbital diameters, d_o=15 mm, 40 mm and 50 mm, and fixed non-dimensional fluid height, h/d_i=0.3 and inner diameter, d_i=100 mm. Two major conclusions can be drawn from these flow fields. First it is evident that for greater d_o the free surface inclination increases, with critical wave amplitudes $(\mathit{\Delta} h/h)_c \approx 0.39$, 0.63 and 0.71 for d_o=15 mm, 40 mm and 50 mm, respectively. This indicates that the critical wave amplitude, $(\mathit{\Delta} h/h)_c$, for which the two counter-rotating vortices reach to the bottom of the cylinder varies with the orbital diameter, d_o, when the inner diameter, d_i, is fixed. The second point that is worth to stress is that the intensity of the vortices for the critical conditions reported in Figure 3.20 increases with increasing d_o. For instance the maximum absolute intensity of the two counter-rotating vortices is, $|\omega_{\theta_{max}}/\pi N|$=0.8 and 1.2, for d_o=15 mm and 50 mm, respectively. The reason for the increase in the circulation levels for increasing d_o can be explained by considering the results previously presented in Figure 3.6 (a). From Figure 3.6 (a) it was seen that the circulation levels of the vorticies increased with increasing Fr. It should be noted that in that case the only parameter that was varied in the Froude number definition was the shaking frequency, N. However in the case of Figure 3.20 both N and d_o are varied. Therefore for increasing d_o the Froude number, Fr, increases which corresponds to higher circulation levels of the vortices.

The flow fields with a non-dimensional fluid height, h/d_i=0.5, for three different orbital diameters, d_o=15 mm, 40 mm and 50 mm, were further investigated for fixed d_i=100 mm and characteristic results are shown in Figure 3.21. In Figure 3.21 (a) the two zones (i.e. convection and diffusion zone) can clearly be seen and for this operating configuration (h/d_i=0.5 and d_o/d_i=0.15), a shaking frequency for which the two counter-rotating vortices extend all the way to the bottom of the cylinder was not found like was the case of h/d_i=0.7 and d_o/d_i=0.25 (see Figure 3.5). However when d_o=40 mm and 50 mm, a shaking frequency for which the two counter-rotating vortices reach to the bottom of the cylinder was identified and the corresponding critical wave amplitudes were, $(\Delta h/h)_c \approx 0.63$ and 0.71, respectively.

A second set of experiments was carried out to assess how the critical wave amplitude varies with greater non-dimensional fluid heights. Figure 3.22 shows the flow fields of h/d_i=0.55 and 0.6 for d_o/d_i=0.5 (d_o=50 mm and d_i=100 mm). For both fluid heights it can be seen that the two counter-rotating vortices reach to the bottom of the tank for the same critical wave amplitude, $(\Delta h/h)_c \approx 0.71$. It should be stressed that when Figure 3.19 was discussed, it was found that for d_o/d_i=0.25 the two counter-rotating vortices did not reach to the bottom of the tank for any shaking frequency when the non-dimensional fluid heights, $h/d_i > 0.5$. These results therefore show clearly that the value of of the maximum non-dimensional fluid height, h/d_i, for which the toroidal vortex extends to the bottom of the tank is controlled by the orbital to cylinder diameter ratio, d_o/d_i, and its value increases as d_o/d_i increases.

The third set of experiments addressed the variation of the critical wave amplitude, $(\Delta h/h)_c$, for different inner diameters, d_i, when the orbital diameter, d_o, and non-dimensional fluid height, h/d_i, are fixed (d_o=15 mm and h/d_i=0.3). Figure 3.23 shows the phase-resolved vector fields and contour plots of the tangential components of the vorticity, ω_θ, for two different inner diameters, d_i=70 mm and

d_o=130 mm. From the free surface heights at the sides of the bioreactor it can be seen that the critical wave amplitudes are, $(\varDelta h/h)_c \approx 0.46$ and 0.34, for d_i=70 and 130 mm, respectively. This indicates that the critical wave height, $(\varDelta h/h)_c$, for which the two counter-rotating vortices reach all the way to the bottom of the cylinder, is a function of the cylinder diameter, d_i, as is evident from the variation of the non-dimensional orbital to cylinder diameter ratio from 0.21 to 0.11 in Figures 3.23 (a) and (b), respectively.

A compilation of all the different combinations of h, N, d_o and d_i examined so far is provided in Figure 3.24 where the variation of the critical wave amplitude, $(\varDelta h/h)_c$, is plotted against d_o/d_i for two different non-dimensional fluid heights, h/d_i=0.3 and 0.5 and three different tank sizes, d_i=70 mm, 100 mm and 130 mm. It should be noted that the critical wave amplitude, $(\varDelta h/h)_c$, shown in Figure 3.24 corresponds to a condition when the two vortices reach to the bottom of the tank. In agreement with the descriptive analysis shown in Figures 3.20- 3.23, the current results show that the critical wave amplitude, $(\varDelta h/h)_c$, increases with increasing d_o/d_i and can be modelled with a square root power law.

This behavior is also visible in the data reported in Figure 3.18 (b). Data associated to higher values of d_o/d_i deviate from the linear relationship related to the toroidal vortex flow at a greater Fr and therefore at a greater inclination θ (see Equation 3.5). For example data points of d_o/d_i=0.5 are still close to the linear relationship at Fr=0.25, while for d_o/d_i=0.25 they deviate at Fr=0.15 (cf. Figure 3.18 b). The reason for this behaviour can be explained by considering two hypothetical flow configurations for a given inner diameter d_i and fluid height h with $d_{o1} < d_{o2}$. When the critical Froude number Fr_{c1} is achieved, both configurations will exhibit the same wave amplitude $\varDelta h$ (or free surface inclination θ), but the rotational speed of configuration 1 will be greater than that of configuration 2 and therefore the free surface vertical speed, $(\varDelta hN)_1$, will be also greater than that of configuration 2, $(\varDelta hN)_2$. In other words configuration 2 associated with greater d_o will not experience the flow transition at Fr_{c1} because its free surface vertical speed is not large enough to push the circulation of the toroidal vortex to the bottom of the tank. This is well summarized in Equation 3.7, derived from $(\varDelta h/h)_c = (d_o/d_i)^{0.5}$, which shows the ratio of critical wave speeds for two configurations with same non-dimensional fluid height, h/d_i, as a function of the critical Froude number, Fr_c, and inner diameter, d_i, ratios. In particular for a constant d_i, the ratio of the critical wave speeds must be equal to the square root of the critical Froude number ratio and therefore of the critical centrifugal accelerations.

$$\frac{(\varDelta h_c N_c)_1}{(\varDelta h_c N_c)_2} = \sqrt{\frac{(d_o/d_i)_1}{(d_o/d_i)_2}\frac{N_{c1}}{N_{c2}}\frac{h_1}{h_2}} = \sqrt{\frac{Fr_{c1}}{Fr_{c2}}}\sqrt{\frac{d_{i1}}{d_{i2}}} \tag{3.7}$$

The flow transition map of Figure 3.19 is valid only for d_o/d_i= 0.25, and can be extended to different orbital to cylinder diameter ratios d_o/d_i, by redrawing the inclined and vertical transition lines after substitution of the critical wave amplitude, $(\varDelta h/h)_c$=$(d_o/d_i)^{0.5}$, in Equation 3.6. When the non-dimensional fluid height h/d_i> $(d_o/d_i)^{0.5}$, flow transition will occur without the vortex reaching to the bottom of the tank and a diffusion zone will be present. This latter condition is occurring in the map of Figure 3.19 for h/d_i>0.5 when d_o/d_i=0.25. In this case the transitional velocity for a given configuration does not depend on the orbital diameter but is limited by the inner cylinder diameter and can be found from Equation 3.8.

$$a_{ow} Fr_{d_i} = 1 \tag{3.8}$$

where Fr_{d_i} is the Froude number based on the cylinder diameter, d_i. Figure 3.25 shows the variation of $a_{ow}Fr_{d_i}$ with non-dimensional fluid height, h/d_i> $(d_o/d_i)^{0.5}$, for different combinations of d_o and d_i. The results shown in Figure 3.25 confirm that the transitional velocity does not depend on the orbital diameter but is a function of the cylinder inner diameter for non-dimensional fluid heights, $h/d_i > (d_o/d_i)^{0.5}$. To conclude, when the non-dimensional fluid height, $h/d_i < (d_o/d_i)^{0.5}$, the transitional speed can be derived from Equation 3.6 by using the critical wave amplitude, $(\Delta h/h)_c = (d_o/d_i)^{0.5}$, while for $h/d_i > (d_o/d_i)^{0.5}$ Equation 3.8 must be used.

The proposed scaling law was also assessed against the experimental free surface visualisations of Zhang *et al.* (2009), which show flow transitions occurring at rotational speeds in the range of 80-100 rpm and 60-80 rpm for a 5 l and 30 l bioreactor, respectively (cf. Figure 3.26). Their data show good agreement with the present ones, and the model proposed in this work predicts transitional speeds of 86 rpm and 66 rpm. These values were estimated from Equation 3.8 because $h/d_i > (d_o/d_i)^{0.5}$ in both the configurations. Similarly the experimental free surface visualisations of Tissot *et al.* (2010) were also examined using the proposed scaling law. Figure 3.27 shows two snapshots of the free surface of a 30 l bioreactor for shaking frequencies of 65 and 80 rpm. From the two images it is evident that the free surface is very different between the two flow conditions and transition must have taken place within the two shaking frequency considered. In agreement with these considerations the proposed scaling law predicts a transitional speed of 66 rpm. Also in this case the flow transition was again estimated from Equation 3.8 because $h/d_i > (d_o/d_i)^{0.5}$ (0.61>0.41).

3.7 Concluding remarks

In this chapter a detailed and improved understanding of the flow dynamics inside a shaken bioreactor was presented. In the first part of the chapter, PIV measurements were presented for a fixed orbital diameter, d_o=25 mm, and inner diameter, d_i=100 mm. The measurements revealed that the flow consisted mostly of two counter-rotating vortices, observed near the free surface for $(\mathit{\Delta} h/h)_c < 0.5$, that might strongly affect the mixing process. These vortices extended all the way to the bottom of the cylinder for $(\mathit{\Delta} h/h)_c = 0.5$ and $h/d_i < 0.5$. These measurements were also assessed against the findings of Tissot *et al.* (2010) who measured the mixing time in a cylindrical shaken bioreactor. The two counter-rotating vortices can be used to explain the transport processes observed by Tissot *et al.* (2010) in the region below the free surface that they denoted as “convection zone”. Similarly the so-called “diffusion zone” can be correlated to those regions below the vortical structure where flow activity is less intense.

In the second part of the chapter the flow fields obtained with higher shaking frequencies were investigated. With increasing rotational speed, the two counter-rotating vortices first move towards the vessel wall and then subsequently disappear, when an incipient flow transition to out-of-phase flow is in evidence. Measurements in horizontal planes were also made in order to elucidate further the flow behaviour. A vertical vortex precessing around the cylinder was identified for high Fr flow and the center of this vertical vortex was out-of-phase with respect to the axis of the shaker table. Free surface image analysis showed that the extent of out-of-phase flow increased with Fr. The results confirmed the presence of out-of-phase flow at high rotational speeds or Fr, in agreement with the findings of Büchs *et al.* (2000a). Furthermore, the detailed flow field data obtained show clear evidence that incipient transition to out-of-phase flow starts at Froude number lower than the Fr >0.4 considered by Büchs *et al.* (2000a).

In the final part of the chapter flow field analyses were carried out for different combinations of d_o and d_i. The free surface and PIV measurements showed that the critical wave amplitude, $(\mathit{\Delta} h/h)_c$, is both a function of d_o and d_i. Thus, the scaling laws of Equation 3.6 and 3.8 for $h/d_i < (d_o/d_i)^{0.5}$ and $h/d_i > (d_o/d_i)^{0.5}$ are proposed to identify the dominant flow structures (i.e. toroidal or vertical vortex) and to improve bioprocess design by predicting the flow transition occurring in the bioreactor and by scaling similar flow conditions in cylindrical bioreactors of different sizes.

N [rpm]	Fr [-]	$\Delta\alpha$ [°]	d_v/d_i [-]
70	0.07	105	0.15
90	0.11	128	0.25
110	0.17	71	0.16
130	0.24	0	NA

Table 3.1: Variation of the angle $\Delta\alpha$ and of the non-dimensional toroidal vortex diameter, d_v/d_i, with N and Fr for h/d_i=0.3.

N [rpm]	Fr [-]	$\Delta\alpha$ [°]	d_v/d_i [-]
70	0.07	103	0.13
90	0.11	135	0.27
110	0.17	148	0.44
130	0.24	88	0.21

Table 3.2: Variation of the angle $\Delta\alpha$ and of the non-dimensional toroidal vortex diameter, d_v/d_i, with N and Fr for h/d_i=0.5.

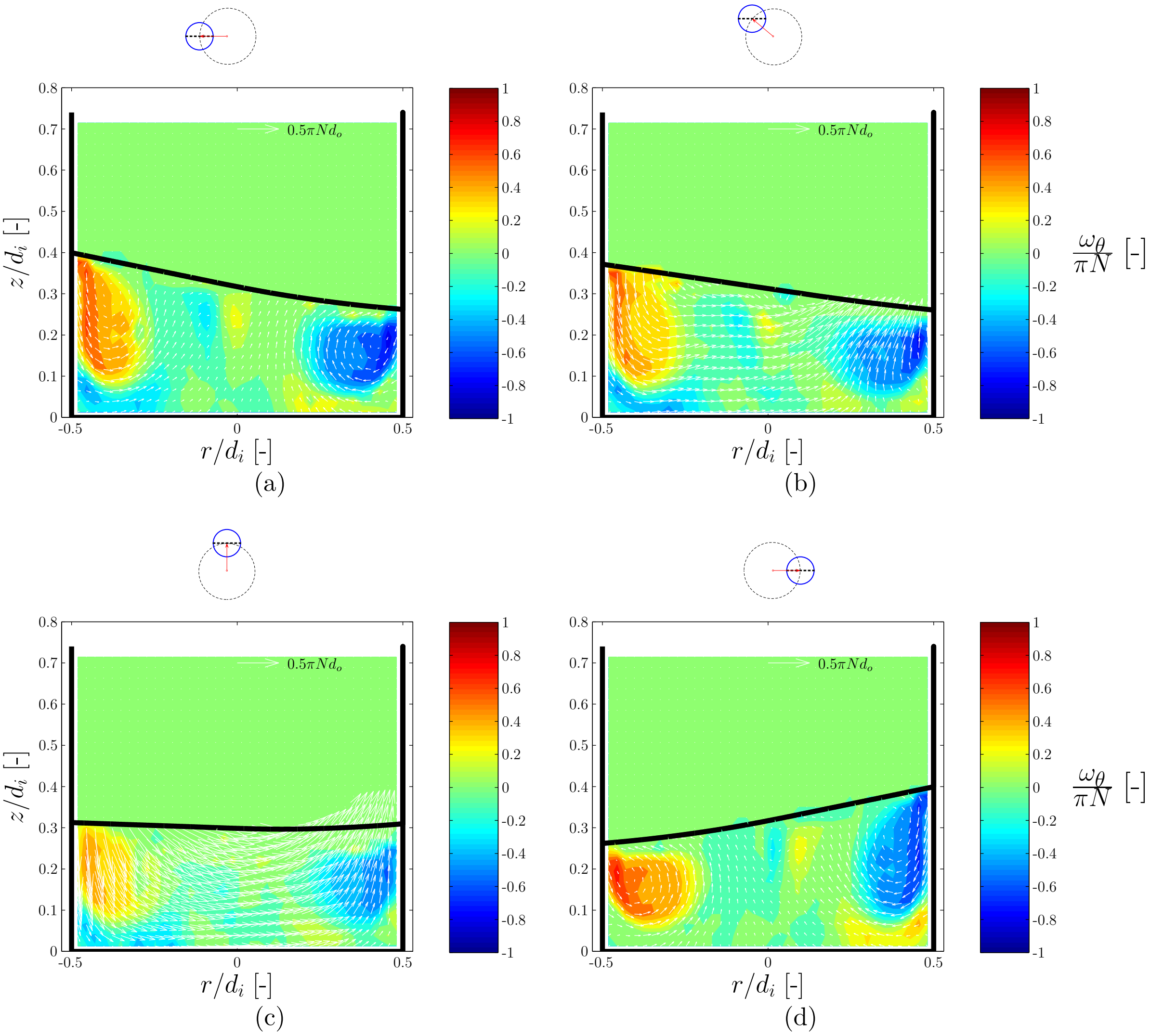

(a)

(b)

(c)

(d)

Figure 3.1: Phase-resolved vector fields and contour plots of the tangential component of the vorticity, ω_θ, for four different phase angles (h/d_i=0.3, N=90 rpm): (a) ϕ=0°; (b) ϕ=40°; (c) ϕ=90°; (d) $\phi = 180°$.

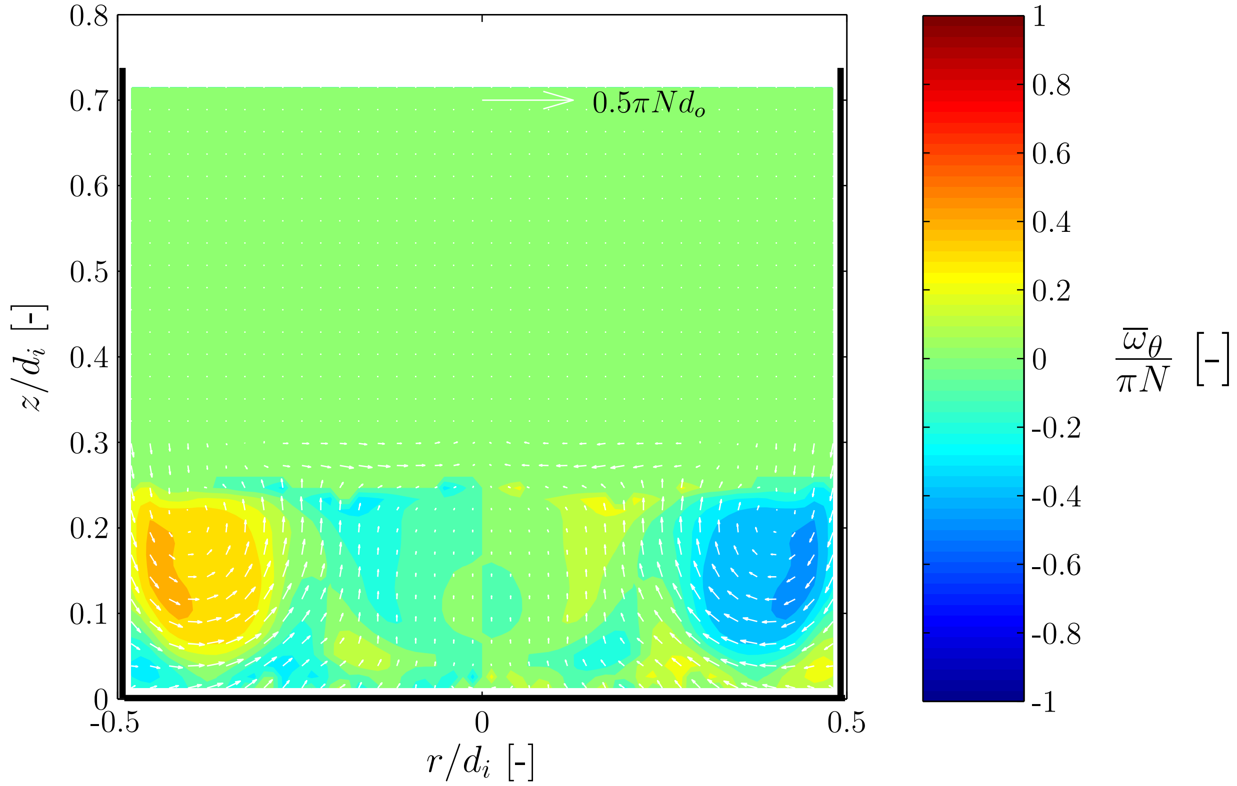

Figure 3.2: Ensemble-averaged velocity vector and vorticity contour plots for h/d_i=0.3, N=90 rpm and d_o/d_i=0.25.

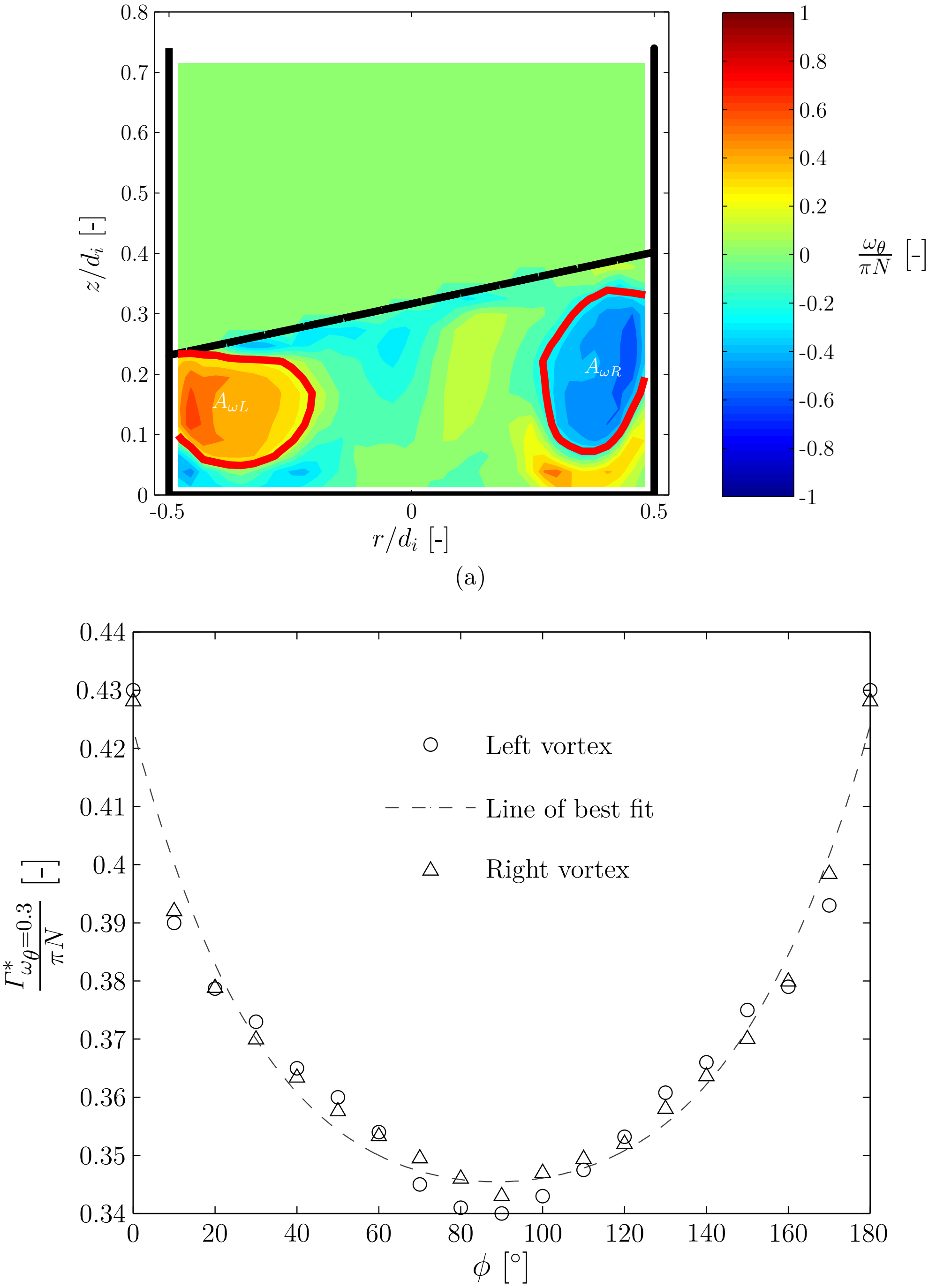

(a)

(b)

Figure 3.3: (a) Visualisation of the areas, $A_{\omega R}$ and $A_{\omega L}$, over which the circulation Γ^* has been estimated (h/d_i=0.3, ϕ=180°, N=90 rpm and d_o/d_i=0.25); (b) Variation of the space-averaged non-dimensional circulation, $\Gamma^*_{\omega=0.3}$, with increasing ϕ, for both the left (○) and right (△) hand side vortices.

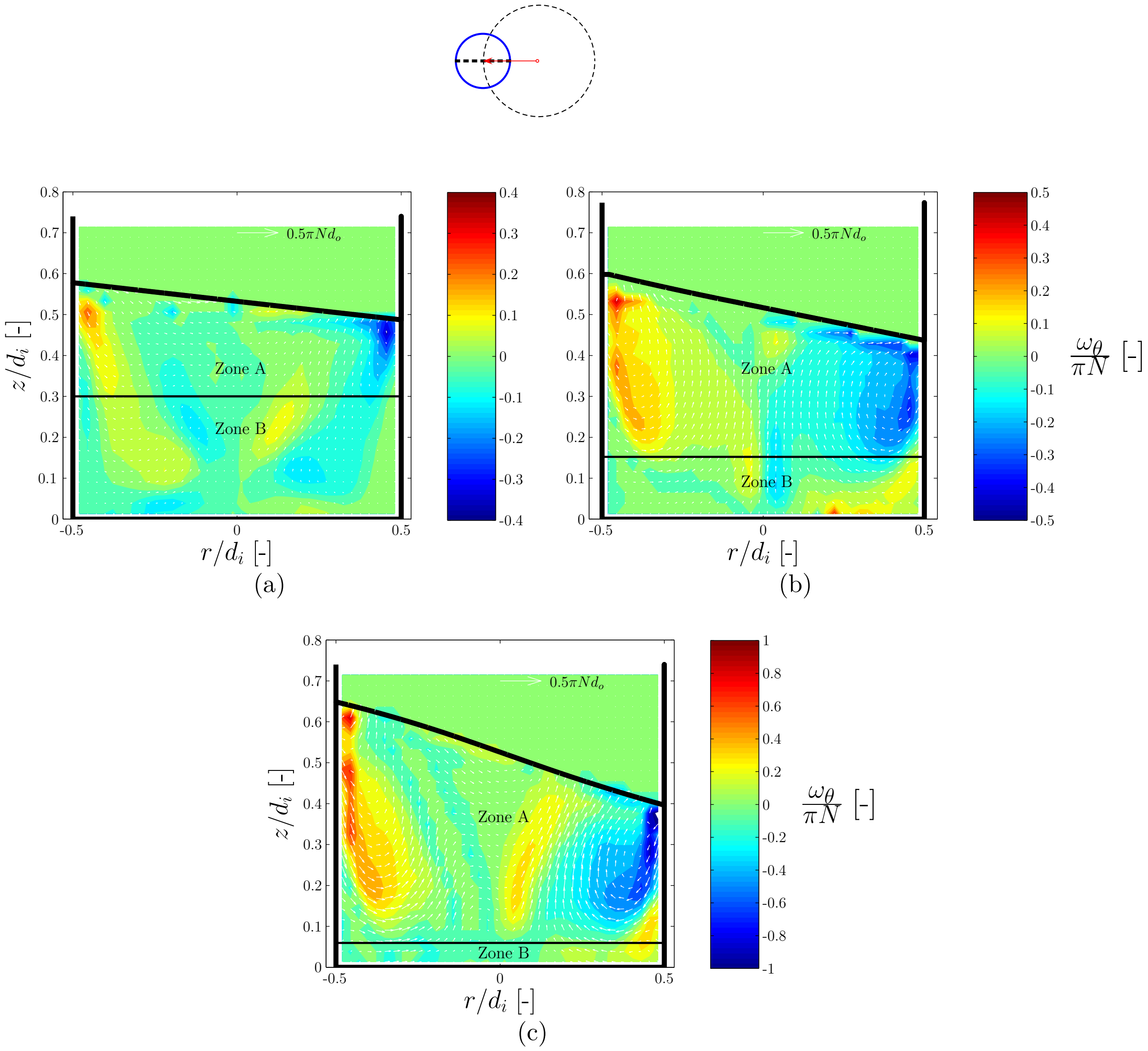

(a) (b) (c)

Figure 3.4: Phase-resolved vector fields and contour plots of the tangential component of the vorticity, ω_θ, for increasing shaking frequency N (h/d_i=0.5 , ϕ=0°): (a) N=70 rpm; (b) N=90 rpm; (c) N=110 rpm.

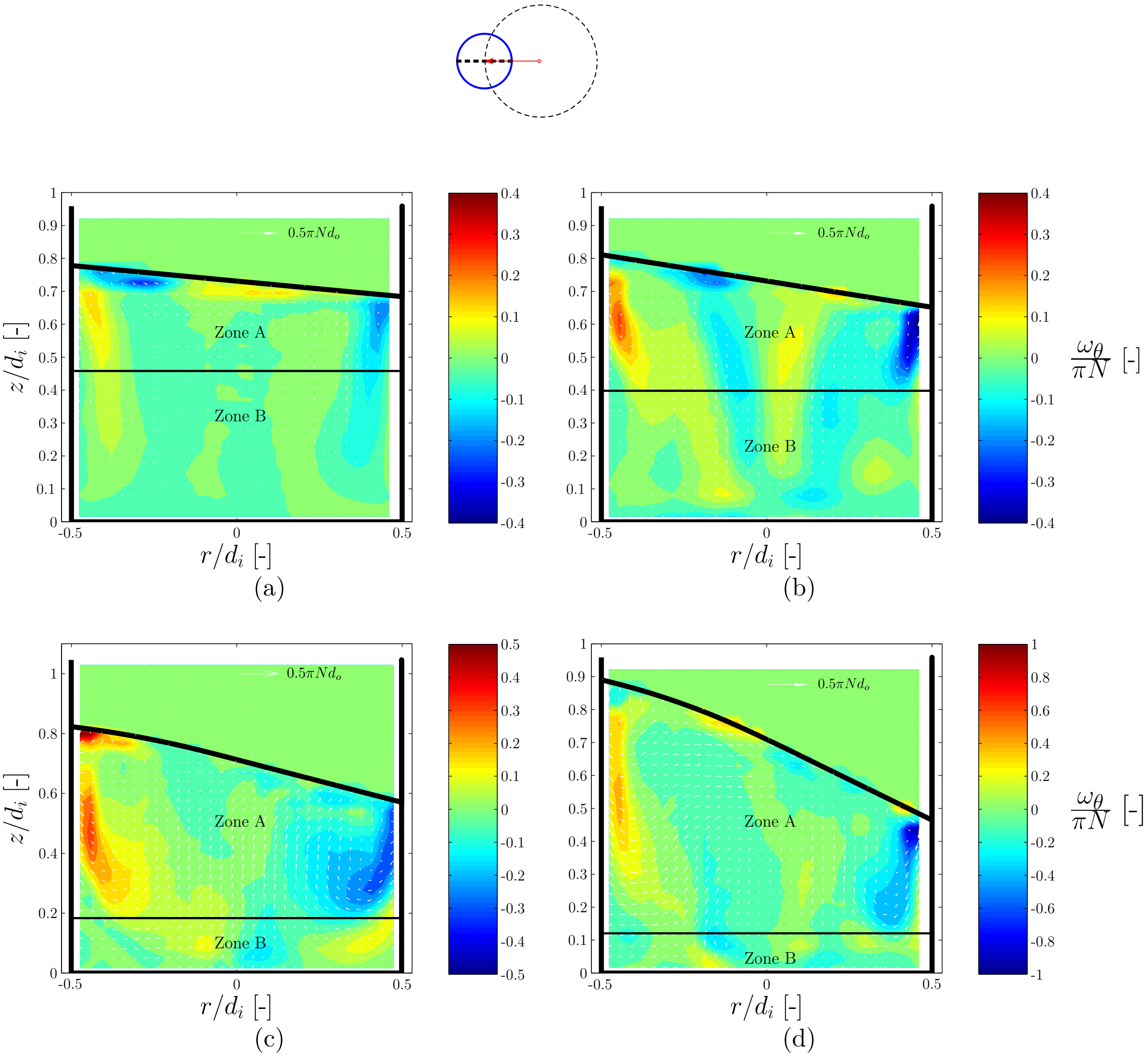

Figure 3.5: Phase-resolved vector fields and contour plots of the tangential component of the vorticity, ω_θ, for increasing shaking frequency N (h/d_i=0.7 , ϕ=0°): (a) N=70 rpm; (b) N=90 rpm; (c) N=110 rpm; (d) N=130 rpm.

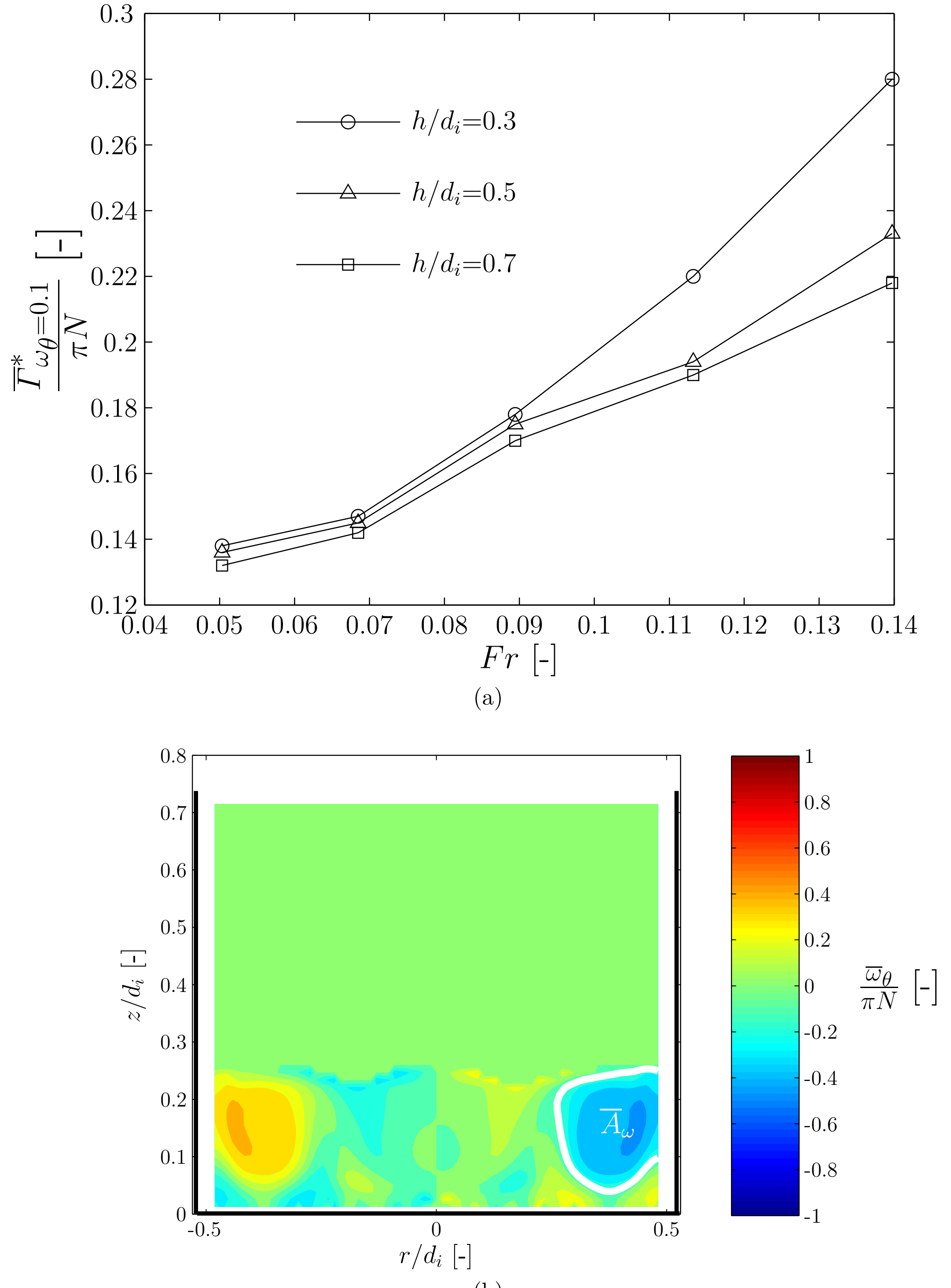

(a)

(b)

Figure 3.6: (a) Variation of the space-averaged non-dimensional circulation, $\overline{\Gamma}^*_{\omega=0.1}$, with increasing Fr for the ensemble-average flow fields; (b) Visualisation of the area, $\overline{A}_\omega$, over which the circulation $\overline{\Gamma}^*$ has been estimated (h/d_i=0.3, N=90 rpm and d_o/d_i=0.25).

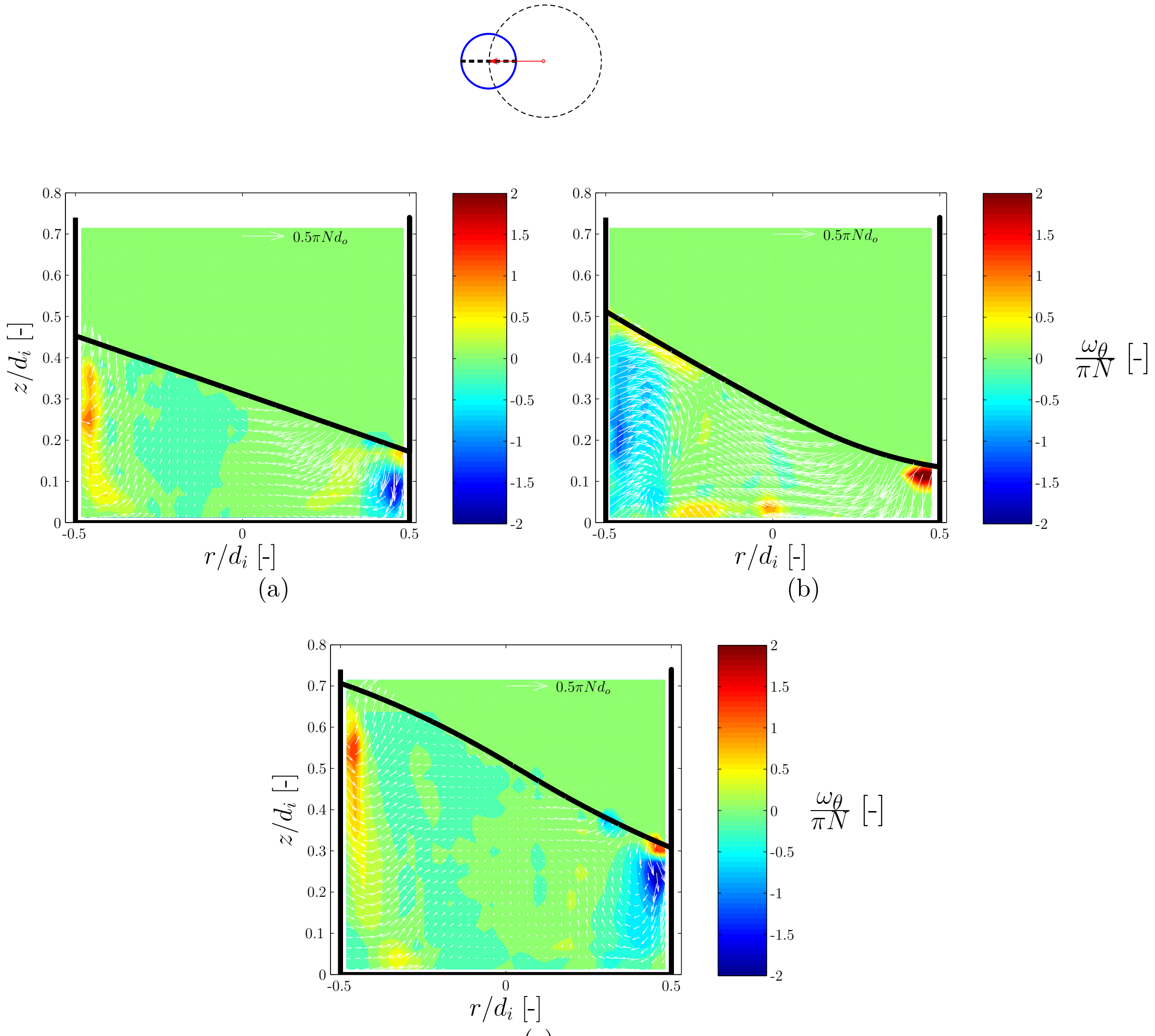

(a)

(b)

(c)

Figure 3.7: Phase-resolved vector fields and contour plots of the tangential component of the vorticity, ω_θ, for increasing shaking frequency N and h (ϕ=0°): (a) N=110 rpm and h/d_i=0.3 ; (b) N=130 rpm and h/d_i=0.3; (c) N=130 rpm and h/d_i=0.5.

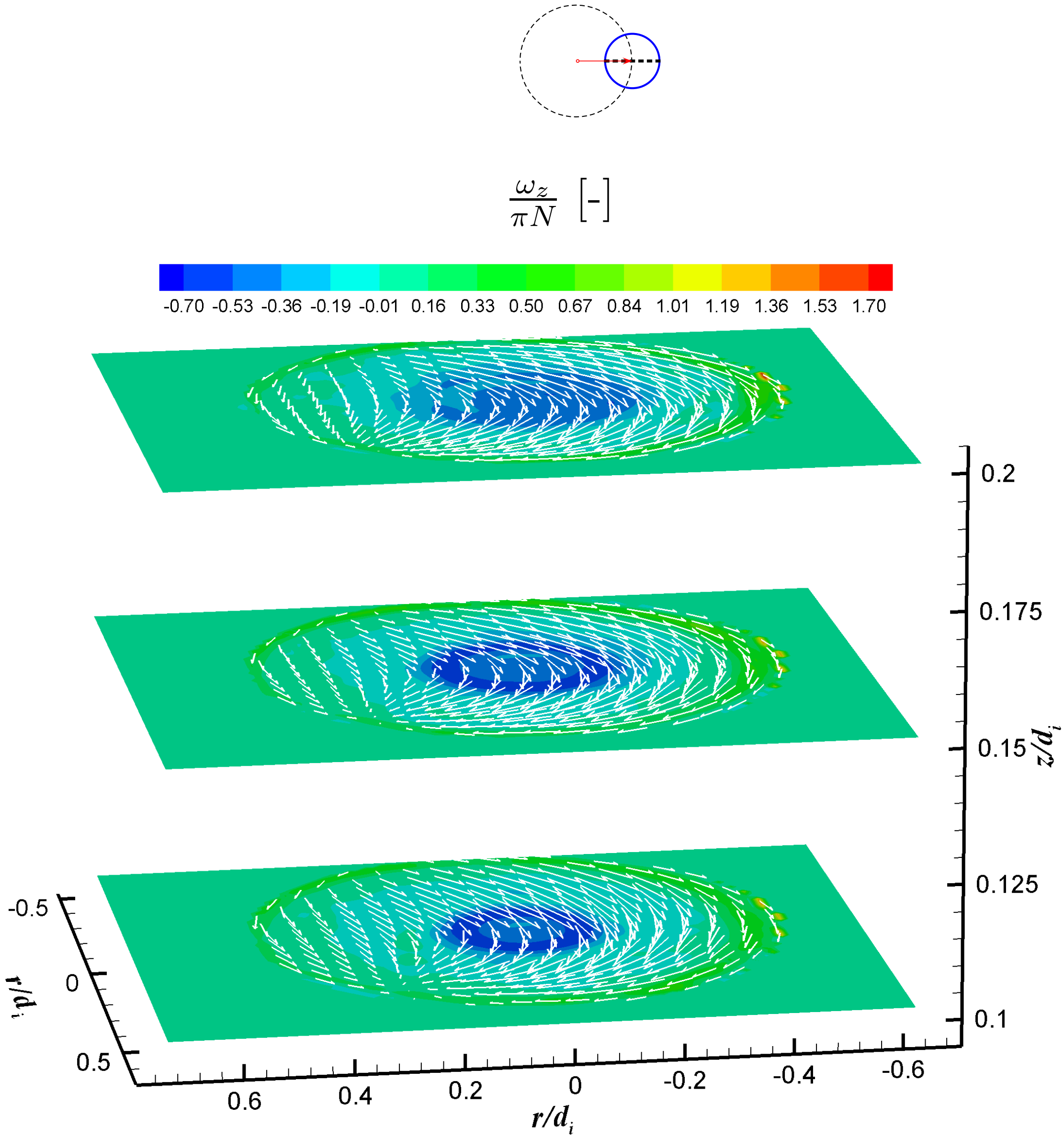

Figure 3.8: Phase-resolved vector fields and contour plots of the vorticity, ω_z, for three different elevations, z/d_i=0.1, 0.15 and 0.2 (h/d_i=0.3, ϕ=180°, N=90 rpm and d_o/d_i=0.25).

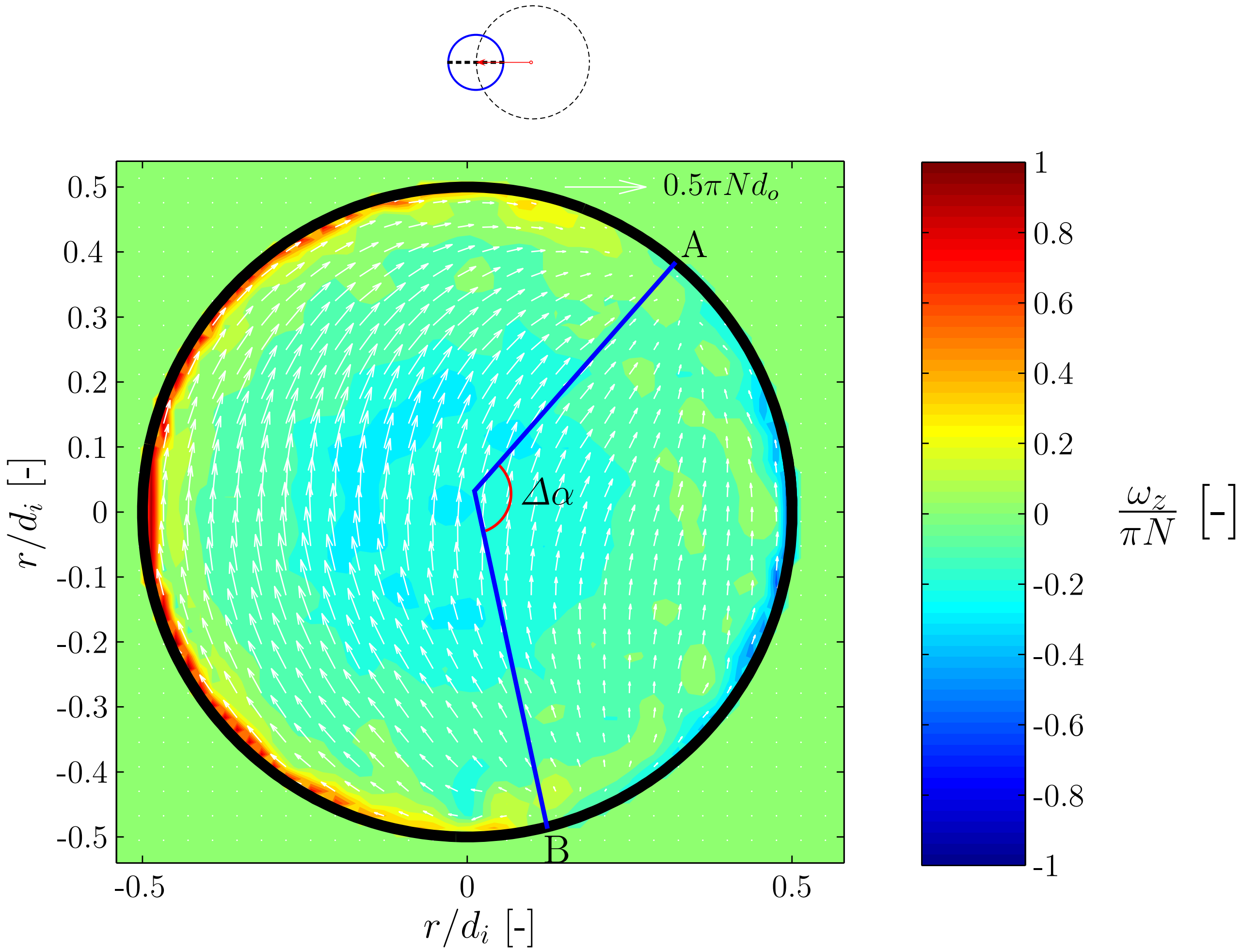

Figure 3.9: Phase-resolved vector field and contour plot of the vorticity, ω_z, for z/d_i=0.075 (h/d_i=0.3, ϕ=0°, N=90 rpm and d_o/d_i=0.25).

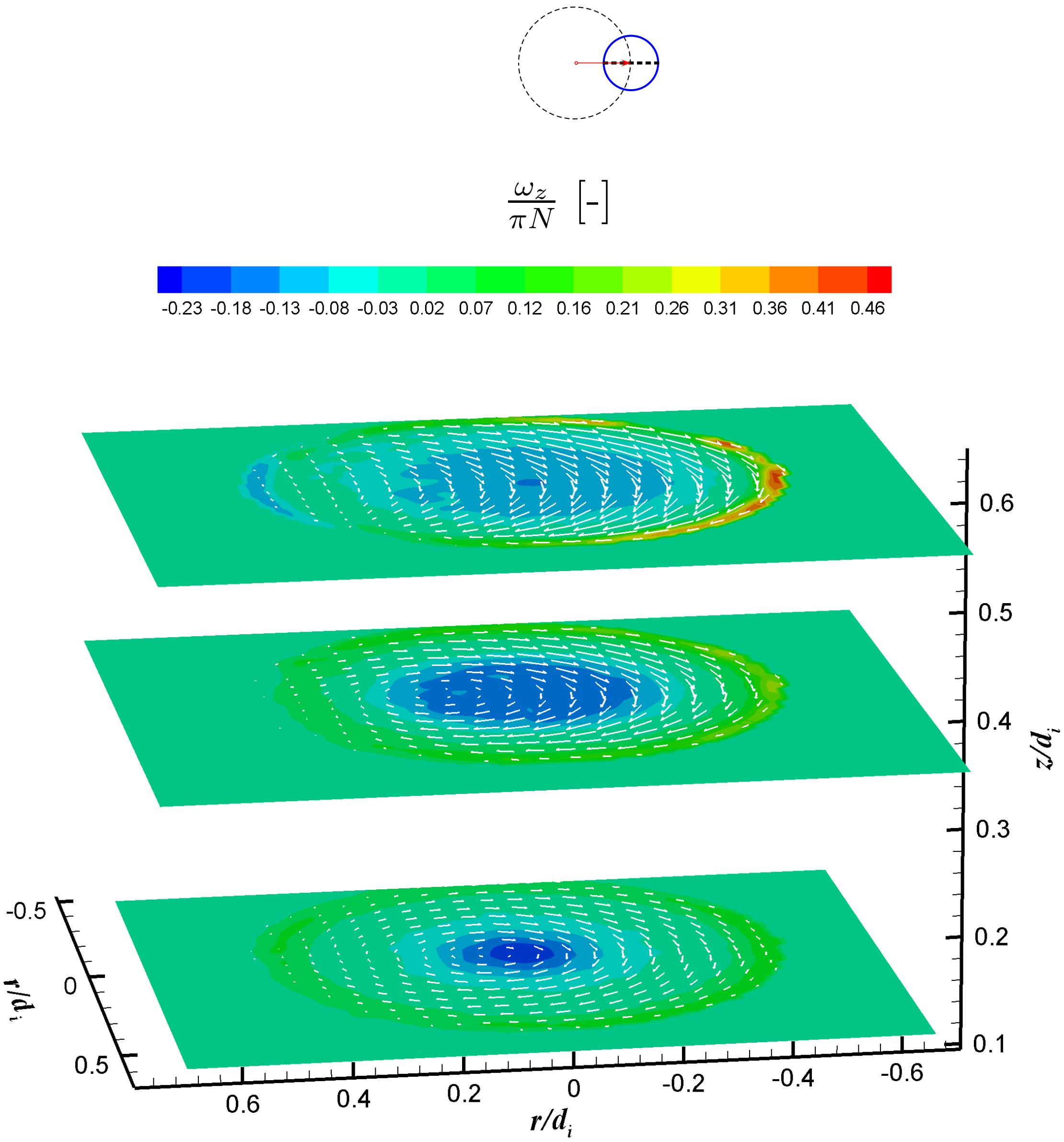

Figure 3.10: Phase-resolved vector fields and contour plots of the vorticity, ω_z, for three different elevations, z/d_i=0.1, 0.35 and 0.6 (h/d_i=0.7, ϕ=180°, N=70 rpm and d_o/d_i=0.25).

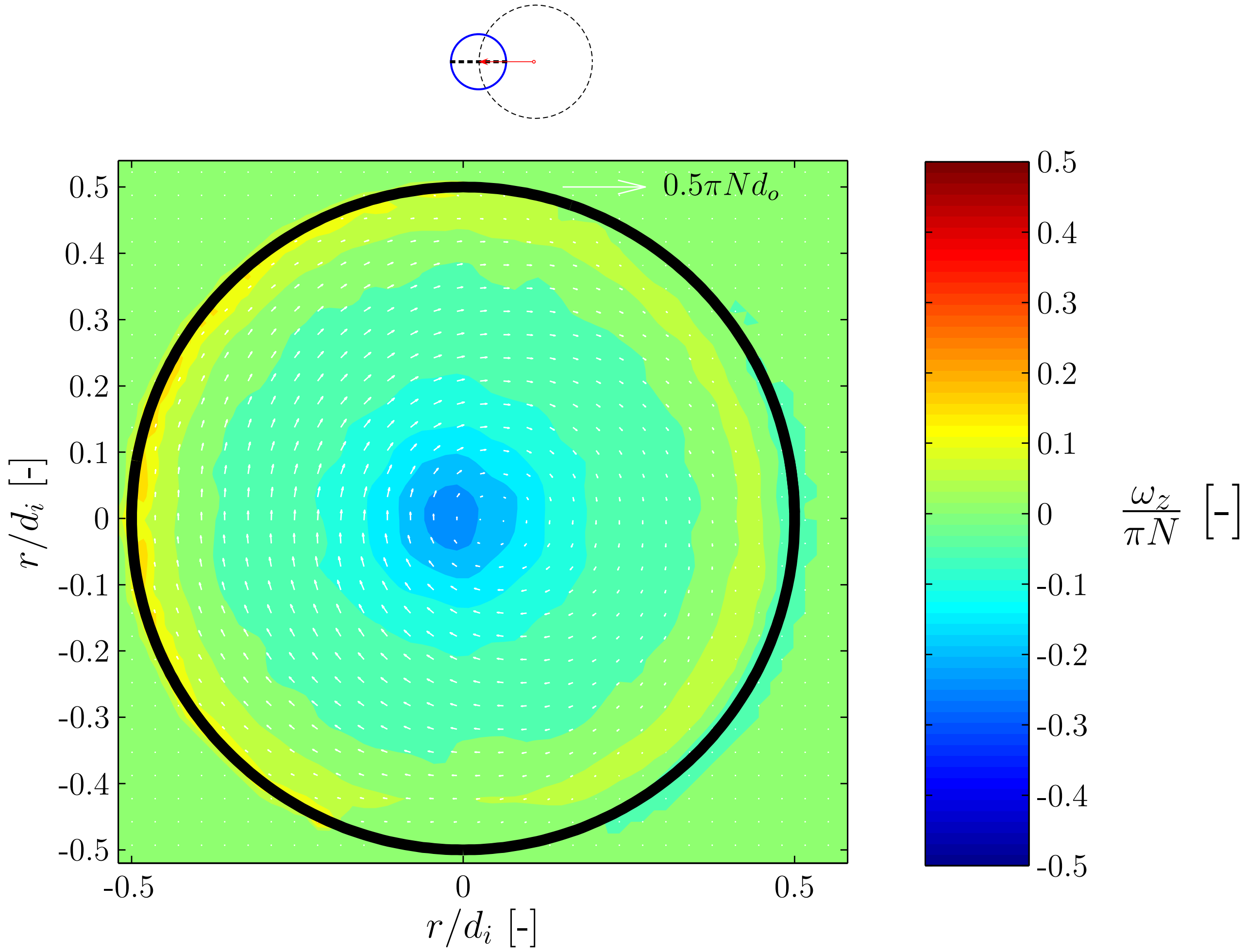

Figure 3.11: Phase-resolved vector field and contour plot of the vorticity, ω_z, for z/d_i=0.1 (h/d_i=0.7, ϕ=0°, N=70 rpm and d_o/d_i=0.25).

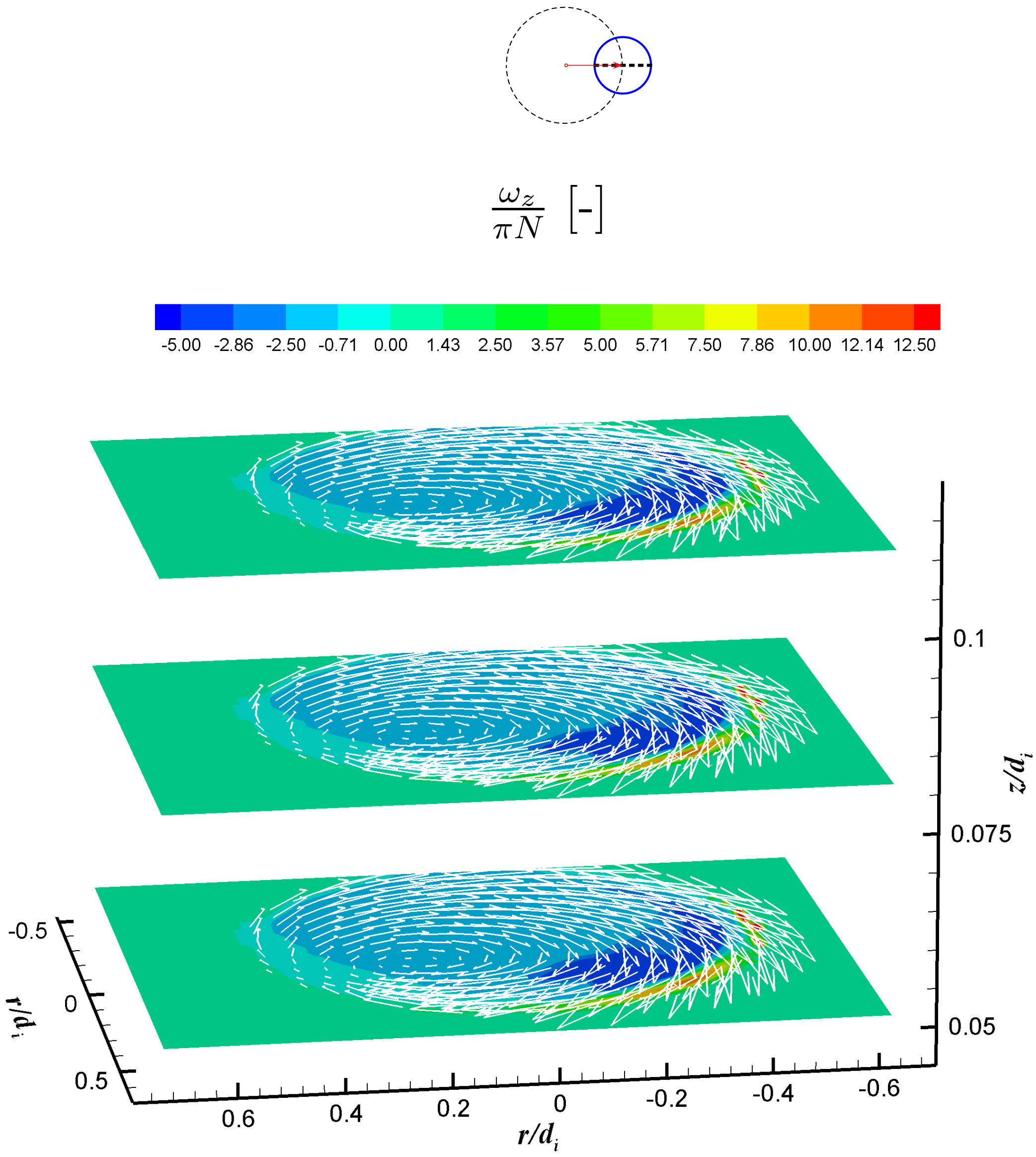

Figure 3.12: Phase-resolved vector fields and contour plots of the vorticity, ω_z, for three different elevations, z/d_i=0.05, 0.075 and 0.12 (h/d_i=0.3, ϕ=180°, N=130 rpm and d_o/d_i=0.25).

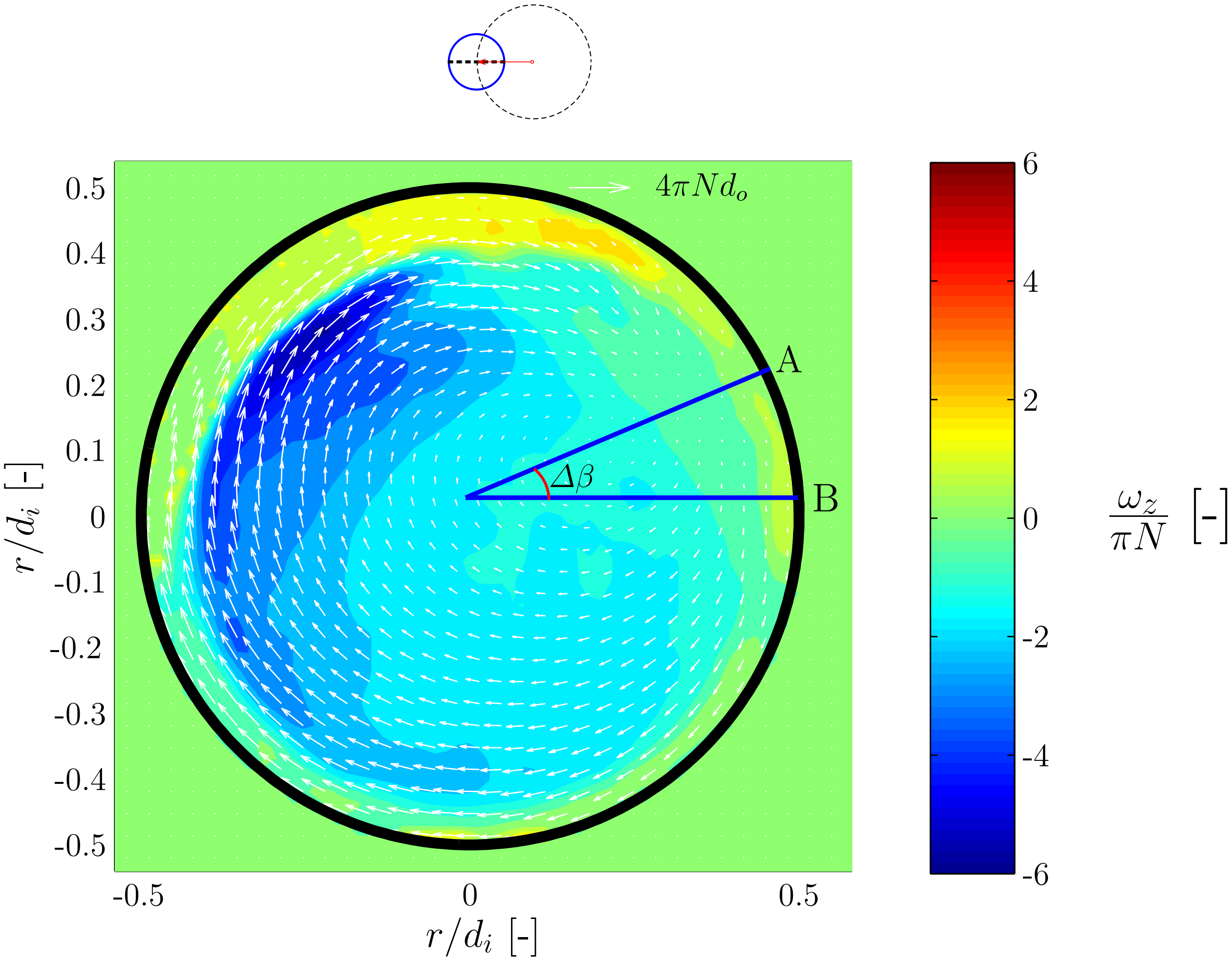

Figure 3.13: Phase-resolved vector field and contour plot of the vorticity, ω_z, for z/d_i=0.075 (h/d_i=0.3, ϕ=0°, N=130 rpm and d_o/d_i=0.25).

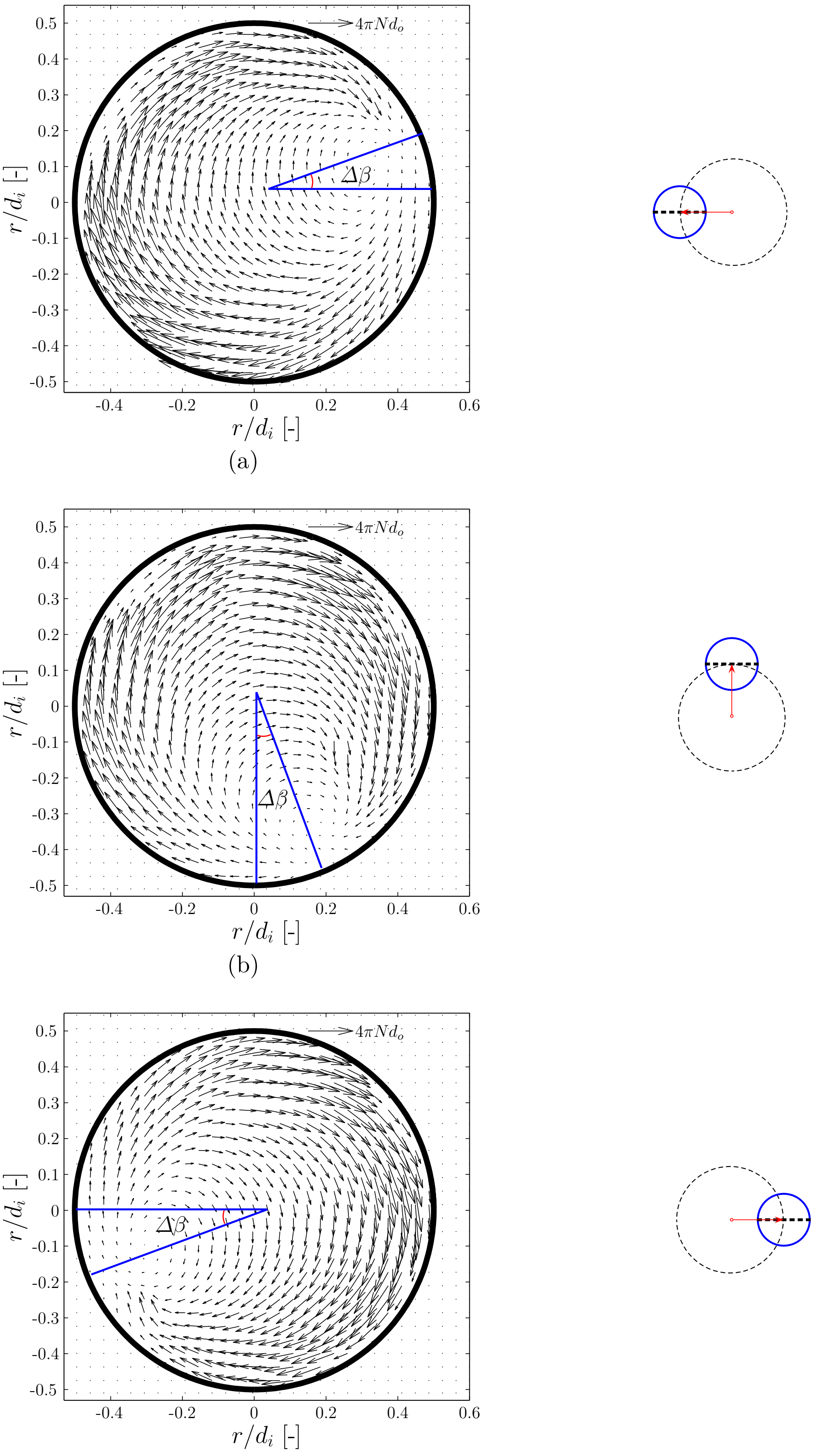

(a)

(b)

(c)

Figure 3.14: Phase-resolved vector fields for h/d_i=0.3 with N=130 rpm and z/d_i=0.08: (a) $\phi = 0°$ (b) $\phi = 90°$ (c) $\phi = 180°$.

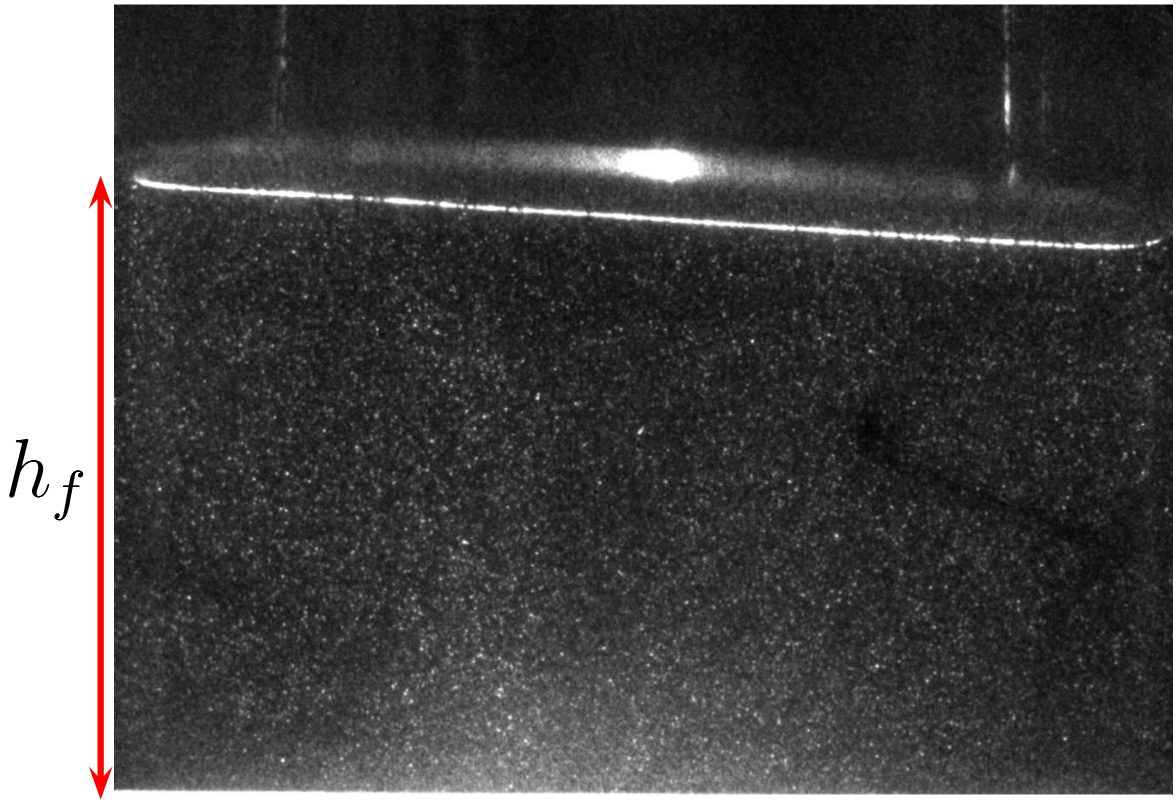

Figure 3.15: Image showing the position where the fluid height, h_f, is measured.

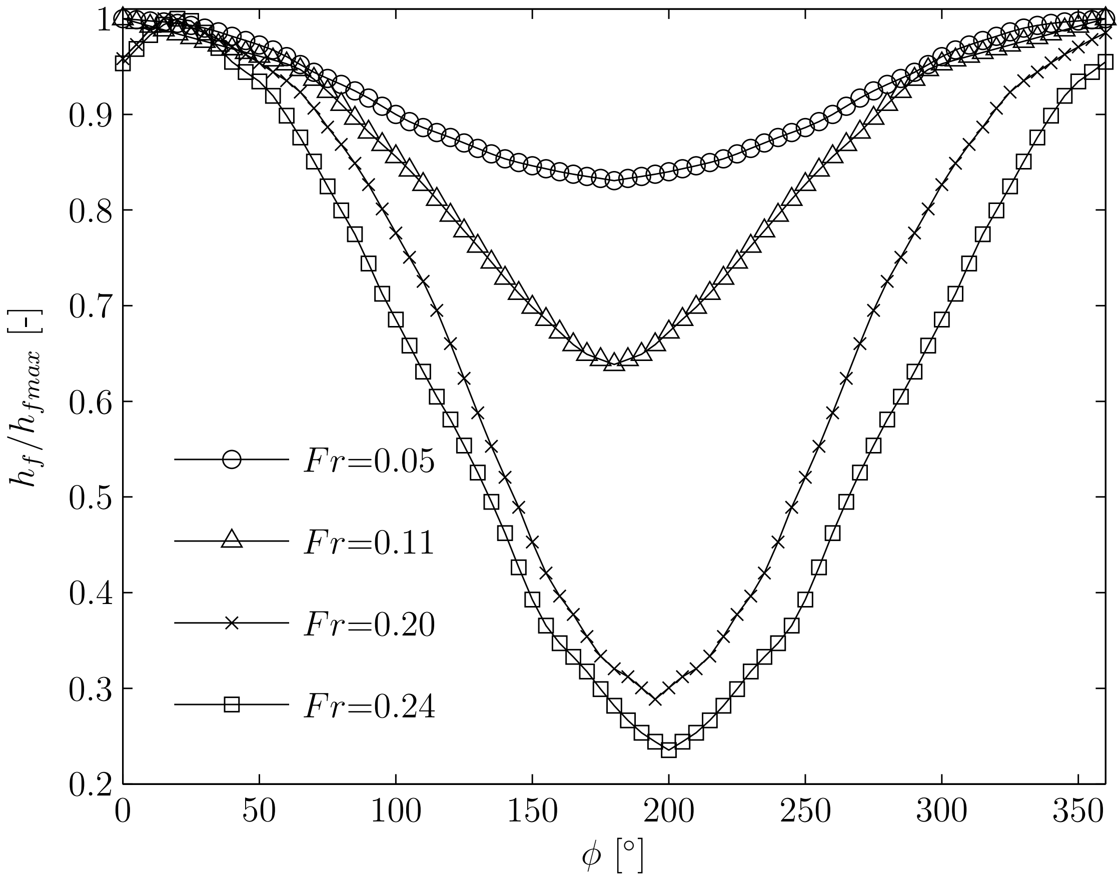

Figure 3.16: Variation of h_f/h_{fmax} with ϕ.

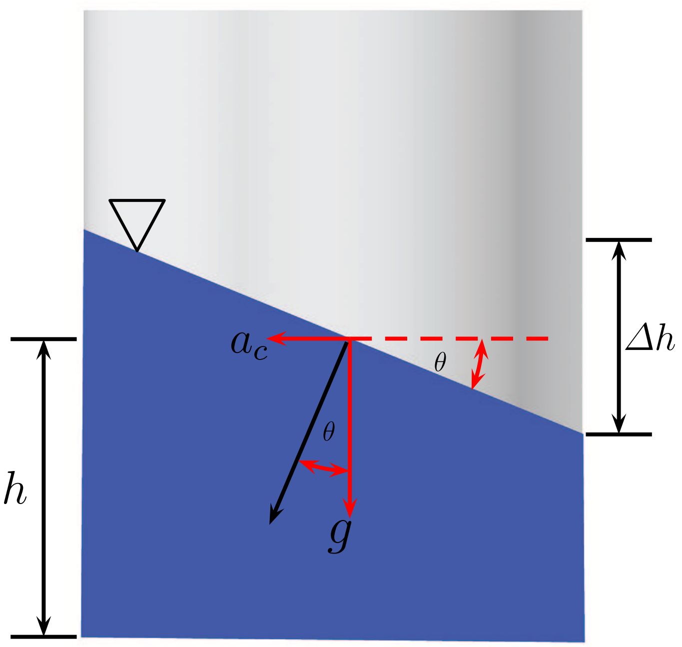

(a)

Figure 3.17: Visualisation of the centrifugal and gravity accelerations and their relationship with the free surface inclination, θ.

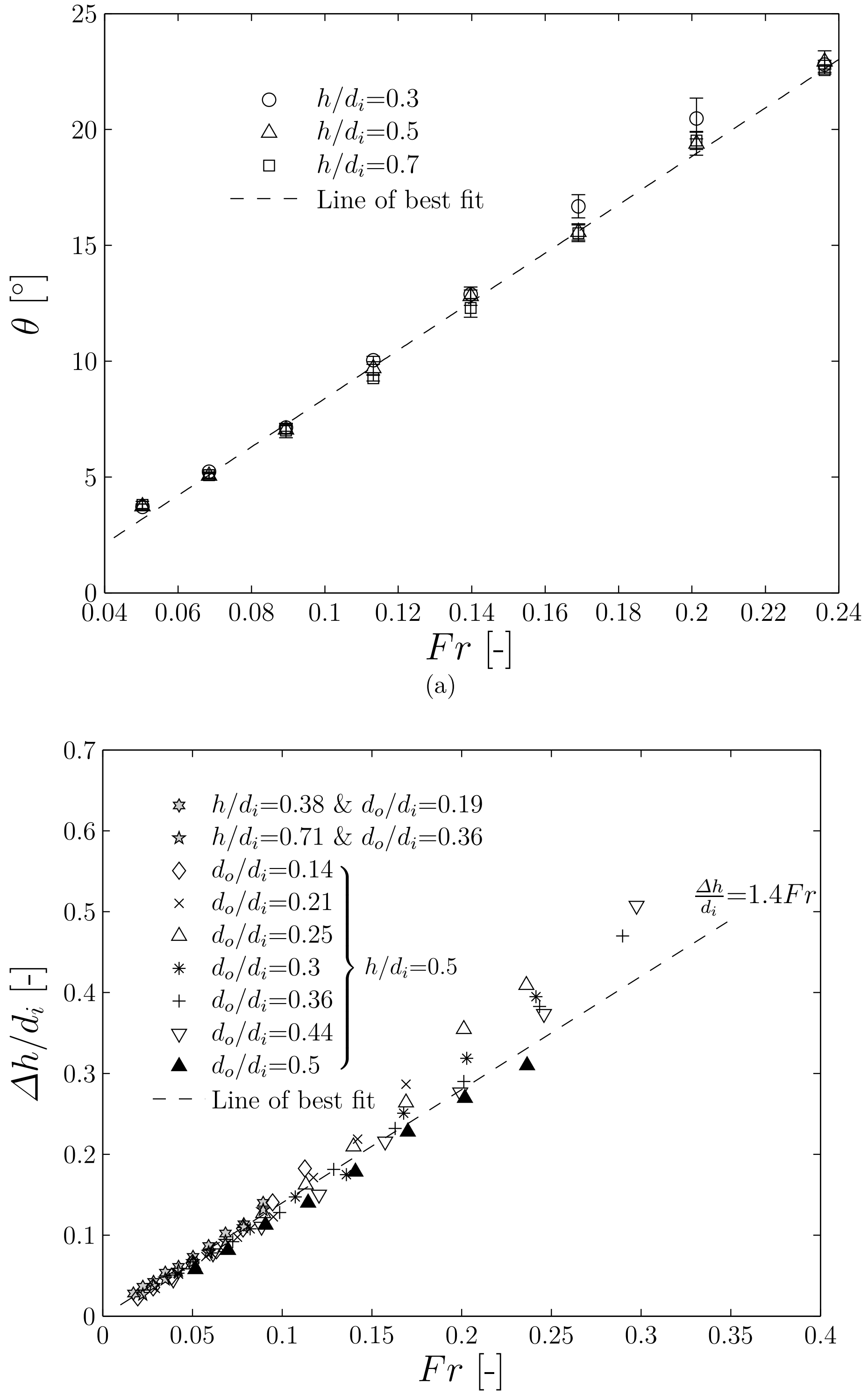

(a)

(b)

Figure 3.18: (a) Variation of θ with respect to Fr at $\phi = 0°$ for three different non-dimensional fluid heights, h/d_i=0.3, 0.5 and 0.7; (b) Variation of $\Delta h/d_i$ with Fr at ϕ=0° for different combinations of h/d_i and d_o/d_i (ϕ=0°).

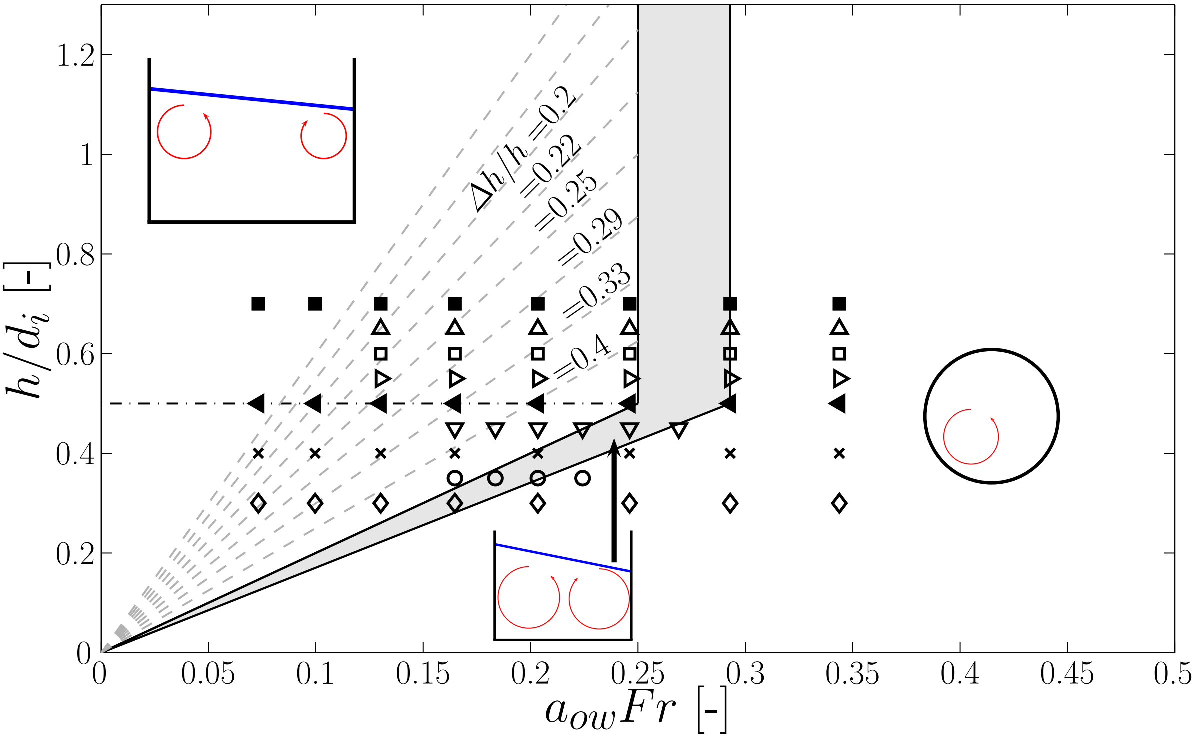

Figure 3.19: Transitional region (grey shaded) from in-phase to out of phase conditions in the h/d_i, Fr plane.

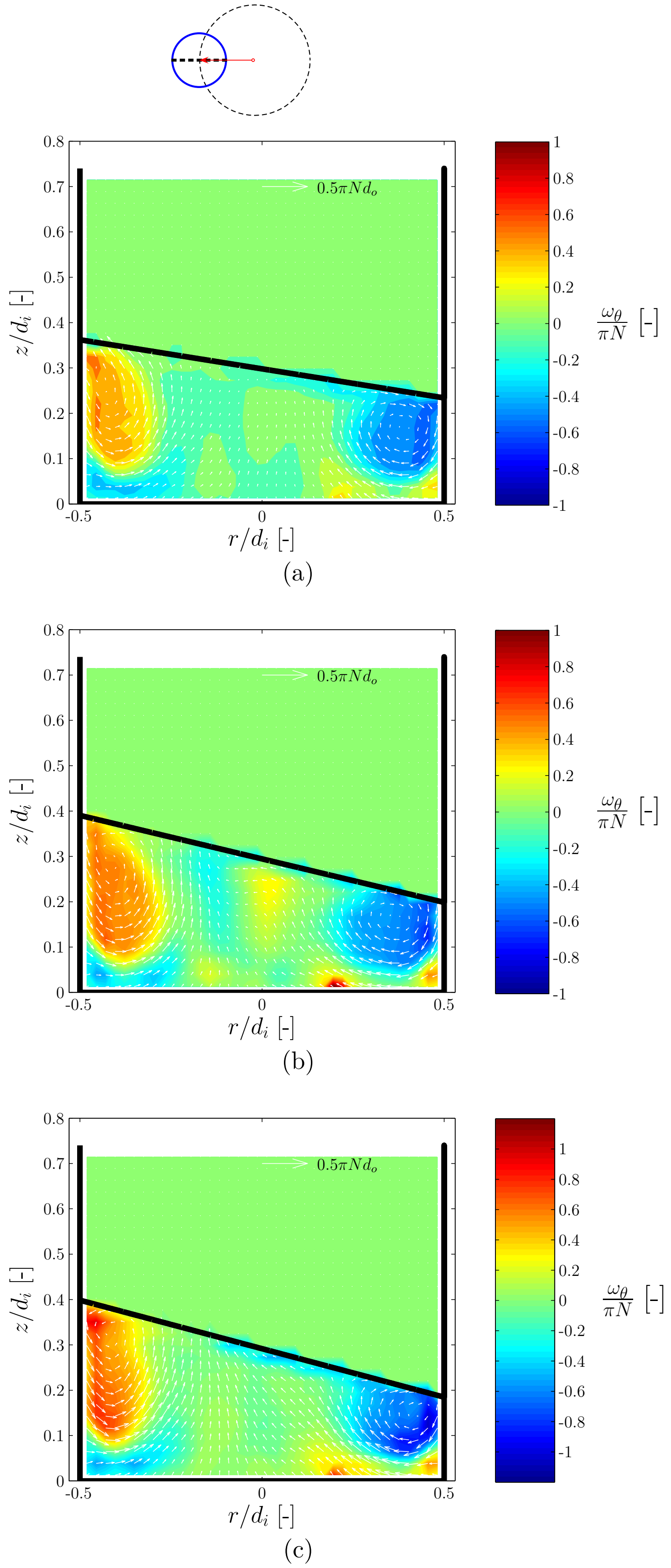

(a)

(b)

(c)

Figure 3.20: Phase-resolved vector fields and contour plots of the tangential component of the vorticity, ω_θ, for (h/d_i=0.3, ϕ=0° and d_i=100 mm): (a) d_o/d_i=0.15 and Fr=0.084 (N=100 rpm); (b) d_o/d_i=0.4 and Fr=0.133 (N=77 rpm); (c) d_o/d_i=0.5 and Fr=0.153 (N=74 rpm).

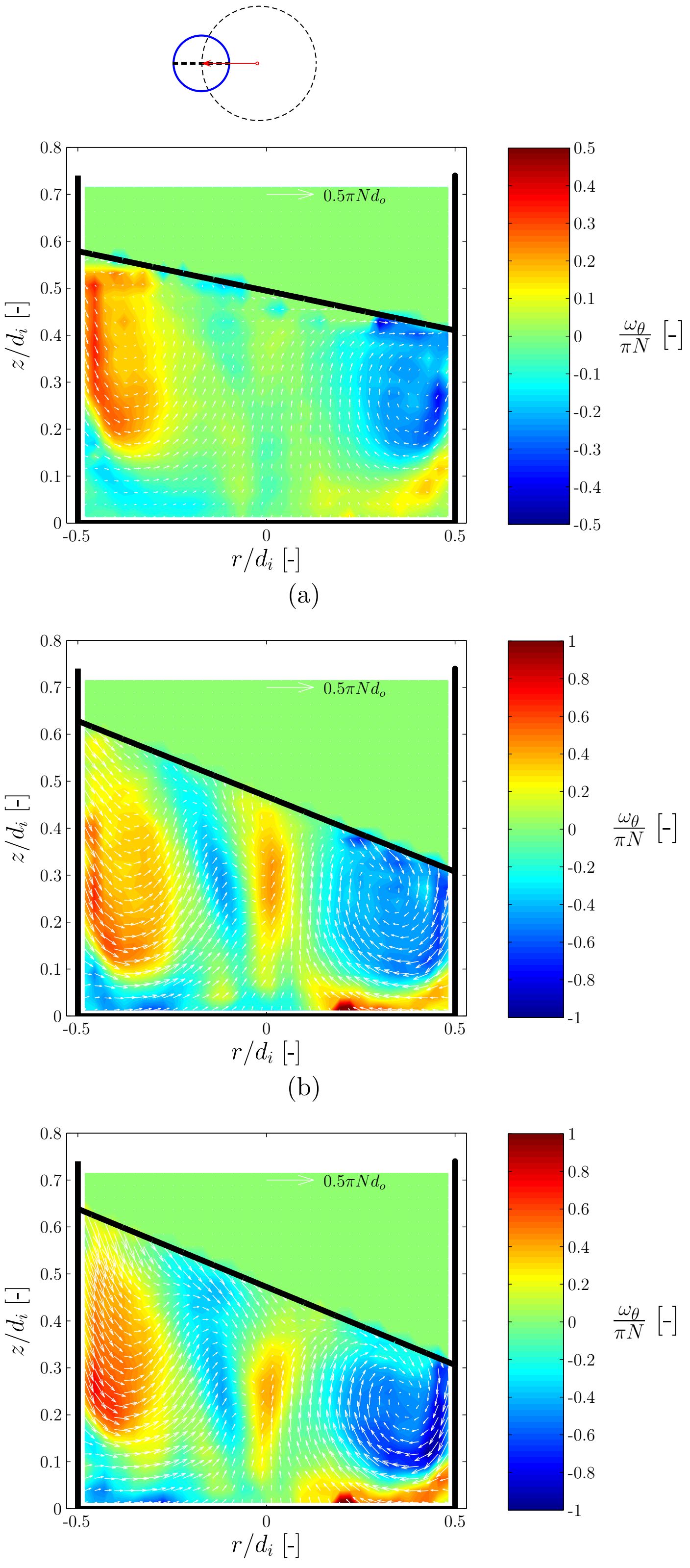

(a)

(b)

(c)

Figure 3.21: Phase-resolved vector fields and contour plots of the tangential component of the vorticity, ω_θ, for (h/d_i=0.5, ϕ=0° and d_i=100 mm): (a) d_o/d_i=0.15 and Fr=0.10 (N=110 rpm); (b) d_o/d_i=0.4 and Fr=0.23 (N=101 rpm); (c) d_o/d_i=0.5 and Fr=0.25 (N=96 rpm).

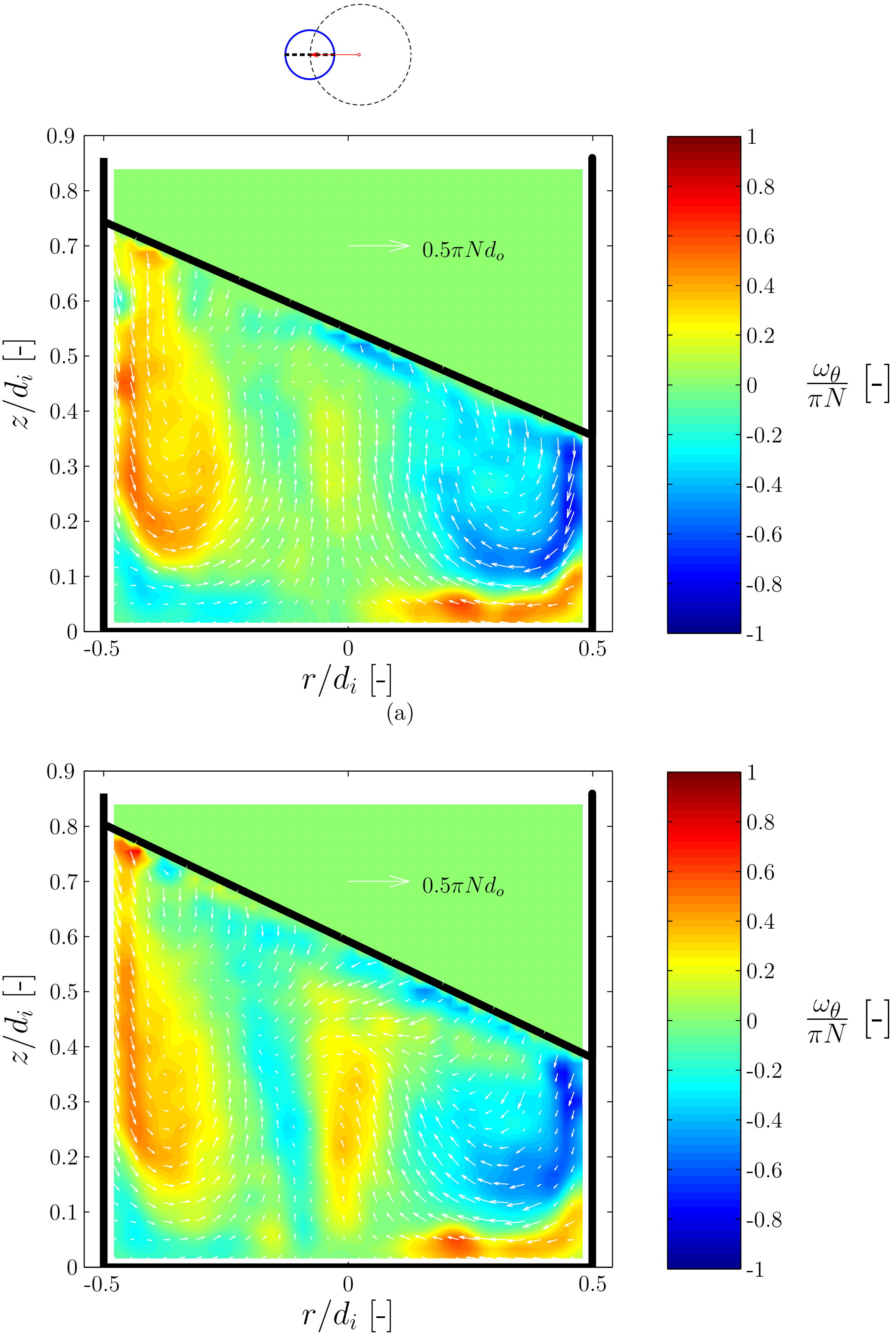

(a)

(b)

Figure 3.22: Phase-resolved vector fields and contour plots of the tangential component of the vorticity, ω_θ, for (ϕ=0° and d_o/d_i=0.5): (a) h/d_i=0.55 and Fr=0.28 (N=100 rpm); (b) h/d_i=0.6 and Fr=0.30 (N=104 rpm).

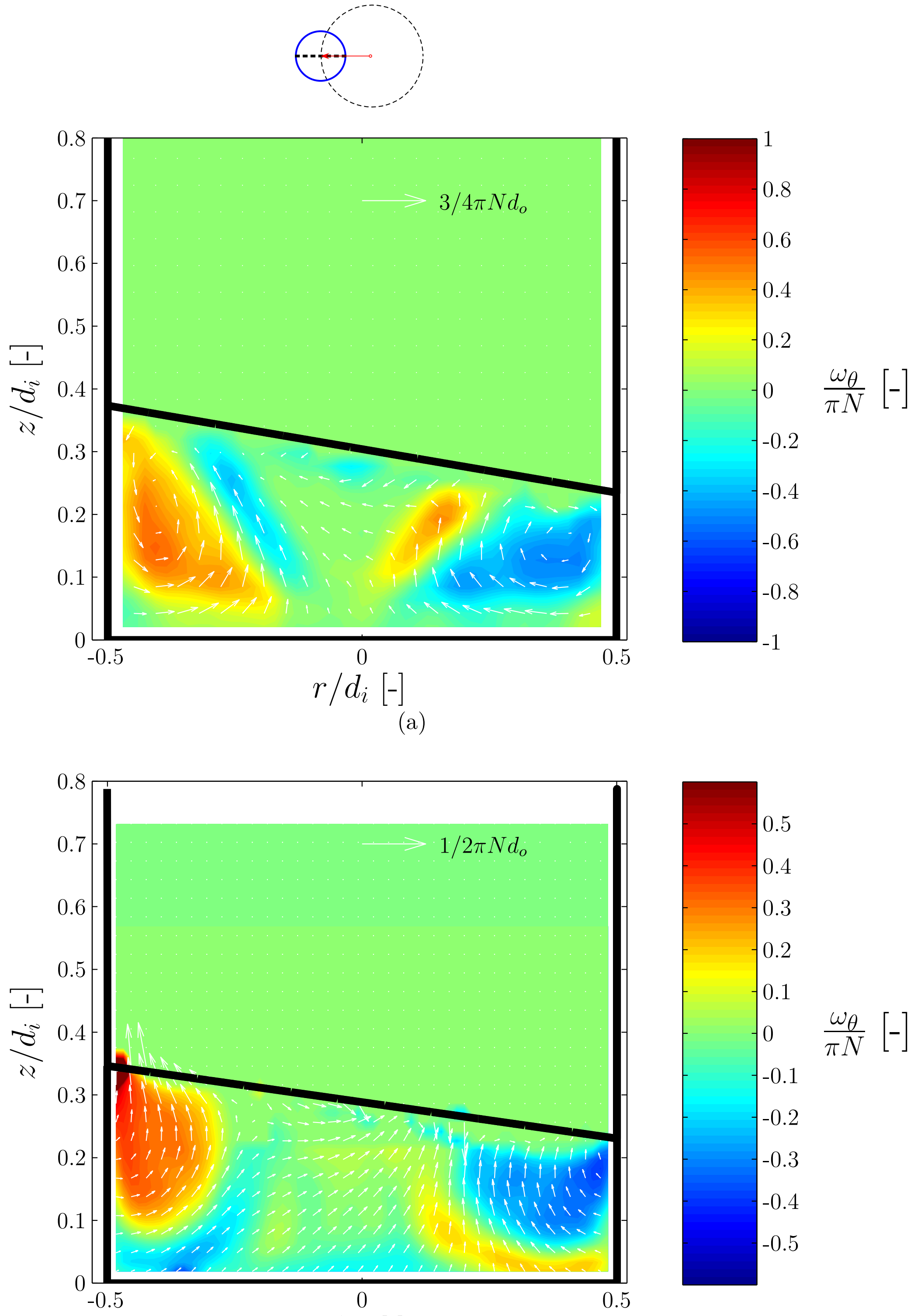

(a)

(b)

Figure 3.23: Phase-resolved vector fields and contour plots of the tangential component of the vorticity, ω_θ, for (h/d_i=0.3, ϕ=0° and d_o=15 mm): (a) d_o/d_i=0.21 and Fr=0.10 (N=110 rpm); (b) d_o/d_i=0.12 and Fr=0.076 (N=95 rpm).

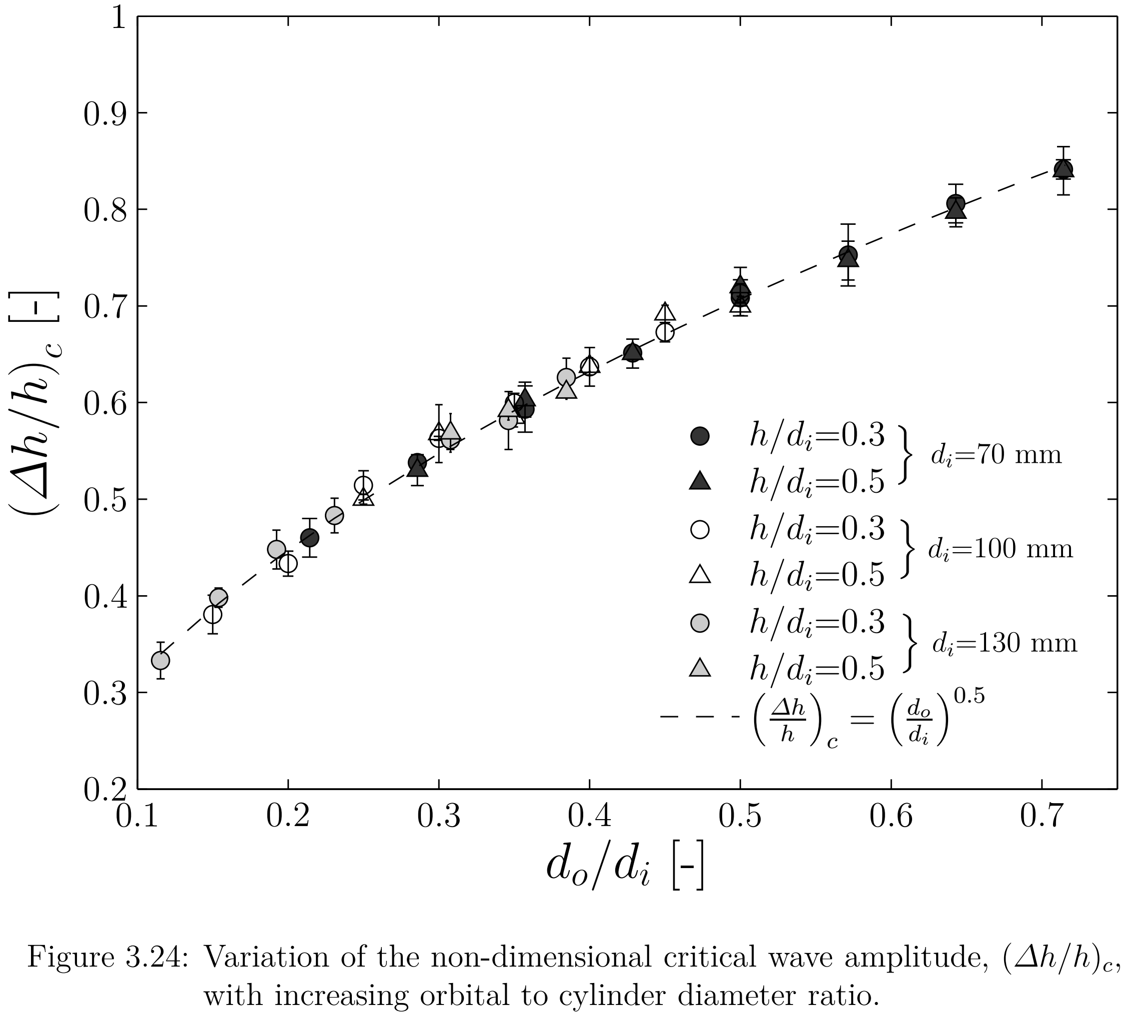

Figure 3.24: Variation of the non-dimensional critical wave amplitude, $(\Delta h/h)_c$, with increasing orbital to cylinder diameter ratio.

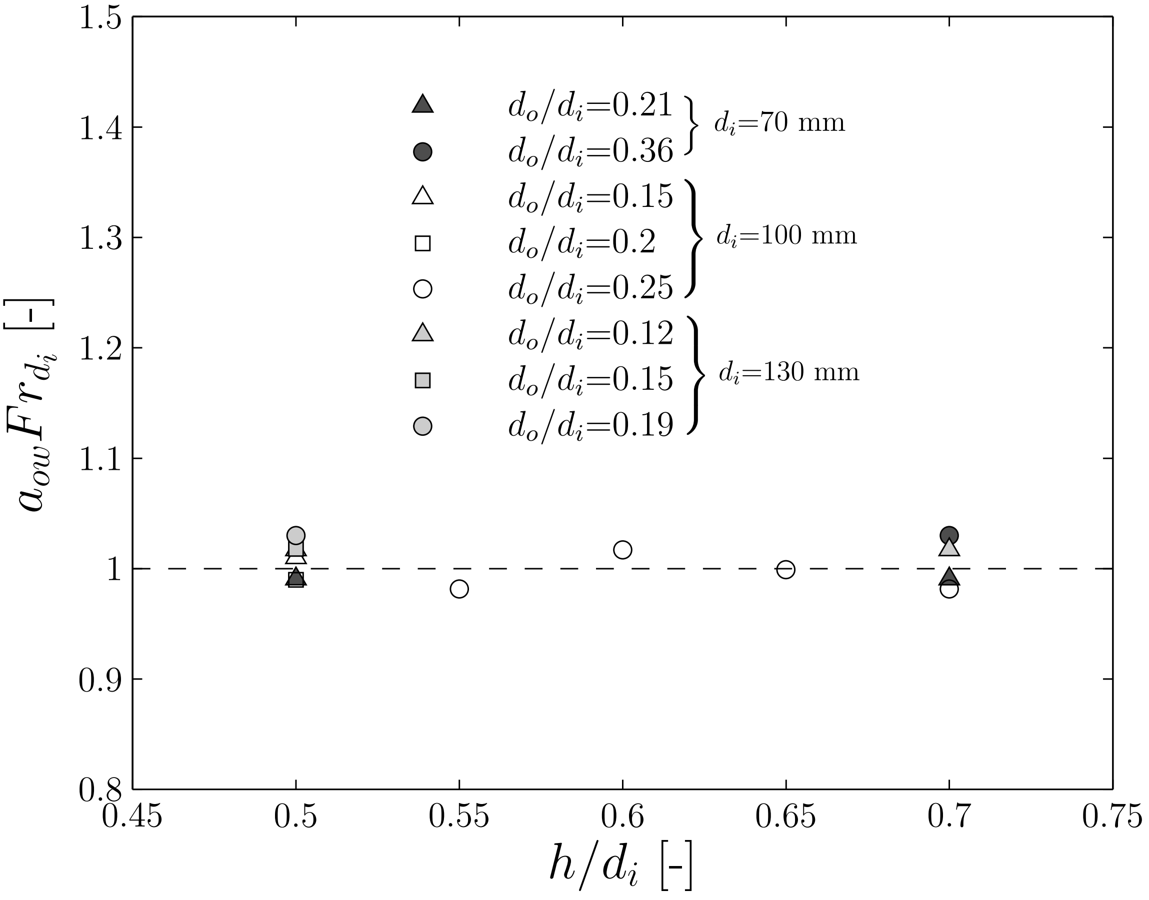

Figure 3.25: Variation of the critical Froude number $a_{ow}Fr_{d_i}$ for different non-dimensional fluid height h/d_i when $h/d_i>(d_o/d_i)^{0.5}$.

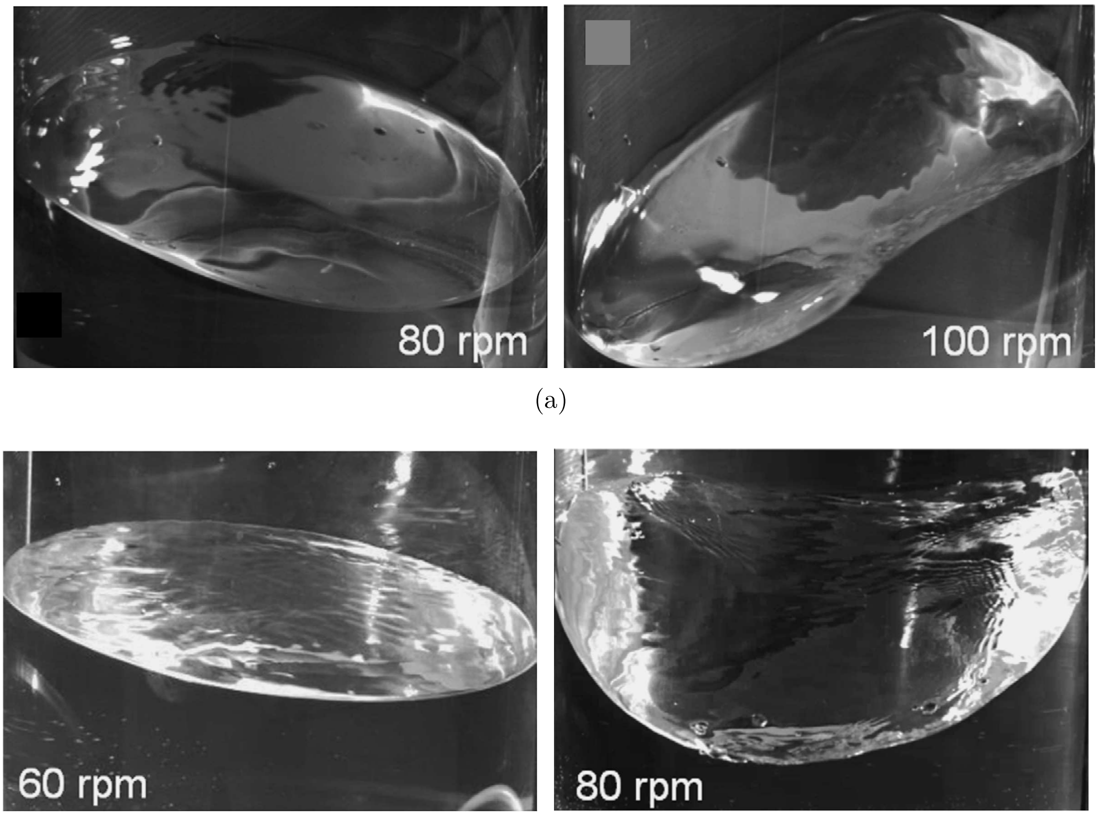

(a)

(b)

Figure 3.26: Images of the free surface from Zhang *et al.* (2009) (d_o=50 mm): (a) h=108 mm and d_i=172 mm; (b) h=185 mm and d_i=287 mm.

(a)

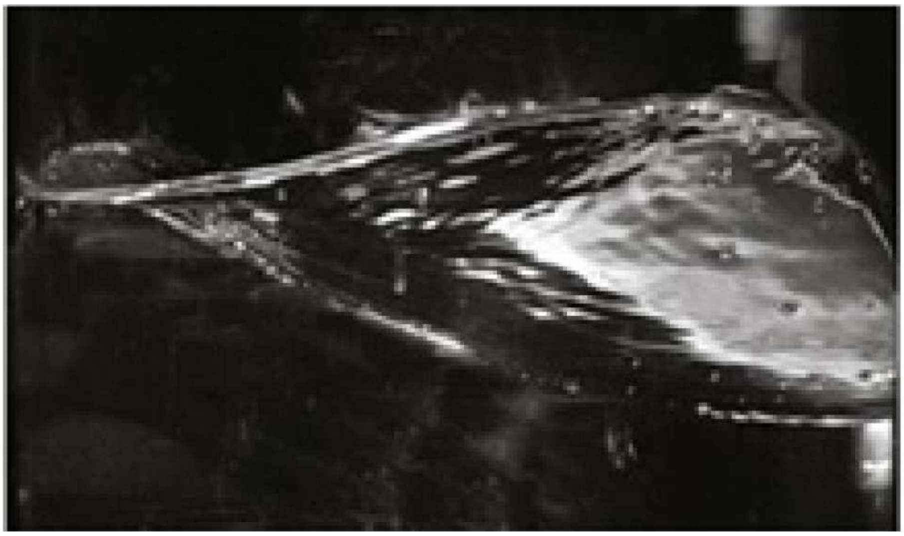

(b)

Figure 3.27: Images of the free surface shape from Tissot *et al.* (2010) (h=200 mm, d_o=50 mm and d_i=287 mm): (a) Fr=0.12 (N=65 rpm) ; (b) Fr=0.18 (N=80 rpm).

Chapter 4

Flow properties and mixing characteristics in a cylindrical shaken bioreactor[†]

4.1 Introduction

This chapter builds upon the flow transition and scaling law described in Chapter 3 to provide estimates of flow characteristics, such as the interfacial area, vortex size, circulation time, kinetic energy content and viscous dissipation rate, that are essential to better design and scale a bioprocess. Similarly to Chapter 3 the aforementioned flow characteristics were estimated for several combinations of medium height, h, shaking frequency, N, orbital shaking diameter, d_o, and cylinder inner diameter, d_i, with water being the working fluid. In Section 4.2 the free surface interfacial area is directly measured by image analysis to assess oxy-

---

[†] Some of the results presented in this chapter are included in:

Weheliye, W., Yianneskis, M. and Ducci, A. (2013), "On the fluid dynamics of shaken bioreactors - Flow characterization and transition", *AIChE J.*, 59, 334-344;

Rodriguez, G., Weheliye, W., Anderlei, T., Micheletti, M., Yianneskis, M. and Ducci, A. (2013), "Mixing time and kinetic energy measurements in a shaken cylindrical bioreactor", *Chem. Eng. Res. Des.* DOI: 10.1016/j.cherd.2013.03.005.

gen transfer potential of the bioreactor, and compared to an analytical solution, derived from the flow scaling law of Chapter 3, valid for low Froude number. In Section 4.3 the circulation times, $T^*_{\omega_\theta}$ and $T^*_{\omega_z}$, of the toroidal vortex and of the axial vortex precessing around the bioreactor axis for conditions before and after flow transition, respectively, are estimated from PIV measurements obtained on horizontal and vertical planes. Furthermore this section provides an estimate of the toroidal vortex diameter and of its centre position for increasing Fr. The onset of a laminar-to-turbulent flow transition is assessed in Section 4.4 through an analysis of the kinetic energy content, both of the turbulent as well as of the periodic flow structures, for different shaker table frequencies. In Section 4.5 an analysis is carried out to determine the optimum spatial resolution to best resolve the flow down to the Kolmogoroff scale, and obtain an accurate estimate of the local viscous dissipation rate of kinetic energy, ϵ. The volumetric power consumption is then obtained from the integral of ϵ and compared to the value estimated from the temperature increase of the fluid within the bioreactor for adiabatic conditions (thermal insulation) at the cylinder wall and base.

4.2 Measurement of the free surface interfacial area, I_a

Cell growth in shaken bioreactors is controlled by the oxygen transfer occurring at the free surface between the air and the cell culture medium (Doig *et al.*, 2005). From this perspective the gas/liquid mass transfer coefficient, k_la, is proportional to the interfacial area of the free surface, I_a, which can be directly estimated once the free surface profile is detected from the PIV images.

3D representations of the free surface shape for Fr=0.05, 0.11 and 0.17 are provided in Figures 4.1 (a), (b) and (c), respectively. These plots were obtained by

(i) splitting a 180° region of the surface into eighteen 10° phase intervals; (ii) determining the surface profile at the start of each interval as an average of 10 profiles measured at that ϕ; (iii) azimuthally stacking the free surface profiles measured at the 18 different phase angles, and (iv) utilising the fact that each measured profile provides the free surface shape at that ϕ (on the side to the left of the reactor axis) and at $\phi + 180°$ (on the side to the right of the reactor axis). From Figures 4.1 (a-c) it is evident that as the shaken rotational speed is increased the free surface inclination also increases. Moreover for Fr <0.15, Figures 4.1 (a) and (b), the free surface is planar and can be approximated by the elliptic disk obtained at the intersection of the free surface plane and the cylinder walls. This characteristic is also in evidence in the free surface profile of Figure 2.9 (d), which is denoted by an inclined line of constant slope nearly throughout the cylinder diameter. It should be remarked that this approximation fails at the two ends of the cylinder diameter, where the local free surface curvature is determined by the fluid surface tension. At the highest speed the free surface starts exhibiting a curved profile on the vertical plane of measurement and assumes a more complex 3D shape (Figure 4.1 c).

The variation of the non-dimensional interfacial area of the free surface, I_a/d_i^2, with Froude number, Fr, is shown in Figure 4.2 (a) for an orbital-to-cylinder diameter ratio d_o/d_i=0.25. The interfacial area was estimated by a trapezoidal integration of the different points comprising the free surface. Taking into account the considerations previously made, in Figure 4.2 (a) the measured interfacial area, I_a, is compared against the area of an inclined ellipse determined from the analytical solution of Equation 4.1.

$$I_a = d_i \frac{\pi}{4} \sqrt{(\mathit{\Delta} h)^2 + (d_i)^2} \tag{4.1}$$

Where the longest and shortest axes of the ellipse are $\sqrt{(\mathit{\Delta} h)^2 + (d_i)^2}$ and d_i and the free surface wave amplitude, $\mathit{\Delta} h$, is the maximum height difference between two points on opposite sides of the free surface ellipse. In Section 3.5 a linear relationship was found between the angle of inclination of the free surface and the Froude number ($\mathit{\Delta} h/d_i$ =1.4 Fr) for low Fr and water as working fluid. Thus Equation 4.1 can be rewritten in a non-dimensional form as:

$$\frac{I_a}{d_i^2} = \frac{\pi}{4}\sqrt{(1.4Fr)^2 + 1} \tag{4.2}$$

In Figure 4.2 (a) the analytical and measured estimates of the interfacial area show a relatively good agreement for Fr <0.15, with the maximum discrepancy between the two being 2 %. This difference is within the error involved in detecting the free surface profile. It should be noted that for higher Fr the measured interfacial area starts to deviate from the analytical solution, and the difference between the measured and analytical estimates increases to 4.6%. This behaviour is expected, as at higher Fr the free surface exhibits a 3D wavy profile, which inevitably has a greater area than that of an elliptic disk for the same wave amplitude, $\mathit{\Delta} h$. Furthermore, it is worth noting that the present data indicate that the interfacial area is independent of the fluid liquid height. This is well shown in Figure 4.2 (a), where I_a was estimated for two non-dimensional fluid heights, h/d_i=0.3 and h/d_i=0.5. This can be explained by considering that the free surface inclination is always orthogonal to the direction of the total acceleration, centrifugal plus gravitational, and therefore it is dependent only on the centrifugal to gravitational acceleration ratio, Fr.

In Figure 4.2 (b) an assessment is made to ascertain how the measured fluid volume, V_{fm}, obtained from the integral underneath the measured free surface compares to the nominal fluid volume, V_f. Two different sources of error can be distinguished. The first is a systematic error, and it is visualised in Figure 4.2 (b) by the difference between the nominal volume ratio line, V_{fm}/V_f=1, and that, V_{fm}/V_f=1.025, obtained from the average of the data points measured at different Fr. This discrepancy is related to the accuracy of the method employed to determine the filling volume, which was monitored by measuring with a ruler the fluid height in the bioreactor at rest. To put this in perspective, a systematic percentage error of $(\Delta V_{fm}/V_f)_{sys}$=0.025, corresponds to an error of the order of 1 mm on the measured fluid height (i.e. Δh=0.75 mm and 1.25 mm for h=30 mm and 50 mm, respectively). The second source of error is random, and is related to the accuracy of the free surface detection algorithm outlined in Section 2.4. This source of error was found to be $(\Delta V_{fm}/V_f)_{rnd}$=0.86% and it was estimated from the average of the absolute deviations of the data points in Figure 4.2 (b) from the horizontal line $\Delta V_{fm}/V_f$=1.025.

Figures 4.3 (a, b) show the variation of I_a for two different orbital diameters, d_o=35 mm and 50 mm, and a fixed inner diameter, d_i=100 mm. It should be noted that most of the points selected in Figure 4.3 are for in-phase conditions and therefore the maximum difference observed between the analytical and measured interfacial area is relatively small for orbital diameters, d_o/d_i=0.35 and 0.5, and equal to 1.8% and 1.5%, respectively. The anayltical solution proposed in this study to estimate the interfacial area was further assessed for two different inner cylinder diameters, d_i=70 mm and 100 mm, with a fixed orbital diameter, d_o=25 mm (see Figures 4.4 a and b). For in-phase conditions the maximum discrepancy between the measured value and the analytical solution estimates is 1.09% and 0.89% for inner diameters of d_i=70 mm and 130 mm, respectively.

The proposed analytical equation of the interfacial area was also compared against the numerical simulations of the interfacial area, I_a, by Zhang *et al.* (2009) who carried out their simulations for a rotational speed of 70 rpm and a 30 l cylindrical bioreactor. The non-dimensional interfacial area they found was $\frac{I_a}{d_i^2}\approx 0.81$, while the one obtained from Equation 4.2 using their operating conditions is $\frac{I_a}{d_i^2}=0.8$ with a discrepancy between the two of 1.2%. It should be noted that according to the flow scaling law described in Chapter 3, the operating conditions (h=200 mm, d_o=50 mm and d_i=287 mm) selected by Zhang *et al.* (2009) correspond to the early stage of out-of-phase flow, for which the shape of the free surface can be approximated by an elliptic disk.

4.3 Characterisation of the vortical structures

Vortical structures are encountered in most chemical and biochemical flow processes and their utilisation may help enhance mixing of the fluids. For instance Ducci and Yianneskis (2007) showed that mixing times can be reduced by 20-30% when the insertion is made in the macro-instability (MI) vortex core in stirred vessels. This behaviour might seem counter-intuitive as vortices, by definition, are not the most efficient flow structures to provide the shear necessary to segregate the feed. However, Ducci and Yianneskis (2007) showed that Macro-Instability vortices offered a shortcut mechanism to draw the feed towards the impeller, where the local high turbulence and viscous shear stresses broke up the feed and dispersed it more efficiently into the tank. From this perspective the vortical motions present in shaken bioreactors could aid optimisation of macromixing either by exploiting their sucking characteristics or by identifying unfavourable regions of the tank where the feed could be trapped during the mixing process. This potential optimisation is hindered by the lack of detailed information about vortex strength, location and size. The objective of this section is to estimate the vortex circulation time and identify potential locations for optimum insertion of cell nutrients.

The variation of the circulation time, $T^*_{\omega_\theta=0.3}$, with increasing ϕ is shown in Figure 4.5 for h/d_i=0.3, Fr=0.11 (N=90 rpm) and d_o/d_i=0.25. The circulation time, T^*, is defined in Equation 4.3.

$$T^* = \frac{1}{\Gamma^*} \tag{4.3}$$

where the phase-resolved circulation, Γ^*, is obtained from Equation 3.4 and integrated over the areas denoted as $A_{\omega R}$ and $A_{\omega L}$ represented in Figure 3.3 (a). As already discussed in Section 3.2 at a phase angle, ϕ=0°, the two counter-rotating vortices can be clearly identified from the velocity vector field and the contour plot of the vorticity, and therefore it is expected that the circulation time, $T^*_{\omega_\theta=0.3}$, is the shortest at this phase angle (see Figure 4.5). However as the shaker table moves along its orbit it is observed that $T^*_{\omega_\theta=0.3}$ gradually increases and peaks at ϕ=90°. After this maximum the circulation time decreases again because the two counter-rotating vortices increase in strength and rotate faster as the phase angle ϕ=180° is approached. The maximum of the circulation time, $T^*_{\omega_\theta=0.3}$, at ϕ=90° can be explained by considering that a strong radial motion is observed at this ϕ and the intensity of the vorticity decreases corresponding to a longer $T^*_{\omega_\theta=0.3}$. It is worth mentioning that the variation of the circulation time, $T^*_{\omega_\theta=0.3}$, with increasing ϕ was obtained from phase-resolved flow fields and the subscript $\omega_{\theta=0.3}$ refers to the non-dimensional iso-vorticity contour selected to delimit the vortex ($\frac{\omega_\theta}{\pi N} = 0.3$).

The ensemble-averaged circulation time, $\overline{T^*}$, and the mean vortex diameter, $\overline{d}_v$, defined in Equation 4.4, were further investigated for increasing Fr and h/d_i.

$$\overline{d}_v = \frac{d_{v_1} + d_{v_2}}{2} \tag{4.4}$$

where d_{v_1} and d_{v_2} are the horizontal and vertical distances of the two opposite points placed on the iso-vorticity boundary delimiting the vortex (see Figure 4.6). Similarly to the analysis carried out for the phase-resolved circulation time, the ensemble-averaged one, $\overline{T}^*_{\omega_\theta=0.1}$, was estimated from Equation 4.3 using the circulation, Γ^*, integrated over the area enclosed by an iso-vorticity contour $\frac{\omega_\theta}{\pi N} = 0.1$. For example, for h/d_i=0.3 and Fr=0.11, this vortex area is denoted as $A_{\omega E}$ in Figure 3.6 (b), where the ensemble-averaged vorticity contour plot is shown. It should be noted that for ensemble average quantities the vorticity threshold selected to determine the vortex border was lower than that used in Figure 4.5 for analogous phase resolved quantities, because the intensity of the maxima and minima of the ensemble average vorticity is inevitably lower than that exhibited by the phase resolved one (compare Figures 3.1a and 3.2). Therefore direct comparison between phase resolved and ensemble averaged circulation times should be made with care.

The variation of the non-dimensional ensemble-averaged circulation time, $\overline{T}^*_{\omega_\theta=0.1}$, with Fr and h/d_i is provided in Figure 4.7. As expected the circulation time is decreasing for increasing Fr, as the strength of the toroidal vortex increases in magnitude for greater values of the shaking frequency, N. Moreover it is worth to point out that lower h/d_i corresponds to shorter circulation time, implying that advection is greater for those operating conditions, and enhanced mixing could be expected. This is indeed confirmed by the mixing time measured by Tissot *et al.* (2010) who found that for decreasing fluid volume and increasing N the mixing time in the cylindrical shaken bioreactor becomes shorter. In Figure 4.7 the circulation time at Fr=0.11 for a non-dimensional fluid height h/d_i=0.3 is rather lower than those of the other two heights investigated. This may be explained by considering that at this Fr the flow for this liquid height starts being out-of-phase and therefore different flow dynamics are experienced in the bioreactor.

The variation of $\overline{d}_v$ with Fr is shown in Figure 4.8 for three non-dimensional fluid heights, h/d_i=0.3, 0.5 and 0.7, and fixed d_o/d_i=0.25. The vortex diameter increases linearly for increasing Fr, as the in-phase vortices tend to expand toward the bottom of the tank with increasing shaking frequency, N. In Figure 4.8 it is also possible to see that a sudden drop of $\overline{d}_v$ occurs at Fr=0.11 which is related to the out-of-phase flow transition for h/d_i=0.3. After transition the vortices are pushed against the wall, resulting in a smaller $\overline{d}_v$.

The radial coordinate of the vortex centre, $r_{\omega c}$, visualised in Figure 4.9 (a), was estimated from the average coordinates of the two points on the vortex iso-vorticity contour $\frac{\omega_\theta}{\pi N} = 0.1$ that are the closest and furthest away from the bioreactor axis. The non-dimensional centre coordinate, $r_{\omega c}/d_i$, is plotted in Figure 4.9 (b) for increasing Fr. In this figure the vertical bars shown represent the vortex diameter and how it varies with increasing shaking frequency, N. Similarly to the results presented for $\overline{T}^*_{\omega\theta=0.1}$ and $\overline{d}_v$, the linear relationship between $r_{\omega c}$ and Fr is valid only for in-phase conditions, when the growth of the toroidal vortex towards the bottom and the centre of the reactor results in a decrease of the distance of the vortex centre from the bioreactor axis. It is interesting to note that the same $r_{\omega c}$ is obtained at a given Fr for different h/d_i, which indicates that the growth of the vortex is the same for all the non-dimensional fluid heights considered at a fixed orbital to cylinder diameter ratio. Similarly to the considerations made for Figures 4.7 and 4.8, the sudden increase of $r_{\omega c}$ occurring at Fr >0.11 for h/d_i =0.3 is explained by the incipiency of out-of-phase flow, with the toroidal vortex being pushed against the wall and its centre radial coordinate being greater than those of the other heights considered at same Fr.

The variation of the vortex circulation time, T^*, was further investigated for different orbital to cylinder diameter ratios, d_o/d_i. The analysis was carried out for a fixed non-dimensional fluid height, h/d_i=0.3, and for a phase angle $\phi = 0^o$. Similarly to the phase resolved results presented in Figure 4.5, the circulation time was estimated from Equation 3.4 using a non-dimensional vorticity threshold, $\frac{\omega_\theta}{\pi N} = 0.3$. The data presented in Figure 4.10 are related to transition to incipient flow when the toroidal vortex extends to the bottom of the bioreactor. From the scaling law reported in Chapter 3 this implies that all the combinations (d_o, d_i) analysed satisfy the condition $h/d_i<(d_o/d_i)^{0.5}$. From Figure 4.10 the non-dimensional circulation time associated to transition to incipient out-of-phase flow decreases with increasing d_o/d_i. This behaviour is in agreement with the discussion made for Figure 3.24, where it was found that the critical wave amplitude $(\Delta h/h)_c$ increases with increasing d_o/d_i. In fact greater $(\Delta h/h)_c$ implies greater inclination of the free surface and therefore a greater transitional Froude number, Fr_c, which is associated to a toroidal vortex of greater strength and therefore shorter non-dimensional circulation time. These results compare very well with the mixing time measurements of Tissot *et al.* (2010), who showed that for increasing d_o the mixing time decreased. The implications of these results are potentially useful for the selection of optimum d_o, d_i and N for the design of bio-processes where an in-phase flow is preferable because of the lower level of viscous stresses, and of the improved mixing and cell suspension performance that should be obtained with a stronger toroidal vortex and reduced circulation times.

In the previous part the study focussed on circulation times obtained from the tangential vorticity, ω_θ, which is the most significant component before transition to “out of phase” flow, when the fluid dynamics in the bioreactor is dominated by a toroidal vortex. In the following an analysis of secondary circulation times based on the axial vorticity component, ω_z, for in-phase conditions is performed. As can be seen from Figure 4.11 (a), the enclosed area selected to estimate the circulation time is at the core of the flow and denoted as $A_{\omega z}$. The circulation time was estimated at different horizontal planes which could be either in the "convection" or "diffusion" zones depending on the Froude number and on the non-dimensional fluid height considered. For example in Figure 4.11 (a) with $h/d_i = 0.3$ and $Fr = 0.069$, three horizontal planes were examined, one in the "convection zone", z/d_i=0.2, where the axial vorticity shows maximum absolute intensity of 0.14 πN, and two in the "diffusion" zone, where the flow is locally characterised by solid body rotation (cf. Figure 3.11), and the absolute maximum intensity of the axial vorticity is approximately $\approx$ 0.2 πN. Figures 4.11 (b) and (c) show the variation of the circulation times at different axial planes for three non-dimensional fluid heights, h/d_i=0.3, 0.5 and 0.7 and fixed Froude number, Fr=0.069 (N=70 rpm) and 0.11 (N=90 rpm), respectively. To better compare the vorticity obtained for the different fluid heights investigated a non dimensional axial coordinate, $(h-z)/d_i$, with origin on the free surface at rest has been considered. This implies that horizontal planes located closer to (further away from) the free surface are associated to lower (higher) values of $(h-z)/d_i$ in Figure 4.11 (b). This normalised coordinate is consistent with the data discussed in Figures 3.4 and 3.5, where the same shaking speed was associated to analogous penetration heights of the toroidal vortex towards the bottom of the tank, and therefore analogues size of the convection zone for the two non-dimensional fluid heights considered, h/d_i=0.5 and 0.7. For example, when a shaking speed of 90 rpm was considered, the vortex penetration height was $\approx 0.34d_i$ (cf. Figure 3.4 b) and $\approx 0.31d_i$ (cf. Figure 3.4 b) for h/d_i=0.5 and 0.7, respectively. This analogy is well exemplified in Figures 4.11 (b) and (c), where the circulation time is approximately denoted by similar intensity irrespective of the fluid height considered at a given distance from the free surface. It is worth to point out that the circulation time obtained from the axial vorticity is smaller (larger) in the diffusion (convection) zone, resulting in a longer time for a fluid parcel to complete a loop around the vertical axis of the bioreactor in the region dominated by the toroidal vortex. This behaviour is clearly present in the horizontal flow fields of Figure 4.11 (a), where the maximum vorticity intensity is located in the plane closer to the bottom of the tank. As expected when the shaken speed is increased from 70 rpm to 90 rpm the range of variation of the circulation times decreases from $\pi N T^{*}_{\omega_z=0.1}$=6.5-9.75 to $\pi N T^{*}_{\omega_z=0.1}$=4-8 (cf Figures 4.11 b and c).

4.4 Kinetic energy content

The current section provides a general description of the flow for two different conditions, before and after flow transition, and estimates of the kinetic energy content due to the velocity variations associated with the periodic nature of the flow and of that associated with the random velocity fluctuations. This analysis allows to establish whether the mean flow transition identified in Chapter 3 can also be linked to the potential onset of a laminar-turbulent flow transition.

Characteristic phase-resolved velocity fields of the vertical and horizontal plane measurements for a phase angle ϕ=270°, at a low Froude number (Fr=0.11), before the transition to out-of-phase flow takes place, are shown in Figures 4.12 (a, b). For ϕ=270° the vertical plane of measurement is parallel to the direction of the orbital velocity of the shaker table, and therefore the 2D velocity field of Figure 4.12 (a) exhibits a strong radial flow, which moves fluid from one side of the bioreactor to the other. The phase-resolved velocity field measured on a horizontal plane at z/d_i=0.08 is shown in Figure 4.12 (b) for Fr=0.11, h/d_i=0.3 and ϕ=270°. In Figure 4.12 (b) two regions can be distinguished where the local flow dynamics are different: in the upper part of Figure 4.12 (b) (r/d_i >0.22), which is closer to the center of the bioreactor orbit, the flow is mainly parallel to the shaker table movement, which, for this phase angle, is directed from right to left. In this region the orbital diameter, d_o, is the relevant length scale. On the contrary, in the bottom part of Figure 4.12 (b), the centrifugal force pushes the fluid against the wall and the flow is locally forced to follow the bioreactor wall curvature. For this region the cylinder diameter, d_i, is the relevant length scale, and together with the orbital rotational speed, $\pi N d_o$, determines the size of the area which is most affected by the wall boundary. It is worth noting that the phase-resolved velocity field of Figure 4.12 (b), for ϕ=270°, is the same as that encountered at every other phase angle provided that the velocity field is rotated around the cylinder axis by an appropriate angle.

Phase-resolved velocity fields in the vertical and horizontal planes of measurement are shown in Figures 4.13 (a) and (b), respectively, for Fr=0.24, h/d_i=0.3 and ϕ=270°. These velocity fields are characteristic of the higher range of Fr investigated and are representative of the flow in the bioreactor after the transition to out-of-phase flow has taken place. The flow fields obtained from measurements on a vertical plane for Fr=0.11 (Figure 4.12 a) and Fr=0.24 (Figure 4.13 a) at ϕ=270° are similar, as they both show a radial motion from the right hand side of the bioreactor to the left. The major differences between the two flows are more evident when the horizontal plane measurements of Figures 4.12 (b) and 4.13 (b) are compared. The flow for Fr=0.24 at different horizontal planes was found to be characterised by a vortex with a vertical axis that precesses around the cylinder axis as the shaker tray moves along its circular orbit (see Figure 3.12). Similarly to the flow stream in the tangential direction previously described for Figure 4.12 (b), the nature of this vortex is induced by the cylinder wall curvature, which at this higher orbital speed induces a tangential flow stream that spreads over the entire plane. In other words, the high momentum imparted to the fluid by the fast motion of the shaker, in conjunction with the presence of the cylinder wall, forces the fluid to follow a circular motion along a closed loop that results in the vertical-axis vortex shown in Figure 4.13 (b).

The kinetic energy contour plots of Figures 4.12 and 4.13 allow a quantitative comparison between conditions before and after the transition to out-of-phase flow. It should be noted that the kinetic energy of Figures 4.12 and 4.13 has been estimated according to the two dimensional approximation of Equation 4.5, where indices i and j refer to the velocity components measured in the plane considered, while the third component contribution is estimated as the average of the other two (i.e. $\langle u_k \rangle^2 = 0.5\left(\langle u_i \rangle^2 + \langle u_j \rangle^2\right)$).

$$k_{ij} = \frac{3}{4}\left(\langle u_i \rangle^2 + \langle u_j \rangle^2\right) \tag{4.5}$$

When comparing Figures 4.12 (a) and (b) for Fr=0.11 it is evident that the ranges of variation of k_{rz} and $k_{r\theta}$ are similar, with $k_{ij}/(\pi N d_o)^2$=0-0.2, indicating that the three components comprising the kinetic energy are of comparable magnitude. However, this is not the case after the transition to out-of-phase flow for Fr=0.24 (Figure 4.13), where the maximum intensity of $k_{r\theta}$ is more than three times greater than that measured in the vertical plane, k_{rz}. This clearly implies that the tangential velocity component, $\langle u_\theta \rangle$, is significantly higher than the other two, and for this operating condition it dominates the flow dynamics inside the cylindrical bioreactor. Moreover, when comparing $k_{r\theta}$ of Figure 4.12 (b) and that of Figure 4.13 (b), it is evident that in the latter case the kinetic energy is more evenly distributed over a larger area spreading around 270° in this plane.

A comparison between the kinetic energy content of the random velocity fluctuations obtained from measurements on a vertical plane is provided in Figures 4.14

(a) and (b) for Fr=0.11 and Fr=0.24, respectively. Similarly to the analysis carried out for the phase-resolved periodic flow, the kinetic energy was estimated according to Equation 4.6 using only the velocity components obtained from the vertical plane measurements.

$$k'_{ij} = \frac{3}{4}\left(\left\langle u_i'^2 \right\rangle + \left\langle u_j'^2 \right\rangle\right) \tag{4.6}$$

From Figure 4.14 (a) it is evident that for Fr=0.11 the random velocity fluctuations are nearly negligible, as the average intensity of k'_{rz} is at least two orders of magnitude lower than the energy content of the periodic flow, k_{rz}, for the same phase angle, ϕ=270° (cf. Figure 4.12 a). On the contrary, for Fr=0.24 regions of higher content of kinetic energy associated to the random fluctuations start being present at the sides of the bioreactor. In these regions $\frac{k'_{rz}}{(\pi N d_o)^2}$ is in the range of 0.1-0.3 and has the same order of magnitude of the energy associated to the periodic flow (cf. k_{rz}=0.1-0.7 in Figure 4.13 a).

The variations of the kinetic energy content of the phase-resolved flow, k^*_{ij}, and of the random velocity fluctuations, k'^*_{ij}, with Froude number, Fr, are shown in Figures 4.15 (a) and (b), respectively. As reported in Equation 4.7 the asterisk denotes the space average of k_{rz} and k'_{rz} over the entire plane of the flow investigated.

$$k^*_{ij} = \frac{1}{A}\int_A k_{ij} dA \tag{4.7}$$

The results of Figure 4.15 (a) show that the two 2D approximations k^*_{rz} and $k^*_{r\theta}$ increase exponentially with Fr. As previously described the two approximations exhibit similar magnitudes for Fr <0.11, while above this value $k^*_{r\theta}$ is greater than k^*_{rz} because the flow is dominated by the tangential velocity component. When looking at the results of the energy associated to the random velocity fluctuations of Figure 4.15 (b), it is evident that the flow is laminar for Fr <0.11 with negligible kinetic energy at these low Froude numbers, while the onset of a laminar-turbulent flow transition is corroborated by turbulence levels of approximately 2% and 7% occurring at Fr=0.235 and 0.274, respectively.

A comparison between the radial profiles of the periodic kinetic energy obtained from the complete definition, using all the three velocity components, k, and from the 2D approximation, $k_{r\theta}$, is given in Figure 4.16 for z/d_i=0.08 and 0.15 (h/d_i=0.3, Fr=0.11 and ϕ=270°). It should be noted that in Figure 4.16 black and blue data points discriminate between radial positions to the right and left hand sides of the bioreactor axis. For both the heights considered the radial profiles of the complete kinetic energy, k, and of the 2D approximation, $k_{r\theta}$, show good agreement only at radial coordinates further away from the centre, for r/d_i >0.35. In this region the axial velocity component is relatively high (see Figure 4.12 a) and comparable to the tangential velocity component. On the contrary for r/d_i <0.35 the 2D approximation is less accurate and, despite the similarities in shape of the two radial profiles for positions both to the left and right hand sides of the cylinder axis, it tends to over-estimate the kinetic energy content by a nearly constant amount of 40% and 30% for z/d_i=0.15 and z/d_i=0.08, respectively. The current data indicate that knowledge of the complete 3D flow is useful to obtain accurate measurements of the kinetic energy and also to quantify the uncertainties involved in extrapolating the kinetic energy behavior for varying operating conditions such as Fr, h/d_i and d_o/d_i from 2D approximations.

4.5 Viscous dissipation rate of kinetic energy

The rate at which transport processes occur in the bulk of the liquid is highly dependent on the volumetric power consumption and on the distribution of the viscous dissipation rate of kinetic energy, ϵ, within the bioreactor. For example, Zhang *et al.* (2008) report that liquid mixing and oxygen transfer rates of a shaken bioreactor are critically affected by both the volumetric power consumption and local levels of viscous dissipation rate of kinetic energy. Although accurate estimates of the local dissipation rate, ϵ, have been obtained in stirred tank reactors, either by direct measurements of the velocity gradients, (Baldi and Yianneskis, 2003; Ducci and Yianneskis, 2005), or indirectly from the kinetic energy balance equation, (Escudié and Liné, 2003) no such information is available for cylindrical shaken bioreactors.

Measurements of the local viscous dissipation rate of the kinetic energy and its distribution in the cylindrical shaken bioreactor for in-phase condition are provided in Section 4.5.1, while comparisons of the measurement spatial resolution against the Kolmogoroff length scale, and the variation of ϵ with Fr are analysed in Section 4.5.2. The temperature measurement method adopted by Sumino and Akiyama (1987) is employed in Section 4.5.3 to estimate the volumetric power consumption, P_v, in the cylindrical vessel, and compared against the value of P_v obtained from the integral of the viscous dissipation rate of the kinetic energy over the tank volume. In this work the viscous dissipation rate of kinetic energy was estimated directly from its definition (see Equation 4.8).

$$\epsilon = \nu \left[\frac{\partial u_i}{\partial x_j} \left(\frac{\partial u_i}{\partial x_j} + \frac{\partial u_j}{\partial x_i} \right) \right] \tag{4.8}$$

where repeated indices imply summation. Direct measurement of ϵ requires the estimation of twelve terms comprising nine mean squared velocity gradients and three cross product gradients. The estimation of all the terms present in Equation 4.8 is difficult to achieve as it requires the use of advanced multi-channel anemometers with high spatial resolution. Sharp and Adrian (2001) used a 2-D PIV system in a vessel stirred by a Rushton turbine to determine the dissipation rate from five out of the twelve terms of Equation 4.8. The terms not directly measured were estimated assuming statistical isotropy (see Sharp and Adrian, 2001; Baldi and Yianneskis, 2003). With this assumption the viscous dissipation of kinetic energy for the vertical plane measurements can be approximated according to Equation 4.9.

$$\epsilon = \nu\left[2\left(\frac{\partial u_r}{\partial r}\right)^2 + 2\left(\frac{\partial u_z}{\partial z}\right)^2 + 3\left(\frac{\partial u_z}{\partial r}\right)^2 + 3\left(\frac{\partial u_r}{\partial z}\right)^2 + 2\left(\frac{\partial u_r}{\partial z}\frac{\partial u_z}{\partial r}\right)\right] \tag{4.9}$$

4.5.1 Distribution of ϵ in the shaken bioreactor

The simulations of Zhang *et al.* (2005) and Zhang *et al.* (2008) have shown that most of the kinetic energy in shaken flasks and wells is dissipated at the bioreactor walls. In order to correctly estimate the velocity gradients at the walls, the PIV measurements obtained within the bioreactor were combined with boundary conditions to impose a zero velocity ($u_r = u_\theta = u_z = 0$) in all locations at z/d_i=0 or r/d_i=0.5.

The distribution inside the bioreactor of the viscous dissipation rate of kinetic energy for h/d_i=0.3, $\phi = 270^o$, Fr=0.11 (N=90 rpm) and d_o/d_i=0.25, is shown in Figure 4.17. In agreement with the simulations of Zhang *et al.* (2005) and Zhang *et al.* (2008) obtained for different types of bioreactor, it is evident that for a shaken cylinder the largest amount of kinetic energy is also dissipated near the walls, with a three order difference in magnitude between the local dissipation rate in the bulk of the flow and at the walls. It should be noted that the flow field at this ϕ exhibits a strong radial flow, with movement of fluid from one side of the bioreactor to the other one (cf. Figure 4.12 a). For $\phi = 270$° the highest energy is dissipated at the right wall with the maximum reaching 330, while the energy dissipated at the free surface is not as high ($\frac{\epsilon}{\nu(\pi N)^2}$ ≈70).

4.5.2 Assessment of the measurement spatial resolution

In this section an analysis is carried out to assess to what extent the measurement spatial resolution, Δx_i, affects the final estimate of the dissipation rate, and to compare the measurement spatial resolution against the Kolgomoroff scale. The analysis is carried out for in-phase flow conditions, when the toroidal vortex is fully developed. Two different phase angles were considered that are most representative of the flow in the cylindrical bioreactor: $\phi = 0°$, when the free surface reaches its maximum inclination, and $\phi = 270°$, when the free surface profile is horizontal on the plane of measurement. Four different sets of experiments were made with decreasing interrogation area, 10×10 cm^2, 4×4 cm^2, 3×3 cm^2, 2×2 cm^2 and 1×1 cm^2 close to the left wall of the cylindrical bioreactor, and increasing spatial resolution, $\Delta x_i/d_i$=0.013, 0.005, 0.0037, 0.0025 and 0.0012. A visualisation of the different interrogation areas analysed is provided in the schematic diagram of Figure 4.18 (a). To compare in a consistent manner the different spatial resolution sets of measurements, the dissipation rate, ϵ^*, was averaged according to Equation 4.10, over the area A_s encompassed by the shaded region of Figure 4.18 (a), which is in common to all the interrogation windows considered. The area, A_s, was 1 cm high and twice the spatial resolution, Δx_i, of each set of experiment in the horizontal direction.

$$\epsilon^* = \frac{1}{A_s}\int_{A_s} \epsilon \; dA_s \tag{4.10}$$

Figure 4.18 (b) shows the variation of ϵ^* with decreasing Δx_i for h/d_i=0.3, Fr=0.11, d_o/d_i=0.25. From Figure 4.18 (b), it can be seen that the average energy dissipation, ϵ^*, increases as the window size of the flow field is reduced.

The influence of the spatial resolution on ϵ^* can be explained by the strong dependence of the velocity gradient estimation on the distance between two adjacent measurement locations. The estimates of ϵ^* show small differences at low spatial resolutions ($\frac{\Delta x_i}{d_i}$ $>5\times10^{-3}$), while they differ significantly at higher spatial resolutions ($\frac{\Delta x_i}{d_i}$ $<5\times10^{-3}$). In the latter case, a small change in spatial resolution produces significant variations in the value of the estimated ϵ^*. Furthermore it should be noted that a higher ϵ^* is observed for ϕ=270°, which is almost double that obtained for ϕ=0° when the finer resolution is considered ($\frac{\Delta x_i}{d_i}$ $=1.2\times10^{-3}$). This behaviour is expected since the dominating velocity component for ϕ=0° is u_θ, at the inner and outer regions of the cylinder, while the other two velocity components u_r and u_z are relatively small (cf. Figure 2.16 a). This implies that for this phase angle it is not possible to extract from the 2D PIV measurement, the term $(\partial u_\theta/\partial r)^2$ which is more likely to account for the largest amount of energy dissipation at $\phi = 0°$. On the contrary for ϕ=270° the main velocity components lie on the plane of measurement, with u_z being the greater component in the region, next to the wall, of maximum energy dissipation (cf. Figure 2.16 d).

The effect of increasing Fr on ϵ^* is subsequently investigated. For this analysis the highest spatial resolution achievable, $\frac{\Delta x}{d_i}$=1.2×10^{-3}, corresponding to an interrogation window of 1×1 cm^2, is employed for h/d_i=0.3, ϕ=270° and d_o/d_i=0.25 (see Figure 4.19 a). The results of Figure 4.19 (b) show that the average energy dissipation, ϵ^*, increases with increasing Fr. As previously described the 2D approximation of the kinetic energy content of the phase-resolved flow, k^*_{rz}, increased with Froude number in the range of Fr=0.05-0.15, while for the same Fr range the contribution due to the random velocity fluctuations, k'^*_{rz}, was relatively low. This implies that at this low Fr regime turbulence is not yet developed, and therefore the kinetic energy is mainly dissipated by the viscous stresses generated by the large scale flow structures (toroidal vortex) next to the cylinder wall.

Another important parameter that has to be considered in the design of a bioprocess is the Kolmogoroff length scale, η, which indicates the size of the eddies dissipating most of the kinetic energy, and should be compared to the size of the cultivated cells and/or micro-carriers to establish whether local viscous stresses could potentially determine cell damage. The definition of η is given in Equation 4.11.

$$\eta = \left(\frac{\nu^3}{\epsilon}\right)^{1/4} \tag{4.11}$$

with ϵ being the rate of viscous dissipation of kinetic energy, and ν the fluid kinematic viscosity. It has to be stressed that the Kolmogoroff length scale and its definition of Equation 4.11 are generally used in turbulent flow, nevertheless the rate of viscous dissipation of kinetic energy and the associated length scale are necessarily present also in a laminar flow. The variation of the dissipative length scale, η_k, with increasing spatial resolution, $\varDelta x_i$, and Froude number, Fr, is shown in Figure 4.20 (a) and (b), respectively. Similarly to the analysis carried out for ϵ_k, also η_k was obtained from the dissipation rate averaged over the shaded regions of Figures 4.18 (a) and 4.19 (a). For a small $\varDelta x_i$ a small dissipative length scale, η_k, is observed, whilst for the coarser spatial resolution considered in this study it was found that the dissipative length scale increases almost twofold. From the variation of η_k with Fr (Figure 4.20 b), it is observed that for the lower shaking frequency analysed, N=60 rpm (Fr=0.05), a large normalized dissipative length scale, $\frac{\eta_k}{di}$=1×10^{-3} is observed, whereas for the greater speed considered, N=100 rpm (Fr=0.14), the dissipative length scale is $\frac{\eta_k}{di}$= 5×10^{-4}. This analysis indicates that both the measurement spatial resolution and the Froude number, Fr, have a great impact on the estimated size of the dissipative eddies, and careful selection of the spatial resolution, especially at high Fr, should be sought to produce reliable results that can advise on the possibility of cell damage in a bioprocess.

4.5.3 Estimation of volumetric power consumption in the cylindrical bioreactor

In this section two methods are employed to determine the volumetric power consumption, P_v, in the bioreactor. The first method is based on the temperature measurement technique adopted in the literature by Sumino and Akiyama (1987) and by Kato *et al.* (2004) to determine P_v in a shaken flask and in a 20 l shaken cylindrical bioreactor, respectively. To prevent heat losses the vessel was insulated using aluminised mylar film to cover the external surface of the glass cylinder and the base of the reactor, while the top side and the free surface were in contact with the surrounding air. All the temperature measurements were carried out using a thermocouple and a thermometer with a resolution of 0.1 °C. The thermocouple was used to determine the temperature inside the bioreactor, while the thermometer was used to monitor the temperature of the surrounding air. Once the cylinder was insulated, it was filled with distilled water previously heated to a temperature of 70°C, and the temperature was recorded at 30 minute time intervals.

A schematic diagram of the heat transfer process occurring in the bioreactor and of its boundary conditions is provided in Figure 4.21. The surrounding temperature can be assumed constant, as the room volume and mass are considerably greater than those of the reactor. Similarly the heat generation term, $\dot{G}$, of Equation 1.7, which is directly related to the amount of kinetic energy dissipated as heat in the bioreactor, can be considered constant, and over a long period independent of the periodic nature of the flow inside the bioreactor. Based on these assumptions the analytical expression of T_f shown in Equation 4.12 can be obtained by solving the heat transfer differential equation (Equation 1.7).

$$T_f = T_o + \frac{\dot{G}}{UA} + \left(T_f - T_o - \frac{\dot{G}}{UA}\right)_{t=0} e^{-\frac{UA}{mc_p}t} \tag{4.12}$$

The variations in time of the temperatures of the fluid inside the reactor and of the surroundings are shown in Figure 4.22 (a) for h/d_i=0.3 (V_f= 235 ml), Fr=0.11 (N=90 rpm) and d_o/d_i=0.25. In agreement with the assumptions made above the surrounding temperature, T_o, remains constant (19 °C) throughout the measurement period, while the fluid temperature T_f exhibits the exponential decay of Equation 4.12. According to Equation 4.12 the temperature of the fluid at steady state will be greater than the temperature of the surroundings of $\mathit{\Delta} T_\infty = \dot{G}/(UA)$. From the measurements shown in Figure 4.22 (a) it was found that for the last data point, obtained after 6 hours, the temperature difference between the fluid and the surrounding air was equal to the temperature resolution of the thermometer employed ($T_f - T_o$=19.1-19=0.1 °C). This implies that at steady state the difference between the two temperatures is below this value, indicating that heat generated through energy dissipation is rather small, and an accurate estimate could not be established with the apparatus employed. Nevertheless it was thought that the current data could still provide an estimate of the order of magnitude of the heat generated, and an indication of the range of variation of $\dot{G}$.

Taking into account this, two different exponential curves were fitted through the experimental data to determine the decay coefficient, $UA/(mc_p)$, for $\mathit{\Delta} T_\infty = 0.1$ °C and 0.01 °C. The first value of $\mathit{\Delta} T_\infty$ was selected based on the resolution of the thermometer and should provide the upper limit of $\dot{G}$, while the second threshold, one tenth of the first one, was considered an informed guess to determine the lower limit of $\dot{G}$. It is worth to point out that both the fitted curves give nearly the same overall heat transfer coefficient, UA, with a 1.1% difference between the two (cf. legend of Figure 4.22 a), while the correlation coefficient is well above 0.99 for both cases. Based on these exponential decay curves it was possible to retrieve a range of variation of the rate of heat generated per unit volume of $14.8 < P_v < 149.6$ W/m^3.

A second interpolation procedure was proposed by Sumino and Akiyama (1987) to determine the rate of heat generated within the bioreactor from temperature measurements. This methodology is based on Equation 1.7, and it is implemented by determining $\dot{G}$ from the line which best fits the measured data points ($T_f - T_o$, dT_f/dt), and estimating its interception with the ordinate axis. This methodology is attempted in Figure 4.22 (b), where the best fitting line is characterised by a slope $UA/(c_p m)$=3.4×10^{-4}s^{-1}, while the interception with the ordinate axis corresponds to $\dot{G}/(\rho c_p)$=-1.27×10^{-4}s^{-1} °C/s. This solution is contrary to the heat transfer dynamics expected from the system, as a negative heat generation term implies that the fluid in the bioreactor is absorbing heat rather than generating. This discrepancy might be a consequence of the the error made on the time derivative of the temperature, with a 30 minute interval between consecutive readings, and of the small amount of energy being dissipated in the bioreactor for the operating condition considered. In fact the error made on dT_f/dt directly affects the slope of the line which best fits the data, and even small variations of the slope, combined to the low value of $\dot{G}$, might result with the intersection of the negative side of the ordinate axis. It is therefore recommended that such a procedure should be carried out when temperature measurements are more frequent and when the heat dissipated is considerably greater than the values occurring at the Fr considered in this work.

The second method that is employed to determining P_v is based on the volumetric integral of the local rate of dissipation of kinetic energy. Based on the analysis reported in 4.5.2 the measurements were limited only to the regions next to the bottom and side walls, with the maximum possible spatial resolution employed, $\frac{\mathit{\Delta} x}{d_i}$=1.2×$10^{-3}$. To take into account the three dimensionality of the system, the measurements were carried out over the entire range of phase angles with a 10° increment. A representation of the different interrogation areas used to obtain an estimate of P_v is shown in Figure 4.23. Subsequently the power consumption was obtained from Equation 4.13, where the integration is made in a cylindrical coordinate system and carried across the trapezoidal elements represented in Figure 4.24 with sides $\mathit{\Delta}\phi$=10°, and $\mathit{\Delta} z = \mathit{\Delta} r$=1.2×$10^{-4}$ m.

$$\frac{P}{V_f} = \frac{\int_{V_f} \epsilon dV_f}{V_f} \tag{4.13}$$

Using this methodology the power consumption was estimated to be P_v=45.6 W/m^3. This value is within the range identified previously from the temperature measurements, and is consistent with the results of Klöckner *et al.* (2012), who estimated P_v in a shaken cylinder by means of torque measurements, and found for similar operating conditions (N = 90 rpm and d_o = 2.5 cm) P_v ≈50 W/m^3. The results of the preceding two sections indicate that the PIV and temperature measurement methodologies involve considerable uncertainties, and therefore only estimates of the power consumption may be obtained with such methods.

4.6 Concluding Remarks

In this chapter, 3D reconstructions of the free surface and of the variation of the interfacial area with Fr were investigated at first. The analysis allowed to conclude that the free surface can be approximated by an inclined elliptic disk with $\frac{I_a}{d_i^2} = \frac{\pi}{4}\sqrt{(1.4Fr)^2+1}$ for in-phase flow conditions, while at greater

Fr the measured interfacial area deviates from this analytical solution, as the free surface assumes a more pronounced 3D shape. A thorough discussion of the non-dimensional circulation time and length scales of the vortical structures dominating the flow at different operating conditions was also carried out to provide further insight into the mixing dynamics of the bioractor.

A Reynolds decomposition analysis was carried out to estimate the energy content of the large scale periodic motion produced by the orbital movement of the shaker table and of the velocity fluctuations induced by random and cycle-to-cycle variations. It is known (from Chapter 3) that the flow exhibits a transition to the out-of-phase flow when $Fr > 0.11$ for a non-dimensional height, $h/d_i = 0.3$, and an orbital to cylinder diameter ratio, $d_o/d_i = 0.25$. The kinetic energy results provided evidence that onset of a laminar-turbulent flow transition also occurs for $Fr > 0.11$, as indicated by the variation of kinetic energy content of the random and cycle-to-cycle velocity fluctuations with Fr: the flow was laminar for $Fr < 0.11$ with negligible kinetic energy at these low Froude numbers, while turbulence levels of approximately 2% and 7% occurred at $Fr = 0.235$ and 0.274, respectively.

The distribution of the rate of viscous dissipation of kinetic energy in the bioreactor and the volumetric power consumption were also determined by means of PIV and temperature measurements. The power consumption estimates obtained with the two methodologies showed a reasonable agreement, and were consistent with those obtained by Klöckner *et al.* (2012) for a similar system through torque measurements. Nevertheless, it should be stressed that only estimates of the dissipation rate and power consumption may be acquired through such methods.

The effect of spatial resolution on the estimation of the energy dissipation and of the Kolmogoroff length scale was investigated in this chapter. It was observed that for high spatial resolution ($\frac{\Delta x}{d_i}$=1.2×10^{-3}) the normalised ϵ for ϕ=270° was twice that for ϕ=0°. Furthermore, the normalised dissipation rate varied significantly with spatial resolution, as values of the dissipation rate at the highest spatial resolution, $\frac{\Delta x}{d_i}$=1.2×10^{-3}, were 10 times greater than those obtained at the lowest spatial resolution investigated ($\frac{\Delta x}{d_i}$=1.3×10^{-2}). Consistently with this behaviour, a more accurate estimation of the Kolgomoroff length scale, η_k, could be obtained with increasing spatial resolution, with η_k being subject to almost a twofold increase when the spatial resolution was reduced from the highest to the lowest one examined.

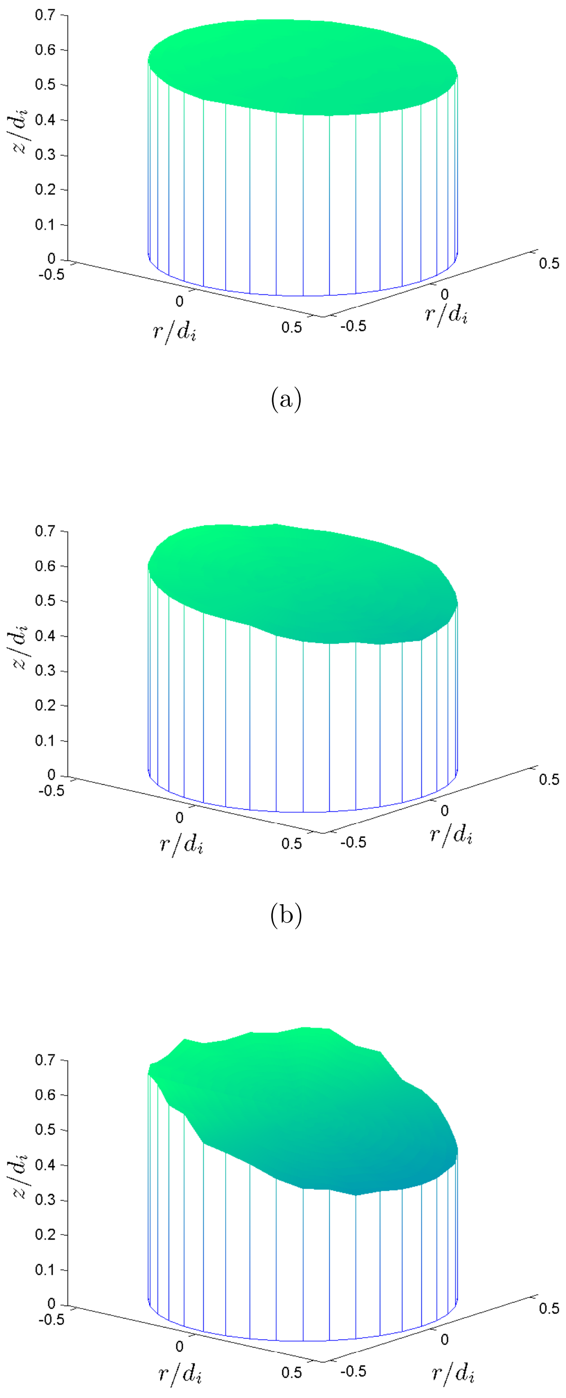

(a)

(b)

(c)

Figure 4.1: 3D reconstruction of the free surface for increasing Froude number (h/d_i=0.5, d_o/d_i=0.25): (a) Fr=0.05 (N=60 rpm); (b) Fr=0.11 (N=90 rpm); (c) Fr=0.17 (N=110 rpm).

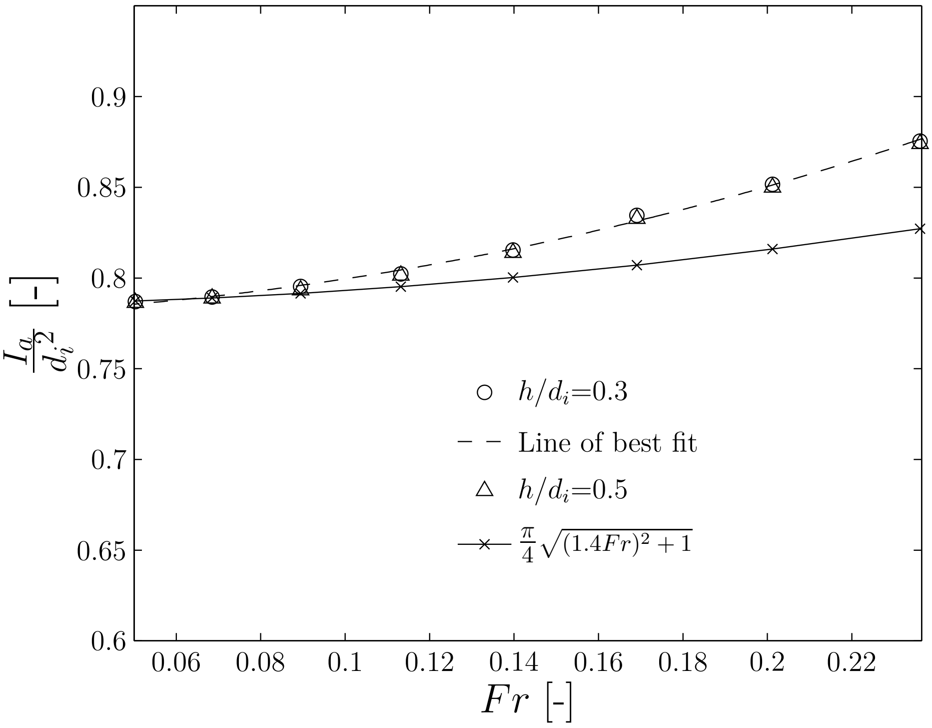

(a)

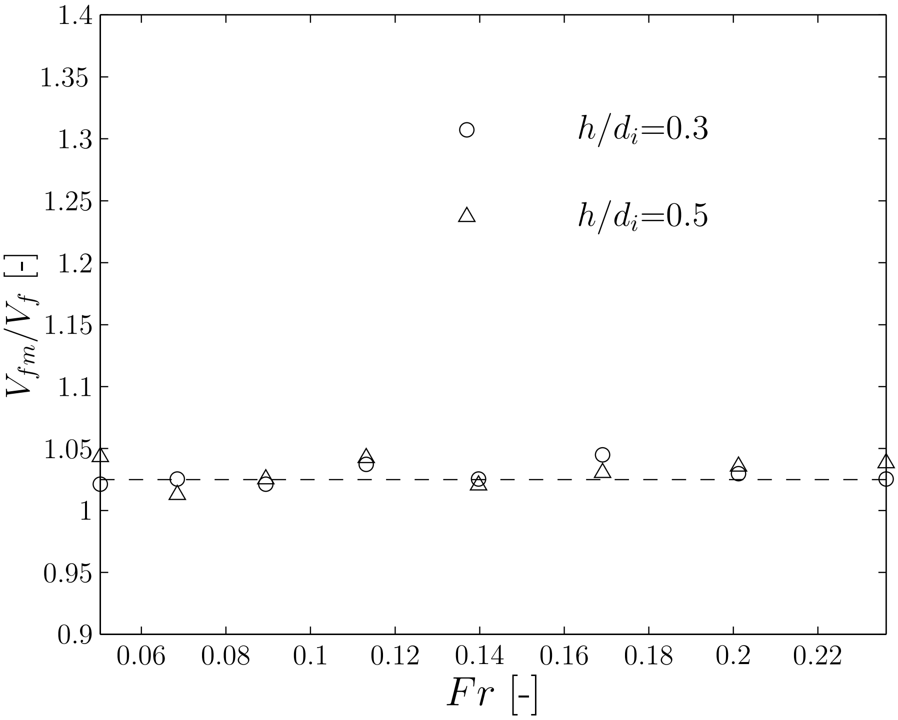

(b)

Figure 4.2: Variation of the interfacial area of the free surface, I_a, and of the measured fluid volume, V_{fm}, with Froude number (d_o/d_i=0.25): (a) I_a/d_i^2; (b) V_{fm}/V_f.

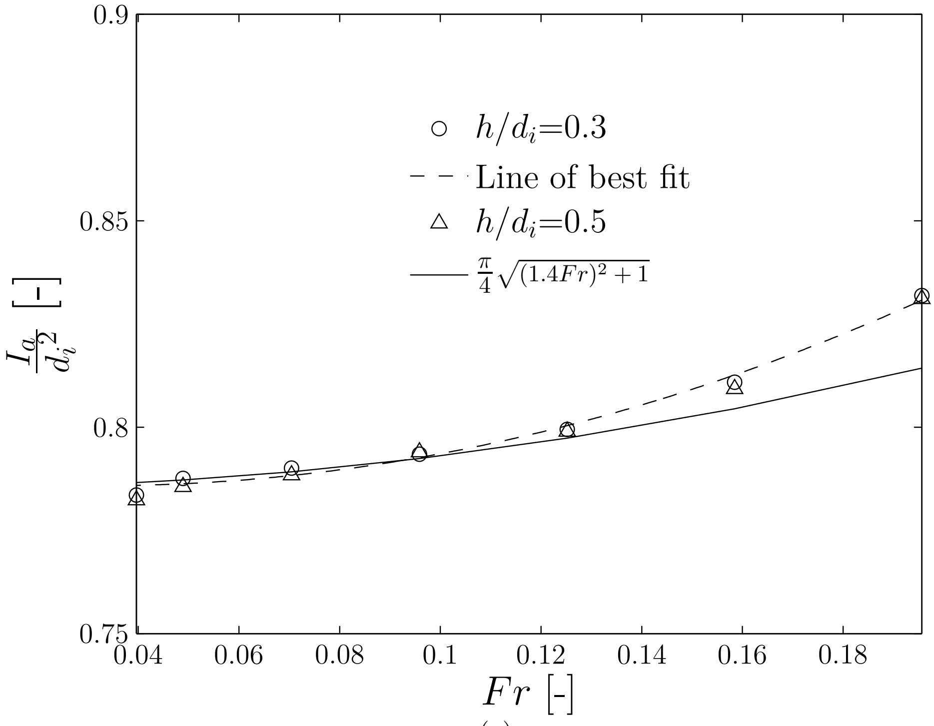

(a)

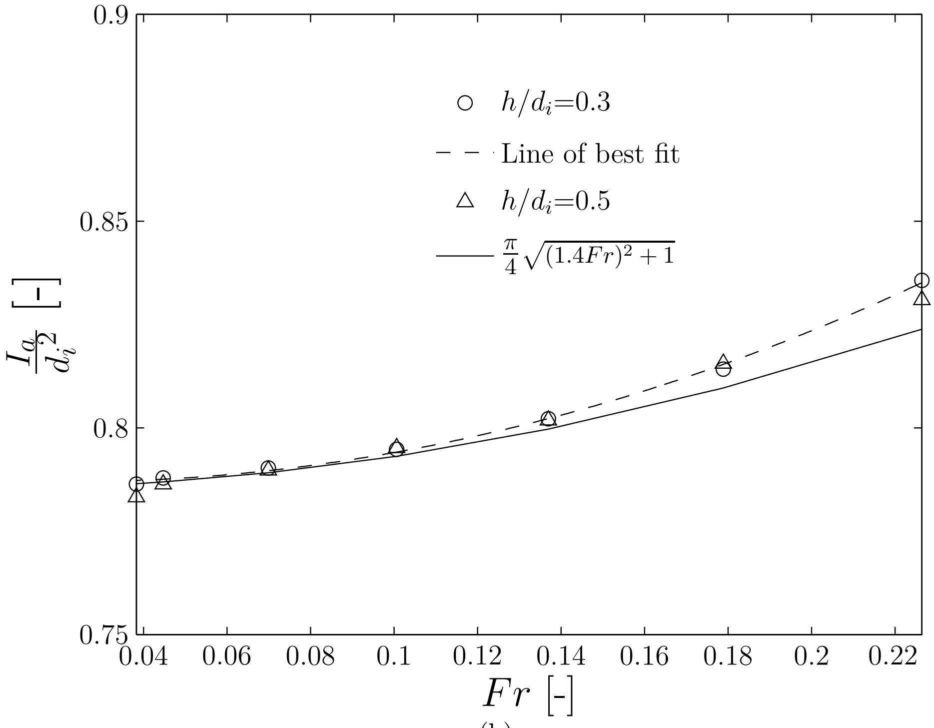

(b)

Figure 4.3: Variation of the non-dimensional interfacial area, I_a, with increasing Fr for two different orbital diameters: (a) d_o/d_i=0.35 (d_o=35 mm and d_i=100 mm); (b) d_o/d_i=0.5 (d_o=50 mm and d_i=100 mm).

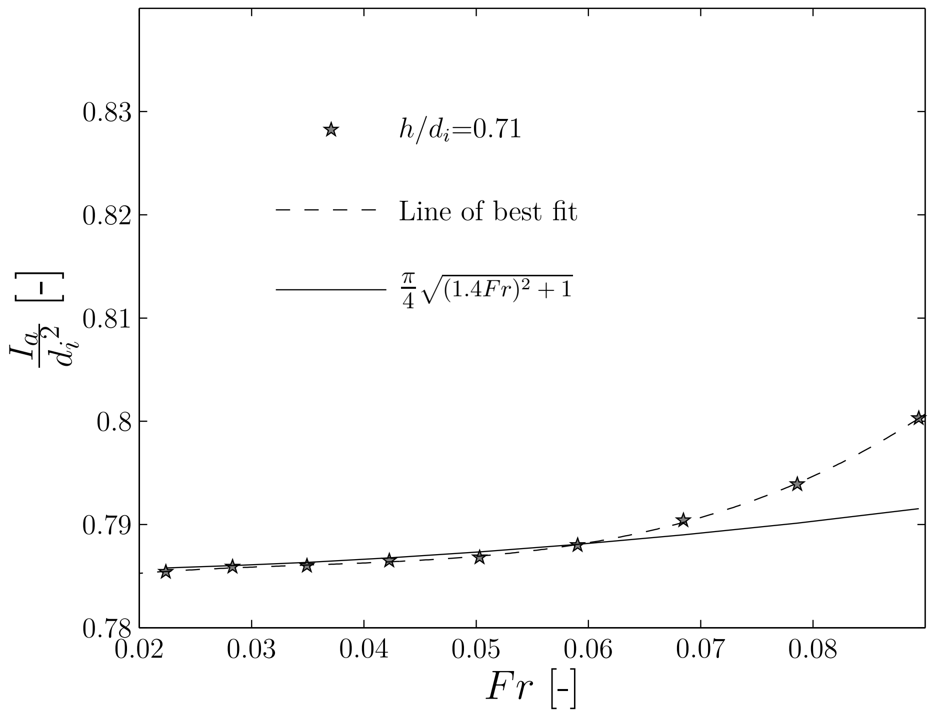

(a)

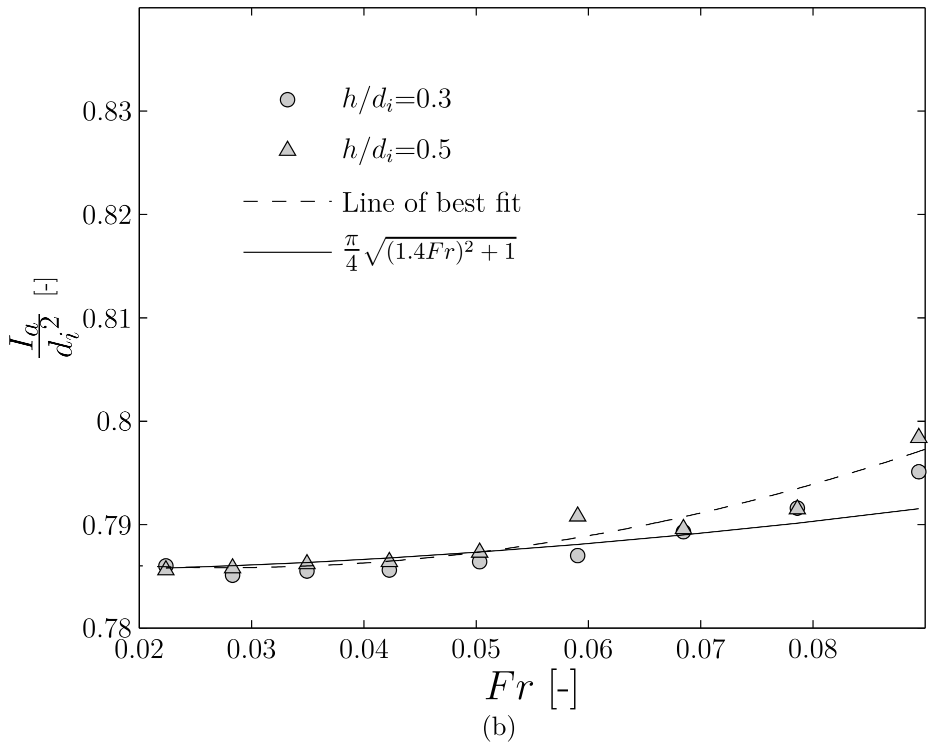

(b)

Figure 4.4: Variation of the non-dimensional interfacial area, I_a, with increasing Fr for two different inner diameters: (a) d_o/d_i=0.36 (d_o=25 mm and d_i=70 mm); (b) d_o/d_i=0.19 (d_o=25 mm and d_i=130 mm).

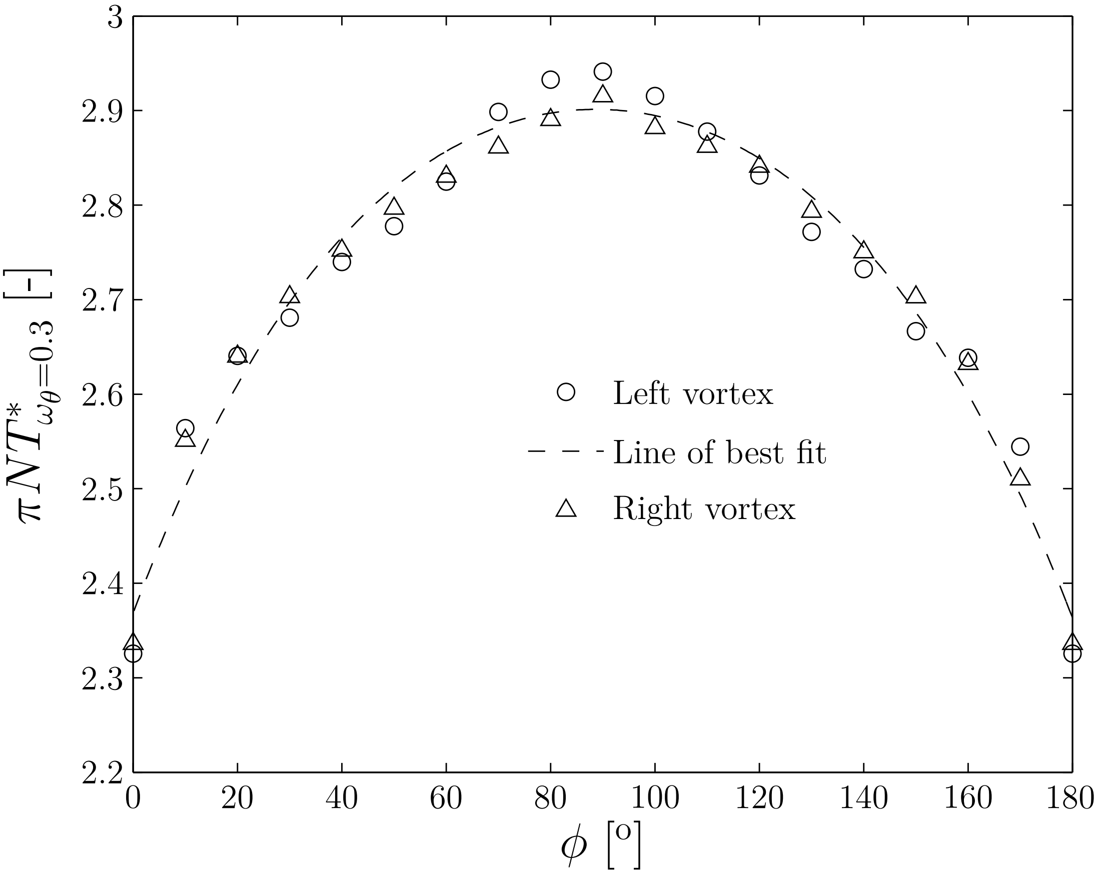

Figure 4.5: Variation of the non-dimensional circulation time, $T^*_{\omega\theta=0.3}$, of the left (○) and right (△) hand side vortices with increasing ϕ, for h/d_i=0.3, Fr=0.11 (N=90 rpm) and d_o/d_i=0.25.

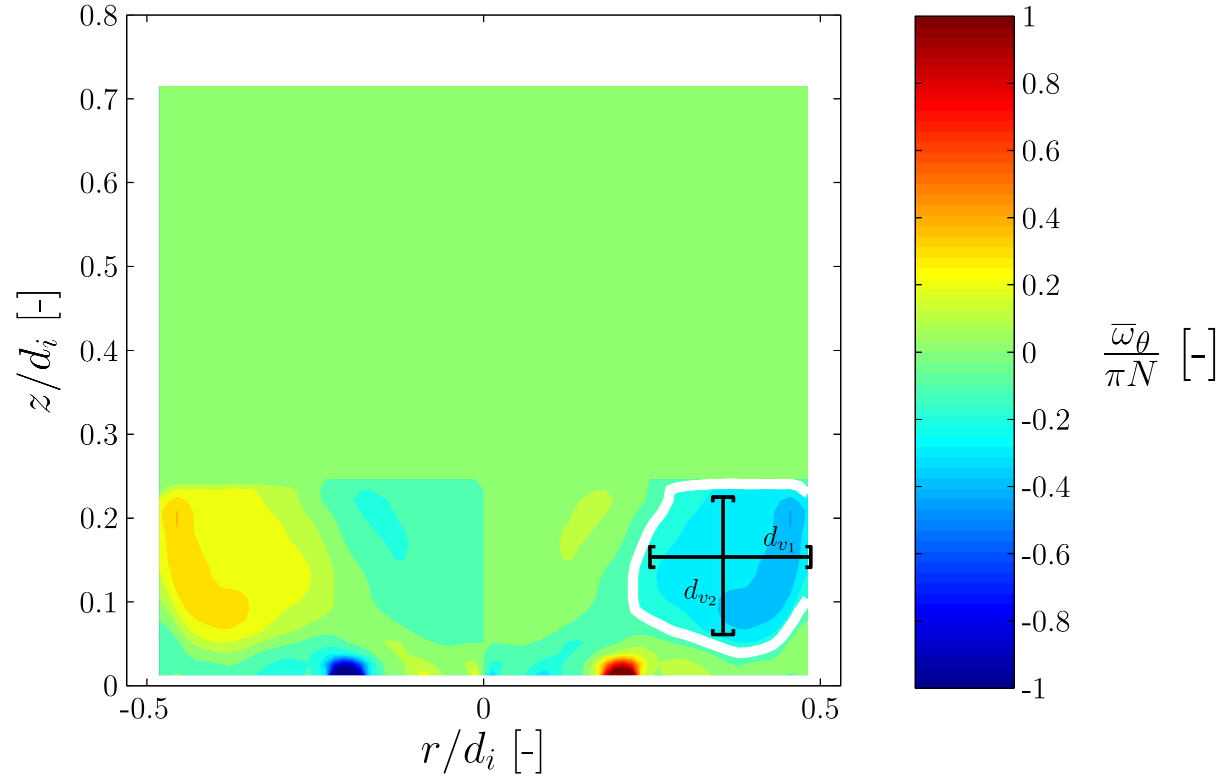

Figure 4.6: Visualisation of the two diameters d_{v_1} and d_{v_2} used to estimated the size of the vortex for the ensemble-averaged measurements.

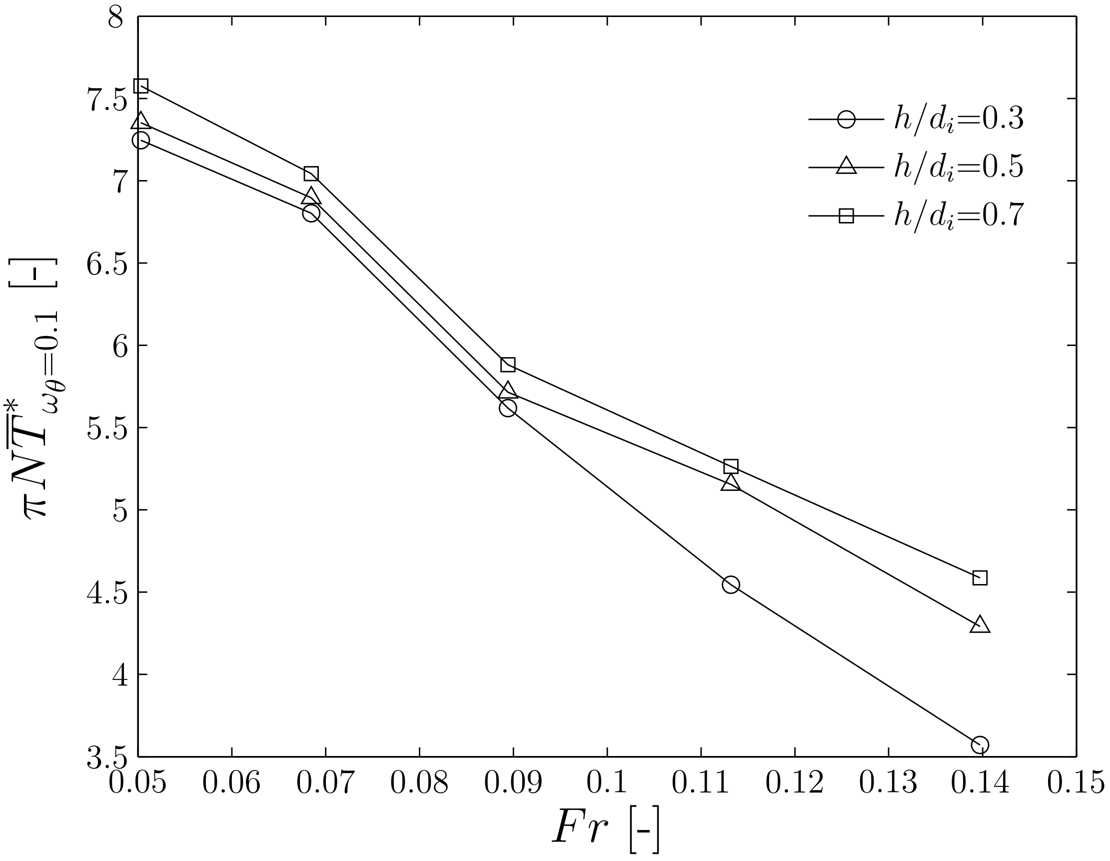

Figure 4.7: Variation of the ensemble-averaged non-dimensional circulation time, $\overline{T}^*_{\omega\theta=0.1}$, with increasing Fr for h/d_i=0.3, 0.5 and 0.7.

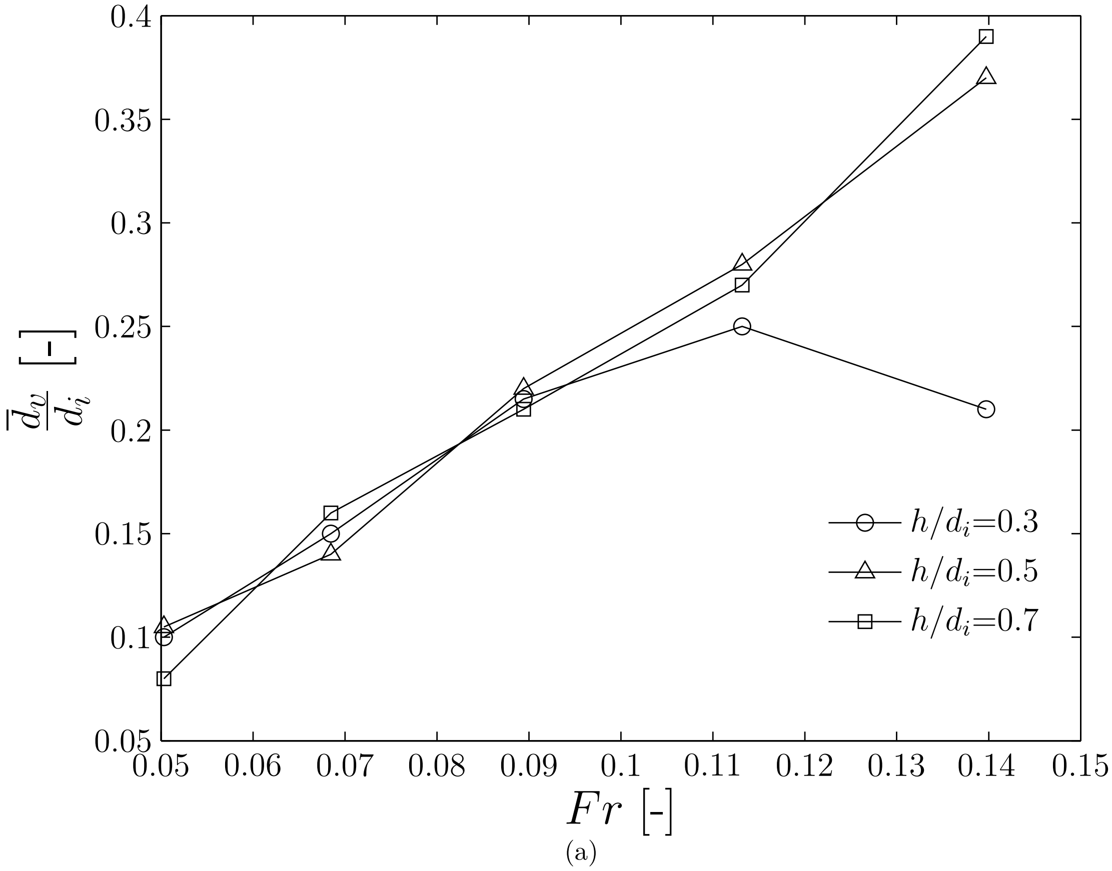

(a)

Figure 4.8: Variation of the non-dimensional mean vortex diameter, $\overline{d}_v$, with increasing Fr for the ensemble-averaged flow fields.

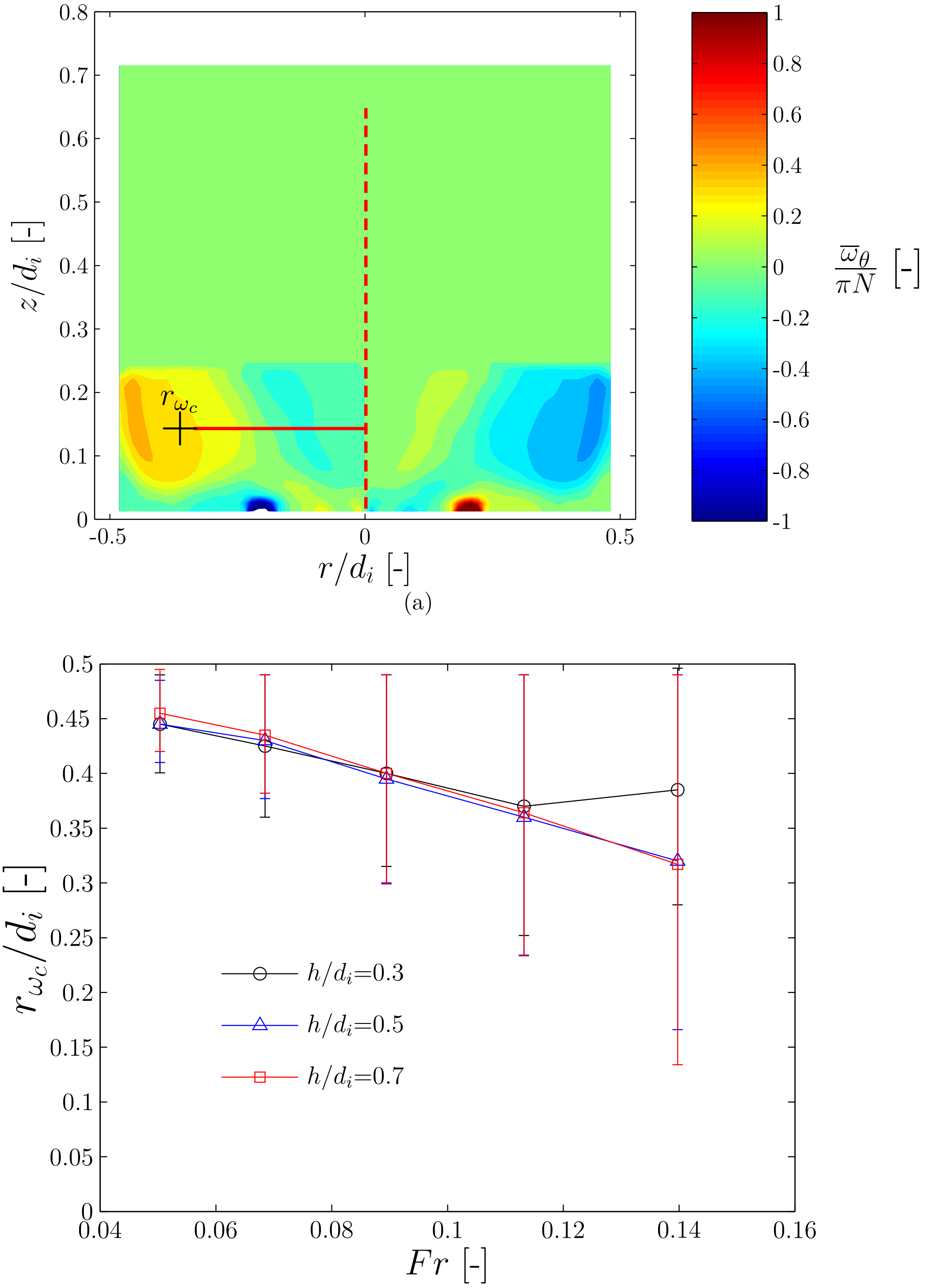

(a)

(b)

Figure 4.9: (a) Visualisation of the radial coordinate of the vortex center, $r_{\omega c}$ (h/d_i=0.3, N=90 rpm and d_o/d_i=0.25); (b) Variation of the non-dimensional vortex centre, $r_{\omega c}$, with increasing Fr.

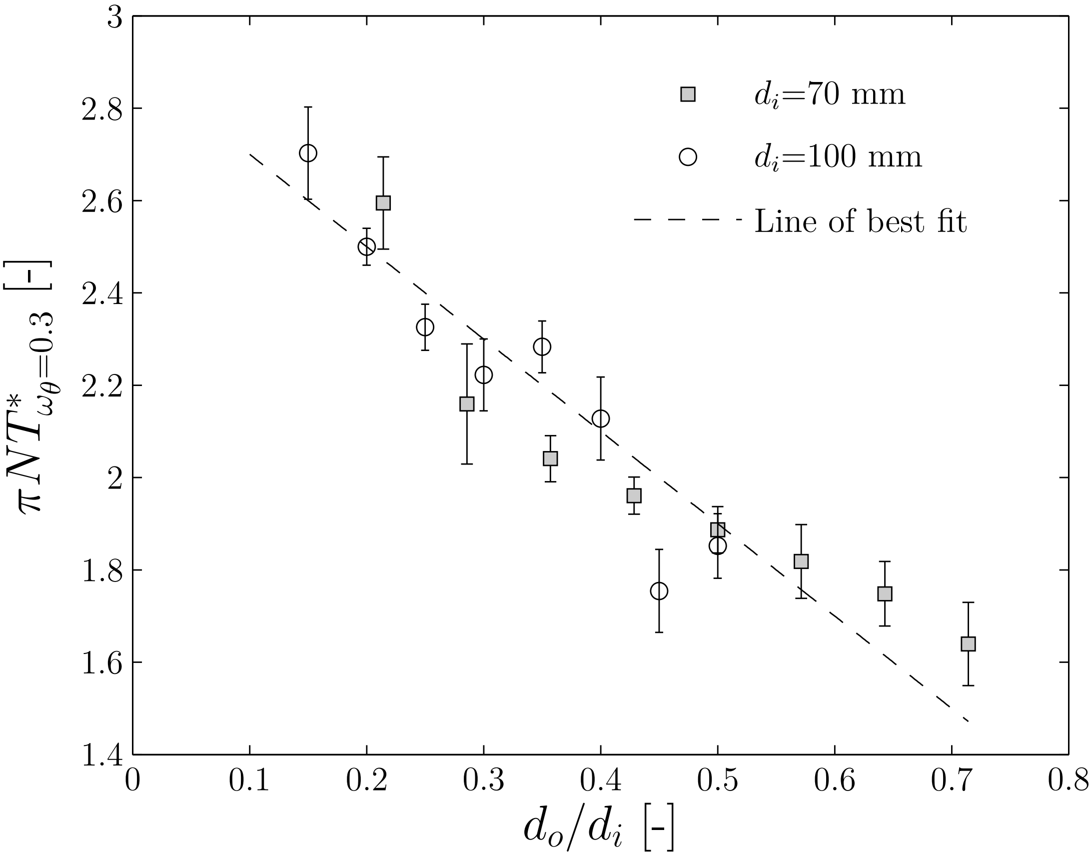

Figure 4.10: Variation of the non-dimensional circulation time, $T^*_{\omega\theta=0.3}$, of the right vortex with increasing d_o/d_i for a flow condition incipient out-of-phase transition (h/d_i=0.3 and ϕ=0°).

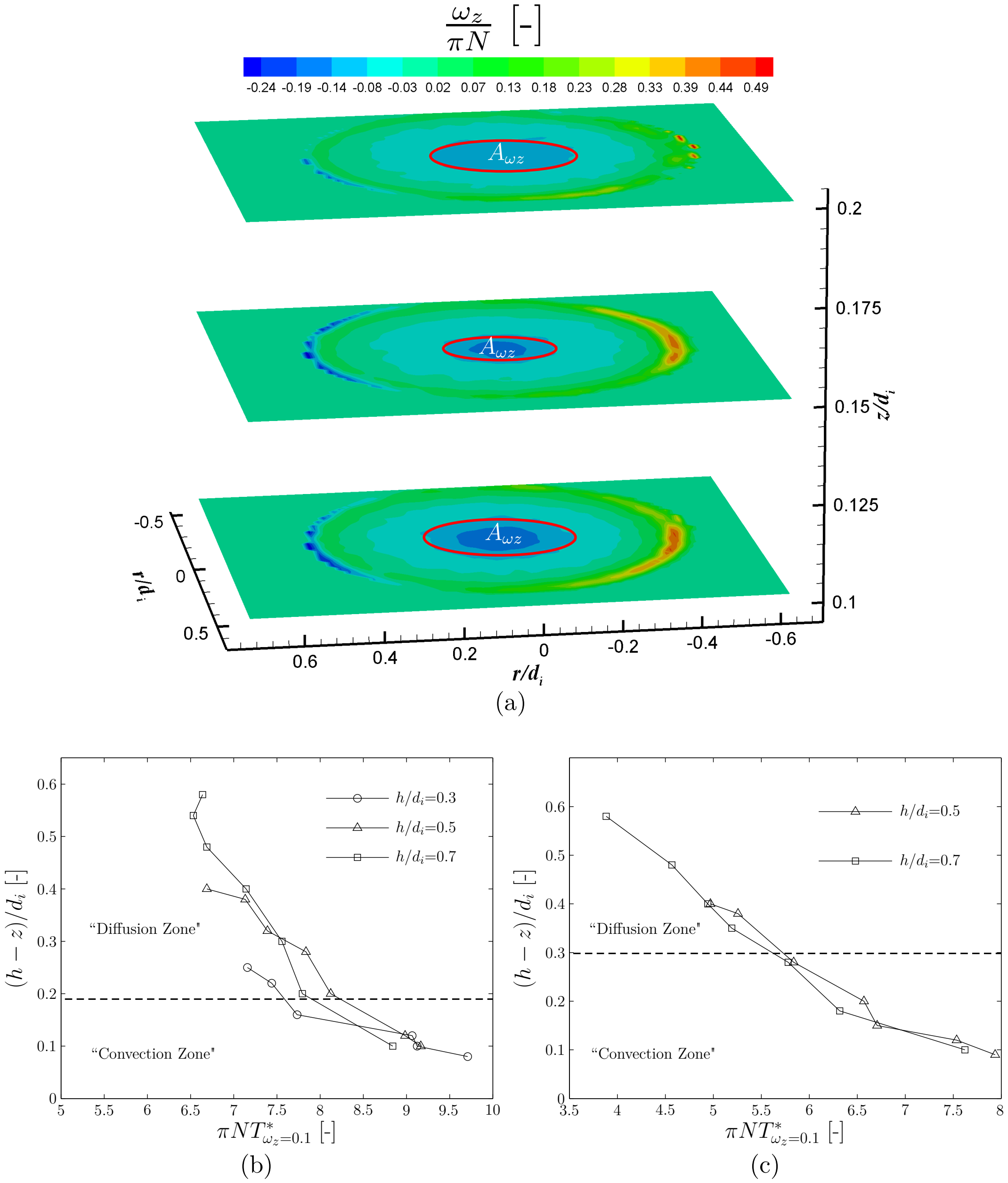

(a)

(b)

(c)

Figure 4.11: (a) Contour plots of the axial vorticity, ω_z, and visualisation of the area, $A_{\omega z}$, used to estimate the circulation time, $T^*_{\omega z=0.1}$, at three non-dimensional elevations z/d_i=0.1, 0.15 and 0.2 (h/d_i=0.3, ϕ=0°, Fr=0.069 and d_o/d_i=0.25); Variation of the space-averaged non-dimensional circulation time, $T^*_{\omega z=0.1}$, against the axial coordinate, $(h-z)/d_i$: (b) Fr=0.069 (N=70 rpm); (c) Fr=0.11 (N=90 rpm).

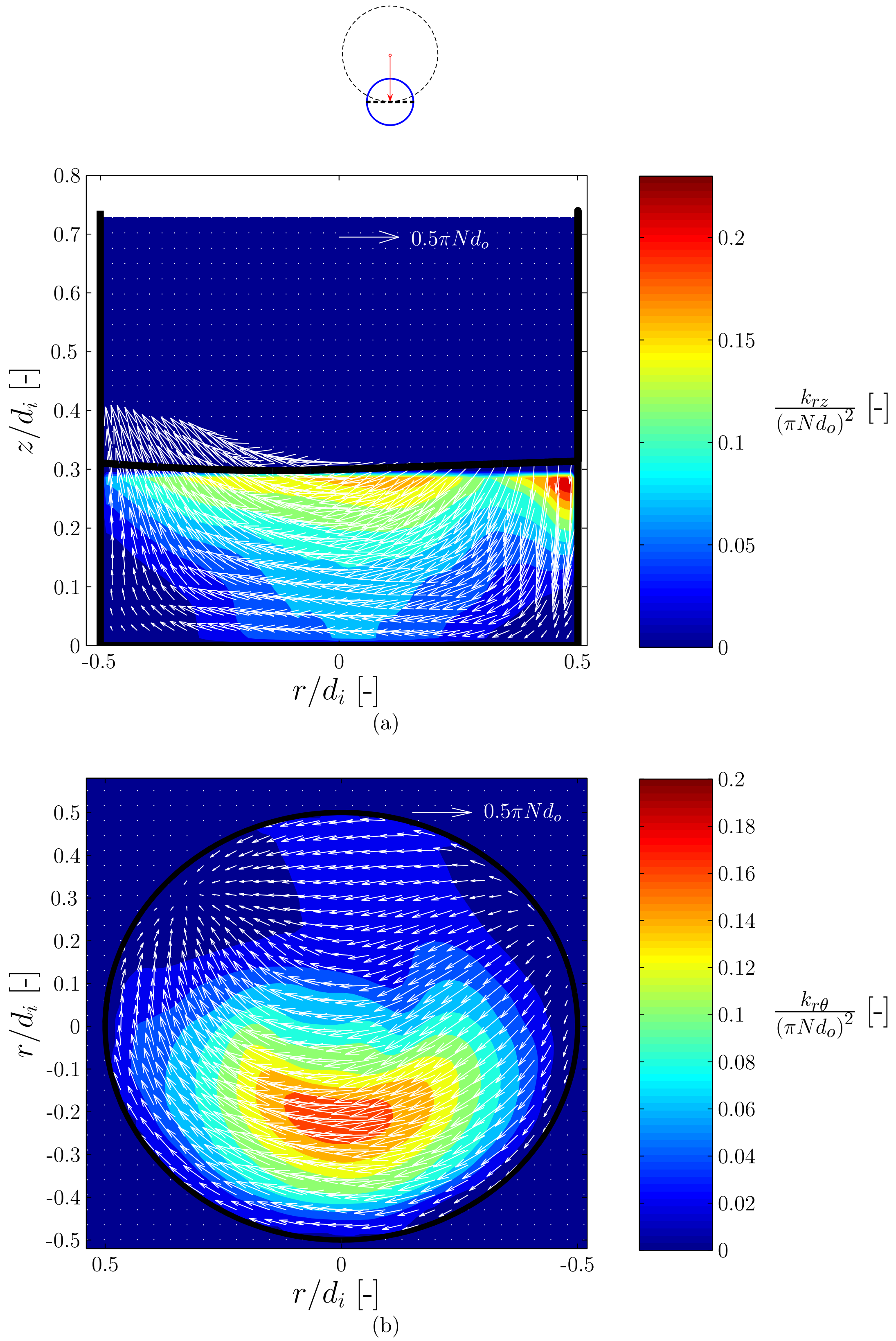

(a)

(b)

Figure 4.12: Phase-resolved velocity vector fields and kinetic energy contour plots for vertical and horizontal planes of measurement (h/d_i=0.3, ϕ=270°, Fr=0.11 and d_o/d_i=0.25): (a) Vertical plane; (b) Horizontal plane, z/d_i=0.08.

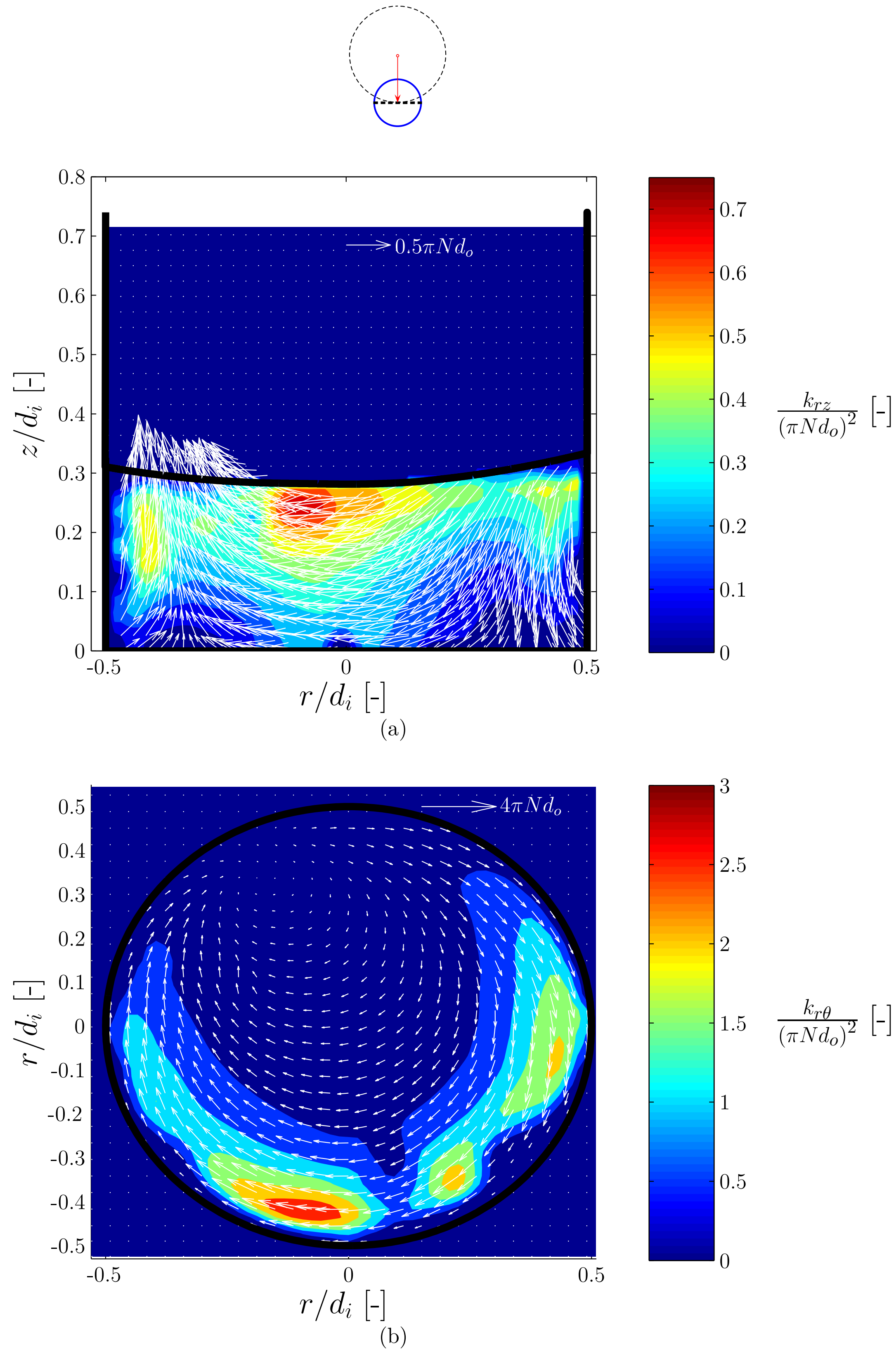

Figure 4.13: Phase-resolved velocity vector fields and kinetic energy contour plots for vertical and horizontal planes of measurement (h/d_i=0.3, ϕ=270°, Fr=0.24 and d_o/d_i=0.25): (a) Vertical plane; (b) Horizontal plane, z/d_i=0.08.

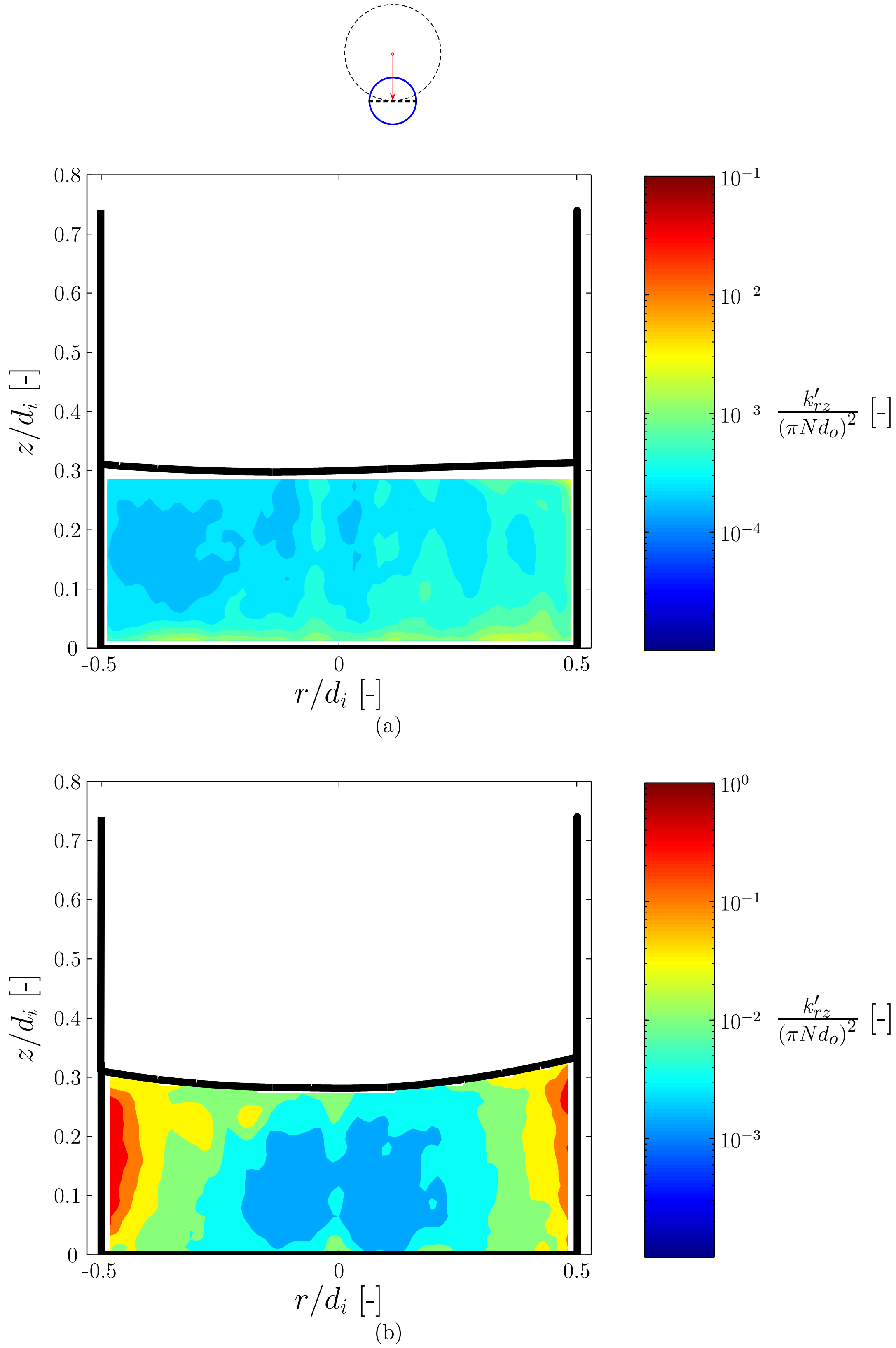

(a)

(b)

Figure 4.14: Phase-resolved contour plots of the kinetic energy due to random velocity fluctuations (h/d_i=0.3, ϕ=270° and d_o/d_i=0.25): (a) Fr=0.11 (N=90 rpm); (b) Fr=0.24 (N=130 rpm).

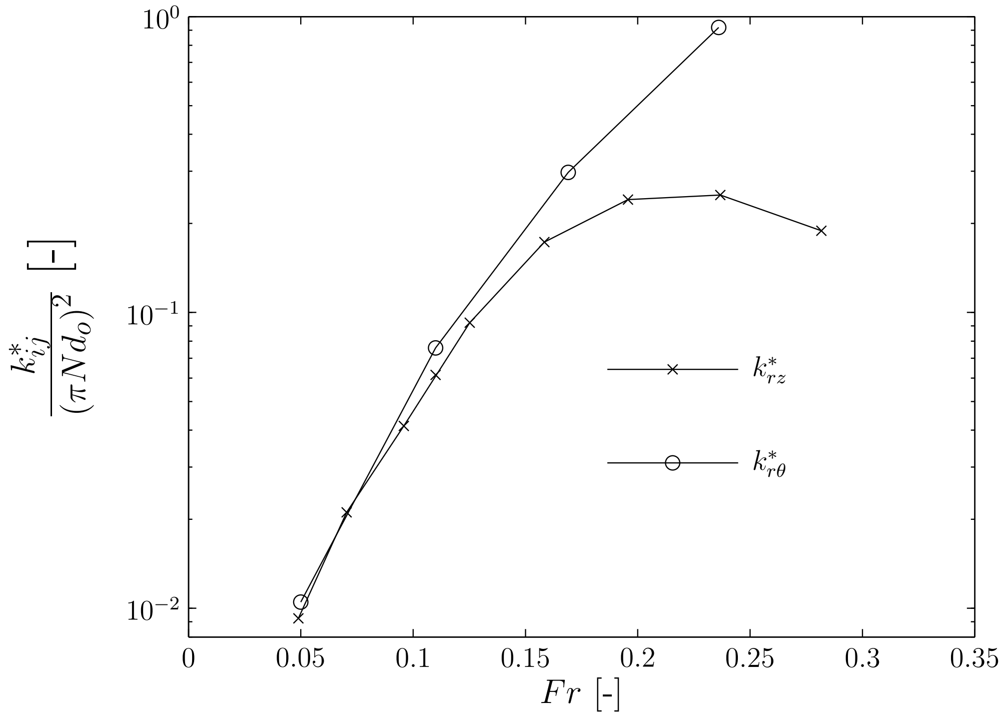

(a)

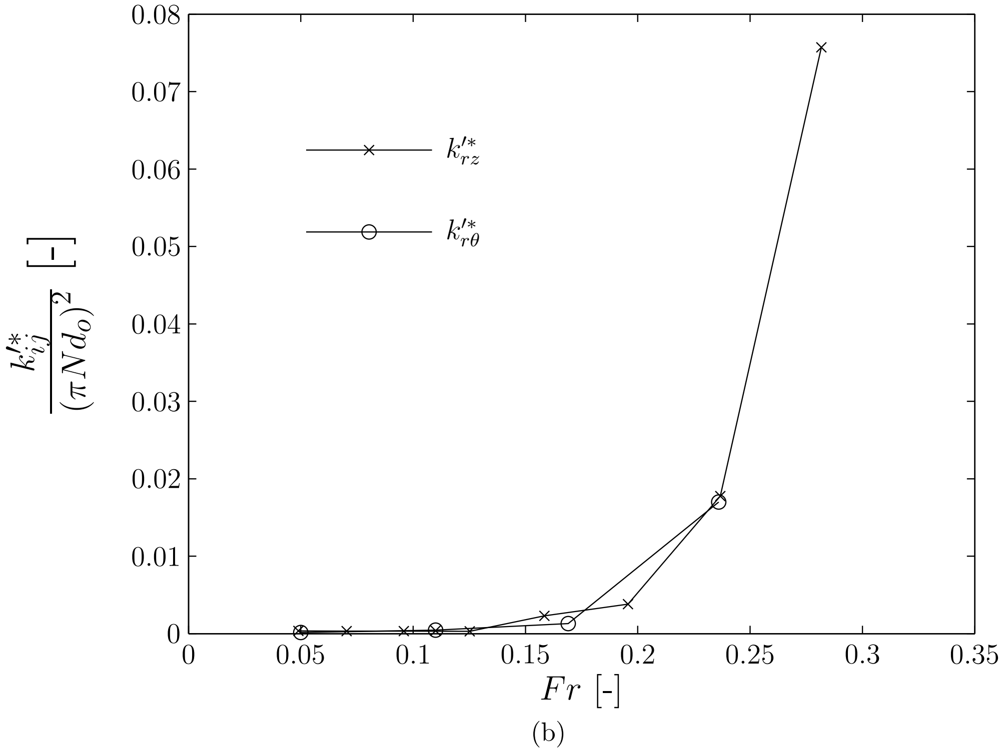

(b)

Figure 4.15: Variation of the space-averaged kinetic energy with Fr number (h/d_i=0.3, ϕ= 270° and d_o/d_i=0.25): (a) Kinetic energy of the periodic mean flow, k^*_{rz} and $k^*_{r\theta}$; (b) Kinetic energy of the random velocity fluctuations, k'^*_{rz} and $k'^*_{r\theta}$.

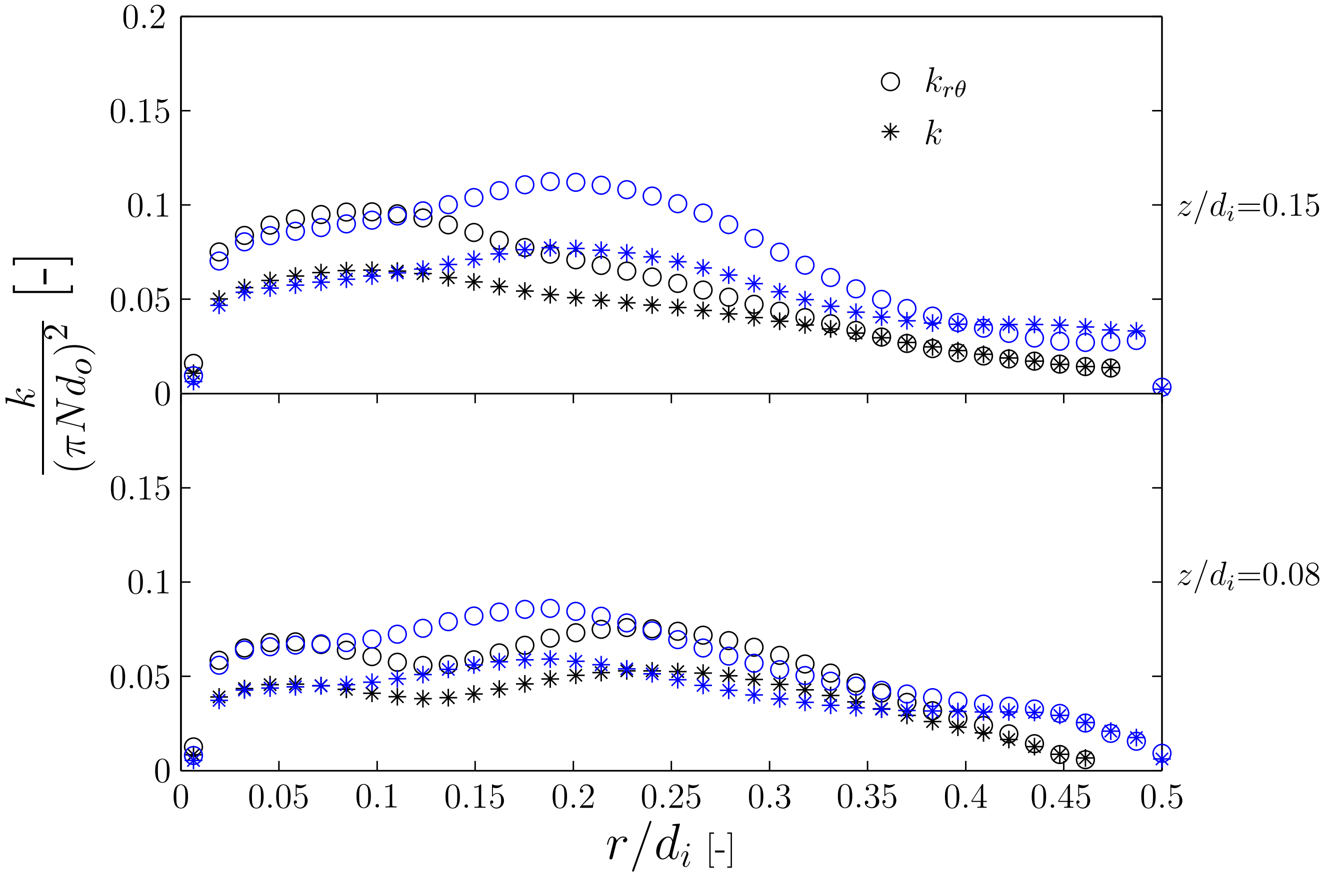

Figure 4.16: Comparison of the radial profiles of kinetic energy obtained from all the three velocity components, k, and from a 2D approximation taking into account only velocity components on the horizontal plane of measurement, $k_{r\theta}$, for h/d_i=0.3, ϕ= 270°, Fr=0.11 (N=90 rpm) and d_o/d_i=0.25.

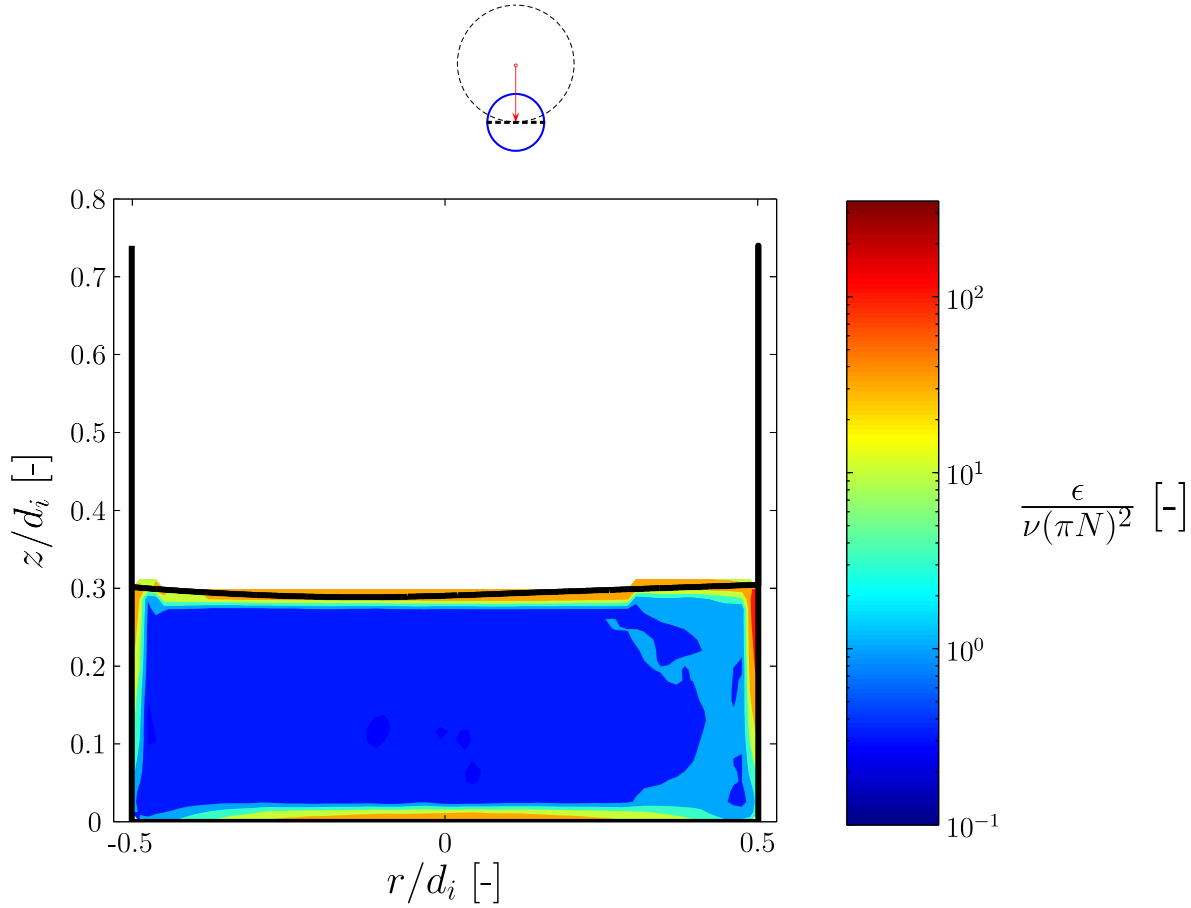

(a)

Figure 4.17: Contour plot of the viscous dissipation rate of kinetic energy, ϵ, for ϕ=270°, Fr=0.11, h/d_i=0.3, and d_o/d_i=0.25.

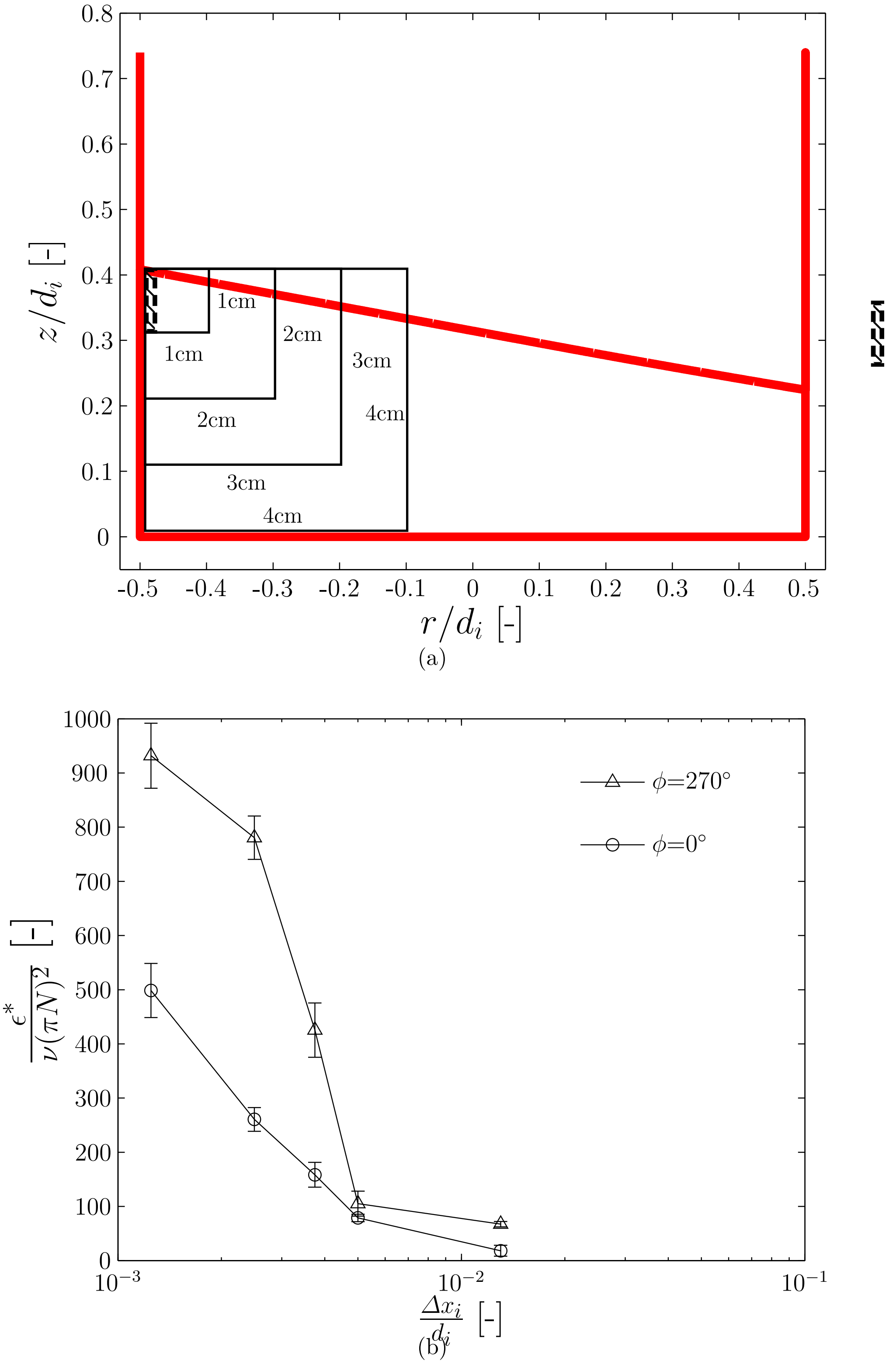

(a)

(b)

Figure 4.18: (a) Schematic diagram showing the five interrogation windows employed, and the shaded region used to estimate ϵ^*; (b) Variation of ϵ^* with decreasing spatial resolution, Δx_i, for h/d_i=0.3, d_o/d_i=0.25 and Fr=0.11 (N=90 rpm).

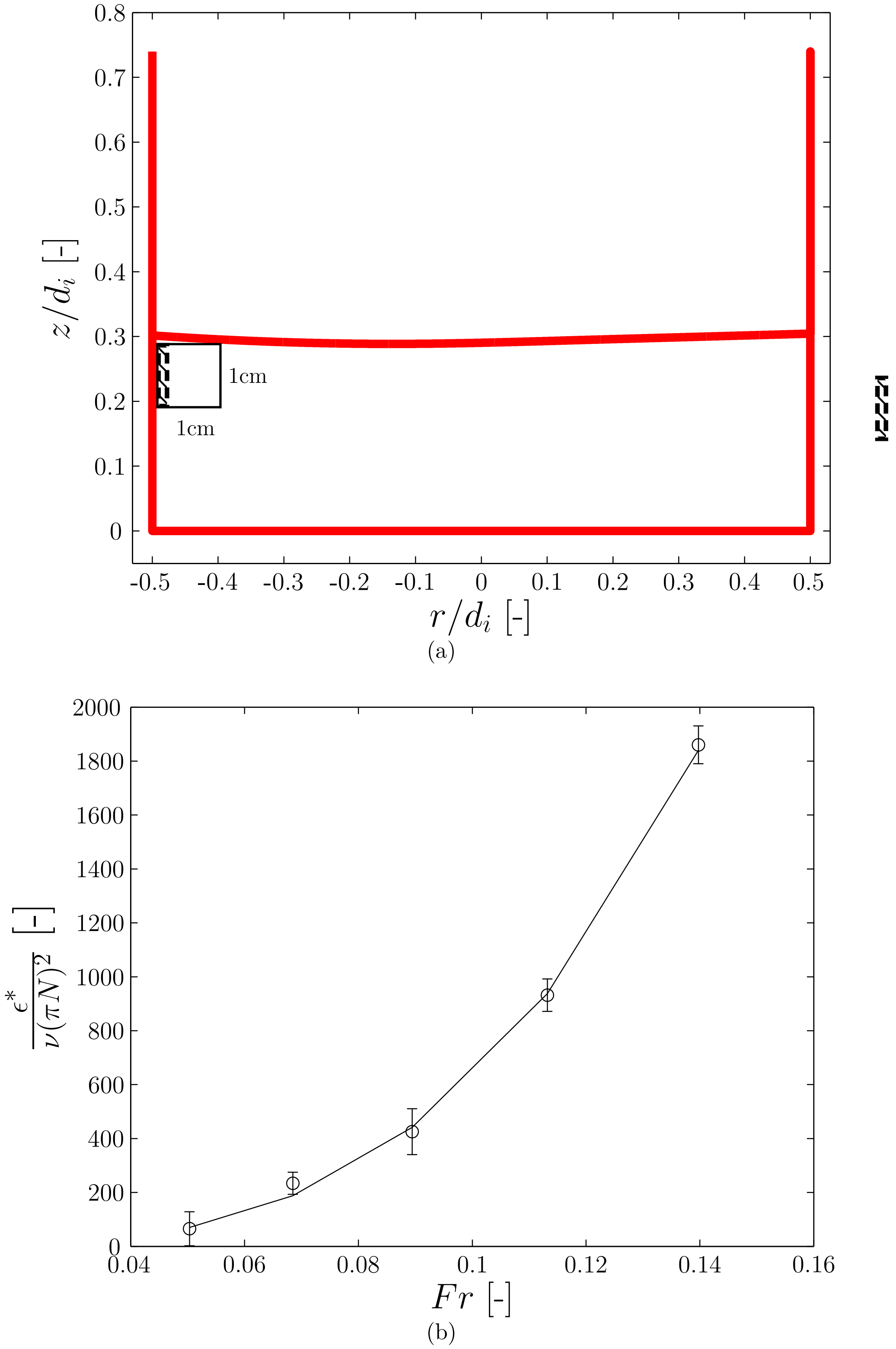

Figure 4.19: (a) Schematic diagram showing the shaded region used to estimate ϵ^*, when the analysis was carried out for increasing Fr (fixed spatial resolution, $\frac{\Delta x}{d_i}$=1.2×10^{-3}); (b) Variation of ϵ^* with increasing Fr for h/d_i=0.3, ϕ=270° and d_o/d_i=0.25.

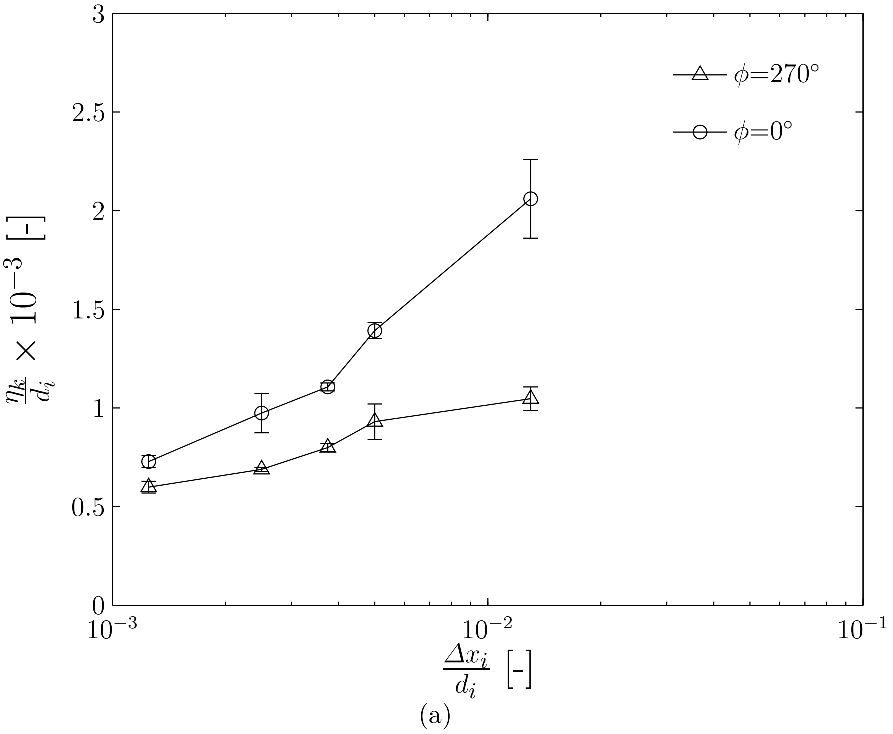

(a)

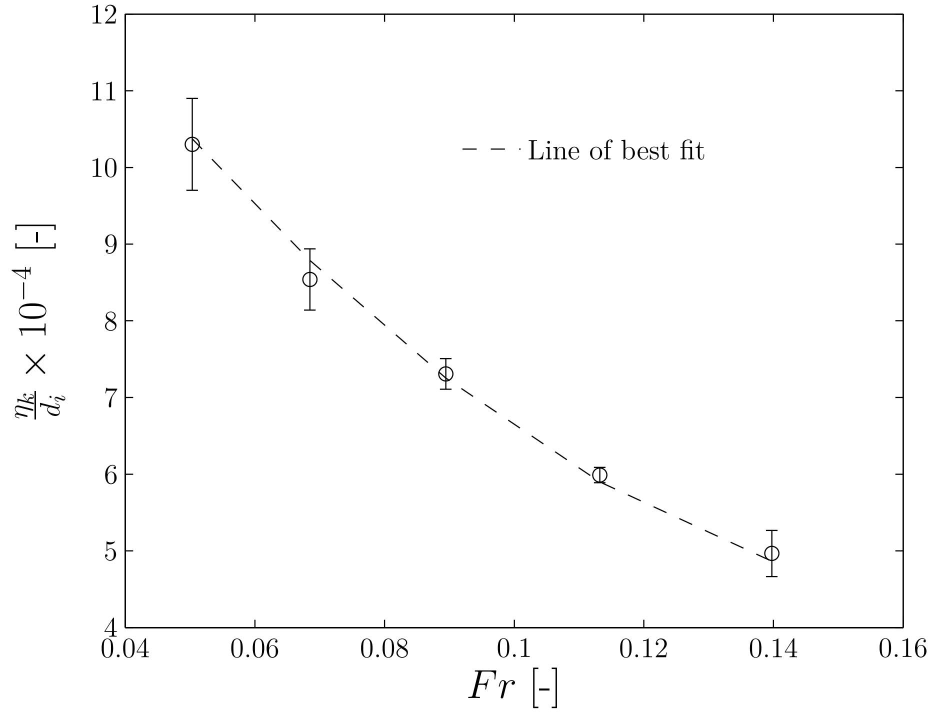

(b)

Figure 4.20: Variation of η_k with spatial resolution, (a), and increasing Fr, (b) (h/d_i=0.3, ϕ=270°, d_o/d_i=0.25).

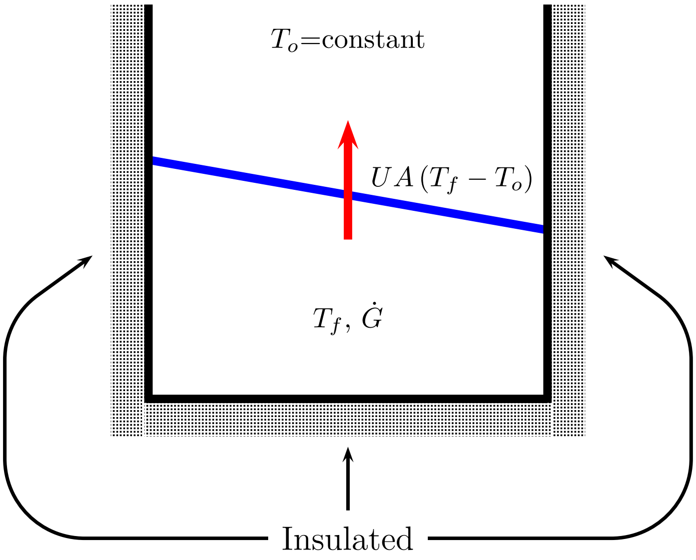

Figure 4.21: Schematic diagram visualising the heat transfer process and temperature boundary conditions within the insulated vessel.

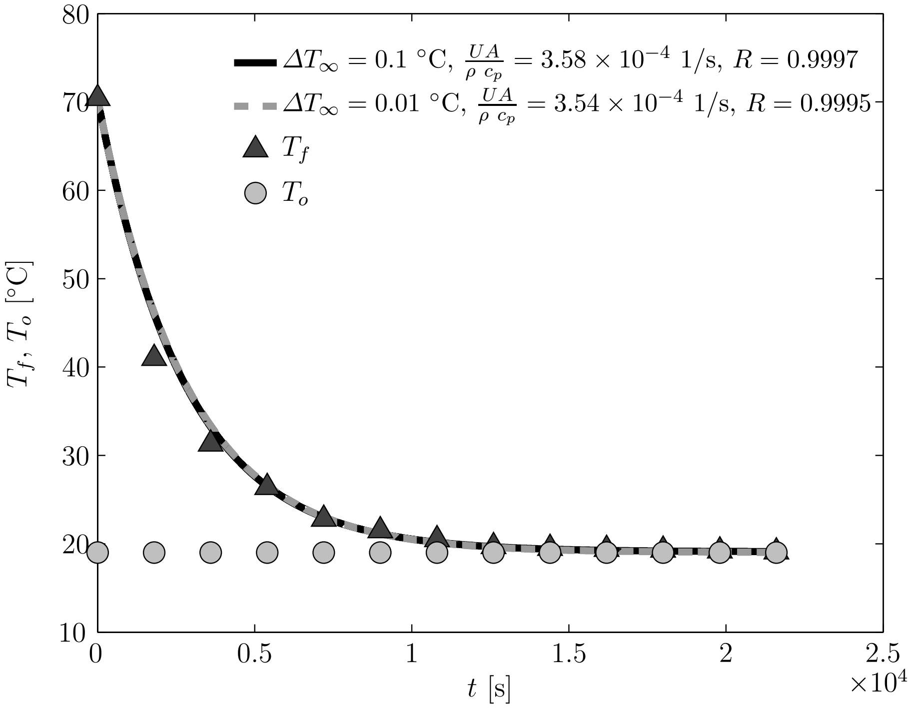

(a)

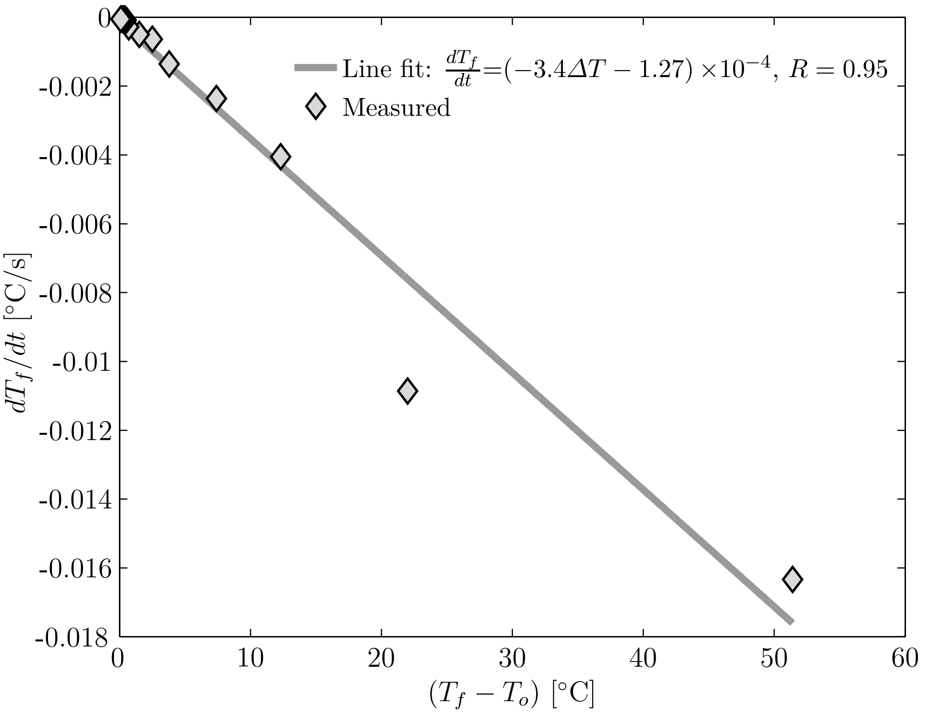

(b)

Figure 4.22: (a) Variation with time of the measured temperature of the fluid inside the bioreactor, T_f, of the surroundings, T_o, and of exponential models for ΔT_∞=0.01 °C and 0.1 °C; (b) Variation of the cooling rate of the fluid inside the bioreactor against the temperature difference between the fluid and the surroundings, $T_f - T_o$ (h/d_i=0.3, Fr=0.11 and d_o/d_i=0.25).

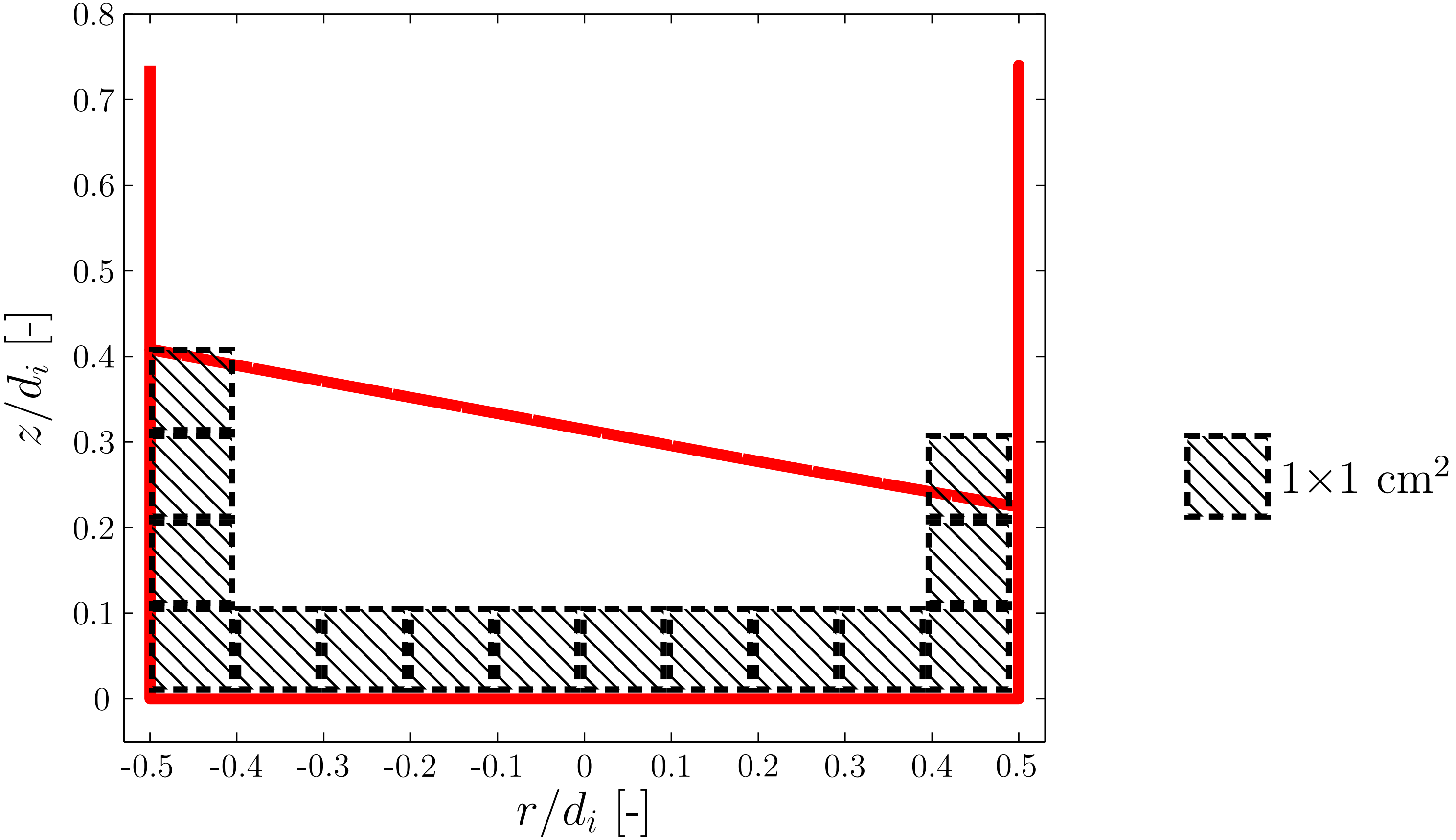

Figure 4.23: Visualisation of the interrogation areas used to integrate ϵ and determine the volumetric power consumption, P_v.

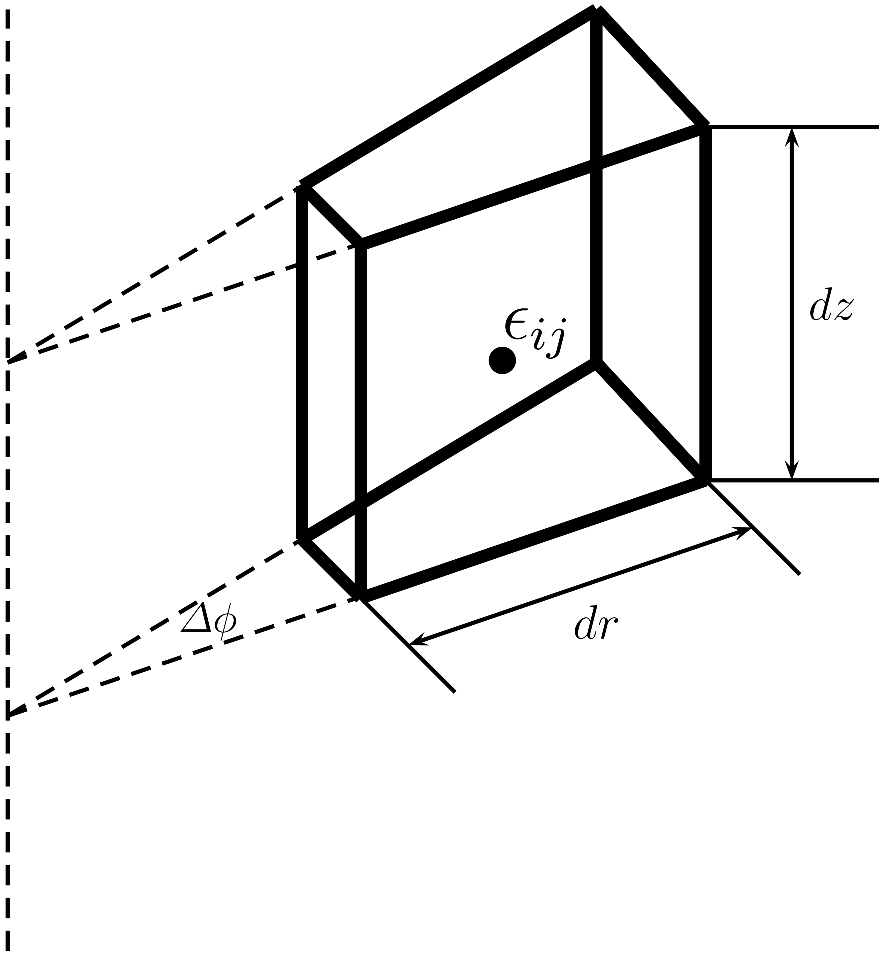

Figure 4.24: Schematic of the trapezoidal integration volume.

Chapter 5

Characterisation of the flow in a shaken cylindrical bioreactor for high viscosity fluids[†]

5.1 Introduction

The majority of the studies available in the literature, that aimed at an engineering characterisation of the flow in shaken bioreactors, have mainly been carried out with fluids of water-like viscosity (see for example, Büchs *et al.*, 2000b; Maier *et al.*, 2004; Micheletti *et al.*, 2006; Zhang *et al.*, 2008). This type of fluid is closer to the culture media most commonly used for growth of mammalian and microbial cells. However, caution should be exerted when micro-organisms characterised by a filamentous morphology are considered. In this case the viscosity of the fermentation broth increases with fermentation time due to the formation of biomass (Peter *et al.*, 2004). Büchs *et al.* (2000a) report that this viscosity

---

[†] Some of the results presented in this chapter are included in:

Weheliye, W., Rodriguez, G., Anderlei, T., Micheletti, M., Yianneskis, M. and Ducci, A., "Appraisal of shaken bioreactor mixing efficiency for different operating conditions", *Proceedings of the 14th European conference on mixing*, Warsaw, Poland, 2012.

increase over fermentation time will promote “out of phase” conditions with a significant reduction of oxygen transfer and mixing intensity, and altered cell metabolism. In a such a case the whole screening process would unintentionally suffer from inadequate substrate supply to the cells, and would fail to identify improved strains and media. From this perspective the study of Büchs *et al.* (2000a) investigated the power consumption of newtonian fluids with dynamic viscosity up to μ=200 Pa s (cf. water, μ=1 mPa s), while the simulations of Kim and Kizito (2009) provided a visual analysis of the time averaged velocity flow fields for $1\times10^{-6} \leq \nu \leq 1.6\times10^{-5}$ m^2/s.

This chapter provides a description of the flow dynamics in a cylindrical shaken bioreactor for fluids of increasing viscosity, ν. In Section 5.2 the variation with ν of the constant of proportionality between the inclination of the free surface and the Froude number, Fr, is discussed, whilst in the latter part of Section 5.2 the flow scaling law determined for water is extended to Newtonian fluids of higher viscosity. The characteristic flow fields of in-phase and out-of-phase conditions associated to highly viscous fluids are analysed in Sections 5.3 and 5.4, respectively. A flow transition map based on the Froude number, Fr, and Reynolds number, Re, is provided in Section 5.5, and four main map regions, characterised by different mean flow dynamics, are identified. Furthermore, the turbulent kinetic energy levels and shear rate magnitudes are assessed in this section for different combinations of Fr and Re.

5.2 Variation of free surface inclination with viscosity and extension of the flow scaling law

In Chapter 3 a linear relationship was found between the inclination of the free surface and the Froude number when the working fluid was water, and this relationship was used to derive the flow scaling law of Equations 3.6 and 3.8. A similar analysis is carried out in this section to assess how the inclination of the free surface, which is the flow driving mechanism, is affected by the viscosity of the fluid. For this study either silicon oils or different percentage mixtures of glycerine and water were employed. Three different fluid viscosities are considered in Figures 5.1 (a-c), with the free surface inclination being measured at ϕ=0°, when the bioreactor occupies its position further to the left when the orbital motion is seen from above, and for a combination of orbital to cylinder diameter ratio and non-dimensional fluid height of d_o/d_i=0.25, h/d_i=0.5, respectively. It should be noted that for the data set associated to ν=4.97×10^{-5} two additional combinations of d_o/d_i and h/d_i are considered (cf. Figure 5.1 b).

The current results are consistent with those obtained when water was the working fluid, with the data being characterised by a linear relationship between the wave height of the free surface, $\varDelta h$, and the Froude number, Fr. The constant of proportionality a_o decreases with increasing viscosity, and its value is equal to 1.38, 1.27 and 1.23 for the three viscosity considered in Figures 5.1 (a), (b) and (c), respectively. This behaviour is expected, as the inertial forces responsible to push the fluid against the cylinder side wall are counterbalanced to a greater extent by the viscous forces generated by fluids of higher viscosity. From Figure 5.1 (b) the angle of inclination of the free surface is independent of the non-dimensional fluid height, h/d_i, and is constant for a given Froude number, Fr. This implies that the maximum inclination of the free surface is not affected by the amount of fluid volume as long as the ratio between the centrifugal and gravitational accelerations is constant. It should be noted that the range of Fr considered in Figures 5.1 (a-b) is lower than that examined in Figure 3.18 (a-b) (i.e. 0.025$\leq Fr \leq$ 0.3), and therefore all the flow conditions selected for this analysis can be considered in the “in-phase regime”, indicating that the shape of the free surface can be approximated to an inclined elliptic disk.

The variation of the constant of proportionality, a_o, of the free surface inclination with working fluid to water viscosity ratio, ν/ν_w, is shown in Figure 5.2. These results show a steep variation of a_o at low viscosity ratio, with a 6 % reduction of the constant of proportionality for a tenfold increase in fluid viscosity, while a further 7 % reduction occurs over a wider range of $\nu/\nu_w = 10 - 180$, with a minimum value of a_o=1.225 at ν=1.8 × 10^{-4} m^2/s. The power law variation of a_o with ν/ν_w can be utilised to extend the applicability of the scaling law reported in Chapter 3 for water to fluids of higher viscosity, ν. In this case the scaling law can be rewritten according to Equation 5.1.

$$\frac{\Delta h}{h} = a_{ow} \left(\frac{\nu}{\nu_w}\right)^{-0.0256} \frac{d_i}{h} Fr \tag{5.1}$$

The effect of viscosity, ν, on the flow pattern is given in Figures 5.3 (a-d), where characteristic vorticity contour plots and velocity vector fields are shown for ν=1.7×10^{-6} m^2s^{-1}, 3.2 ×10^{-6} m^2s^{-1}, 5.2×10^{-6} m^2s^{-1} and 9×10^{-6} m^2s^{-1}, respectively. To facilitate comparison with the data acquired for water all plots of Figures 5.3 (a-d) were obtained for analogous operating conditions of those of Figure 3.1 (a), with a combinations of non-dimensional fluid height and orbital to cylinder diameter ratio of $h/d_i = 0.3$ and $d_o/d_i = 0.25$, respectively, while the shaking speed was set to N=90 rpm (Fr=0.11), which was found to be the critical flow transition speed for water at this fluid height and orbital diameter (see Chapter 3). When a fluid viscosity of ν=1.7×10^{-6} m^2s^{-1} is considered (cf. Figure 5.3, a), the flow pattern is very similar to that already exhibited by water, with the two characteristic counter-rotating vortices extending towards the bottom of the tank. It should be noted that according to Equation 5.1 the flow in the bioreactor should be relatively close to flow transition at this speed and viscosity.

When the viscosity is increased to ν=3.2×10^{-6} m^{2}s^{-1} the counter-rotating vortex configuration cannot be observed anymore and a different flow field is present, with the formation of a vortex region next to the right wall, below the lowest edge of the free surface, which is characterised by a vorticity of opposite direction to that experienced with water-like viscous fluids (cf. Figure 5.3 b). This vortical structure builds up when the viscosity is further increased to ν=5.2×10^{-6} m^{2}s^{-1} and 9×10^{-6} m^{2}s^{-1}, in Figures 5.3 (c) and (d), respectively. For these two conditions the vortex to the right hand side extends towards the centre of the tank with a maximum non-dimensional vorticity of $\frac{\omega_{\theta max}}{\pi N}$=0.8, while a less intense vorticity region also emanates from the bottom of the bioreactor. It should be noted that all the flow fields shown in Figures 5.3 (a-d) are characterised by a smooth inclined elliptic free surface shape, indicating that the flow is in-phase, with the maximum fluid height occurring in the vertical plane of measurement when the bioreactor is in the position further to the left (ϕ=0°).

As mentioned before the current experiments indicate that the toroidal vortex structure occurs only up to a viscosity of 1.7×10^{-6} m^{2}s^{-1}, and in this case Equation 5.1 should be used to determine the shaking speed associated to the in-phase to out-phase flow transition. To ensure the validity of this flow scaling law two additional configurations, complementing that shown in Figure 5.3 (a), were obtained for combinations of h/d_i=0.3, d_o/d_i=0.5 and h/d_i=0.5, d_o/d_i=0.5, and the corresponding flow fields are represented in Figures 5.4 (a) and (b), respectively. In both cases a toroidal vortex extending over the entire fluid height is in evidence, and the shaking speeds predicted from Equation 5.1 for these two configurations, N=74.1 rpm and 95.7 rpm, are in good agreement with those, 75 rpm and 95 rpm, used for the experiments of Figures 5.4 (a) and (b). It can be concluded from this section that the extended flow scaling law of Equation 5.1, which identifies the flow transition from a toroidal to a whirlpool-like type of vortex, should be applied to fluids with $\nu \leq 1.7 \times 10^{-6}$ m^{2}s^{-1}, as such vortical structures do not occur anymore when working fluids of higher viscosity are used.

5.3 In-phase flow for different operating conditions with highly viscous fluids

Based on the considerations made in the previous section a distinction has to be made between fluids of viscosity $\nu \leq 1.7 \times 10^{-6}$ m^{2}s^{-1} and $\nu > 1.7 \times 10^{-6}$ m^{2}s^{-1}, with the first range of fluids exhibiting the toroidal vortex flow pattern encountered when water is the working fluid and thoroughly discussed in Chapters 3 and 4, while the second range of viscosity still shows an inclined free surface of elliptic shape, which is synchronised with the bioreactor position along the circular orbit, but its flow dynamics are considerably different to those observed for water. As a consequence this section aims at elucidating the flow obtained for in phase conditions when the viscosity is $\nu > 1.7 \times 10^{-6}$ m^{2}s^{-1}. Flow field measurements of vertical and horizontal planes were obtained for two silicon oils with viscosity, $\nu = 1 \times 10^{-5}$ m^{2}s^{-1} and 1×10^{-4} m^{2}s^{-1}.

To best compare with water data sets the reference configuration with operating conditions of $h/d_i = 0.3$ and $d_o/d_i = 0.25$ is considered in Figures 5.5 (a) and (b), where the phase-resolved velocity vector fields and contour plots of the tangential component of the vorticity, ω_θ, are represented for $\nu = 1 \times 10^{-5}$ m^{2}s^{-1} and two different shaking frequencies, N=80 rpm and N=90 rpm, respectively. The current experiments are consistent with those already discussed in Figures 5.3 (b-d) for a different set of viscosity, where a counter-clockwise rotating vortex can be clearly distinguished at the right cylinder wall, while a region of lower vorticity intensity is present closer to the bottom of the bioreactor. As the shaking speed is increased the intensity of this vortex also increases, and the contour region denoted by maximum vorticity becomes larger. The flow structures and vorticity contours shown in Figures 5.5 (a-b) are in good agreement with those outlined by the simulations of Kim and Kizito (2009), who also estimated the instantaneous flow field for ν=1×10^{-5} m^{2}s^{-1}.

The variation of the bioreactor flow dynamics with increasing viscosity can be clearly seen in Figures 5.6 (a) and (b), where the vector fields for ν=1×10^{-4} m^{2}s^{-1} are shown for N=70 rpm and 80 rpm, respectively. It is interesting to point out that for both the speeds considered the right hand side vortex has extended towards the centre of the bioreactor, and has merged with the positive vorticity region present at the bottom wall, to form a large and single counter-clockwise rotating vortex. Similarly to the plots of Figures 5.5 (a-b), also for ν=1×10^{-4} m^{2}s^{-1} the maximum vorticity increases with shaking speed, with $\frac{\omega_{\theta max}}{\pi N} \approx 0.3$ and 0.45 for N=70 rpm and 80 rpm, respectively (cf. Figures 5.6 a and b).

To further assess the consistency of the flow field identified in Figures 5.5 and 5.6 for highly viscous fluid, two additional operating conditions were examined with different non-dimensional fluid height, h/d_i=0.38, and orbital to cylinder diameter ratio, $d_o/d_i = 0.19$. It should be noted that to test the scalability of the flow also a larger tank reactor was used with cylinder internal diameter d_i=130 mm and fluid height h=5 cm. These results are provided in Figures 5.7 (a) and (b) for ν=1×10^{-5} m^{2}s^{-1} and ν=1×10^{-4} m^{2}s^{-1}, respectively. Both vector fields and contour plots are denoted by similar flow dynamics to those exhibited for h/d_i=0.3 and d_o/d_i=0.25 for the same viscosity and Fr, with the counter clock wise vortex at the right side wall being merged with the region of positive vorticity present close to the bottom of the reactor only for ν=1×10^{-4} m^{2}s^{-1} (cf. Figure

5.7 b). Nevertheless the three regions of positive vorticity present at the side and bottom walls of the bioreactor in Figure 5.7 (a) could also potentially merge if the rotational speed of the shaken bioreactor is increased, which determines a growth in size and intensity of the main vortex present at the the right hand side wall towards the centre and bottom of the bioreactor. This implies that the single vortex flow pattern can be achieved either by increasing the viscosity, or by increasing the rotational speed of the shaken bioreactor.

The last part of this section focuses on measurements obtained in horizontal planes for highly viscous fluids subject to in-phase flow conditions. The vector fields and axial vorticity contour plots are shown in Figures 5.8 (a) and (b) for ν=1×10^{-5} m^{2}s^{-1} and ν=1×10^{-4} m^{2}s^{-1}, respectively. These were obtained at an elevation of z/d_i=0.1 for analogous operating conditions to those reported in Figures 5.5 (a) and 5.6 (b), with h/d_i=0.3, Fr=0.09 and d_o/d_i=0.25. Similarly to the results presented in Chapter 3 for in phase conditions when water was the working fluid, two stagnation points denoted as A and B can be clearly distinguished in the flow fields of Figures 5.8 (a) and (b), with local flow diverging from stagnation point B, and converging towards stagnation point A. In this case however the two stagnation points are almost 180° apart for both the viscosities considered, while the maximum angle of separation between the two stagnation points observed for ν=1×10^{-6} m^{2}s^{-1} was 148° for h/d_i=0.5 and Fr=0.17 (see Section 3.4). Horizontal planes measurements were repeated at different elevations for both ν=1×10^{-5} m^{2}s^{-1} and ν=1×10^{-4} m^{2}s^{-1} (see Figures 5.9 and 5.10). The characteristic flow pattern with two stagnation points 180° apart is consistently present at all the heights investigated, and the different planar flow fields do not display any azimuthal angular delay, as z/d_i closer to the bottom of the tank are considered.

5.4 Out-of-phase flow for different operating conditions with highly viscous fluids

This section aims at characterising the fluid dynamics occurring in an orbitally shaken bioreactor of cylindrical geometry when the flow is in the out-of-phase regime and a fluid of viscosity ν >1.7 $\times 10^{-6}$ m^2s^{-1} is used. Similarly to Section 5.3 flow field and free surface height measurements were obtained for two silicon oils with viscosity 10 and 100 times greater than that of water (ν=1$\times 10^{-5}$ m^2s^{-1} and 1$\times 10^{-4}$ m^2s^{-1}).

As mentioned in Chapter 1, the out of phase condition has been mainly related in the literature to a phase lag of the free surface height with respect to the angular position of the bioreactor along its orbit (Büchs *et al.*, 2000a,b). Based on this a preliminary analysis, analogous to that carried out for water in Chapter 3 (see Figure 3.16), is first made to identify a range of Fr where the out of phase condition is well established. The variation with phase angle, ϕ, of the non-dimensional free surface height measured at the left hand side wall of the bioreactor for a fluid of ν =1$\times 10^{-5}$ m^2s^{-1} is shown in Figure 5.11, where h_f is defined in Figure 3.15, and $h_{f_{max}}$ is the maximum height obtained for a given Froude number. The reference configuration with operating conditions of h/d_i=0.3 and d_o/d_i=0.25 was used for this investigation, with measurements of h_f being repeated for three shaking speeds N=80 rpm (Fr=0.09), 90 rpm (Fr=0.11) and 105 rpm (Fr=0.15) over the entire bioreactor orbit, 0°< ϕ <360°. For Fr=0.09 and Fr=0.11 the fluid is still in phase with the bioreactor angular position, as the non-dimensional height $h_f/h_{f_{max}}$ reaches its maximum ($h_f/h_{f_{max}}$=1) at ϕ=0°, while at the highest shaking speed considered, N=105 rpm (Fr=0.15), the maximum value of h_f occurs at $\phi\approx$20°. A comparison of these results with those of Figure 3.16 highlights that an equivalent phase delay was obtained for water at a much larger shaking speed corresponding to Fr=0.24. This indicates that the critical Froude number, Fr_c, associated to the in-phase to out-phase flow transition becomes smaller when the fluid viscosity is increased. Similar conclusions were withdrawn by Büchs *et al.* (2000a) through power measurements of shaken flasks obtained with highly viscous fluids.

The vorticity contours and velocity vector fields for N=100 rpm and 110 rpm with $\nu=1\times10^{-5}$ m^{2}s^{-1} are shown in Figures 5.12 (a) and (b), respectively. It can be seen that both plots exhibit a wavy profile of the free surface, while the wave amplitude, $\Delta h/d_i$, is approximately 0.18 and 0.21 for Fr=0.14 and Fr=0.17, respectively. In Figure 5.12 (a) the counter-clockwise vortical structure, already identified below the right hand side of the free surface for in phase conditions (cf. Figures 5.5 a, b), is still visible, while a less intense, but larger clockwise rotating vortex is present below the concave left part of the free surface profile. It is interesting to point out how these two structures recall the toroidal vortex present for in phase condition when fluids of low viscosity are used (cf. Figures 5.4 a, b), but in this case the two vortices are rotating in the opposite direction with an axial stream flowing downwards at the centre of the bioreactor (i.e. r/d_i=0). When the shaking frequency is increased to 110 rpm (see Figure 5.12 b), the two vortical structures are still visible, and characterised by similar non-dimensional vorticity intensity to that displayed at 100 rpm, but a radial stream starts to be present below the lowest side of the free surface, with fluid being pushed from the right to the left hand side of the cylindrical bioreactor. This behaviour has to be attributed to the greater degree of out phase occurring when the shaking speed is increased from 100 rpm to 110 rpm.

A better understanding of this phenomenon can be gained from the horizontal PIV measurements shown in Figure 5.13, which were made at an elevation of z/d_i=0.1 for the same operating conditions of Figure 5.12 (b) (i.e. ν=1×10^{-5} m^{2}s^{-1}, Fr=0.17, h/d_i=0.3, d_o/d_i=0.25). Similarly to the plots obtained for in phase conditions (cf. Figures 5.8 a, b), two in-plane stagnation points are present with local flow diverging from and converging to points denoted as B and A, respectively. To best visualise the degree of out of phase the red and black dashed lines identify the projections of the vertical plane of measurement of Figure 5.12 (b), and of the vertical plane of measurement that can be associated to zero fluid exchange between the two counter-rotating vortical cells present at the left and right sides of the bioreactor, respectively. The latter condition occurs when the radial component of the flow on the vertical plane of measurement is minimum, and can be visualised in Figure 5.13 by determining the orientation of the diameter which is locally orthogonal to the vector field in the largest amount of radial coordinates. For example, when the black dashed line is considered, which corresponds to the projection of the cross section of Figure 5.12 (b) on the horizontal plane of measurement of Figure 5.13, the local flow exhibits a radial component, which is parallel to the black line, with fluid being moved from the right side of the bioreactor (lowest part of the free surface) to the left one (highest side of the free surface). On the contrary, the red dashed line is locally orthogonal to nearly all the vectors across the bioreactor diameter, implying that vertical plane measurements obtained at this phase angle would be characterised by two independent vortical cells with negligible fluid exchange between the lowest and highest sides of the free surface. According to this description the flow of Figure 5.12 (b) obtained at $\phi = 0°$ is out of phase by approximately 21°, with the left (right) side of the free surface profile moving upward (downward) if vertical plane plots were reproduced at intermediate phase angles, ϕ (i.e. $0° < \phi < 21°$).

The increase of out-of-phase delay occurring with fluid of increasing viscosity is well illustrated by the velocity fields and vorticity contour maps of Figures 5.14

(a) and (b), which were obtained with a viscosity of ν=1×10^{-4} m^{2}s^{-1} for Fr=0.11 (N=90 rpm) and Fr=0.14 (N=100 rpm). The higher viscosity induces a wavy free surface profile at a shaking frequency of N=90 rpm (Fr=0.11), while for the same Froude number the silicon oil of ν=1×10^{-5} m^{2}s^{-1} still exhibited in phase flow, with zero phase lag of the free surface (cf. Figure 5.11). This again indicates that an increase of fluid viscosity determines a lower value of the critical Froude number, Fr_c, which marks the threshold for in-phase to out-of-phase flow transition. Both vector fields of Figures 5.14 (a-b) are characterised by a strong radial stream, which moves fluid from the left side of the bioreactor to the right one, with a small recirculation present at the right corner of the cylinder cross section.

As previously mentioned a strong radial jet implies a large degree of out of phase, and this is well exemplified in Figure 5.15, where horizontal plane measurements are presented for the same operating conditions as those of Figures 5.14 (b) (i.e. ν=1×10^{-4} m^{2}s^{-1}, Fr=0.14, h/d_i=0.3, d_o/d_i=0.25). For this viscosity the out of phase flow condition is clearly evident with the imaginary line connecting the two stagnation points being at an angle with respect to the black dashed line visualising the position of the vertical plane of measurement at a phase angle $\phi = 0°$. Similarly to the analysis carried out for ν=1×10^{-5} m^{2}s^{-1} (cf. Figure 5.13), the red dashed line of Figure 5.15 is locally orthogonal to the vector field, and visualises the projection on the horizontal plane of the vertical plane of measurement that would exhibit two distinct vortical cells. For this combination of viscosity, Froude number and non-dimensional height the flow is out of phase of 41°. Horizontal plane measurements were repeated at different elevations for the two silicon oils with viscosity of ν=1×10^{-5} m^{2}s^{-1} and ν=1×10^{-4} m^{2}s^{-1}, and the corresponding contour and vector plots are provided in Figures 5.16 and 5.17, respectively. From both figures it is evident that the degree of out of phase is constant throughout the fluid height.

To further assess the variation of the flow dynamics in the out of phase flow regime of highly viscous fluids, two additional configurations were investigated with a non-dimensional fluid height of h/d_i=0.5 for ν=1×10^{-5} m^{2}s^{-1} and ν=1×10^{-4} m^{2}s^{-1} in Figures 5.18 (a) and (b), respectively. The velocity vector and vorticity contour plots of Figure 5.18 (a) exhibit a flow pattern similar to that of Figure 5.12 (a), with two clear counter-rotating vortices at the sides of the measurement cross section. The fact that the two vortices are discernible and nearly completely separated implies that at this Fr the flow is out of phase by a small phase angle. From this point of view it is interesting to note that for a fluid height of $h/d_i = 0.3$ the two counter-rotating vortices were completely distinct for a Fr=0.14, while at fluid height of $h/d_i = 0.5$ a similar condition occurs at a greater speed corresponding to Fr=0.2. This behaviour is analogous to that already described for low viscous fluids in Chapter 3, where it was found that transition to out of phase flow is retarded when the non-dimensional fluid height is increased. In agreement with previous results for ν=1×10^{-4} m^{2}s^{-1}, the vorticity contour and velocity vector maps of Figures 5.18 (b) are characterised by a strong radial jet pushing fluid from the right side of the bioreactor towards the left one, implying that for these operating conditions, h/d_i=0.5 and Fr=0.15, the flow is out of phase by a large amount, close to that exhibited for a non-dimensional fluid height of $h/d_i = 0.3$ at Fr=0.14 (cf. Figures 5.14b and 5.15).

The current section highlighted that the flow dynamics for out-of-phase flow are different for fluid of high and low viscosity, with a precessional vortex dominating the flow for $\nu \leq$1.7×10^{-6} m^{2}s^{-1} (see Figure 3.12), and two vortical cells with an azimuthal axis characterising the flow for $\nu >$1.7×10^{-6} m^{2}s^{-1} (cf. Figures 5.12a and 5.18a). Moreover it was found that an increase in fluid viscosity promotes out of phase flow, while an increase of fluid height decreases the critical Fr_c associated to the flow transition.

5.5 Flow map for different *Re* and *Fr*

A summary of the different flow regimes encountered in an orbitally shaken bioreactor of cylindrical geometry for different operating conditions is provided in the *Re*-Fr flow map of Figure 5.19. It should be noted that the plot was made for the reference non-dimensional fluid height, h/d_i=0.3. The flow map of Figure 5.19 is based on the Froude number definition of Equation 1.3 using the orbital diameter, while *Re* is defined in Equation 5.2.

$$Re = \frac{\pi N d_o \, d_i}{\nu} \tag{5.2}$$

It should be noted that other definitions of *Re* can be found in previous works on orbitally shaken bioreactors, such as those of Büchs *et al.* (2000b) (see Equation 5.3) and Kim and Kizito (2009) (see Equation 5.4), which are both based on the cylinder diameter.

$$\begin{aligned} Re &= \frac{N {d_i}^2}{\nu} && (5.3) \\ Re &= \frac{\pi N {d_i}^2}{2\,\nu} && (5.4) \end{aligned}$$

In the current work the definition of Equation 5.2 was selected because it is evident from the scaling law derived in Chapter 3, and from the analyses carried out for high viscosity fluids in the previous sections, that the reference speed should be based on the orbital motion (cf. $V = \pi N d_o$), and this is also confirmed by the relevance of the orbital Froude number on the flow transition (cf. § 3.5), while the characteristic length scale should be associated to the inner cylinder diameter, which induces the flow transition to a precessional vortex because it is directly linked to the wall curvature (cf. § 4.4).

The *Re*-Fr map of Figure 5.19 is subdivided into four regions denoted by upwards/downwards arrows to discriminate between high and low values of Froude and Reynolds numbers. The vertical dashed line differentiate between fluid of low viscosity (i.e $\nu \leq 1.7\times10^{-6}$ m^{2}s^{-1} and high *Re*), where the flow is dominated either by a toroidal vortex with an upwards central stream for in phase conditions (i.e. low Fr, right-bottom quadrant), or by a precessional vortex of vertical axis for out of phase conditions (i.e. high Fr, right-top quadrant), and fluid of high viscosity (i.e. $\nu > 1.7\times10^{-6}$ m^{2}s^{-1} and low *Re*), where the in phase flow is characterised by a single vortex formed below the lowest side of the free surface spreading towards the bottom of the bioreactor (i.e. low Fr, left-bottom quadrant), or by a toroidal vortex with a downwards central stream and a wavy free surface profile for out of phase conditions (i.e. high Fr, left-top quadrant). To improve the readability of the figure a visual representation of the different flows occurring for the four combinations of *Re*-Fr can be gained from the vertical and horizontal plane insets of Figure 5.19. Several conditions with varying h, d_o, d_i, N and ν are reported in Figure 5.19, where empty and filled symbols discriminate between in phase and out of phase flows, respectively.

The following sections aim at elucidating the variation of the circulation, turbulent kinetic energy and normal/shear rates when different points across the *Re*-Fr map are considered, and at gaining a better understanding of the implications of the different in phase and out of phase flow transitions occurring at different *Re* for bioprocess design.

5.5.1 Circulation of the periodic mean flow

An analogous study to that reported in Chapters 3 is carried out in this section to assess the variation of the circulation, $\Gamma^*_{\omega_\theta=0.1}$, with Fr and ν, when fluids of high viscosity are considered. Two profiles of $\Gamma^*_{\omega_\theta=0.1}$ against Fr are shown in Figures 5.20 (a) and (b) for ν =1×10^{-5} m^{2}s^{-1} and ν =1×10^{-4} m^{2}s^{-1}, respectively. In both cases the viscosity is ν >1.7×10^{-6} m^{2}s^{-1}, and the flow transition described earlier in this chapter for high viscous fluids should be considered. The circulation $\Gamma^*_{\omega_\theta=0.1}$ was obtained from Equation 3.4, where the area used to carried out the integration is enclosed by the contour of the selected vorticity threshold $\omega_\theta/(\phi N)$=0.1. For example, the area $A_{\omega_{\nu h}}$ visualised in Figure 5.21 was used to estimate the circulation for ν =1×10^{-4} m^{2}s^{-1} and $Fr \approx 0.09$ for the reference operating condition (i.e. $h/d_i = 0.3$ and $d_o/d_i = 0.25$ ϕ=0). When comparing the results of Figures 5.20 (a) and (b), it is evident that the circulation drops with increasing fluid viscosity, with $\Gamma^*_{\omega_\theta=0.1}/\pi N$ varying over the same range of $Fr = 0.07 - 0.14$ between 0.19-0.6 (Figure 5.20 a) and 0.15-0.425 (Figure 5.20 b) for ν =1×10^{-5} m^{2}s^{-1} and ν =1×10^{-4} m^{2}s^{-1}, respectively. This behaviour is further confirmed by Figure 5.22, where the variation of the circulation for increasing ν/ν_w (i.e. decreasing Re) is considered. This corresponds to a horizontal line in the Re-Fr map of 5.19. When looking at Figure 5.22 two distinct regions can be identified, where the circulation increases with different slopes above and below ν/ν_w=5. More specifically an increase of 50 % is registered for $\nu/\nu_w < 5$, while an increase of 25 % occurs for $\nu/\nu_w > 5$. This implies that transport processes associated to the advective action of the vortical structure present in the flow will be significantly slower for more viscous fluids, and this increase in circulation time will be more prominent over the range $\nu/\nu_w < 5$.

5.5.2 Kinetic energy variation with flow regime

In this section the turbulent kinetic energy of the flow is investigated for different combinations of Fr and Re. The turbulent kinetic energy content was estimated according to the 2D approximation of Equation 5.5, where the asterisk denotes the space average of $\sqrt{\langle u_r'^2\rangle + \langle u_z'^2\rangle}$ over the entire vertical plane of measurement, while the angle brackets denote a phase resolved average. It should be noted that the dimensions of $\sqrt{\langle u_r'^2\rangle + \langle u_z'^2\rangle}^*$ are m/s, and therefore it should be considered as a reference velocity of the kinetic energy due to turbulent fluctuations, and here after will be referred to as turbulent kinetic energy reference velocity. The data reported in this section refers to a phase angle $\phi = 0°$.

$$\left(\sqrt{\langle u_r'^2\rangle + \langle u_z'^2\rangle}\right)^* = \frac{1}{A}\int_A \left(\sqrt{\langle u_r'^2\rangle + \langle u_z'^2\rangle}\right) dA \tag{5.5}$$

Initially the variation of the turbulent kinetic energy levels with Re was assessed for two constant Froude numbers selected in the in-phase flow regime ($Fr = 0.11$) and the out-of-phase one ($Fr = 0.17$), respectively. These two Fr conditions are visualised by the two horizontal lines at $Fr = 0.11$ and 0.17 in Figure 5.23 (a). It should be noted that the two lines cross the vertical dashed line discriminating between flow conditions of high and low viscous fluids and identifying different types of flow patterns both for in phase and out of phase conditions. The profiles of the non-dimensional turbulent kinetic energy reference velocity against Re are reported in Figure 5.23 (b). It has to be stressed that Re was varied by changing the fluid viscosity, ν. At Fr =0.11 turbulence levels are extremely low and do not vary with increasing Re. This indicates that, despite the differences in mean flow pattern, the flow regimes occurring for in phase conditions both for high and low viscous fluids are laminar, with negligible turbulent fluctuations. When $Fr = 0.17$ is considered the turbulent kinetic energy reference velocity is close to 5 % of the orbital velocity at the lowest Re considered (i.e. most viscous fluid), indicating that some chaotic fluctuations already occur for out of phase condition of high viscous fluids. The intensity of $\sqrt{\langle u_r'^2 \rangle + \langle u_z'^2 \rangle}$ shows a gradual growth for Re<2000, while a steeper increase occurs as the dashed vertical line is approached and the out of phase flow starts to exhibit the precessional vortex characterising low viscous fluid. For the highest Re considered the turbulent kinetic energy content is more than 20 % of that associated to the orbital shaken motion.

Estimates of the turbulent kinetic energy content for increasing Fr are reported in Figures 5.24 (a, b) for three different constant Reynolds numbers, Re=9163, 13090 and 17017. To assess thoroughly the relevance of Re on the turbulent kinetic energy content, data sets of Re=9163 and 13090 were repeated twice using for each data set two different combinations of ν and d_i such that d_i/ν was constant. This experimental methodology can be better understood from the definition of Re in Equation 5.2, where it is evident that for a given Fr (i.e. fixed combination of N and d_o), the same Re can be achieved by varying ν and d_i such that their ratio d_i/ν is constant. For example, the same flow regime of $Re = 9163$ was obtained either by using water (ν_w) in a cylinder of diameter d_i=70 mm or a water-glycerine mixture (ν_w=1.4) in a cylinder of diameter d_i=100 mm, such that in both cases $d_i/\nu \approx 70/\nu_w$.

A visualisation on the Re-Fr map of the five sets of data used to assess the variation of the turbulent kinetic reference velocity against Fr is provided in Figure 5.24 (a). As expected the different data points are aligned along vertical lines of constant Re. The dashed colour coded curves define the transition to out of phase flow for the different combination of d_o/d_i and ν investigated. In fact it is worth to remind that according to Equation 5.1 and to the critical wave amplitude, $(\Delta h/h)_c$, of Figure 3.24, flow transition to out of phase flow in the high Re range will occur at a lower speed (i.e. lower Fr) for a less viscous fluid and/or for a cylinder of larger internal diameter. For instance the dashed blue curve associated to d_i=100 mm and $\nu = \nu_w$ is lower than that of a glycerine mixture with same diameter but higher viscosity (i.e. red curve, $\nu = 1.4\nu_w$) and higher than the green curve associated to a larger diameter of $d_i = 130$ mm and same viscosity (i.e. $\nu = \nu_w$).

The variation of $\frac{\left(\sqrt{\langle u_r'^2\rangle + \langle u_z'^2\rangle}\right)^*}{\pi N d_o}$ with increasing Fr is shown in Figure 5.24 (b). For all the different Re considered the turbulent kinetic energy content is negligible at low values of Fr, as all the data sets are in the in-phase flow regime. Two main points can be learnt from Figure 5.24 (b):

1. The increase of the turbulent kinetic energy occurs at different transitional Fr, with data sets associated to a greater Re undergoing the out of phase transition at a lower Fr. For example at $Fr = 0.2$, data associated to $Re = 17017$ and 13090 (ν_w, $d_i = 130$ mm) already exhibit a non-dimensional turbulent kinetic energy reference velocity of 48 %, while for the lowest Re considered $\frac{\left(\sqrt{\langle u_r'^2\rangle + \langle u_z'^2\rangle}\right)^*}{\pi N d_o} \approx 10\%$.

2. The turbulent kinetic energy content is different even when the same Re is considered. This aspect is clearly present when comparing the data sets for Re=13090 (empty circles and red triangles) and 9163 (filled squares and blue triangles). For example at Fr=0.18 water data exhibit a $\frac{\left(\sqrt{\langle u_r'^2\rangle + \langle u_z'^2\rangle}\right)^*}{\pi N d_o}$ of 20 % and 6% at Re=13090 and Re=9163, respectively, while for analogous Re water-glycerine mixtures are denoted by values of turbulent kinetic energy of 37 % and 20 %.

This behaviour can be explained by considering that in the high Re range flow transition is promoted by a lower viscosity and by a larger cylinder diameter. From this point of view, contrary to the data of Figure 5.24 (b), water-glycerine mixtures should exhibit lower turbulence levels than those reported for water at analogous Re, because flow transition should occur at a higher transitional Fr_c than water. However, it should be stressed that in order to keep Re constant water-glycerine mixture experiments were carried out in larger cylinders than those used for water, implying that flow transition should occur in these geometries at a lower transitional Fr_c than water. From the greater turbulence levels exhibited by the water-glycerine mixture data at analogous Re, it is clear that the fluid viscosity has a lower impact on the transitional Froude number, Fr_c, than the cylinder diameter d_i when $\nu \leq 1.7\times10^{-6}$ $\mathrm{m^2s^{-1}}$.

To take into account the difference in transitional Fr_c due to the different selection of viscosity and cylinder diameter, the five data sets of Figure 5.24 were replotted in Figure 5.25 using the ratio Fr/Fr_c. As shown in Figure 5.25 (a) this parameter allows to superimpose all the transitional colour-coded dashed curves of Figure 5.24 (a) on a single horizontal line of Figure 5.25 (a). When looking at Figure 5.25 (b) the advantages of employing the ratio Fr/Fr_c are evident, as all the data sets tend to collapse on each other irrespective of their Re, and a single curve can be identified towards a more effective scaling of the turbulent kinetic energy between cylindrical bioreactors of different sizes and employing different working fluids.

5.5.3 Strain rate tensor

The evaluation of the shear rate magnitude and the identification of high shear zones in the bioreactor are important aspects of bioprocess design, as they directly affect the viability of the cell culture. High shear stress can disrupt the cell membrane, leading to cell death. In this section a 2D analysis of the phase resolved strain and shear rates occurring in the vertical plane of measurement is carried out. The 2D phase resolved rate of strain tensor is defined in Equation 5.6:

$$\boldsymbol{S}_{ij} = \begin{pmatrix} 2\frac{\partial\langle u_r\rangle}{\partial r} & (\frac{\partial\langle u_r\rangle}{\partial r} + \frac{\partial\langle u_z\rangle}{\partial z}) \\ (\frac{\partial\langle u_r\rangle}{\partial r} + \frac{\partial\langle u_z\rangle}{\partial z}) & 2\frac{\partial\langle u_z\rangle}{\partial z} \end{pmatrix} \tag{5.6}$$

where S_{rr}, S_{zz}, are the radial and axial strain rates, while S_{rz} is the shear rate. It should be noted that positive (negative) values of the strain rates (i.e. S_{rr}, S_{zz}) correspond to local stretching (compression) of the fluid element.

Figure 5.26 shows the radial profiles of the strain rates, S_{rr}, S_{zz} and of the shear rate, S_{rz}, at an elevation z/d_i=0.1 for two different viscosities, ν_w and $10\nu_w$ (h/d_i=0.3 and ϕ=270°). It should be noted that in Figure 5.26 black and blue data points are again used to discriminate between positions to the right and left hand sides of the bioreactor axis, respectively.

From Figure 5.26 (a) the absolute value of the non dimensional strain rate, S_{rr}, is highest near the walls of the cylinder, with compression in the radial direction ($S_{rr} < 0$) occurring to the left hand side of the cylinder axis (blue symbols), and stretching ($S_{rr} > 0$) to the right one (black symbols). It is interesting to point out that the non-dimensional strain rate has nearly the same intensity for the two viscosity considered in Figure 5.26 (a). Apart from the points closer to the wall, the radial profiles of S_{zz} are similar in absolute magnitude to those displayed by the radial strain rate, but in this case the left hand side of the bioreactor is subject to stretching in the axial direction, while the right one is subject to compression. This behaviour is consistent with the flow dynamics occurring at this phase angle, $\phi = 270°$, where the free surface profile is horizontal on the plane of measurement and fluid is displaced from the right to the left hand side of the bioreactor (i.e. opposite to the flow of Figure 3.1 c for $\phi = 90°$). As the bioreactor proceeds in the orbital motion towards greater ϕ the centrifugal acceleration determines a downwards force on the right hand side of the free surface (hence compression in the axial direction to the right side of cylinder axis), and an upwards force on the left one (hence stretching to the left side of the cylinder axis). The shear rate, S_{rz}, assumes values nearly three times greater than those of the normal strain rates close to the walls of the bioreactor (cf. Figure 5.26 c), where the local flow changes its direction from the axial to the radial directions, while nearly negligible shear is observed closer to the cylinder axis for $0< r/d_i <0.45$.

The variation of the strain and shear rates, S_{rr}, S_{zz} and S_{rz} of the phase-resolved flow with Froude number, Fr, are shown in Figures 5.27 (a), (b) and (c), respectively. Two sets of data with different cylinder diameter and viscosity but same *Re* are investigated. As reported in Equation 5.7 the asterisk denotes the space average of the absolute value of S_{ij} over the entire vertical plane of measurement.

$$|S_{ij}|^* = \frac{\int_A |S_{ij}| dA}{A} \tag{5.7}$$

The results of Figure 5.27 (a-c) show a similar behaviour for the different $|S_{ij}|^*$ considered with a nearly linear increase of the strain and shear rates with Fr for both the two *Re* data sets. The axial strain and shear rates are denoted by a higher magnitude over the range of Fr considered ($|S_{zz}|^*=|S_{rz}|^*=0\text{-}1.4\pi N$), while the space averaged radial strain rate, $|S_{rr}|^*$, does not exceed $1\pi N$ for any Froude number.

5.6 Concluding remarks

In the first part of the chapter the variation of the free surface angle against Fr was investigated for different working fluids, and a power law that correlates the constant of proportionality, a_o, and the fluid viscosity was determined (cf. Figure 5.2). This allowed to extend the flow scaling law derived in Chapter 3 to fluids of viscosity higher than water (cf. Equation 5.1). A thorough analysis of the phase resolved flow fields occurring in an orbitally shaken bioreactor of cylindrical geometry was then carried out, and it was found that the in-phase and out-phase flow characteristics associated to a toroidal and precessional vortices, respectively, did only occur for fluids of low viscosity with $\nu \leq 1.7\times10^{-6}$ (cf. Figures 5.4). The in phase flow of fluids of higher viscosity was characterised by a vortical structure observed below the lowest side of the free surface and extending towards the bottom of the tank with increasing Fr (cf. Figure 5.5). On the contrary a toroidal vortex with a central downward stream is formed below the wavy free surface when the flow is out of phase and $\nu > 1.7\times10^{-6}$ (cf. 5.12). Measurements on horizontal planes allowed to determine the degree of out of phase occurring for different fluid viscosity. It was found that viscosity significantly promotes out of phase transition, with the flow of silicon oils of $10\nu_w$ and $100\nu_w$ being out of phase by 21° and 41°, respectively (cf. Figures 5.13 and 5.15).

The different flow dynamics occurring for high and low viscous fluids were summarised in a flow transition map based on Fr and Re, where four main regions were identified to discriminate between the different in phase and out of phase flows associated to different ν (cf. Figure 5.19). A non-dimensional reference velocity of the turbulent velocity fluctuations was defined in Equation 5.5 to assess how the turbulence levels changed with varying Fr and Re. It was found that turbulence levels rise when a low viscous fluid is considered and the flow is out of phase (i.e. combination of high Fr and Re). The variation of the turbulent kinetic energy content was further investigated considering three different Re obtained with combinations of ν and d_i. The data show that turbulence growth is promoted or retarded depending on the transitional Fr set by the operating conditions (i.e. d_o, d_i, ν, N, h). Even data for the same Re displayed different behaviour, with turbulence content of more viscous fluids obtained in a larger cylinder rising at a lower transitional Fr_c than that obtained with water in a smaller one (cf. Figure 5.24). To better compare the data sets obtained at different Re and overcome their differences in terms of transitional Fr_c, a turbulent kinetic energy scaling methodology based on the ratio Fr/Fr_c is proposed in Figure 5.25. This normalisation proved to be effective as the curves associated to the different Re collapsed on each other. Finally a 2D analysis was carried out to investigate the strain and shear rates in the cylindrical bioreactor. A linear increase with Froude number was observed for the space averaged strain/shear rate considered, with the axial strain and shear rates, $|S_{zz}|^*$=$|S_{rz}|^*$=0-1.4πN, being greater than the radial strain rate, $|S_{rr}|^*$=0-1πN, over the Froude number range investigated.

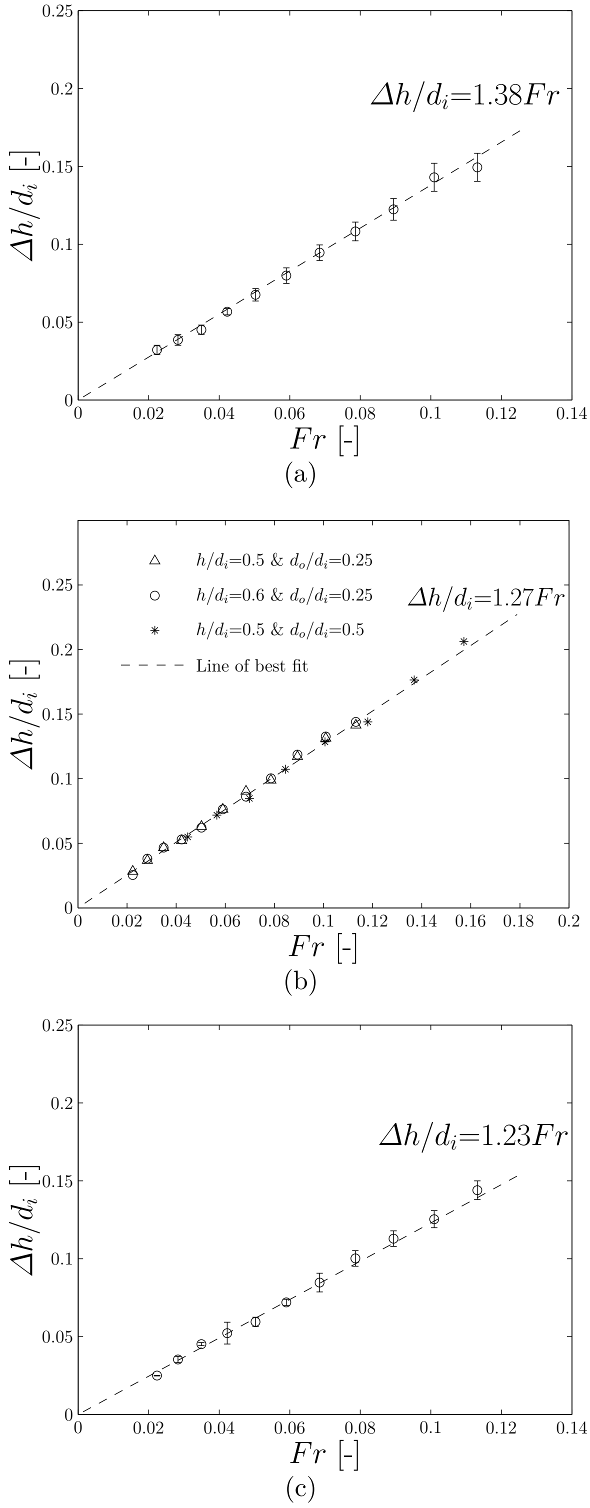

Figure 5.1: Variation of the free surface inclination with Fr and increasing viscosity: (a) ν=1.7×10^{-6} m^{2}s^{-1} (d_o/d_i=0.25, h/d_i=0.5, ϕ=0°); (b) ν=4.97×10^{-5} m^{2}s^{-1}, (ϕ=0°); (c) ν=1.8×10^{-4} m^{2}s^{-1} (d_o/d_i=0.25, h/d_i=0.5, ϕ=0°).

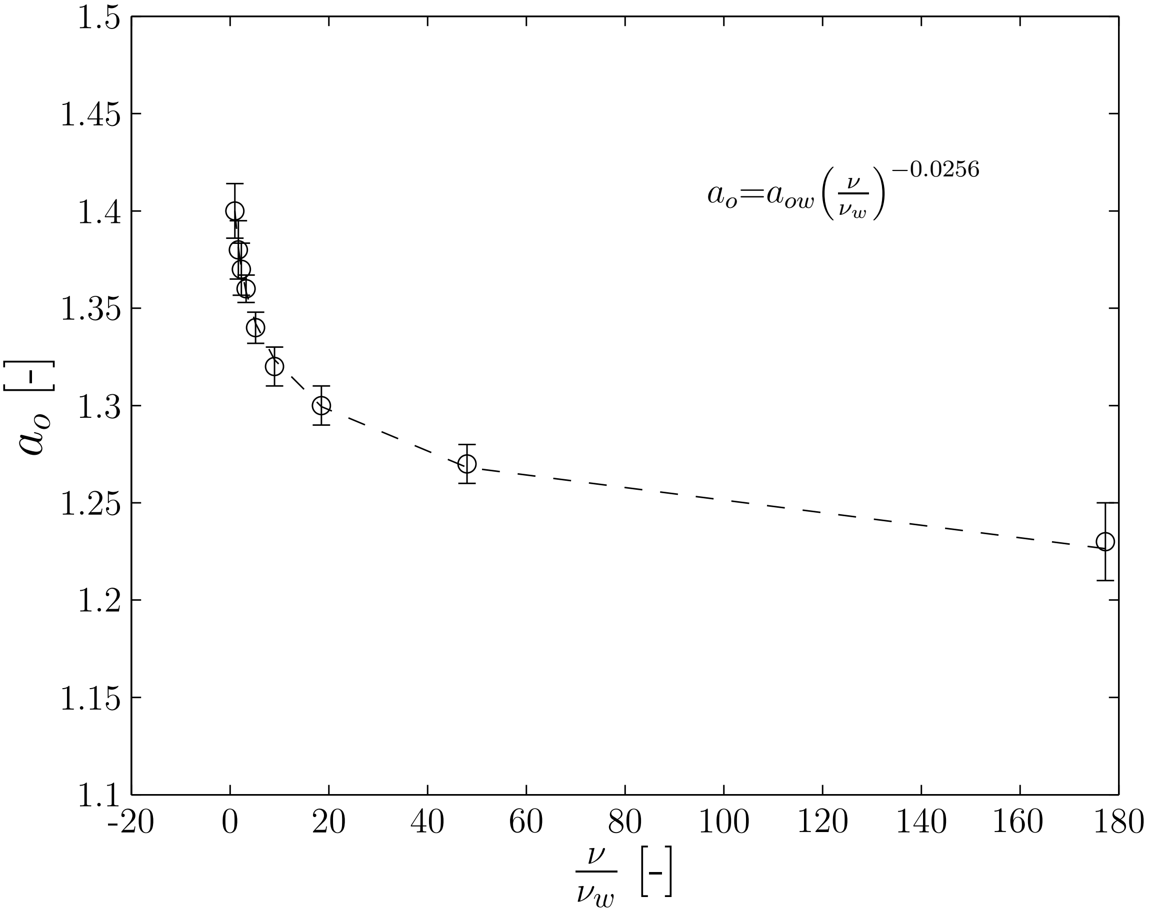

Figure 5.2: Variation of the free surface constant of proportionality, a_o, for increasing fluid viscosity, ν.

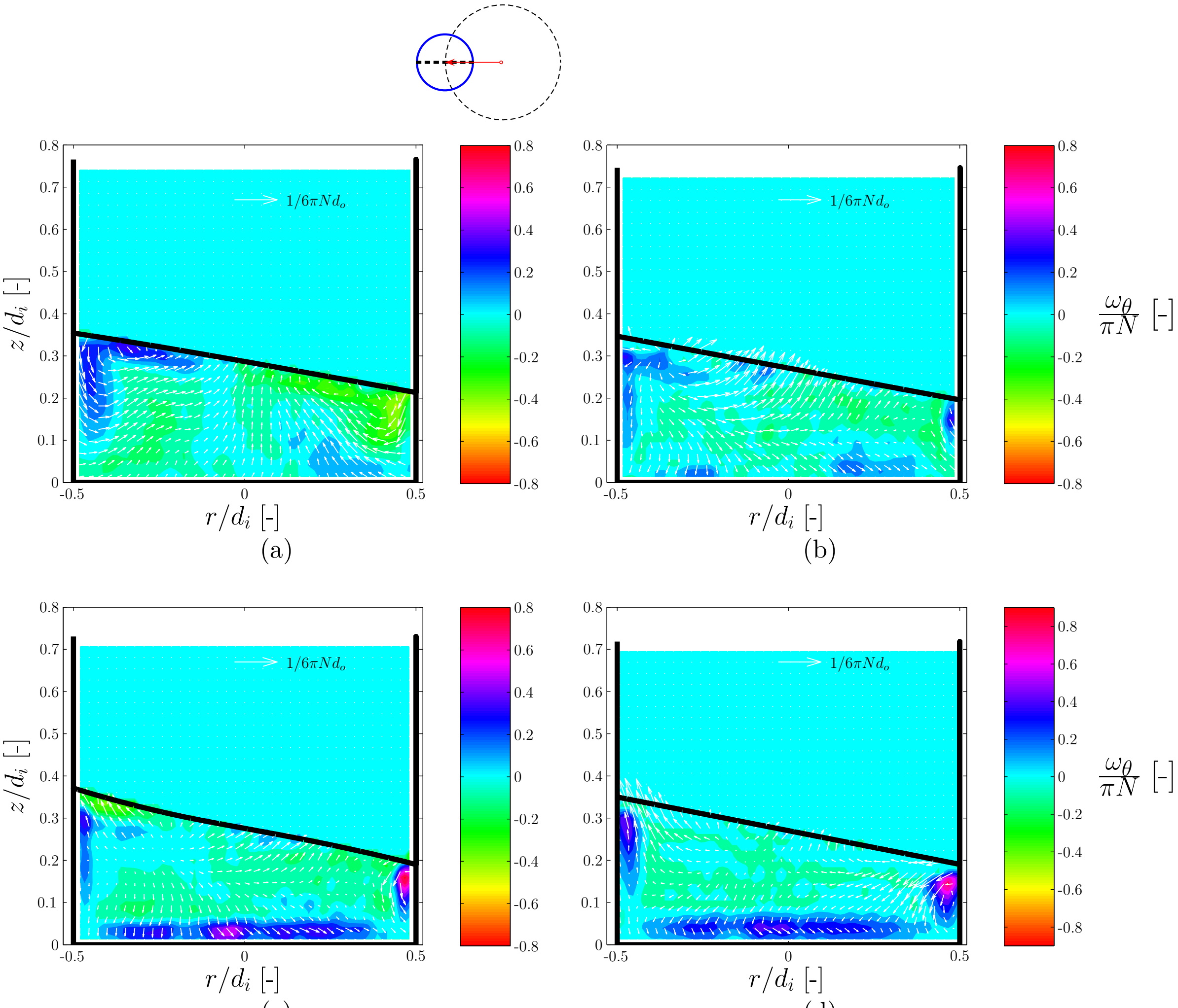

(a) (b) (c) (d)

Figure 5.3: Phase-resolved vector fields and contour plots of the tangential component of the vorticity, ω_θ, for different viscosity at ϕ=0° (h/d_i=0.3, Fr=0.1, d_o/d_i=0.25): (a) $\nu=1.7\times10^{-6}$ m^{2}s^{-1}; (b) $\nu=3.2\times10^{-6}$ m^{2}s^{-1}; (c) $\nu=5.2\times10^{-6}$ m^{2}s^{-1}; (d) $\nu=9\times10^{-6}$ m^{2}s^{-1}.

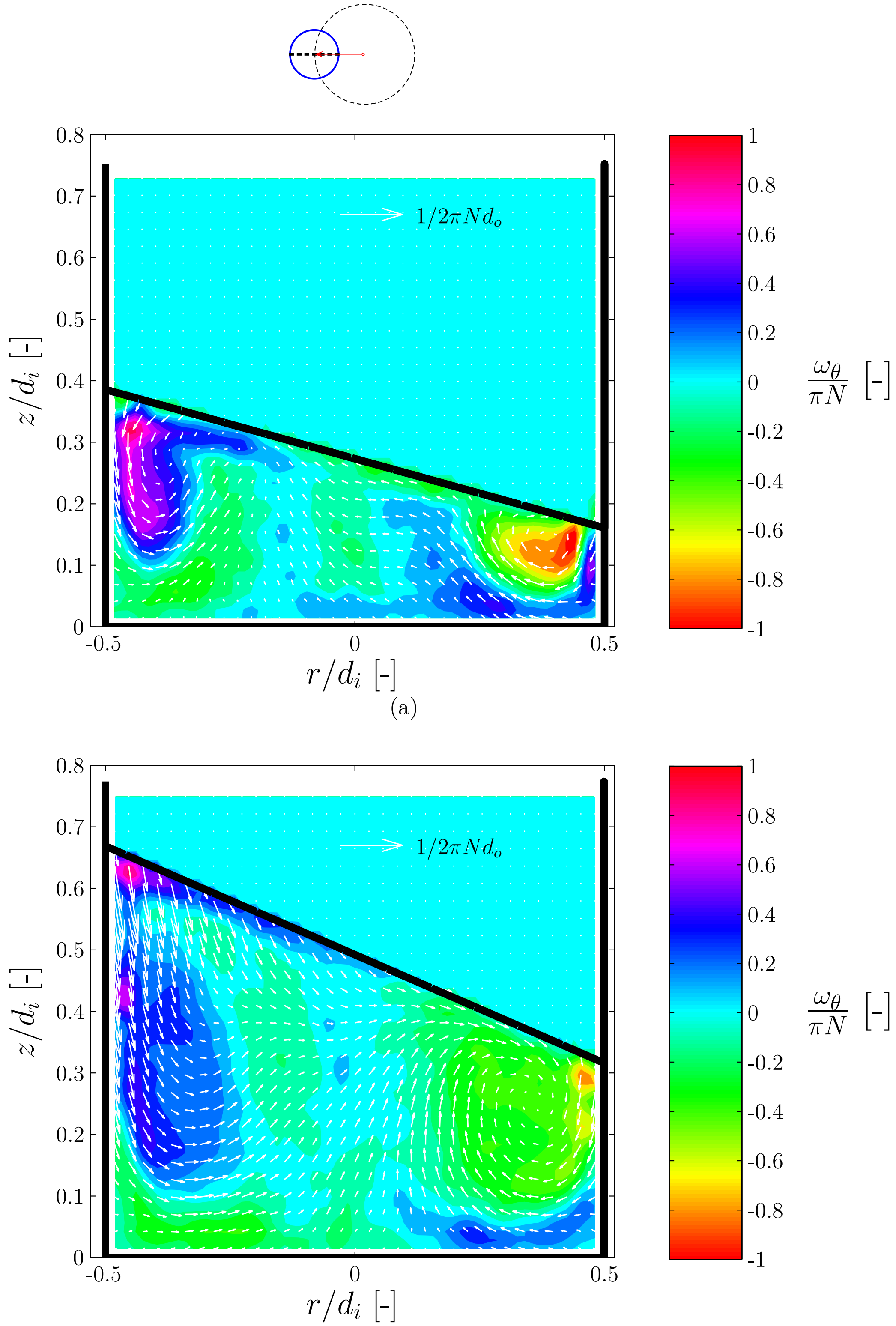

(a)

(b)

Figure 5.4: Phase-resolved vector fields and contour plots of the tangential component of the vorticity, ω_θ, for ν=1.7×10^{-6} m^{2}s^{-1} (ϕ=0°, d_o/d_i=0.5): (a) h/d_i=0.3 and Fr=0.16 (N=75 rpm); (b) h/d_i=0.5 and Fr=0.25 (N=95rpm).

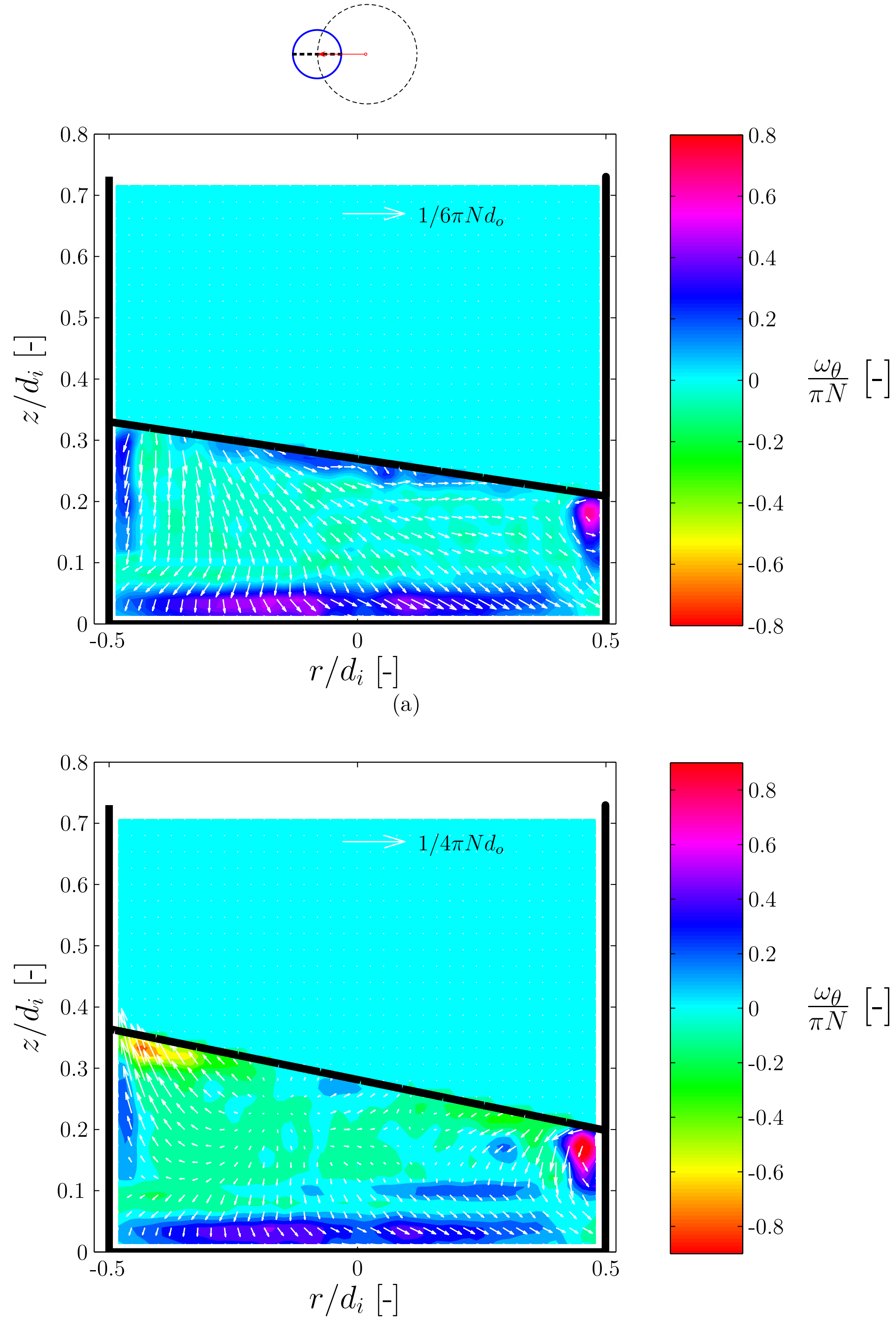

(a)

(b)

Figure 5.5: Phase-resolved vector fields and contour plots of the tangential component of the vorticity, ω_θ, for ν=1×10^{-5} m^{2}s^{-1} (h/d_i=0.3, ϕ=0°, d_o/d_i=0.25): (a) Fr=0.09 (N=80 rpm); (b) Fr=0.11 (N=90 rpm).

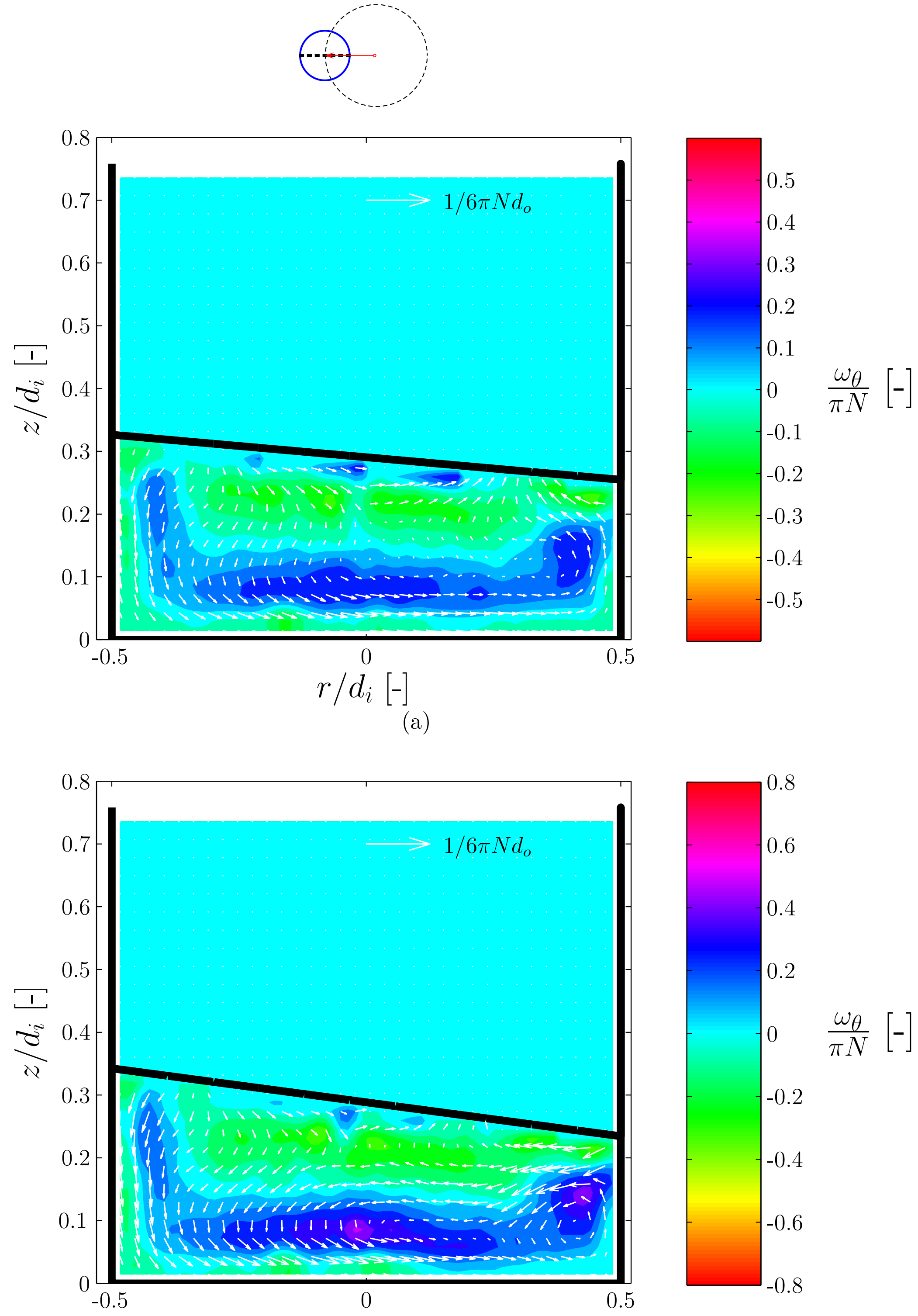

(a)

(b)

Figure 5.6: Phase-resolved vector fields and contour plots of the tangential component of the vorticity, ω_θ, for ν=1×10^{-4} m^{2}s^{-1} (h/d_i=0.3, ϕ=0°, d_o/d_i=0.25): (a) Fr=0.07 (N=70 rpm); (b) Fr=0.09 (N=80 rpm).

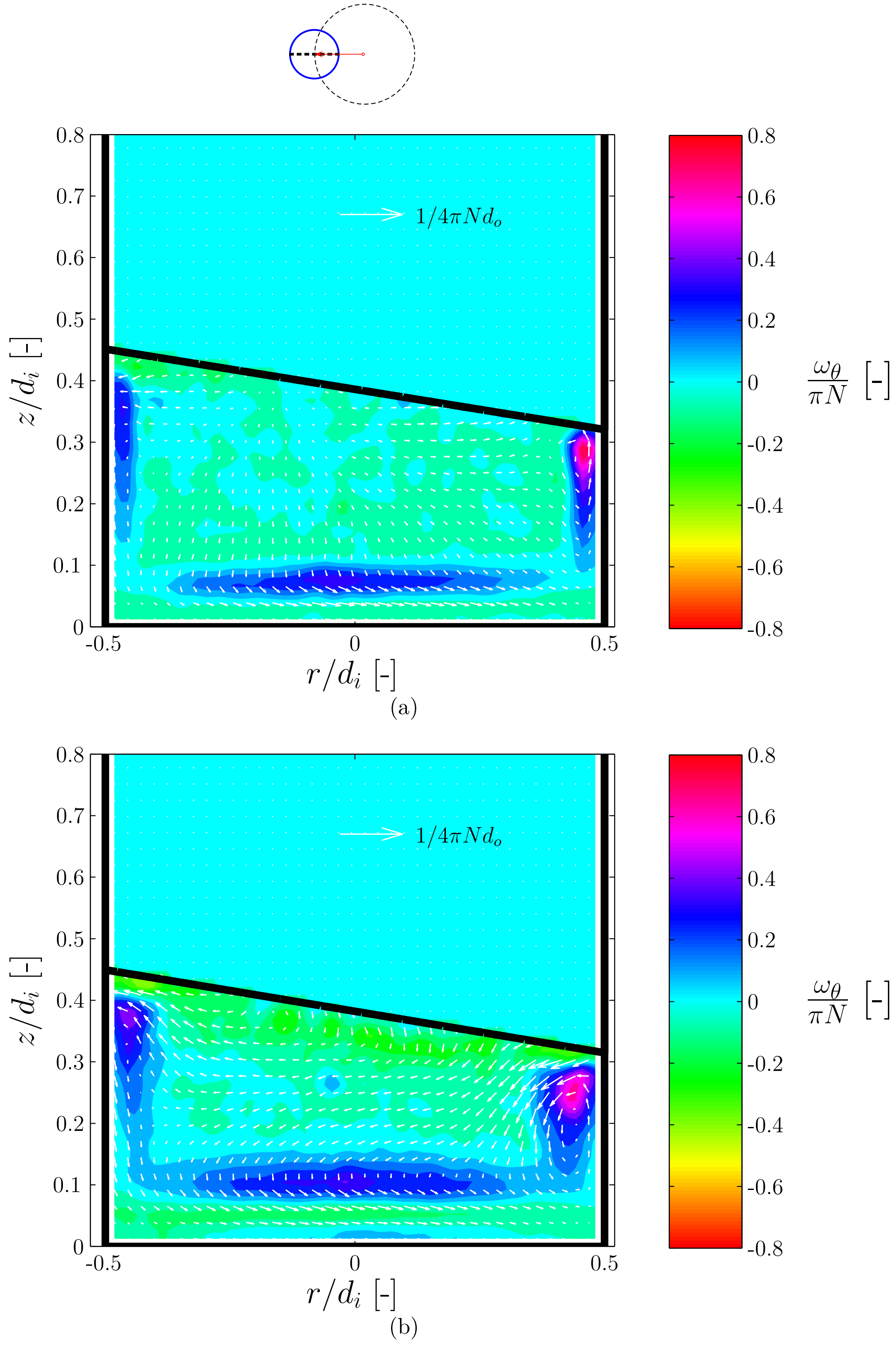

(a)

(b)

Figure 5.7: Phase-resolved vector fields and contour plots of the tangential component of the vorticity, ω_θ, for h/d_i=0.38, Fr=0.09 and d_o/d_i=0.19 (ϕ=0°): (a) ν=1$\times$10^{-5} m^{2}s^{-1}; (b) ν=1$\times$10^{-4} m^{2}s^{-1}.

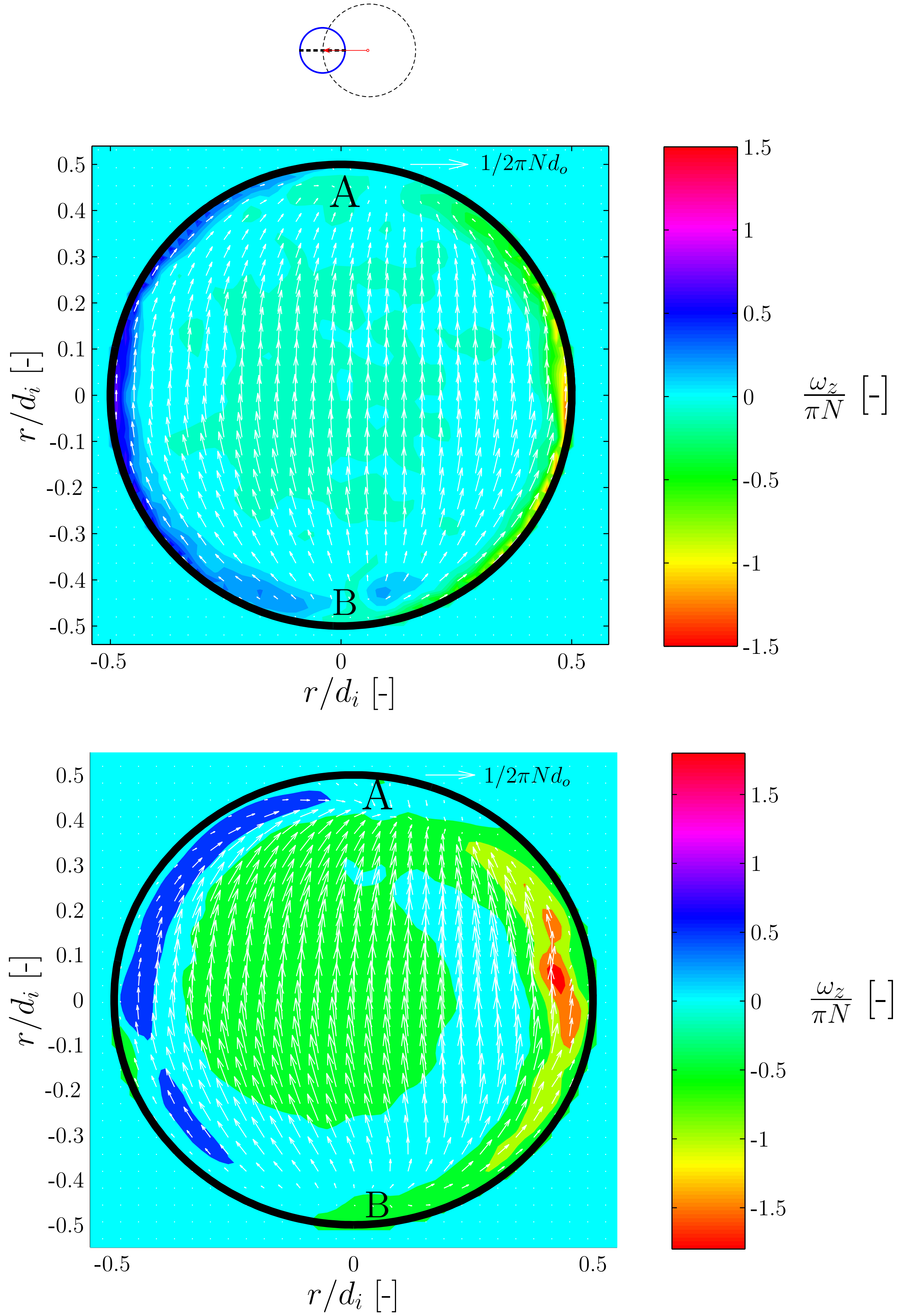

Figure 5.8: Phase-resolved vector fields and contour plots of the vorticity, ω_z, at an axial coordinate of z/d_i=0.1 (h/d_i=0.3, Fr=0.09, d_o/d_i=0.25, ϕ=0°): (a) $\nu=1\times10^{-5}$ m^{2}s^{-1}; (b) $\nu=1\times10^{-4}$ m^{2}s^{-1}.

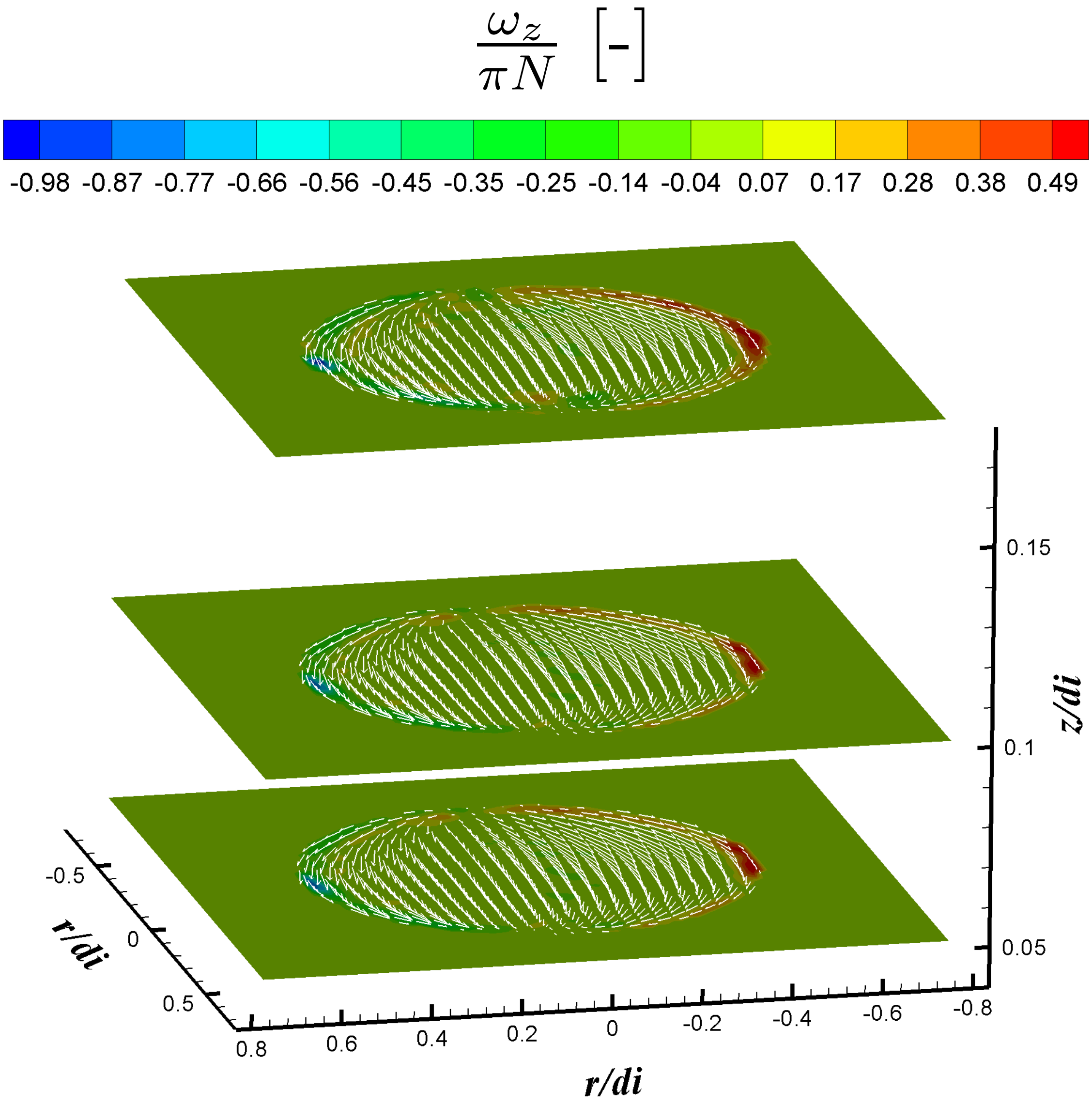

Figure 5.9: Phase-resolved vector fields and contour plots of the axial vorticity, ω_z, at three different elevations, z/d_i=0.05, 0.1 and 0.175 for ν=1×10^{-5} m^{2}s^{-1} (h/d_i=0.3, ϕ=180°, Fr=0.09, d_o/d_i=0.25).

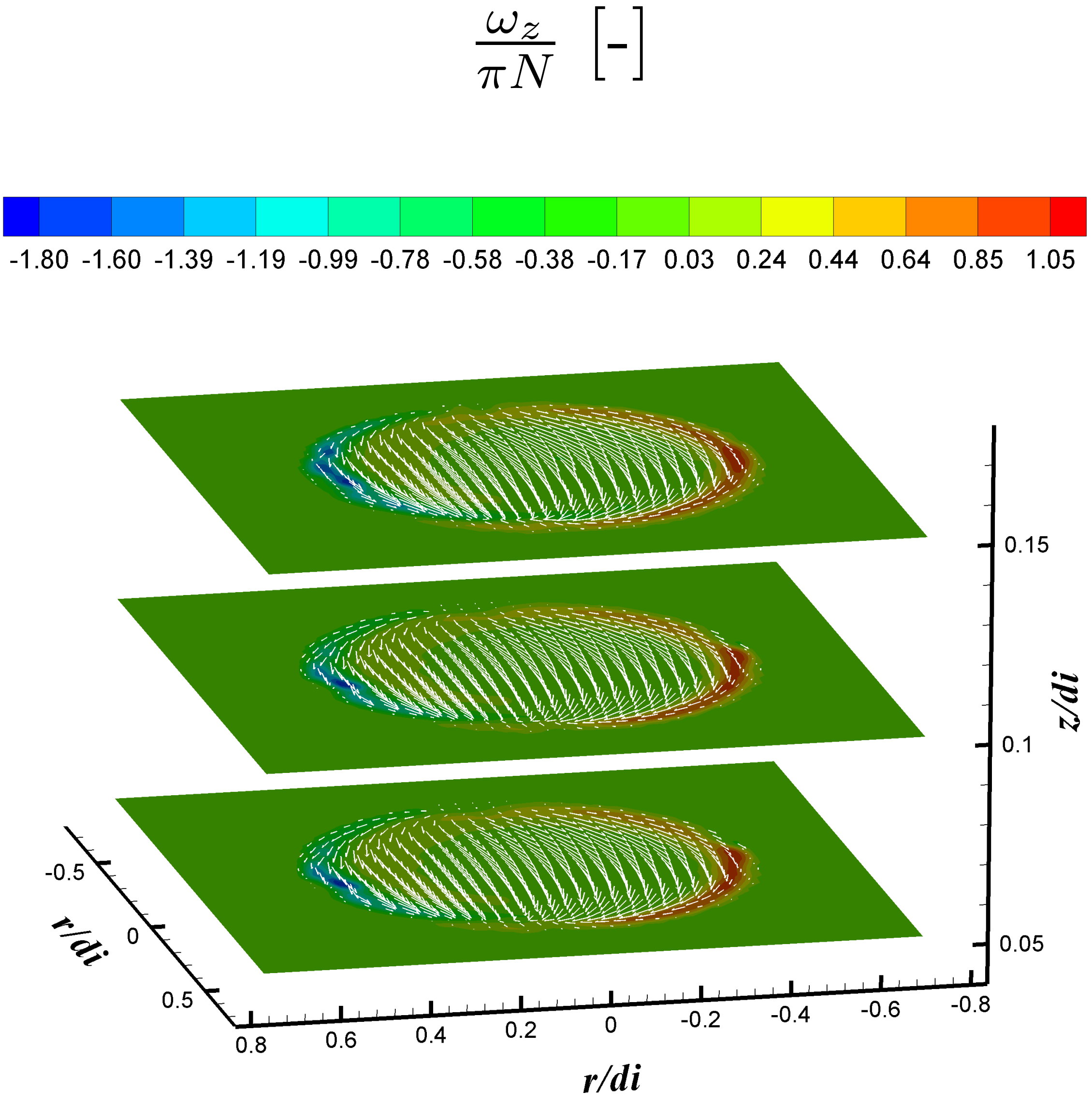

Figure 5.10: Phase-resolved vector fields and contour plots of the axial vorticity, ω_z, at three different elevations, z/d_i=0.05, 0.1 and 0.15 for ν=1×10^{-4} m^{2}s^{-1}(h/d_i=0.3, ϕ=180°, Fr=0.09, d_o/d_i=0.25, z/d_i=0.1).

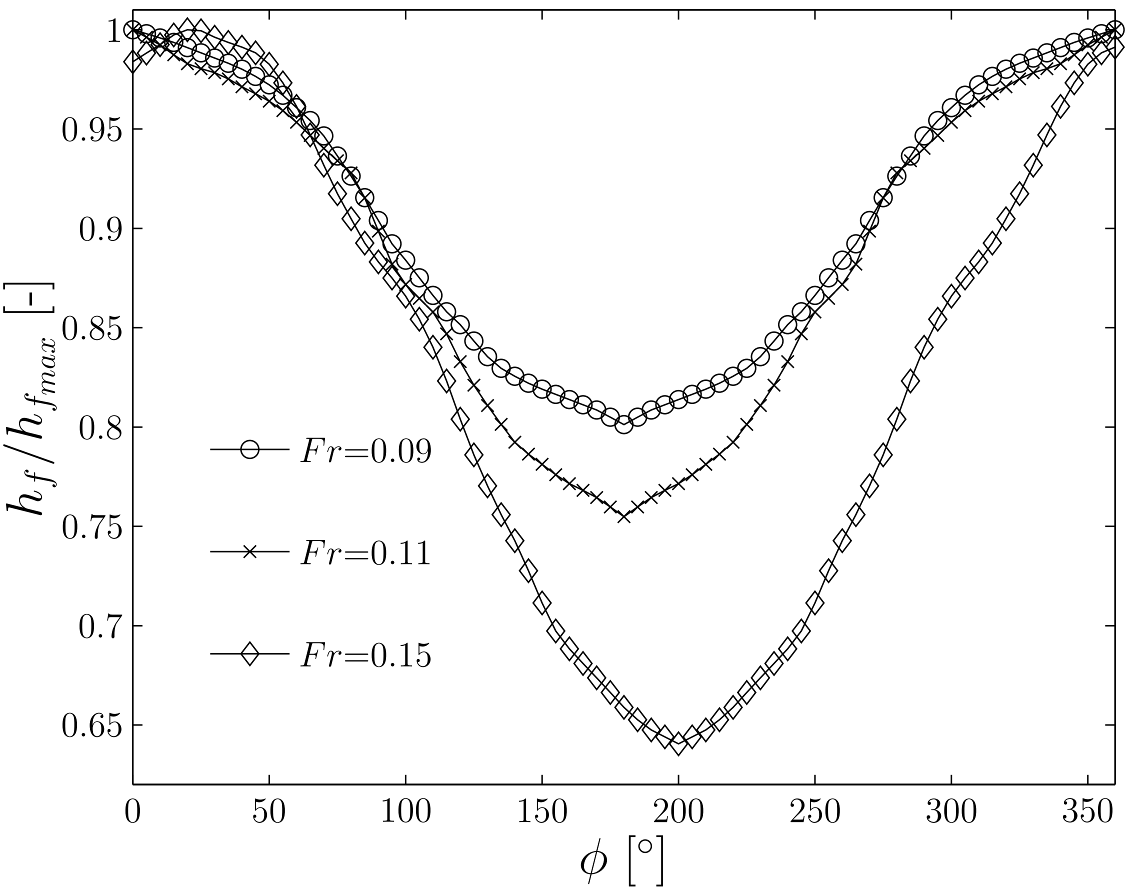

Figure 5.11: Variation of the non-dimensional free surface height at the left side wall, $h_f/h_{f_{max}}$, with phase angle, ϕ, for ν=1×10^{-5} m^{2}s^{-1} (h/d_i=0.3, d_o/d_i=0.25).

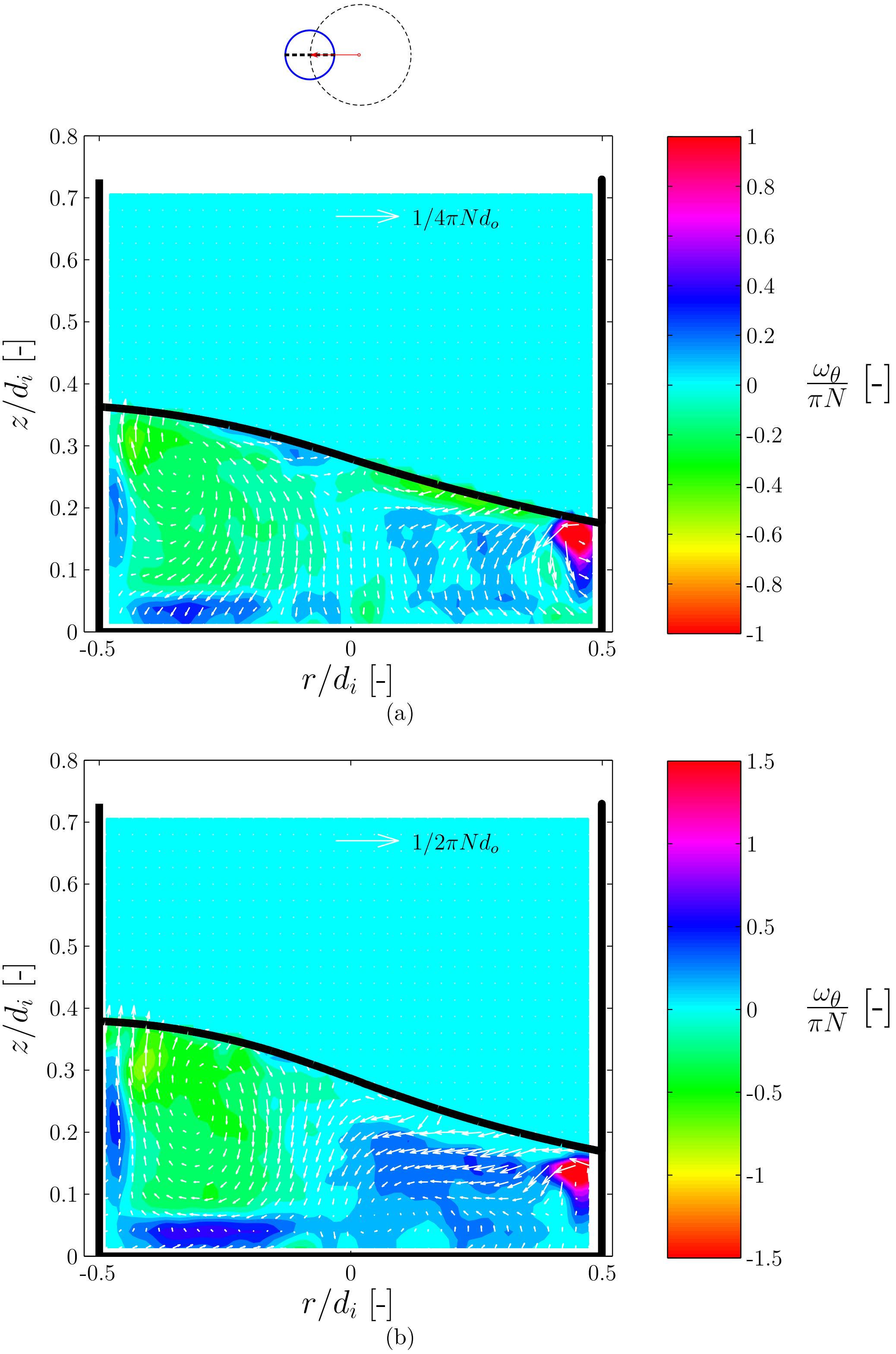

Figure 5.12: Phase-resolved vector fields and contour plots of the tangential component of the vorticity, ω_θ, for $\nu=1\times10^{-5}$ $\mathrm{m^2s^{-1}}$ ($h/d_i=0.3$, $\phi=0°$, $d_o/d_i=0.25$): (a) $Fr=0.14$ ($N=100$ rpm); (b) $Fr=0.17$ ($N=110$ rpm).

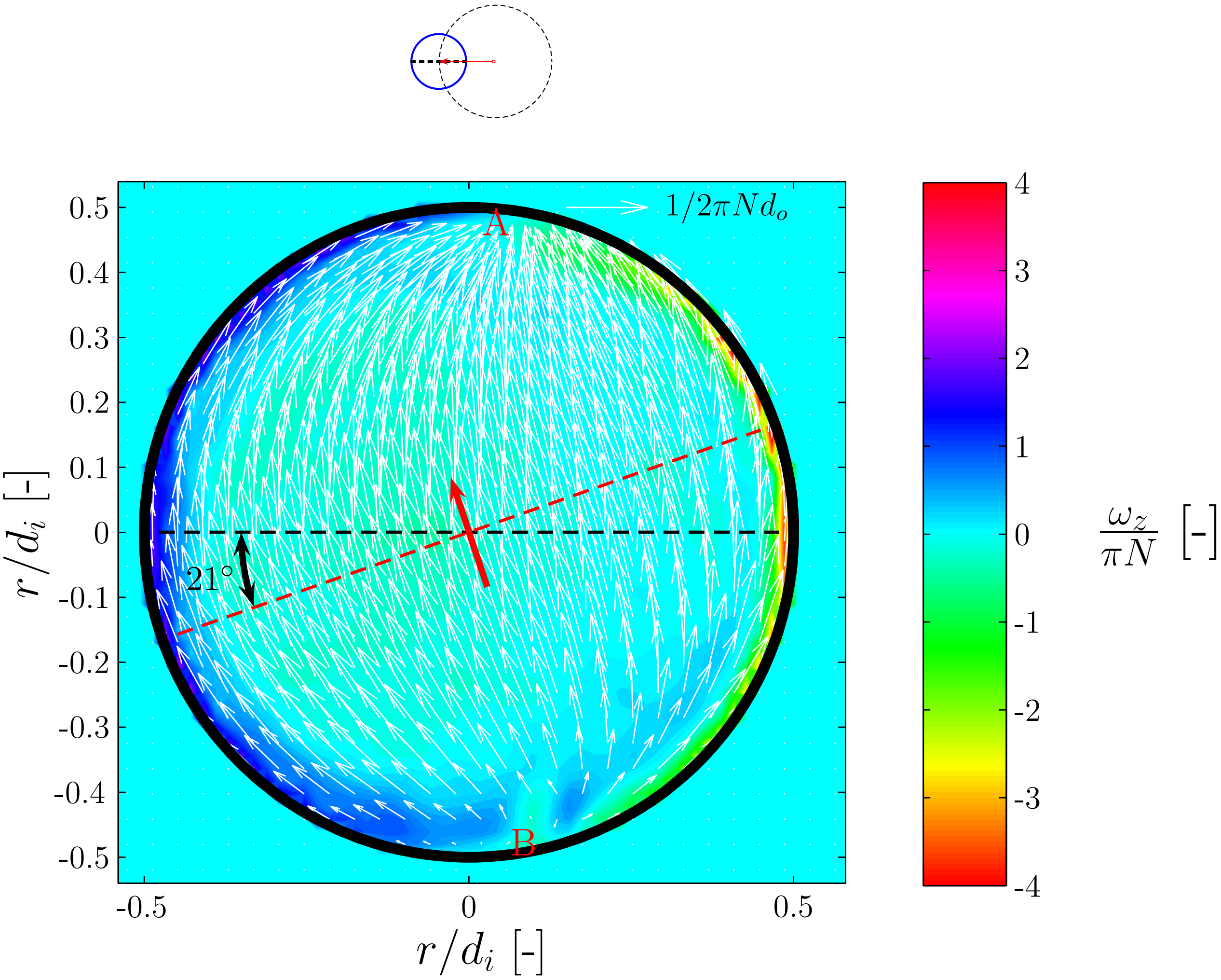

Figure 5.13: Phase-resolved vector field and contour plot of the axial component of the vorticity, ω_z, at an elevation of z/d_i=0.1 for ν=1×10^{-5} m^{2}s^{-1} (h/d_i=0.3, ϕ=0°, Fr=0.17, d_o/d_i=0.25).

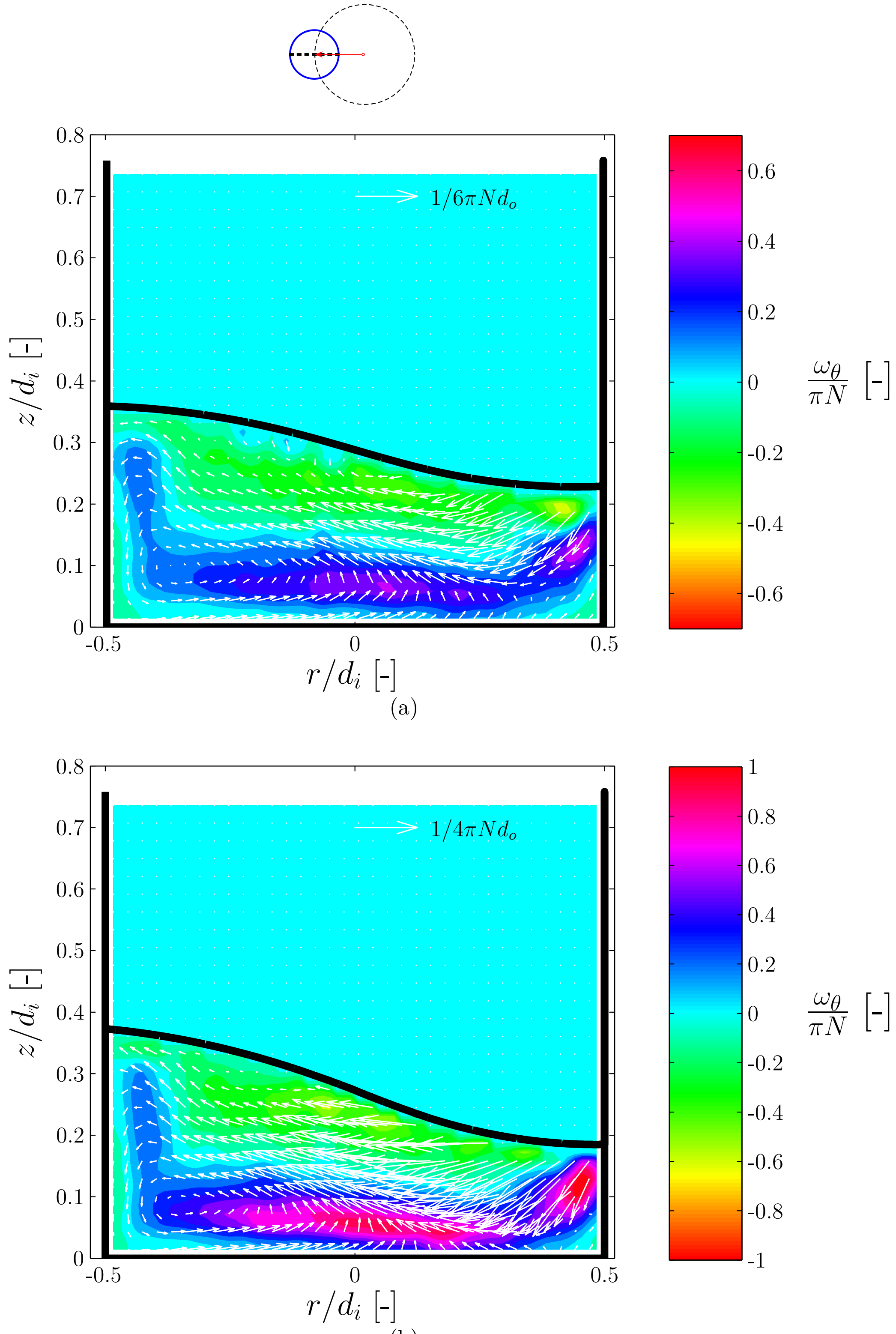

(a)

(b)

Figure 5.14: Phase-resolved vector fields and contour plots of the tangential component of the vorticity, ω_θ, for ν=1×10^{-4} m^{2}s^{-1} (h/d_i=0.3, ϕ=0°, d_o/d_i=0.25): (a) Fr=0.11 (N=90 rpm); (b) Fr=0.14 (N=100 rpm).

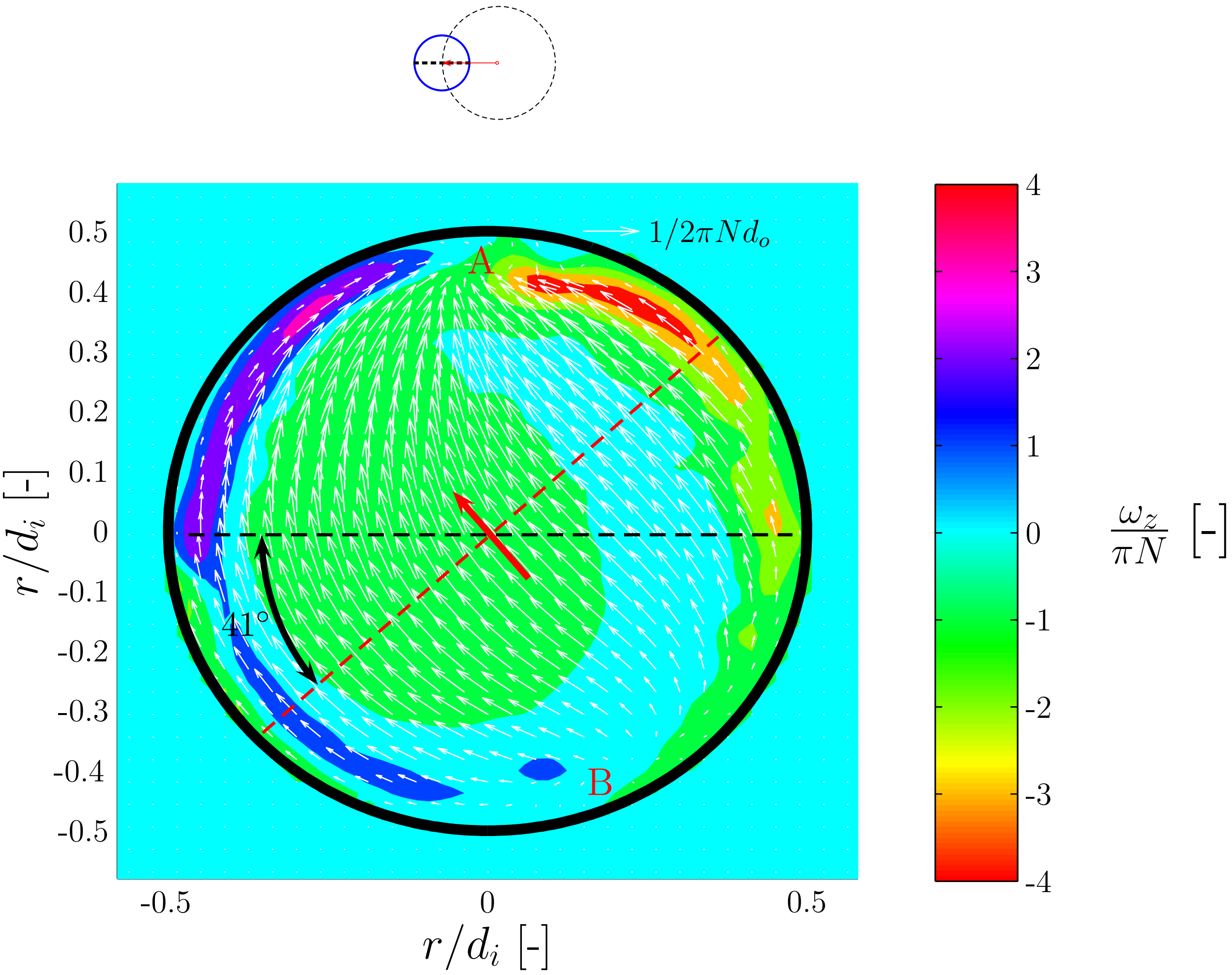

Figure 5.15: Phase-resolved vector field and contour plot of the axial component of the vorticity, ω_z, at an elevation of z/d_i=0.1 for ν=1×10^{-4} m^{2}s^{-1} (h/d_i=0.3, ϕ=0°, Fr=0.14, d_o/d_i=0.25) .

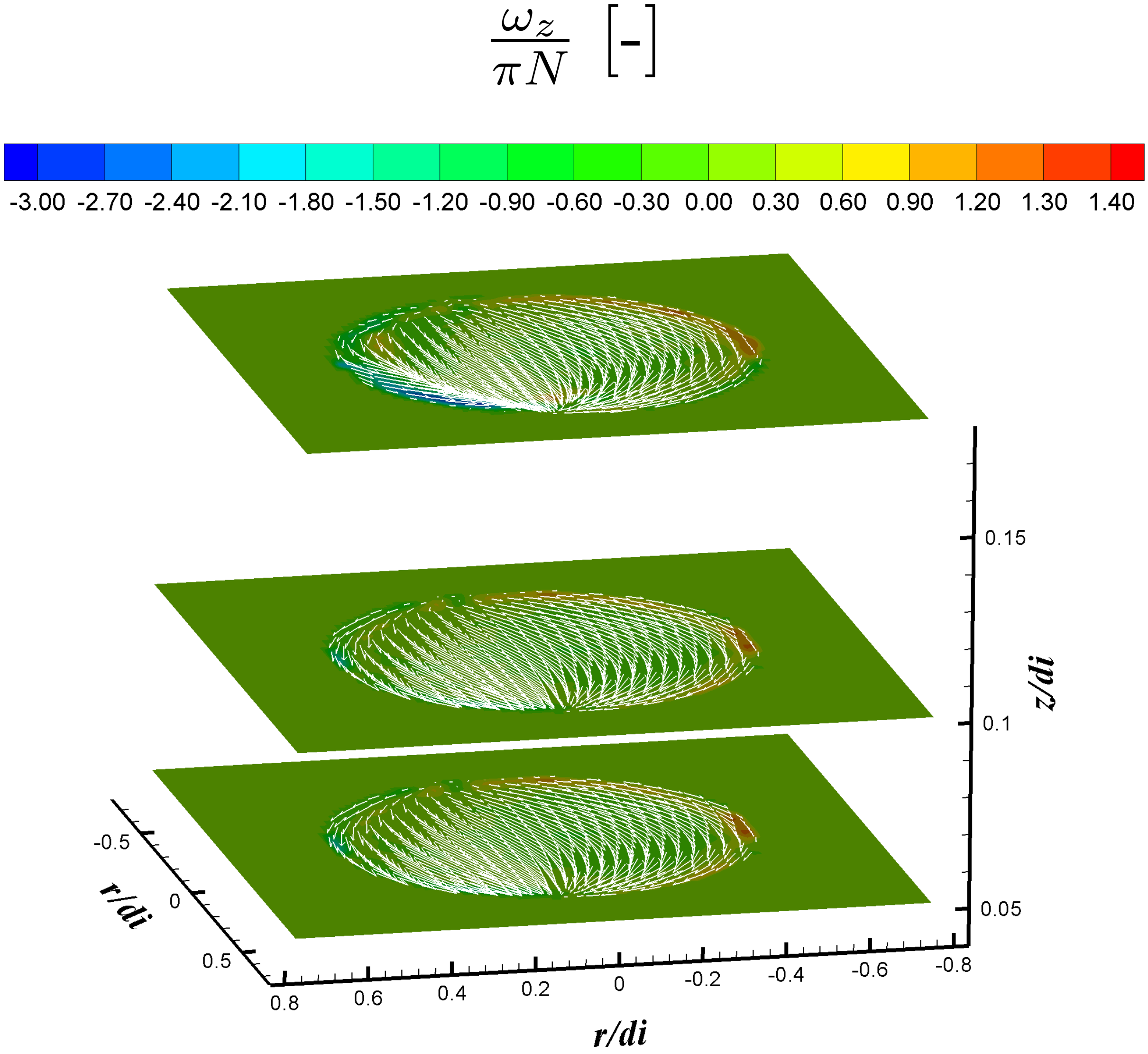

Figure 5.16: Phase-resolved vector fields and contour plots of the axial component of the vorticity, ω_z, at three different elevations, z/d_i=0.05, 0.1 and 0.175 for ν=1×10^{-5} m^{2}s^{-1} (h/d_i=0.3, ϕ=180°, Fr=0.17, d_o/d_i=0.25).

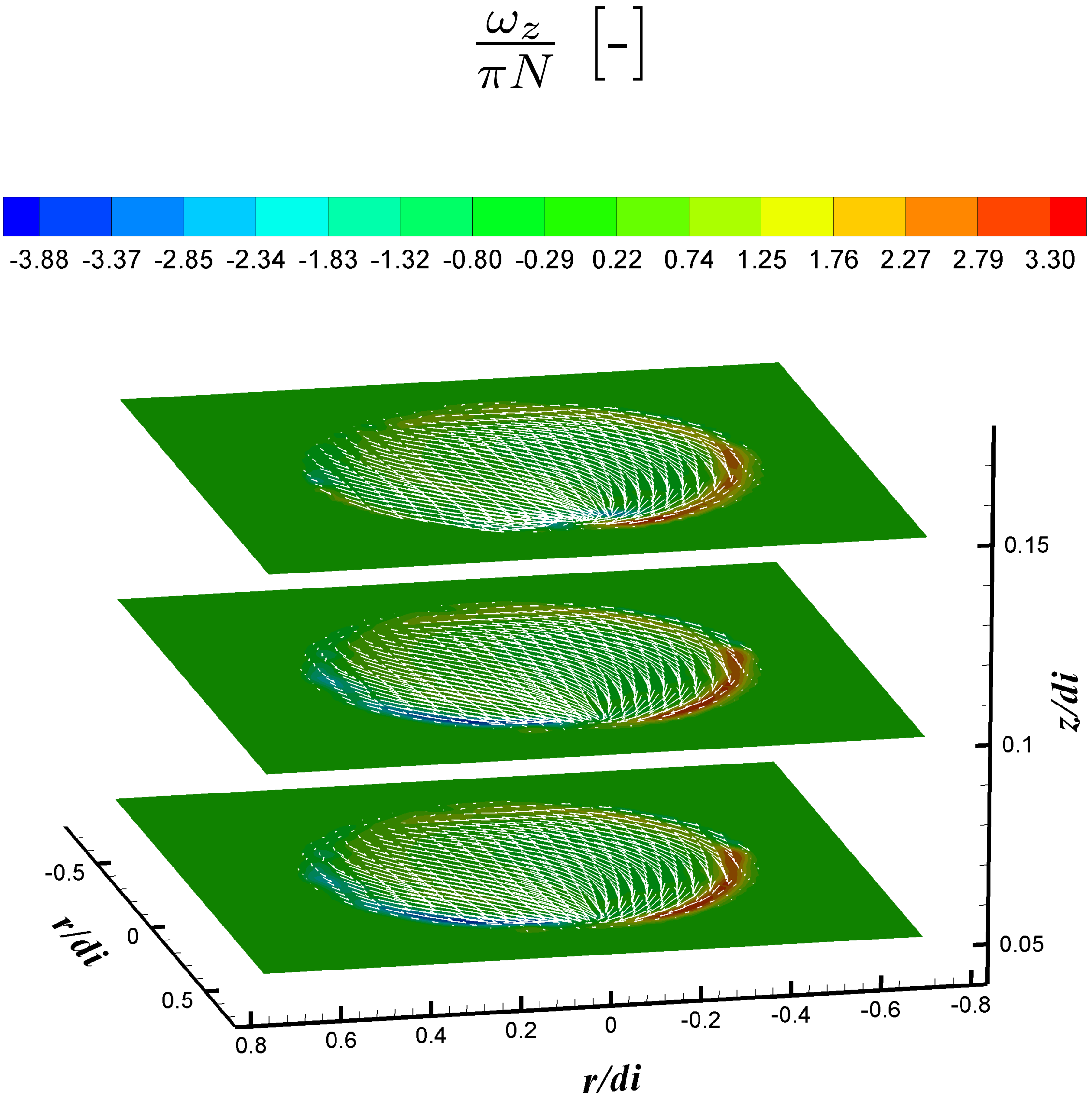

Figure 5.17: Phase-resolved vector fields and contour plots of the axial component of the vorticity, ω_z, at three different elevations, z/d_i=0.05, 0.1 and 0.15 for $\nu=1\times10^{-4}$ m^{2}s^{-1} (h/d_i=0.3, ϕ=180°, Fr=0.14, d_o/d_i=0.25).

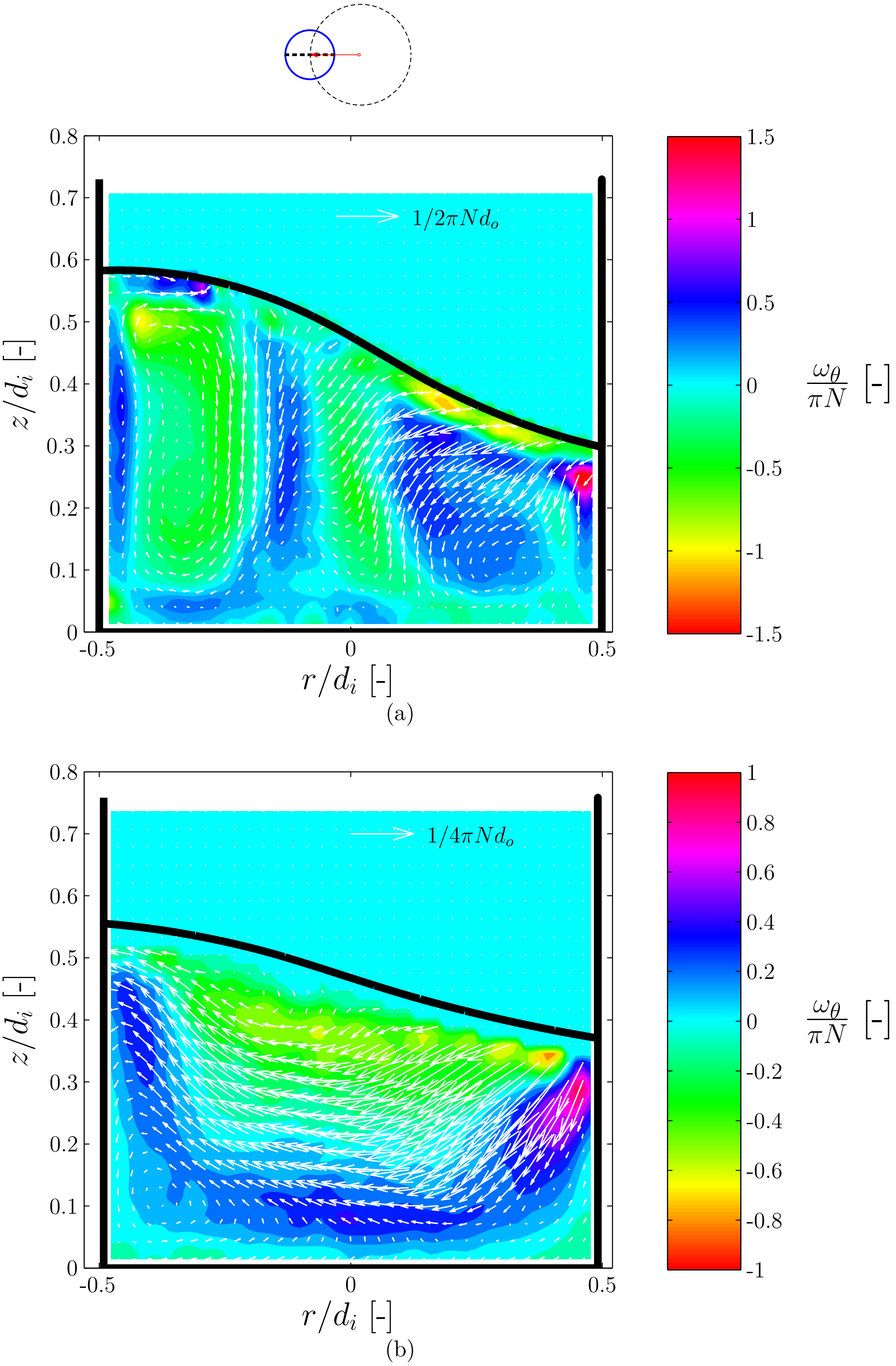

(a)

(b)

Figure 5.18: Phase-resolved vector fields and contour plots of the tangential component of the vorticity, ω_θ, for h/d_i=0.5 (ϕ=0°, d_o/d_i=0.25): (a) Fr=0.2 (N=120 rpm) and ν=1×10^{-5} m^{2}s^{-1}; (b) Fr=0.15 (N=102 rpm) and ν=1×10^{-4} m^{2}s^{-1}.

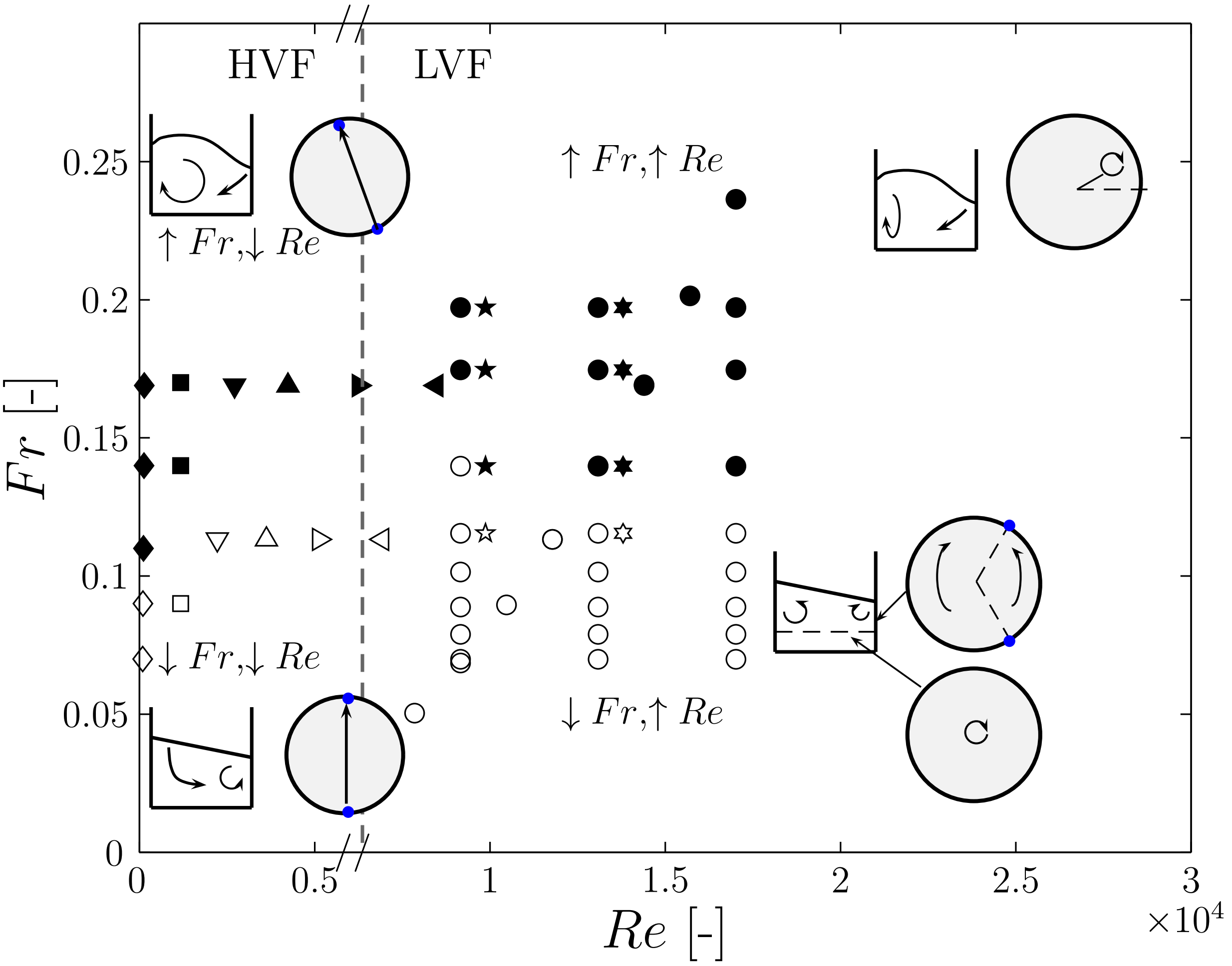

Figure 5.19: Map of the combinations of Fr and Re examined with schematic visualisations of the associated in-phase and out-of-phase flow fields (h/d_i=0.3).

Low Viscous Fluids (LVF): ν=1×10^{-6} m^2s^{-1} (○ in-phase, ● out-of-phase), ν=1.3×10^{-6} m^2s^{-1} (✡ in-phase, ✶ out-of-phase), ν=1.4×10^{-6} m^2s^{-1} (☆ in-phase, ★ out-of-phase), ν=1.7×10^{-6} m^2s^{-1} (◁ in-phase, ◀ out-of-phase);

High Viscous Fluids (HVF): ν=2.3×10^{-6} m^2s^{-1} (▷ in-phase, ▶ out-of-phase), ν=3.25×10^{-6} m^2s^{-1} (△ in-phase, ▲ out-of-phase), ν=5.3×10^{-6} m^2s^{-1} (▽ in-phase, ▼ out-of-phase), ν=1×10^{-5} m^2s^{-1} (□ in-phase, ■ out-of-phase), ν=1×10^{-4} m^2s^{-1} (◊ in-phase, ♦ out-of-phase).

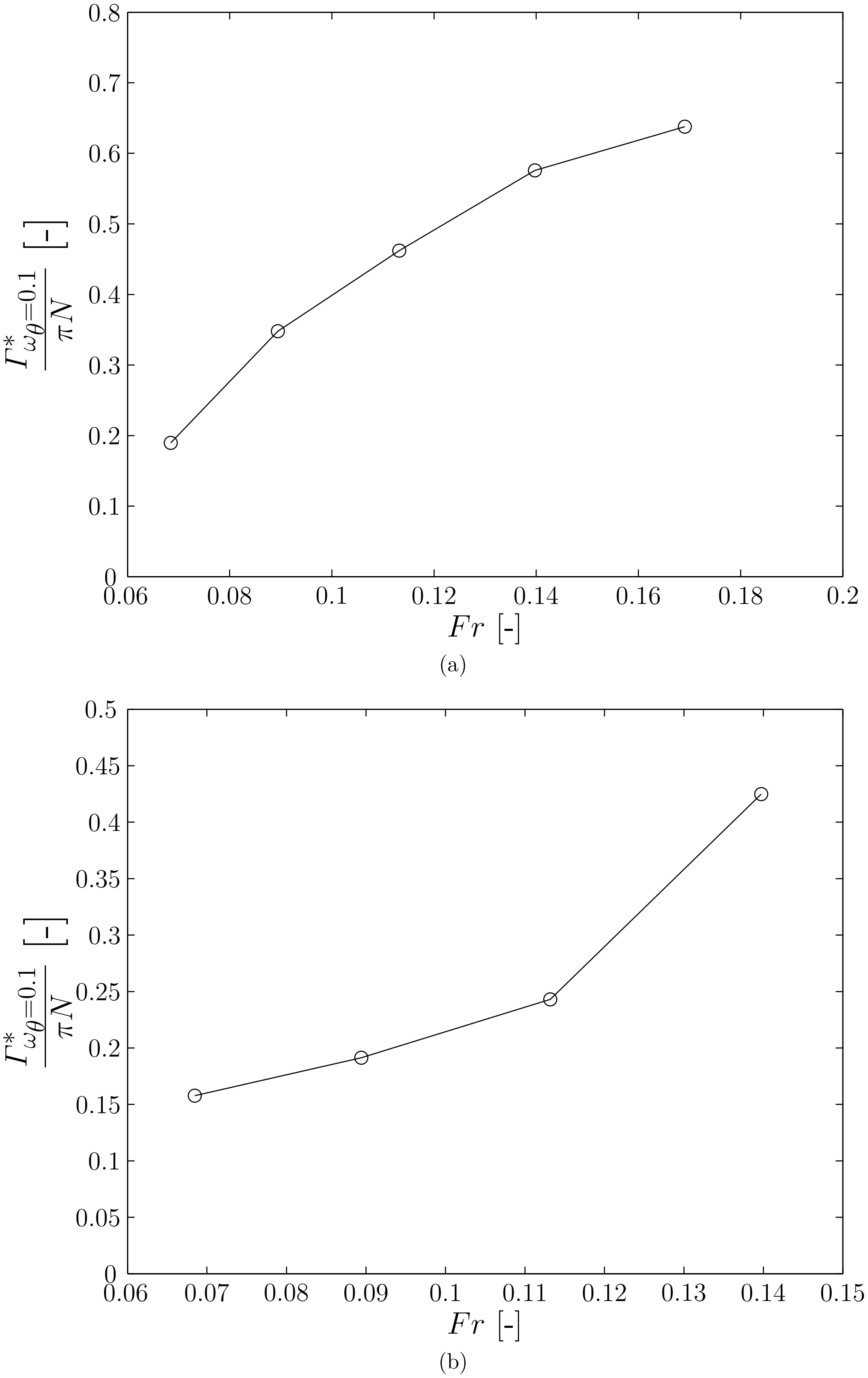

(a)

(b)

Figure 5.20: Variation of the space-averaged non-dimensional circulation, $\Gamma^*_{\omega_\theta=0.1}$, with increasing Fr (h/d_i=0.3, ϕ=0°, d_o/d_i=0.25): (a) ν=1×10^{-5} m^{2}s^{-1}; (b) ν=1×10^{-4} m^{2}s^{-1}.

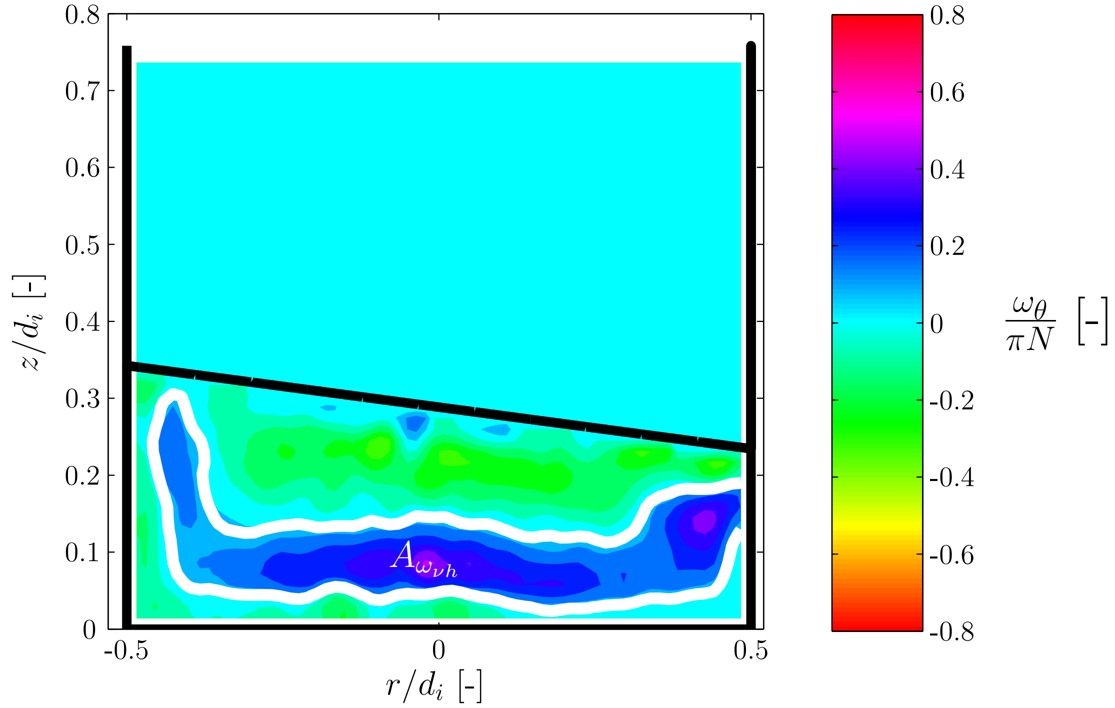

Figure 5.21: Visualisation of the area, $A_{\omega_{\nu h}}$, used to estimate the circulation $\Gamma^*_{\omega_\theta=0.1}$ for ν=1×10^{-4} m^{2}s^{-1} (h/d_i=0.3, ϕ=0°, N=80 rpm, d_o/d_i=0.25)

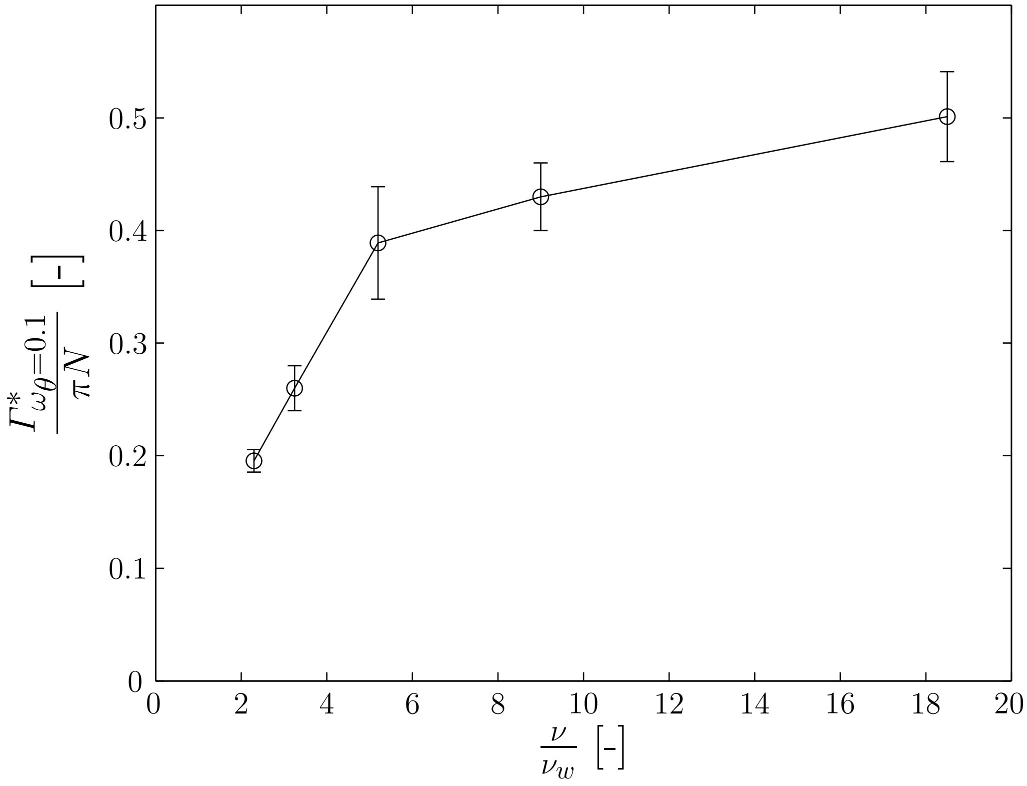

Figure 5.22: Variation of the space-averaged circulation, $\Gamma^*_{\omega_\theta=0.1}$, with the non-dimensional viscosity ν/ν_w (h/d_i=0.3, ϕ= 0° and d_o/d_i=0.25).

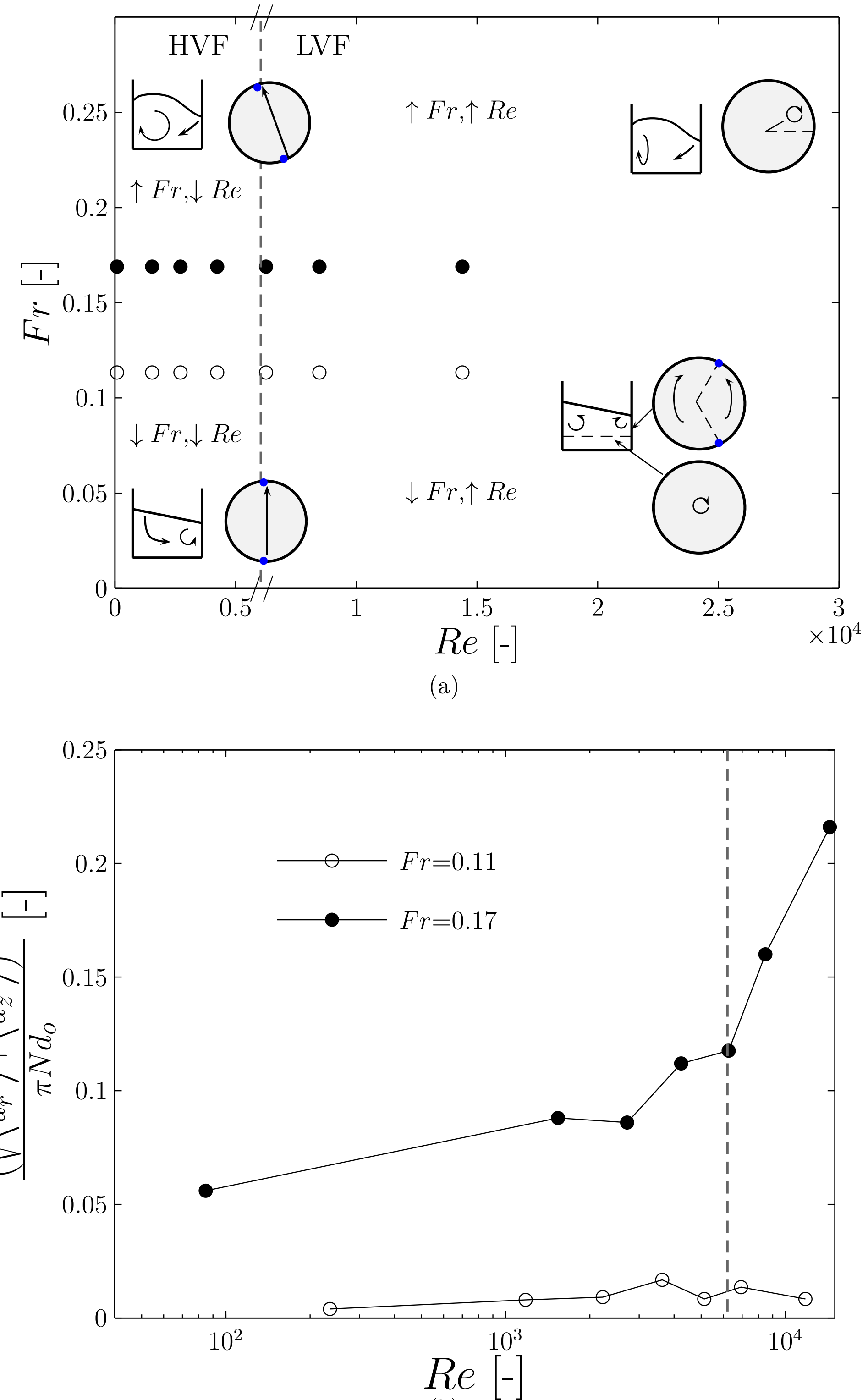

(a)

(b)

Figure 5.23: (a) Visualisation on the Fr-Re map of the two sets of data of constant Fr used to measure the turbulent kinetic energy, $\left(\sqrt{\langle u_r'^2\rangle^* + \langle u_z'^2\rangle}\right)^*$, (○ in-phase, ● out-of-phase); (b) Variation of the turbulent kinetic energy reference velocity, $\left(\sqrt{\langle u_r'^2\rangle + \langle u_z'^2\rangle}\right)^*$, with Re for high and low Fr.

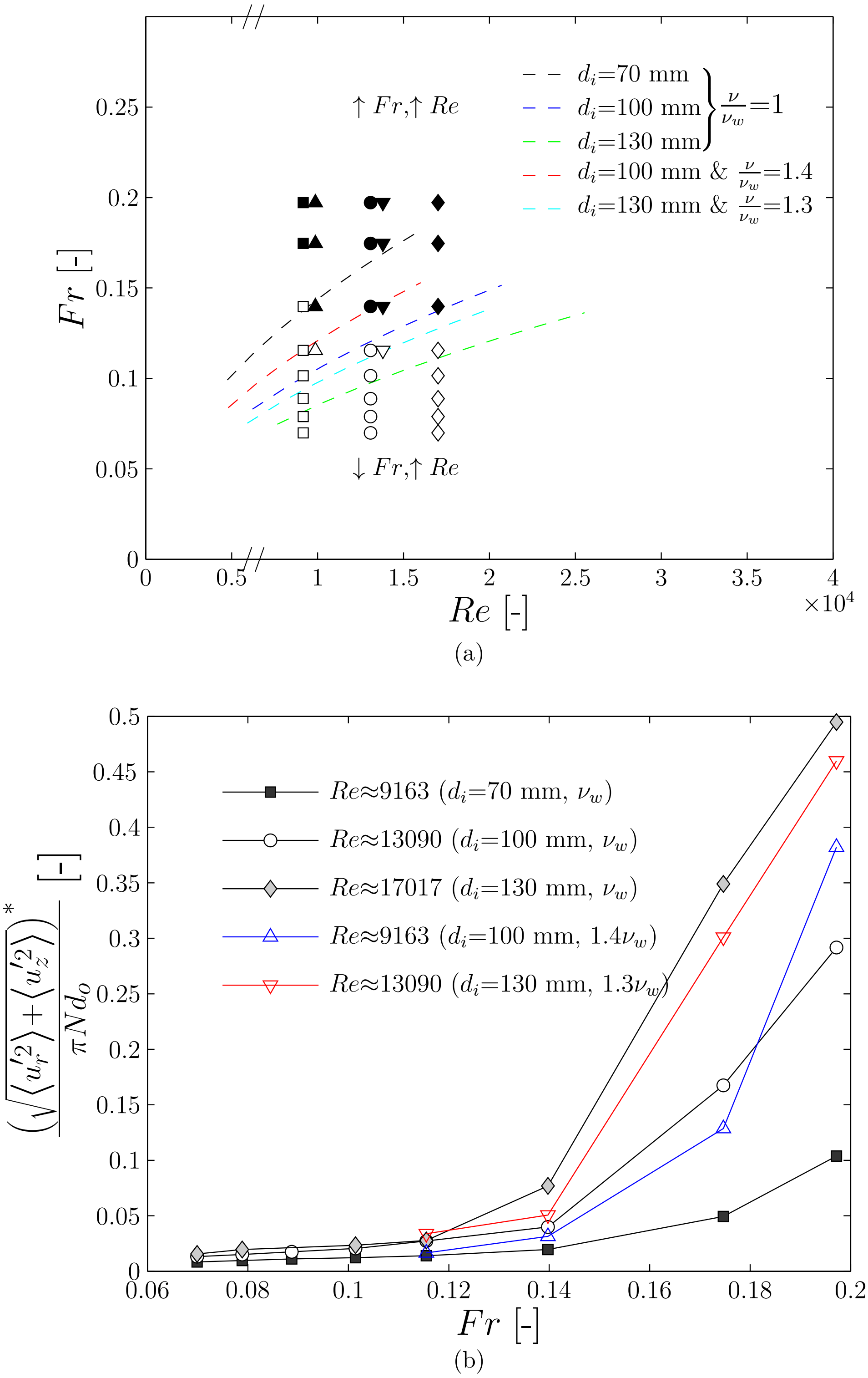

(a)

(b)

Figure 5.24: (a) Points on the Re-Fr map used to assess the variation of the space-averaged turbulent kinetic energy, $\left(\sqrt{\langle u_r'^2\rangle + \langle u_z'^2\rangle}\right)^*$: d_i=70 mm and $\frac{\nu}{\nu_w}$=1 (□ in-phase, ■ out-of-phase); d_i=100 mm and $\frac{\nu}{\nu_w}$=1 (○ in-phase, ● out-of-phase); d_i=130 mm and $\frac{\nu}{\nu_w}$=1 (◇ in-phase, ♦ out-of-phase); d_i=100 mm and $\frac{\nu}{\nu_w}$=1.4 (△ in-phase, ▲ out-of-phase); d_i=130 mm and $\frac{\nu}{\nu_w}$=1.3 (▽ in-phase, ▼ out-of-phase); (b) Variation of the turbulent kinetic energy reference velocity with Froude number, Fr, for three sets of Reynolds number.

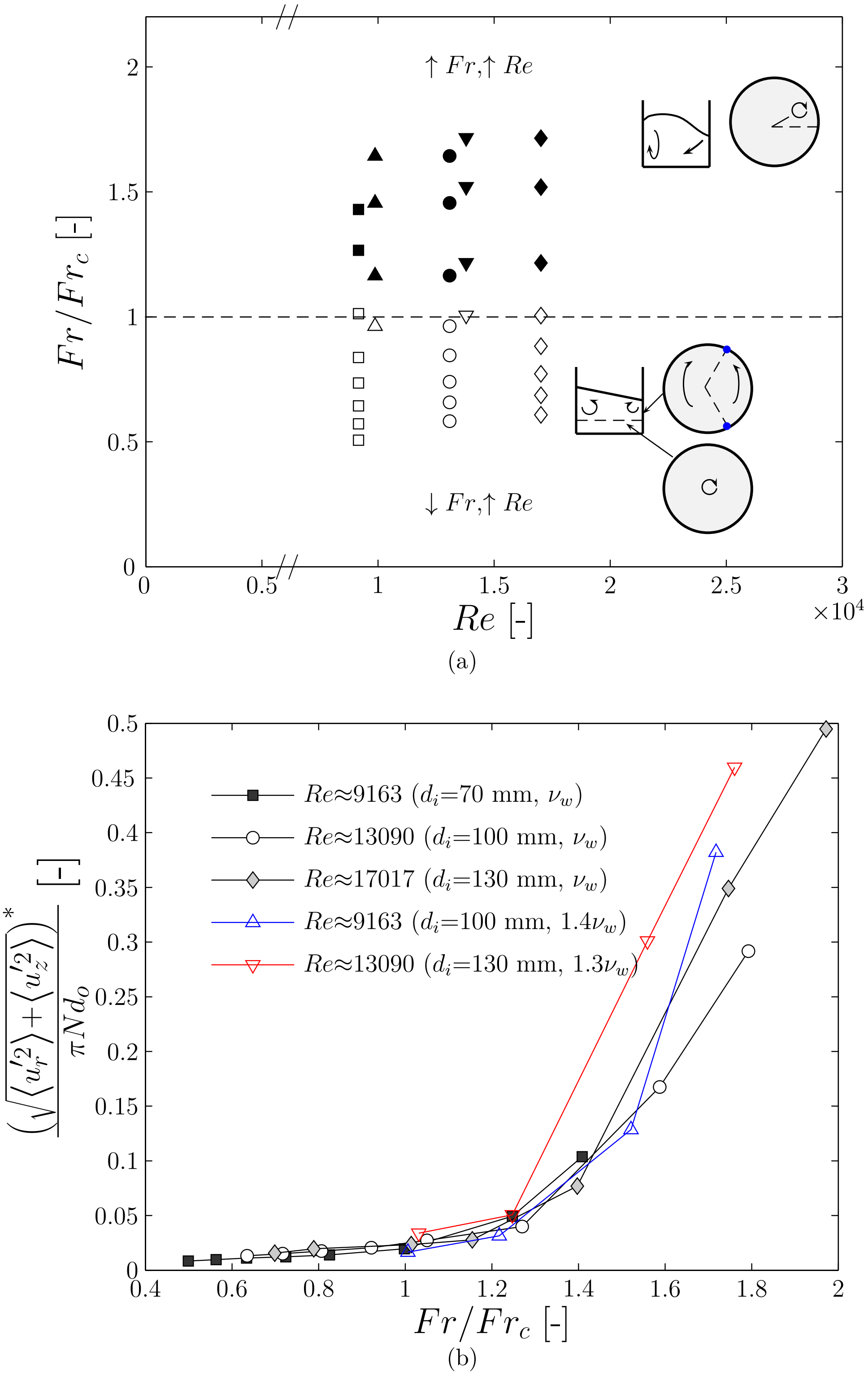

Figure 5.25: (a) Points on the Re-Fr/Fr_c map used to assess the variation of the space-averaged turbulent kinetic energy, $\left(\sqrt{\langle u_r'^2\rangle+\langle u_z'^2\rangle}\right)^*$: d_i=70 mm and $\frac{\nu}{\nu_w}$=1 (□ in-phase, ■ out-of-phase); d_i=100 mm and $\frac{\nu}{\nu_w}$=1 (○ in-phase, ● out-of-phase); d_i=130 mm and $\frac{\nu}{\nu_w}$=1 (◇ in-phase, ◆ out-of-phase); d_i=100 mm and $\frac{\nu}{\nu_w}$=1.4 (△ in-phase, ▲ out-of-phase); d_i=130 mm and $\frac{\nu}{\nu_w}$=1.3 (▽ in-phase, ▼ out-of-phase); (b) Variation of the space-averaged turbulent kinetic energy with Fr/Fr_c, for three sets of Reynolds number.

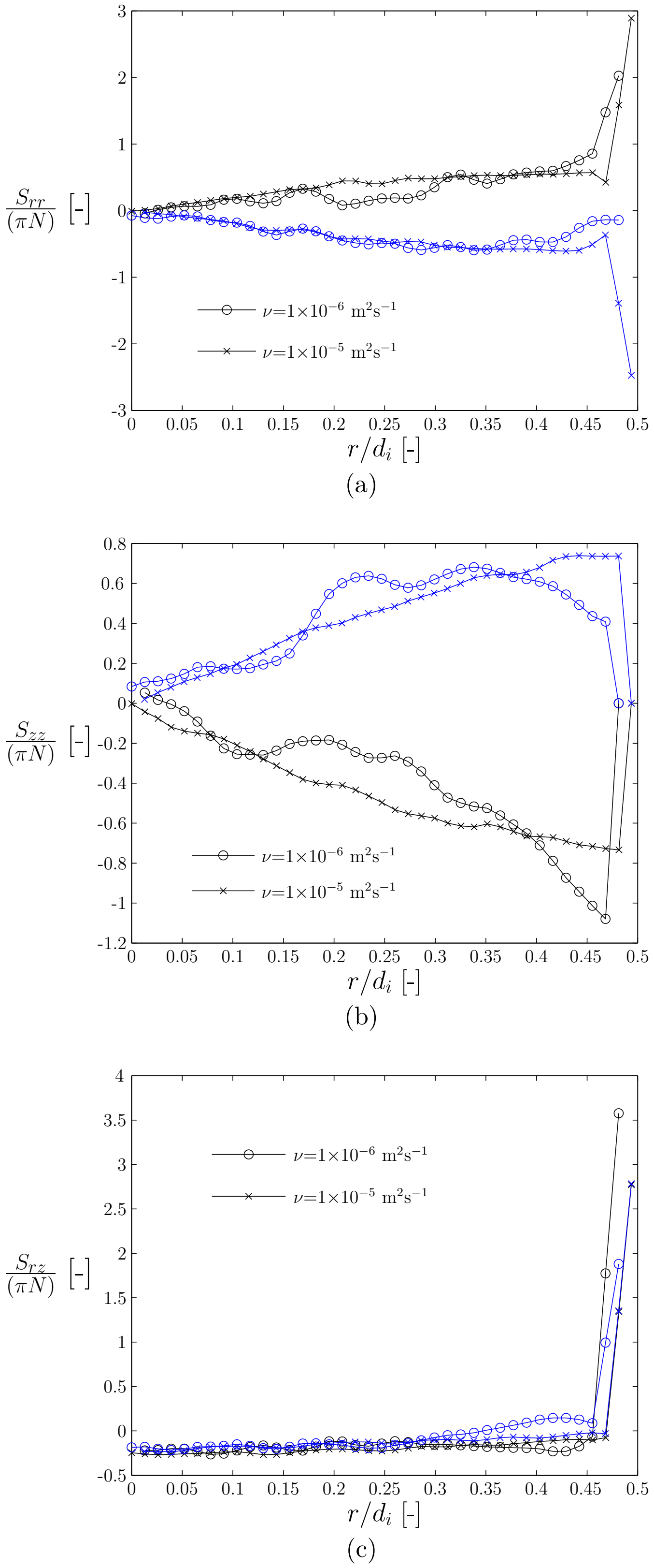

Figure 5.26: Radial profiles of the strain and shear rates for ν=1×10^{-6} m^{2}s^{-1} and ν=1×10^{-5} m^{2}s^{-1} at an elevation of z/d_i=0.1 (h/d_i=0.3, ϕ=270°, Fr=0.11 and d_o/d_i=0.25) (a) S_{rr}; (b) S_{zz}; (c) S_{rz}.

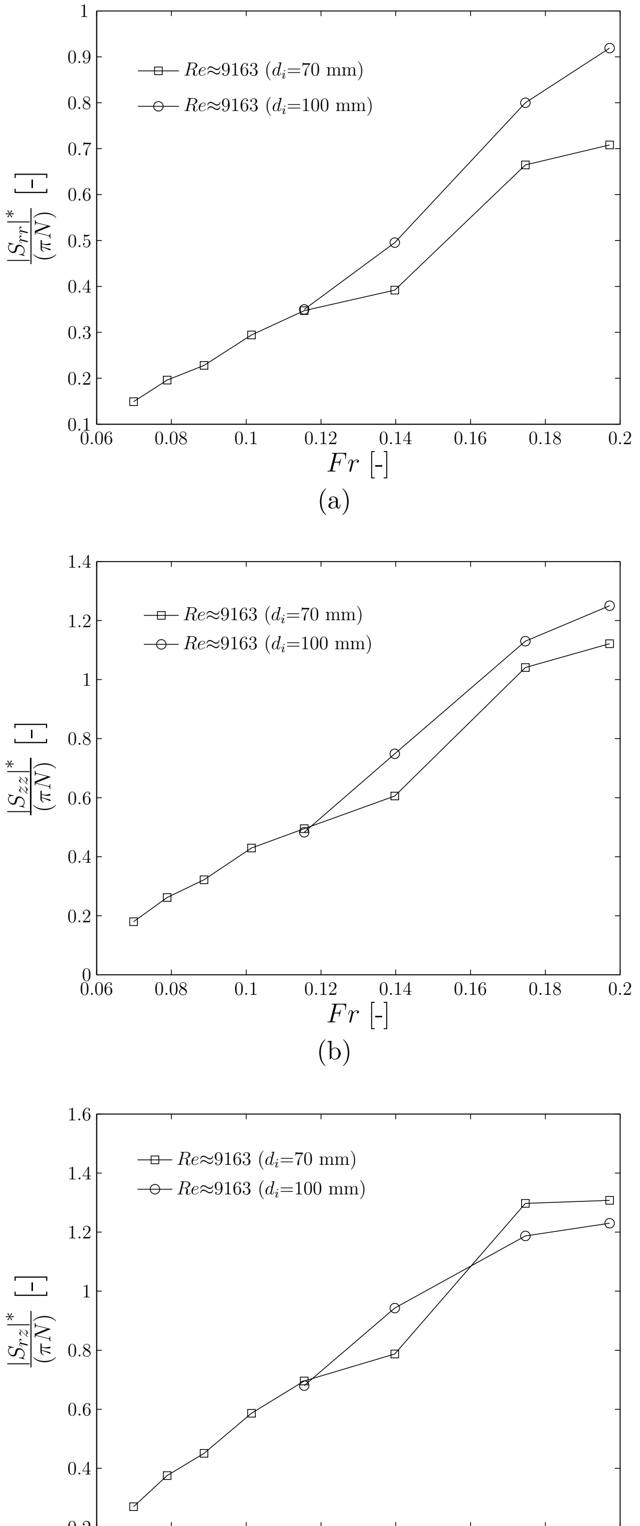

(a)

(b)

(c)

Figure 5.27: Variation of the space-averaged strain and shear rates with increasing Fr (h/d_i=0.3, ϕ= 270°); (a) $|S_{rr}|^*$; (b) $|S_{zz}|^*$; (c) $|S_{rz}|^*$.

Chapter 6

Conclusions and recommendations for future work

6.1 The present contribution

The major objective of the research presented in this thesis was to provide a detailed analysis of the fluid dynamics in a cylindrical shaken bioreactor, and to shed light on the transition between in phase and out of phase flow regimes documented in the literature. The research was organised in the attempt to address both fundamental and engineering aspects of the flow in a cylindrical shaken bioreactor, and to improve bioprocess design and scale-up by deriving a scaling law that allows to predict the flow transition to out-of-phase conditions, and to select the most suitable turbulence levels for the bioprocess considered. Quantification of flow parameters relevant to shaken bioreactor operations, such as the free surface interfacial area, the kinetic energy, the viscous dissipation rate of kinetic energy, the circulation time and the vortex size was provided by means of phase resolved PIV measurements for a broad range of operating conditions.

In the first stage of the research project an optimum set up of the camera, laser and mirrors had to be found to be able to accurately resolve the flow in vertical and horizontal planes of measurement for every angular position ϕ assumed by the bioreactor along its orbit. The final set up allowed to address the optical distortion induced by refraction at the moving free surface, while free surface identification and masking algorithms were developed and implemented to improve PIV adaptive correlation routines (cf. Chapter 2).

An extensive analysis of the flow dynamics occurring in a shaken bioreactor when working with a fluid of low viscosity (i.e water) was carried out for different operating conditions, ϕ, h, N, d_o and d_i (cf. Chapter 3). These measurements allowed to characterise the different flows for in phase and out of phase conditions, and a flow scaling law based on the orbital Froude number was identified, that correlates the shape and inclination of the free surface to the occurrence of the flow transition. The law was derived from physical considerations based on the inclination of the free surface when subject to the concurrent action of the gravitational and centrifugal accelerations. Beside Fr, non-dimensional geometrical characteristics such as the orbital to cylinder diameter ratio, d_o/d_i, and the non-dimensional fluid height, h/d_i were found to significantly affect the flow in the bioreactor. The scaling law was further validated using the free surface visualisations provided in the works of Tissot *et al.* (2010) and Zhang *et al.* (2009).

In the first part of Chapter 4 free surface measurements were carried out to determine the interfacial area, I_a, for different h, N, d_o and d_i at low ν. The measured interfacial area was compared to that obtained from an analytical solution and valid only at low Froude number. In the second part of Chapter 4 the strength, size and location of the large scale vortical structures occurring in the cylindrical shaken bioreactor for in phase and out of phase regimes were discussed. Measurements of the kinetic energy due the periodic and random velocity fluctuations were obtained, and it was found that the in phase to out of phase flow variation corresponds to the onset of a laminar-turbulent flow transition. In the final part of Chapter 4 estimates of the viscous dissipation rate of kinetic energy for different spatial resolutions and of the volumetric power consumption were provided.

The flow dynamics analysis was extended to fluids of higher viscosity than water in Chapter 5. Depending on the fluid viscosity two distinguished in phase and out of phase flow transitions were found for low and high Reynolds number. The flow scaling law determined for water was found to be still valid for $\nu \leq 1.7\times10^{-6}$ $\mathrm{m}^2\mathrm{s}^{-1}$. A *Re*-*Fr* flow transition map was formulated between the four different flows occurring in the cylindrical bioreactor for different operating conditions. An analysis of the turbulent kinetic energy content showed that improved scaling procedures should be based on the ratio between the working Froude number and the transitional one, Fr/Fr_c. A 2D approximation of the rate of strain tensor was investigated for different combinations of Fr and *Re* to determine local areas of fluid elements compression and stretching.

The main findings of the research are outlined in the following section. The chapter and the thesis close with recommendations for future work which are given in the Section 6.3.

6.2 Main findings of the investigation

In the first stage, the large scale vortical structures occurring in an orbitally shaken bioreactor of cylindrical bioreactor were investigated. Phase resolved PIV measurements were carried out in water for varying phase angles, ϕ, using a reference configuration with operating conditions, h =30 mm, N =90 rpm, d_o = 25 mm and d_i =100 mm. It was found that at this phase angle ϕ=0° the free surface reaches its maximum inclination and two counter-rotating vortices are observed close to the cylinder walls. For increasing ϕ the free surface starts to oscillate and a radial flow develops from the left vortical cell towards the right one.

A study was then carried out to assess the variation of the flow field with increasing shaking frequency, N. In this case measurements were obtained for a fixed phase angle $\phi = 0°$, and operating conditions (d_o =25 mm, h = 30 mm and d_i =100 mm). In agreement with the literature two different zones, characterised by different mixing dynamics, were observed. A first zone close to the free surface where mixing is enhanced by the transport action of the two counter-rotating vortices (denoted as "convection zone"), and a second zone close to the bottom of the cylinder where mixing is mainly controlled by diffusion (denoted as "diffusion zone"). The size of the two zones changed as the shaking frequency was increased, with the "convection zone" extending towards the bottom of the tank for higher N. The free surface tracking measurements showed that at low shaking frequency, N, the free surface can be approximated by an elliptical disk, while at higher N the free surface becomes 3D and its intersection with the vertical laser plane exhibited a wavy profile. Under these conditions (i.e. high N range) a significant change in flow pattern occurs, and the two counter-rotating vortices are pushed against the wall to eventually disappear for the highest N investigated.

Similarly the flow pattern obtained from horizontal planes of measurement varied significantly when the shaking speed was increased. In the low N range it was found that solid body rotation occurred in the "diffusion zone", while to streams emanating from and merging into two in plane stagnation points were identified in the "convective zone" on planes closer to the free surface. When the speed was increased in the high N range the stagnation points disappeared and one vortex with off-centred vertical axis was found to precess around the cylinder axis.

The degree of out of phase determined from the horizontal PIV measurements matched that estimated from the variation of the free surface height, h_f, at the left wall of the bioreactor with phased angle ϕ.

A scaling law based on the free surface wave amplitude, $\Delta h/d_i$, and orbital Froude number, Fr, was derived to predict the type of flow field occurring in the cylindrical shaken bioreactor when the speed was increased. In the first stage the orbital and cylinder diameters were set constant to d_o =25 mm and d_i =100 mm, respectively. A linear relationship was obtained between the free surface wave amplitude, $\Delta h/d_i$, and Fr when the flow is in-phase and the free surface inclination is constant across the free surface profile, while at higher N the data were more scattered about the reference line due to the wavy nature of the free surface for out-of-phase condition. For d_o=25 mm and d_i=100 mm it was found that transition occurs when h/d_i=$2a_{ow}Fr$ if the non-dimensional fluid height h/d_i <0.5, while for h/d_i >0.5 the transitional speed can be derived from $a_{ow}Fr$=0.25. In the latter case the toroidal vortex does not reach the bottom of the cylinder for any shaking speed N.

The scaling law obtained for fixed d_o and d_i was extended to different combinations of d_o and d_i, and it was shown that when $h/d_i < (d_o/d_i)^{0.5}$ transition occurs for $(d_o/d_i)^{0.5} = (d_i/h)\ Fr\ a_{ow}$, while the critical shaking speed can be found from Fr_{d_i} using $a_{ow}Fr_{d_i} = 1$ when $h/d_i > (d_o/d_i)^{0.5}$. Again it should be noted that Fr_{d_i} is the Froude number based on the cylinder diameter, d_i, and for $h/d_i > (d_o/d_i)^{0.5}$ the toroidal vortex does not reach to the bottom of the cylinder for any speed.

A thorough analysis to determine the interfacial area of the free surface, I_a, was carried in the first part of Chapter 4. It was found that for a low Froude number the free surface can be approximated by an inclined elliptic disk, while at greater Froude number the free surface is characterised by a more pronounced 3D shape. The interfacial area directly measured was compared against that obtained from the linear relationship of the free surface wave amplitude and Fr, and a good agreement was found between the two estimates at low Fr when the flow is fully in-phase. The non-dimensional time and length scales of the vortical structures occurring in the cylindrical bioreactor were determined to provide an insight into the mixing dynamics. It was observed that the circulation time of the two counter rotating vortices decreased for increasing Fr, while the mean vortex diameter increased.

A Reynolds decomposition analysis was carried out to estimate the energy content of the large scale periodic motion produced by the orbital movement of the shaker table and of the velocity fluctuations induced by random and cycle to cycle variations for a fluid of low viscosity. When the periodic flow incurs in a transition to out-of-phase flow, the onset of a laminar-turbulent flow transition also occurs, as indicated by the variation of the kinetic energy content of the random and cycle to cycle velocity fluctuations with Fr. It was shown that for in-phase conditions the flow is laminar with negligible kinetic energy of the random velocity fluctuations.

The distribution of the viscous dissipation rate of kinetic energy in the cylinder and estimates of the volumetric power consumption were obtained with PIV and temperature measurements. In agreement with the works of Zhang *et al.* (2005) and Zhang *et al.* (2008) it was found that most of the energy dissipation occurs over a very narrow region next to the reactor walls. Considerable attention was paid to the effects of the spatial resolution on the estimation of the energy dissipation rate and Kolmogoroff scale. For high spatial resolution, $\frac{\Delta x_i}{d_i} < 5\times10^{-3}$, the estimates of the energy dissipation rate and Kolmogoroff scale showed a significant increase and decrease, respectively. The power consumption estimates obtained from PIV and temperature measurements showed a reasonable agreement, and were consistent with those obtained by Klöckner *et al.* (2012) for a similar system through torque measurements.

In Chapter 5 the study focused on the flow dynamics and characteristics occurring in a cylindrical bioreactor when newtonian fluids of viscosity higher than water are used. Similarly to the research carried out for water, the variation of the free surface wave amplitude with Fr was investigated for fluids of increasing viscosity. A linear relationship was found between $\varDelta h/d_i$ and Fr, and the constant of proportionality a_o, was found to decrease with a power law for increasing fluid viscosity. This allowed to formulate Equation 5.1 and extend the scaling law to fluids of viscosity higher than water.

A thorough analysis of the phase resolved flow fields showed that the in-phase and out-phase flow characteristics associated to a toroidal and precessional vortices, respectively, did only occur for fluid of low viscosity with $\nu \leq 1.7\times10^{-6}$. The in phase flow of fluids of higher viscosity was characterised by a vortical structure observed below the lowest side of the free surface and extending towards the bottom of the tank with increasing Fr. On the contrary a toroidal vortex with a central downward stream is formed below the wavy free surface when the flow is out of phase and $\nu > 1.7\times10^{-6}$ m^{2}s$^-$1. Measurements on horizontal planes allowed to determine the degree of out of phase occurring for different fluid viscosity. It was found that viscosity significantly promotes out of phase transition $\nu > 1.7\times10^{-6}$ m^{2}s$^-$1, with the flow of silicon oils of $10\nu_w$ and $100\nu_w$ being out of phase by 21° and 41°, respectively (cf. Figures 5.13 and 5.15).

The different flow dynamics occurring for high and low viscous fluids were summarised in a flow transition map based on Fr and Re, where four main regions were identified to discriminate between the different in phase and out of phase flows associated to different ν. An investigation was carried out to assess how the turbulence levels changed with varying Fr and Re. It was found that turbulence levels rise when a low viscous fluid is considered and the flow is out of phase (i.e. combination of high Fr and Re). The variation of the turbulent kinetic energy content was further investigated considering three different Re obtained with combinations of ν and d_i. The data show that turbulence growth is promoted or retarded depending on the transitional Fr set by the operating conditions (i.e. d_o, d_i, ν, N, h). Even data for the same Re displayed different behaviour, with turbulence content of more viscous fluids obtained in a larger cylinder rising at a lower transitional Fr_c than that obtained with water in a smaller one.

To better compare the data sets obtained at different Re and overcome their differences in terms of transitional Fr_c, a turbulent kinetic energy scaling methodology based on the ratio Fr/Fr_c was proposed in Figure 5.25. This normalisation proved to be effective as the curves associated to the different Re collapsed on each other. Finally a 2D analysis was carried out to investigate the strain and shear rates in the cylindrical bioreactor. A linear increase with Froude number was observed for the space averaged strain/shear rate considered, with the axial strain and shear rates, $|S_{zz}|^*$=$|S_{rz}|^*$=0-1.4πN, being greater than the radial strain rate, $|S_{rr}|^*$=0-1πN, over the Froude number range investigated.

6.3 Recommendations for future work

The results presented in this thesis shed light on the flow dynamics of shaken bioreactors and on the influence of critical non-dimensional operating parameters on the transport phenomena of such vessels. Flow characteristics, such as circulation time, vortex size, viscous dissipation rate, interfacial area and strain/shear rates can improve process design methodologies and help guide the selection of optimal feed insertion locations to enhance mixing performances. Physical insight suggests that insertion at the edges of the vortical structures should produce faster mixing because of the greater dissipation rate levels, but this should be further investigated through mixing time measurements. From this point of view the validity of the flow scaling law determined in Chapters 3 and 5 should be further assessed by using mixing time measurements based on pH-colorimetric method, while laser induced fluorescence technique could bring a deeper insight into the “convection” and “diffusion” zones identified in this study. More over the implications of turbulence on mixing time and on cell cultures should be further investigated for cylinder of different sizes to further assess the exploitability of the scaling law based on Fr/Fr_c.

The single phase measurement of the current work should be extended to two phase solid-liquid flows with the intent to gain a better understanding of the flow dynamics in an orbitally shaken bioreactor when cells are attached to microcarriers or grown inside microcapsules. It might be possible that the presence of the solid phase would suppress part of the turbulence and possibly retards the laminar to turbulent flow transition.

Future work should also address the fluid and mixing of shaken vessel of more complex geometries. To the author knowledge this thesis is the first to provide a thorough experimental investigation on the flow of a shaken bioreactor, and a similar analysis could be carried out on flasks, cylindrical geometry with different bottom shapes and or baffled reactor. The flow scaling law identified in this work could be extended to other geometries and used as a benchmark to correlate different types of orbitally shaken reactors.

References

Baldi, S. and M. Yianneskis (2003). On the direct measurement of turbulence energy dissipation in stirred vessels with PIV. *Ind. Eng. Chem. Res.* ***42***, 7006–7016.

Barret, T. A., A. Wu, H. Zhang, M. Levy, and G. Lye (2009). Microwell engineering characterisation for mammalian cell culture process development. *Biotechnol Bioeng.* ***105***, 260–275.

Bouremel, Y. (2010). *On the circulation, strain dynamics and scalar mixing in vortical flows.* Ph. D. thesis, King's College London, University of London, United Kingdom.

Bouremel, Y., M. Yianneskis, and A. Ducci (2009). On the utilisation of vorticity and strain dynamics for improved analysis of mixing in stirred vessels. *Chem. Eng. Res. Des.* ***87***, 377–385.

Büchs, J. (2001). Introduction to advantages and problems of shaken cultures. *Biochemical Eng. J.* ***7***, 91 – 98.

Büchs, J., S. Lotter, and C. Milbradt (2001). Out-of-phase operating conditions, a hitherto unknown phenomenon in shaking bioreactors. *Biochemical Eng. J.* ***7***, 135–141.

Büchs, J., U. Maier, C. Milbradt, and B. Zoels (2000a). Power consumption in shaking flasks on rotary shaking machines: II. Nondimensional description of specific power consumption and flow regimes in unbaffled flasks at elevated liquid viscosity. *Biotechnol Bioeng.* ***68***, 594–601.

Büchs, J., U. Maier, C. Milbradt, and B. Zoels (2000b). Power consumption in shaking flasks on rotatory shaking machines: I. Power consumption measurement in unbaffled flasks at low liquid viscosity. *Biotechnol Bioeng.* ***68***, 589–593.

Butcher, M. and W. Eagles (2002). Fluid mixing re-engineered. *The Chemical Engineer* ***733***, 28–29.

Discacciati, M., D. Hacker, A. Quarteroni, S. Quinodoz, S. Tissot, and F. Wurm (2013). Numerical simulation of orbitally shaken viscous fluids with free surface. *Int. J. Numer. Meth. Fluids* ***71***, 294–315.

Doig, S., S. Pickering, G. Lye, and F. Baganz (2005). Modelling surface aeration rates in shaken microtitre plates using dinmensionless groups. *Chem. Eng. Sci.* ***60***, 2741–2750.

Doulgerakis, Z. (2010). *Large scale vortex and strain dynamics in mixing vessels and implications for macro-mixing enhancement.* Ph. D. thesis, King's College London, University of London, United Kingdom.

Doulgerakis, Z., M. Yianneskis, and A. Ducci (2011). On the manifestation and nature of macro-instabilities in stirred vessels. *AIChE J.* ***57***, 2941–2954.

Ducci, A. (2004). *Direct measurement of the viscous dissipation rate of turbulent kinetic energy in a stirred vessel with two-point LDA.* Ph. D. thesis, King's College London, University of London, United Kingdom.

Ducci, A., Z. Doulgerakis, and M. Yianneskis (2008). Decomposition of flow structures in stirred reactors and implication for mixing enhancement. *Ind. Eng. Chem. Res.* ***47***, 3664–3676.

Ducci, A. and M. Yianneskis (2005). Direct determination of dissipation rate in stirred vessels with multi-channel LDA. *AIChE J.* ***51***, 2133–2149.

Ducci, A. and M. Yianneskis (2007). Vortex identification methodolgy for feed insertion guidance in fluid mixing processes. *Chem. Eng. Res. Des.* ***85***, 543–550.

Escudie, R., D. Bouyer, and A. Line (2004). Characterisation of trailing vortices generated by a rushton turbine. *AIChE J.* ***49***, 585–603.

Escudié, R. and A. Liné (2003). Experimental analysis of hydrodynamics in a radially agitated tank. *AIChE J. 49*(3), 585 – 603.

Gardner, J. and G. Tatterson (1992). Characterization of mixing in shaker table containers. *Biotechnol Bioeng.* ***39***, 794–797.

Henzler, H. and M. Schedel (1991). Suitability of the shake flask for oxygen supply to microbial cultures. *Bioproces. Eng.* ***7***, 123–131.

Hermann, R., N. Walther, U. Maire, and J. Büchs (2001). Optical method for the determination of the oxygen-transfer capacity of small bioreactor based on sulfite oxidation. *Biotechnol Bioeng.* ***74***, 355–363.

Kaeppel, M. (1979). Development and application of a method for measuring the mixture quality of miscible liquids. *Int. Chem. Eng.* ***2***, 196–215.

Kato, Y., S. Hiraoka, Y. Tada, and T. Nomura (2001). Performance of a shaking vessel with current pole. *Biochemical Eng. J.* ***7***, 143–151.

Kato, Y., S. Hiraoka, Y. Tada, K. Sato, and T. Ohishi (1997). Measurement of mass transfer rate from free surface in shaking vessel type bioreactor. *J. Chem. Eng. Japan* ***30***, 362–365.

Kato, Y., H. Honda, S. Hiraoka, Y. Tada, T. Kobayashi, K. Sato, T. Saito, T. Nomura, and T. Ohishi (1997). Performance of shaking vessel-type bioreactor with current pole. *J. Fermen. Bioeng.* ***84***, 65–69.

Kato, Y., C. Peter, A. Akgün, and J. Büchs (2004). Power consumption and heat transfer resistance in large rotary shaking vessels. *Biochemical Eng. J.* ***21***, 83 – 91.

Kim, H. and P. Kizito (2009). Stirring free surface flows due to horizontal circulatory oscillation of partially filled container. *Chem. Eng. Commun.* ***11***, 1300–1321.

Klöckner, W. and J. Büchs (2012). Advances in shaking technologies. *Trends Biotechnol.* ***30***, 307–314.

Klöckner, W., S. Tissot, F. Wurm, and J. Büchs (2012). Power input correlation to characterize the hydrodynamics of cylindrical orbitally shaken bioreactors. *Biochemical Eng. J.* ***65***, 63–69.

Koelling, M. and K. Chalmers (2002). Fabrication and use of a transient contractional flow device to quantify the sensitivity of mammalian and insect cells to hydrodynamic forces. *Biotechnol Bioeng.* ***80***, 428–437.

Konstantinidis, E. (2001). *Pulsating Flow in Cylinder Arrays.* Ph. D. thesis, King's College London, University of London, United Kingdom.

Lara, A., E. Galindo, O. Ramirez, and L. Palomares (2006). Living with heterogeneities in bioreactor. *Molec. Biotechnol.* ***34***, 355–381.

Lavery, M. and A. Nienow (1986). Oxygen transfer in animal cell culture medium. *Biotechnol Bioeng.* ***30***, 368–373.

Maier, U., M. Losen, and J. Büchs (2004). Advances in understanding and modeling the gas-liquid mass transfer in shake flasks. *Biochemcial Eng. J.* ***17***, 155–167.

Mantell, S. and H. Smith (1983). Cultural factors that influence secondary metabolite accumulations in plant cell and tissue cultures. *Plant Biotchnol. Cambridge Uni. Press* ***2***, 75–108.

Massey, B. (1990). *Mechanics of Fluids.* Chapman and Hall, London.

McDaniel, L., E. Bailey, and A. Zimmerli (1965). Effect of oxygen supply rates on growth of escherichia coli. i. studies in unbaffled and baffled shake flasks. *Applied Microbio.* ***13***, 109–114.

Melton, L., C. Lipp, R. Sprading, and K. Paulson (2002). DISMT-determination of mixing time through color changes. *Chem. Eng. Commun.* ***3***, 322–338.

Micheletti, M., T. Barret, S. Doig, F. Baganz, M. Levy, J. Woodley, and G. Lye (2006). Fluid mixing in shaken bioreactors: Implications for scale-up predictions from microlitre-scale microbial and mammalian cell cultures. *Chem. Eng. Scien.* ***61***, 2939–2949.

Moffat, R. (1988). Describing the uncertainties in experimental results. *Exper.Thermal Fluid Sci.* ***1***, 3–17.

Pena, C., C. Peter, J. Büchs, and E. Galindo (2007). Evolution of the specific power consumption and oxygen transfer rate in alginate-producing cultures of azotobacter vinelandii conducted in shake flasks. *Biochemical Eng. J.* ***36***, 73–80.

Peter, C., S. Lotter, U. Maier, and J. Büchs (2004). Impact of out-of-phase conditions on screening results in shaking flask experiments. *Biochemical Eng. J.* ***17***, 205–215.

Peter, C., Y. Suzuk, K. Rachinskiy, S. Lotter, and J. Büchs (2006June). Volumetric power consumption in baffled shake flasks. *Chem. Eng. Sci.* ***61***, 3771–3779.

Raffel, M., C. Willert, S. Wereley, and J. Kompenhans (1998). *Particle image velocimetry: A practical guide.* Springer.

Rodriguez, G., W. Weheliye, T. Anderlei, M.Micheletti, M.Yianneskis, and A. Ducci (2013). Mixing time and kinetic energy measurements in a shaken cylindrical bioreactor. *Chem. Eng. Res. Des. 81*, 331–341.

Rutherford, K., K. C. Lee, S. M. S. Mahmoudi, and M. Yianneskis (1996). Hydrodynamic characteristics of dual impeller stirred reactors. *AIChE J. 42*, 332–346.

Sharp, K. and R. Adrian (2001). PIV study of small-scale flow structure around a rushton turbine. *AIChE J.* ***47***, 766–778.

Suh, Y. (2000). Analysis of linear viscous flow with a free surface in a circular cylinder subjected to small-amplitude circular oscillations. *Theoret. Computat. Fluid Dynamics* ***14***, 109–134.

Suijdam, J., N. Kossen, and A. Joha (1978). Model for oxygen trasnfer in a shake flask. *Biotechnol Bioeng.* ***20***, 1695–1709.

Sumino, Y. and S. Akiyama (1987). Measurement of the overall volumetric coefficient of heat transfer of a shaking flask. *J. Fermen.Technol.* ***65***, 285–289.

Sumino, Y., S. Akiyama, and H. Fukuda (1972). Performance of the shaking flask. *J. Fermen.Technol.* ***50***, 203–208.

Tan, R., W. Eberhard, and J. Büchs (2011). Measurement and characterization of mixing time in shake flasks. *Chem. Eng. Sci.* ***66***, 440–447.

Tissot, S., M. Farhat, D. Hacker, T. Anderlei, and M. Kühner (2010). Determination of a scale-up factor from mixing time studies in orbitally shaken bioreactors. *Biochemical Eng. J.* ***52***, 181–186.

Veljkovic, V., S. Nikolic, M. Lazic, and C. Engeler (1995). Oxygen transfer in flasks shaken on orbital shakers. *Hem. Ind.* ***49***, 265–272.

Weheliye, W., G. Rodriguez, T. Anderlei, M. Micheletti, M. Yianneskis, and A. Ducci (2012). Appraisal of shaken bioreactor mixing efficiency for different operating conditions. In *Proc. of the 14th European Conference on Mixing*, pp. 503–508.

Weheliye, W., M. Yianneskis, and A. Ducci (2012a). On the flow dynamics and out-of-phase phenomena in orbitally shaken bioreactors. In *Proc. of the 14th European Conference on Mixing*, pp. 509–514.

Weheliye, W., M. Yianneskis, and A. Ducci (2012b). Piv measurements in a shaken cylindrical bioreactor. In *Proc. 16th Int. Symposium on Applications of Laser Techniques to Fluid Mechanics.*

Weheliye, W., M. Yianneskis, and A. Ducci (2013). On the fluid dynamics of shaken bioreactors - flow characterization and transition. *AIChE J. 59*, 334–344.

Zhang, H., W. Dalson, E. Moore, and P. Shamlou (2005). Computational fluid dynamics (CFD) analysis of mixing and gas liquid mass transfer in shake flasks. *Biotechnol. Applicat. Biochemical* ***41***, 1–8.

Zhang, H., S. Lamping, S. Pickering, G. Lye, and P. Shamlou (2008). Engineering characterisation of a single well from 24-well and 96-well microtitre plates. *Biochemical Eng. J.* ***40***, 138–149.

Zhang, X., C. Bürki, M. Stettler, D. Sanctis, M. Perrone, M. Discacciati, N. Parolini, M. DeJesus, D. Hacker, A. Quarteroni, and F. Wurm (2009). Efficient oxygen transfer by surface aeration in shaken cylindrical containers for mammalian cell cultivation at volumetric scales up to 1000 l. *Biochemical Eng. J.* ***45***, 41–47.

Zhang, X., M. Stettler, D. D. Sanctis, M. Perrone, N. Parolini, M. Discacciati, M. D. Jesus, D. Hacker, A. Quarteroni, and F. Wurm (2010). Use of orbital shaken disposable bioreactors for mammalian cell cultures from the milliliter-scale to the 1000-liter scale. *Advan. Biochem. Eng. Biotechnol.* ***115***, 33–53.